TU Delft

Delft University of Technology

Simulation of Electron-Matter Interaction in Electron Beam Lithography and Metrology

Arat, K.T.

DOI
10.4233/uuid:52c5c8c7-edc7-4cf8-9945-bcd94e30f9d8

Publication date
2021

Document Version
Final published version

Citation (APA)
Arat, K. T. (2021). *Simulation of Electron-Matter Interaction in Electron Beam Lithography and Metrology*. [Dissertation (TU Delft), Delft University of Technology]. https://doi.org/10.4233/uuid:52c5c8c7-edc7-4cf8-9945-bcd94e30f9d8

Important note
To cite this publication, please use the final published version (if applicable).
Please check the document version above.

Copyright
Other than for strictly personal use, it is not permitted to download, forward or distribute the text or part of it, without the consent of the author(s) and/or copyright holder(s), unless the work is under an open content license such as Creative Commons.

Takedown policy
Please contact us and provide details if you believe this document breaches copyrights.
We will remove access to the work immediately and investigate your claim.

This work is downloaded from Delft University of Technology.
For technical reasons the number of authors shown on this cover page is limited to a maximum of 10.

Simulation of Electron-Matter Interaction in Electron Beam Lithography and Metrology

Simulation of Electron-Matter Interaction in Electron Beam Lithography and Metrology

Dissertation

for the purpose of obtaining the degree of doctor
at Delft University of Technology
by the authority of the Rector Magnificus, Prof.dr.ir. T.H.J.J. van der Hagen,
chair of the Board for Doctorates
to be defended publicly on Wednesday 9, June 2021 at 12:30 o'clock

by

Kerim Tuğrul ARAT

Master of Engineering in Electrical Engineering & Information Technology
Rosenheim University of Applied Sciences, Germany
born in Samsun, Turkey.

This dissertation has been approved by the promotors.

Composition of the doctoral committee:

Rector Magnificus,	chairperson
Dr. C.W. Hagen	Delft University of Technology, promotor
Prof.dr.ir. P. Kruit	Delft University of Technology, promotor
Independent members:	
Prof.dr. W.M.J.M. Coene	Delft University of Technology
Prof.dr.ir. J.L. Kloosterman	Delft University of Technology
Prof.dr. P.A. Bobbert	Eindhoven University of Technology
Dr. M. Belhaj	ONERA, France
Other member:	
Diplom.-Phys. U. Hofmann	GenISys GbmH, Germany







The work in this dissertation was conducted at the department of Imaging Physics, Faculty of Applied Sciences, Delft University of Technology.

Printed by: Ridderprint | www.ridderprint.nl

ISBN: 978-94-6384-222-8

Cover Design: Yasmin Katlich, Persoonlijk Proefschrift

Description: When high energetic beam electrons enter the material, they start scattering. The scattering volume resembles a tulip bulb or onion (see figures 4.2 and 7.1). When this so-called ”onion” intersects with another surface, such as the sidewall of a topographic edge, more electrons escape from the material. As a result, the number of detected electrons increases, and so the signal does. We call this phenomenon ”edge blooming” (see figure 3.9).
The tulip on the cover not only illustrates this edge blooming phenomenon but also symbolizes my own personal journey. The tulip has become an icon nearly synonymous with the Netherlands, where I have done this research. But tracing this flower to its roots reveals another connection: the tulip, like me, found its way from Turkey to the Netherlands.

Copyright © 2021 by K. T. Arat

An electronic version of this dissertation is available at
http://repository.tudelft.nl/.

”When I had all the answers,
the questions changed.”

Paulo Coelho

Contents

Summary **11**

Samenvatting **13**

1 Introduction **17**
1.1 Introduction . . . 18
1.2 Semiconductor manufacturing process: lithography & inspection . . . 18
1.3 Challenges in electron microscopy and lithography . . . 20
1.4 Simulations as part of the solution . . . 20
1.5 Monte Carlo simulations . . . 23
1.6 Scope of the thesis . . . 27
References . . . 28

2 Monte Carlo Simulators: Theory Models and Experimental Verification **35**
2.1 Introduction . . . 36
2.2 Electron scattering . . . 36
2.3 Physics models in simulators . . . 38
2.3.1 e-Scatter . . . 39
2.3.2 virtualSEM . . . 53
2.4 Description of a ”good” experimental reference . . . 58
2.4.1 Literature examples for yield measurements with charging . 59
2.5 Emission properties . . . 61
2.5.1 SE yield . . . 61
2.5.2 BSE yield . . . 65
2.5.3 BSE yield vs. incidence angle . . . 68
2.5.4 Angular emission . . . 69
2.5.5 Energy spectra . . . 70
2.6 Conclusions . . . 70
References . . . 73

3 Model Sensitivity Analysis of Monte Carlo Based SEM Simulations **79**
3.1 Introduction . . . 80
3.2 Models . . . 81
3.2.1 Elastic scattering models . . . 82
3.2.2 Inelastic scattering models . . . 84
3.2.3 Boundary crossing models . . . 85

3.3 Methods . . . 85
3.4 Results . . . 87
3.4.1 Consequences for 2D measurements . . . 87
3.4.2 Consequences for 3D measurements . . . 91
3.5 Comparison with CASINO and JMONSEL . . . 92
3.6 Comparison with experiments . . . 95
3.7 Model-affected simulation time . . . 96
3.8 Discussion . . . 98
3.9 Conclusion . . . 98
References . . . 99

4 Model Improvements to Simulate Charging 103
4.1 Introduction . . . 104
4.2 Scattering model . . . 105
4.2.1 Improvements on elastic scattering cross-sections . . . 106
4.2.2 Improvements on inelastic scattering cross-sections . . . 107
4.2.3 Improvements on boundary cross-sections . . . 109
4.3 Charging Model . . . 110
4.3.1 Electric field solver . . . 110
4.3.2 Tracing electrons . . . 112
4.3.3 Modeling of sample charging . . . 112
4.3.4 Induced conductivity . . . 112
4.3.5 Dielectric breakdown . . . 113
4.4 Results . . . 114
4.4.1 Effect of new scattering models - no charge up scenarios . . . 114
4.4.2 Effect of model improvements on SE emission . . . 115
4.4.3 Effect of model improvements on the grating coupler simulations . . . 117
4.4.4 Effect of the EBIC model . . . 120
4.5 Discussion . . . 122
4.6 Conclusions . . . 124
References . . . 125

5 Charge-Induced Pattern Displacement in E-Beam Lithography 129
5.1 Introduction . . . 130
5.2 Modeling . . . 130
5.2.1 Monte Carlo simulator . . . 130
5.2.2 Test pattern: Dot matrix . . . 131
5.2.3 Simulations . . . 131
5.3 Experiment . . . 135
5.3.1 Fabrication of the patterns . . . 135
5.3.2 Exposure layout . . . 136
5.3.3 Inspection . . . 137
5.3.4 Image processing . . . 138
5.4 Results . . . 138
5.5 Conclusions . . . 142
References . . . 143

6 E-Beam Lithography on Curved or Tilted Surfaces: Simulations and Experiments **147**
6.1 Introduction 148
6.2 Monte Carlo simulator 149
6.3 Point exposure of resist on a curved surface 150
6.4 Proximity effect corrected patterning of tilted surfaces 152
6.5 Experiments 157
6.6 Discussion 162
6.7 Conclusion 163
References 163

7 Estimating Step Heights from Top-Down SEM Images **167**
7.1 Introduction 168
7.2 Theory and simulation 169
7.3 Experiments 175
7.4 Discussion 181
7.5 Experiments 183
References 184

8 Valorization **187**
References 188

9 Conclusion **189**
9.1 Monte Carlo simulator, SEM signal, and the CD measurement . . .189
9.2 3D effects 190
9.3 Charging 190

Acknowledgements **193**

Curriculum Vitæ **197**

Summary

Integrated circuit (IC) technology lies at the heart of today's digital world. The immense amount of computational power that came along with the downscaling of circuits allowed us to place faster and smaller chips almost everywhere. However, with today's requirements, even a one-nanometer error on those chips can drastically change the performance of the chip. Therefore, maintaining product quality is challenging, and more accurate techniques are needed to manufacture future generation chips.

Electron beam based techniques are known to provide very high resolution both in production and testing of these chips. However, the ongoing trend is also challenging the established e-beam technologies.

Two common problems in both imaging and lithography are addressed in the thesis. One of them is the emerging importance of the 3rd dimension (3D) in imaging and lithography. The other one is the notorious charging effect when the samples involved, such as gate oxides, are not sufficiently electrically conductive. The experimental trial and error approach to understand and solve these problems is too time-consuming and can also be very expensive. Therefore, tools such as Monte Carlo simulations are needed that aid in getting a better fundamental understanding of these issues. The development of a simulator that can help to find solutions for the problems above is one of the primary objectives of this thesis.

Previously, as a master's student, I developed an electric field solver based on a multigrid method to boost the calculation times of charging simulations in virtualSEM, a Monte Carlo simulator developed by GenISys-GmbH based on approximate low energy electron scattering models. At MInT (former CPO), a graphical processing unit (GPU) accelerated Monte Carlo program (e-Scatter) has been developed with the best possible low energy electron-matter scattering models, but no electric field solver and charging model. Therefore it makes sense to combine e-Scatter, with its first principle scattering models, and virtualSEM, with its electric field solver, to obtain a better simulator, including charging. Furthermore, we wanted to add dynamic recombination models. We have set ourselves the task to develop this combined Monte Carlo simulator and use it for applications in the fields of metrology and lithography.

The first step was to test and develop e-Scatter and then study how sensitive simulated emission properties and SEM images are to the various model ingredients implemented in the simulator. The next step was to build the first principle and physically more sophisticated scattering models into virtualSEM, which already contained an advanced electric field solver and allowed for material charging. This way, a tool was obtained with accurate physics models and charging capability. Finally, the simulators developed were used to develop industry-driven applications involving complex geometries (3D) and charging effects in microscopy and lithography. These applications serve a three-fold purpose. They are leading to novel techniques for nanofabrication and inspection, they serve as very nice test cases of the simulation models, and they

serve as intuitive demonstrations of how Monte Carlo simulations can be used to solve semiconductor industry problems.

Simulation results are compared with various experimental data such as electron yields, angular and energy distributions of emitted electrons. The overall agreement between simulated and experimental data is promising. Although the simulator predicts a higher absolute secondary electron yield than experimental data (in general), the trend of the yield curves is predicted correctly. Simulated angular and energy distributions of the secondary electron emission (of copper) agree well with experimental data. Furthermore, the backscattered electron yield as a function of energy (in general) and incidence angle (for silicon) also agrees well with the experimental data. The agreement between simulated and experimental yield as a function of incidence angle provides more confidence in distributions of electrons in the material and more accurate dimensional metrology.

It is worth mentioning that it is hard to find reliable experimental data. Even data measured under ultra high vacuum conditions show considerable spread. For future experimental works, some important points for a well-defined experiment is discussed.

A detailed sensitivity analysis of model ingredients on simulated results is performed, demonstrating the importance of understanding how the different physics models affect the results. 2D critical dimension (CD) measurements are not sensitive to the model ingredients. However, linescan data are influenced in a non-linear way by models such as the quantum mechanical boundary transmission coefficient and electron-acoustic phonon scattering. From this analysis, the models with the most significant impact on dimensional metrology are identified.

The lessons learned from the sensitivity analysis are used when improving the electron scattering models in virtualSEM to obtain more realistic simulated charge distribution profiles. Also charge redistribution models are introduced, and the electric field solver and ray-tracing are improved.

The charging effect in electron beam lithography is studied with a large set of experiments to understand the charge dynamics. On the one hand, the simulations give insight into the complex charging behavior, and on the other hand, the experiments help to verify the simulation models. As a result, a smart scan-strategy is found that minimizes pattern distortions caused by charging.

Simulations are also used to investigate a complex 3D problem in nanofabrication on curved surfaces (3D). Proof-of-principle experiments show that 3D features of the point spread function should be used to achieve accurate proximity effect correction.

Regarding 3D imaging, a novel technique is introduced to extract 3D information, i.e. step heights, from 2D SEM images by using simulations. The results are verified with three different sets of experiments.

In a nutshell, the predictive power of the Monte Carlo simulators has been increased. The results demonstrate that these simulations do not only provide good electron emission properties (yields, energy, and angular spectra, etc.) but can also be used in much more complex lithography and imaging applications, including 3D and charging effects.

Samenvatting

De technologie van de geïntegreerde cicuits (IC) vormt het hart van de huidige digitale wereld. De immense hoeveelheid rekenkracht die gepaard ging met het verkleinen van de circuits heeft het mogelijk gemaakt om bijna overal snellere en kleinere chips te plaatsen. Echter, met de eisen van vandaag kan zelfs een fout van één nanometer op die chips de prestaties van de chip drastisch veranderen. Daarom is het handhaven van de productkwaliteit een kuitdaging, en zijn nauwkeuriger technieken nodig om toekomstige generaties chips te vervaardigen.

Van technieken op basis van elektronenbundels is bekend dat zij zowel bij de productie als bij het testen van deze chips een zeer hoge resolutie kunnen opleveren. De huidige trend vormt echter ook een uitdaging voor de gevestigde elektronenbundel technologieën.

Twee gangbare problemen in zowel beeldvorming als lithografie worden in het proefschrift behandeld. Eén daarvan is het opkomende belang van de derde dimensie (3D) in beeldvorming en lithografie. De andere is het beruchte oplaadeffect wanneer de betrokken preparaten, zoals poortoxiden (gate-oxides), niet voldoende elektrisch geleidend zijn. De experimentele "trial and error" aanpak om deze problemen te begrijpen en op te lossen is te tijdrovend en kan ook zeer duur zijn. Daarom is er behoefte aan hulpmiddelen zoals Monte Carlo simulaties die helpen om een beter fundamenteel begrip van deze problemen te krijgen. De ontwikkeling van een simulator die kan helpen bij het vinden van oplossingen voor bovenstaande problemen is een van de hoofddoelen van dit proefschrift.

Eerder heb ik als masterstudent een elektrisch veld oplosmethod ontwikkeld op basis van een multigrid methode om de rekentijden van ladingsimulaties in virtualSEM, een Monte Carlo simulator ontwikkeld door GenISys-GmbH op basis van benaderende lage energie elektronenverstrooiingsmodellen, ter verminderen. Bij MInT (voormalig DO) is een GPU (graphical processing unit) versneld Monte Carlo programma (e-Scatter) ontwikkeld met de best mogelijke laagenergetische elektron-materiaal verstrooiingsmodellen, maar geen elektrisch veld oplosmethod en model voor oplading. Daarom is het zinvol om e-Scatter, met zijn fundamentele verstrooiingsmodellen, en virtualSEM, met zijn elektrisch veld oplosmethod, te combineren om een betere simulator te verkrijgen, inclusief oplading. Bovendien wilden wij dynamische recombinatiemodellen toevoegen. Wij hebben ons tot taak gesteld deze gecombineerde Monte Carlo simulator te ontwikkelen en te gebruiken voor toepassingen op het gebied van metrologie en lithografie.

De eerste stap was het testen en ontwikkelen van e-Scatter en vervolgens te bestuderen hoe gevoelig gesimuleerde emissie-eigenschappen en SEM-beelden zijn voor de verschillende modelbestanddelen die in de simulator zijn geïmplementeerd. De volgende stap was het inbouwen van fundamentele en fysisch meer verfijnde verstrooiingsmodellen in virtualSEM, dat reeds een geavanceerde elektrisch veld oplosmethod bevatte en materiaal oplading mogelijk maakte. Op deze wijze werd een programma

verkregen met nauwkeurige fysische modellen en opladingsmogelijkheden. Tenslotte werden de ontwikkelde simulatoren gebruikt voor de ontwikkeling van door de industrie aangedragen toepassingen waarbij complexe geometrieën (3D) en opladingseffecten in microscopie en lithografie een rol spelen. Deze toepassingen dienen een drieledig doel. Ze leiden tot nieuwe technieken voor nanofabricage en -inspectie, ze dienen als zeer mooie testcases van de simulatiemodellen, en ze dienen als intuïtieve demonstraties van hoe Monte Carlo simulaties gebruikt kunnen worden om problemen in de halfgeleiderindustrie op te lossen.

De simulatieresultaten worden vergeleken met verschillende experimentele gegevens zoals elektronenopbrengst, hoek en energieverdeling van uitgezonden elektronen. In het algemeneenis overeenkomst tussen gesimuleerde en experimentele gegevens veelbelovend. Hoewel de simulator een hogere absolute secundaire elektronenopbrengst voorspelt dan de experimentele gegevens (in het algemeen), wordt de trend van de opbrengstcurven correct voorspeld. De gesimuleerde hoek- en energieverdelingen van de secundaire elektronenemissie (van koper) komen goed overeen met de experimentele data. Ook de opbrengst van de teruggestrooide elektronen als functie van de energie (in het algemeen) en de invalshoek (voor silicium) komt goed overeen met de experimentele gegevens. De overeenkomst tussen de gesimuleerde en experimentele opbrengst als functie van de invalshoek geeft meer vertrouwen in de elektronenverdeling in het materiaal en een nauwkeuriger dimensionele metrologie.

Het is vermeldenswaard dat het moeilijk is betrouwbare experimentele gegevens te vinden. Zelfs gegevens gemeten onder ultrahoog vacuüm vertonen aanzienlijke spreiding. Voor toekomstige experimentele werkzaamheden wordt het belang van goed opgezette experimenten besproken.

Een gedetailleerde gevoeligheidsanalyse van modelbestanddelen op gesimuleerde resultaten wordt uitgevoerd, waaruit blijkt hoe belangrijk het is te begrijpen hoe de verschillende fysische modellen de resultaten beïnvloeden. 2D-metingen van de kritische dimensie (CD) zijn niet gevoelig voor de modelbestanddelen. Linescangegevens worden echter op niet-lineaire wijze beïnvloed door modellen zoals de kwantummechanische grensvlak transmissiecoëfficiënt en de elektron-akoestische fononverstrooiing. Uit deze analyse worden de modellen met de meest significante invloed op de dimensionele metrologie geïdentificeerd.

De lessen die uit de gevoeligheidsanalyse zijn getrokken, worden gebruikt bij het verbeteren van de elektronenverstrooiingsmodellen in virtualSEM om realistischer gesimuleerde ladingsverdelingsprofielen te verkrijgen. Ook ladingsherverdelingsmodellen worden geïntroduceerd, en de elektrisch veld oplosmethode en ray-tracing worden verbeterd.

Het opladingseffect in elektronenbundellithografie wordt bestudeerd met een groot aantal experimenten om de dynamica van de oplading te begrijpen. Enerzijds geven de simulaties inzicht in het complexe opladingsgedrag, en anderzijds helpen de experimenten om de simulatiemodellen te verifiëren. Als resultaat wordt een slimme scan-strategie gevonden die patroon-vervormingen ,veroorzaakt door het opladen, minimaliseert.

Simulaties worden ook gebruikt om een complex 3D probleem te onderzoeken bij nanofabricage op gekromde oppervlakken (3D). Proof-of-principle experimenten tonen aan dat 3D-eigenschappen van de point spread function gebruikt moeten worden om

een nauwkeurige correctie van het nabijheidseffect te bereiken. Wat 3D-beeldvorming betreft, wordt een nieuwe techniek geïntroduceerd om 3D-informatie, d.w.z. staphoogtes, te extraheren uit 2D SEM-beelden door gebruik te maken van simulaties. De resultaten worden geverifieerd met drie verschillende reeksen experimenten.

In een notendop, de voorspellende kracht van de Monte Carlo simulatoren is toegenomen. De resultaten tonen aan dat deze simulaties niet alleen goede elektronenemissieeigenschappen opleveren (rendementen, energie en hoekspectra, enz.), maar ook kunnen worden gebruikt in veel complexere lithografie- en beeldvormingstoepassingen, met inbegrip van 3D- en ladingseffecten.

1

Introduction

1

1.1. Introduction

Do you remember the Jetsons? This cartoon series depicted a utopic portrayal of the future. Smartwatches, robot workers, video-conferences via TV were ordinary things in the Jetsons' daily life. However, these were very extraordinary ideas when the cartoon series was first broadcasted in the mid-'60s.

Today, such innovations have become part of the ordinary. For most of us, it is hard to imagine a day without smartphones. Robots are already cleaning our houses and soon self-driving cars will be ready to bring us back home from the office. Furthermore, many other innovations such as ultra-fast internet with 5G platforms, medical diagnosis with artificial intelligence (AI), and the internet of things (IoT) are just around the corner.

How did this come true? Integrated circuit (IC) technology is the technology that lies at the heart of all these applications. Miniaturization of electronic circuits, governed by the celebrated Moore's law [1], enabled us to place more transistors (i.e., functionality) in the same area, allowing us to have more computer chips in smaller sizes since the beginning of the silicon age. For example, in 2019, the semiconductor industry has commercialized the so-called 7 nanometer (nm) process node [2] in smartphones and computers. This node is roughly 100 times smaller in one dimension than the one [3] in 1987. The reader may notice that reducing the transistor size by half (1/2) quadruples (4) the number of transistors (the density) on the chip area. That means computational power increased by four orders of magnitude in this period. Yet to come, in the mid-20s, is a 3 nm process node [4] where even a one nanometer error in the chip size can drastically change the electronic performance of the chip. Maintaining product quality is more challenging from both a technical and economic perspective with such kind of requirements. Therefore, we need very accurate, yet affordable, techniques for the manufacturing of chips. Thus, in this dissertation, I will focus on simulation work that helps us to understand the phenomena for two essential steps in the semiconductor manufacturing process: lithography and inspection. However, the understanding of the underlying electron-matter interaction phenomena is also essential in many other fields, such as the power losses in satellites [5], and radiation damage to DNA [6].

1.2. Semiconductor manufacturing process: lithography & inspection

The fabrication of a chip requires sophisticated and costly cleanroom processes. Fig. 1.1 shows a typical production workflow. In this workflow, one of the essential steps is lithography, where the designed pattern is transferred to the silicon wafer with high accuracy.

For consumer chips, the patterning is done by photo-lithography where deep (or extreme) ultraviolet light shines through (or is reflected by) a mask and falls on a wafer coated with photoresist. To create the mask, however, requires another high-

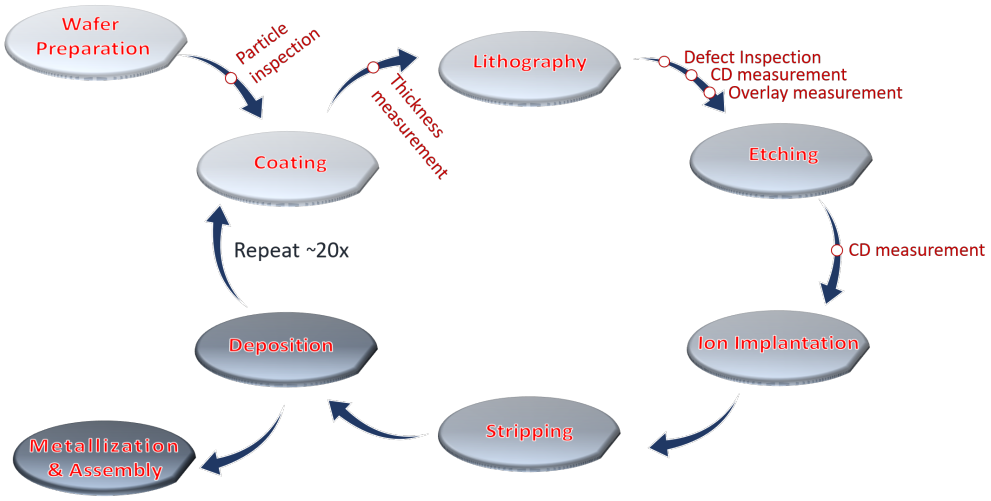


Figure 1.1: Overview of the beginning of a semiconductor manufacturing process. Inspection and metrology occurs in between many of the process steps. CD measurement refers to critical dimension measurement.

resolution and maskless technique. Electron beam lithography (EBL) is such a maskless (direct-write) technology which is often used for mask-making. Compared to light, the wavelength of an electron is ≈1000 times smaller at the same energy. For those not very familiar with the subject, the wavelength can be compared with the size of the brush of an artist who wants to draw fine details. Thus, EBL is suitable for very high resolution (< 10 nm) patterning. Besides, because of its flexibility, it is available in many research centers for prototyping. It is also used for low volume manufacturing of niche devices in aerospace, defense, and secure holograms for anti-counterfeiting. EBL is one of the application areas that I will focus on in this thesis.

During the production process, chips are inspected several times for particle contamination and defects. Furthermore, critical parameters (length, thickness, overlay) are tightly controlled (see Fig. 1.1). This is like the artist who wants to see what he is drawing. Electrons are being used for inspection, where very high resolution is needed to detect nanometer-size defects and deviations on the wafer.

The Scanning Electron Microscope (SEM) is a standard instrument for nanometer resolution imaging in many labs. It provides higher resolution than optical measurement methods. It is much faster compared to the Atomic Force Microscope (AFM). Furthermore, one does not need to slice the sample as in Transmission Electron Microscopy (TEM). Therefore, it is a good compromise of three crucial traits: high-resolution, moderate speed, and non-destructive imaging [7]. A dedicated version of the tool is the Critical Dimension (CD-)SEM, the workhorse in many fabs with which metrology tasks are performed on a massive scale. SEM is the second application area that I will address in this thesis.

1.3. Challenges in electron microscopy and lithography

SEMs do provide very high resolution, but are not easy-to-use. Even an expert SEM operator can spend tens of minutes on finding the best imaging conditions before actually recording an image, which may only take a few tens of seconds. The best conditions provide an image quality sufficient for accurate measurements; nevertheless, the precise system parameters and operating conditions will always influence the SEM image quality (observer effect). The question then is how this affects measurements taken from these images?

An emerging need in metrology is three dimensional (3D) imaging. SEM views the sample from a top-down (2D) perspective, and the signal amplitude (strength) does not directly correspond to the topography of the sample (see Fig. 1.2). This was never an important limitation, as long as the structure height was much smaller than its width. However, the height is becoming a more critical parameter since it has become comparable to the width of the structures. Therefore, new approaches are required, and I am going to propose one in this thesis.

Another major challenge in very high-resolution imaging is beam-induced sample charging occurring in samples which are not sufficiently electrically conductive. In such samples electrons and holes get trapped when exposed to an electron beam. These trapped charges in the material may influence the trajectories of the primary beam electrons as well as the electrons emitted from the sample. These are commonly observed effects of charging. As a consequence, the measurements taken from SEM images of such samples are affected by charging. A typical situation is depicted in Fig. 1.3 where the result obtained is different from the reality because the beam landing position has shifted because of the charging.

Similarly, EBL processes can be affected by sample charging. Charge induced in the sample will influence the electron beam trajectory and alter the lithography pattern. Fig. 1.4 clearly shows the distortion of a pattern due to charging. The charging effect, both in SEM imaging and in EBL, will be studied in more detail in this thesis.

To realize a cost-effective production, the problems mentioned above need to be addressed. Otherwise, the next generation electronics, required for novel applications, may not be as affordable as it is today or not even be technically feasible for many applications. Understanding and solving the charging problem experimentally is too time-consuming and also expensive. Therefore, tools such as simulations are needed that aid in getting a better fundamental understanding of these issues. The development of a simulator that can help to find solutions for the aforementioned problems is one of the primary objectives of this research work.

1.4. Simulations as part of the solution

Simulations are useful tools to predict real-world phenomena efficiently and risk-free. A real-life scenario can be predicted by simulations without the need to build

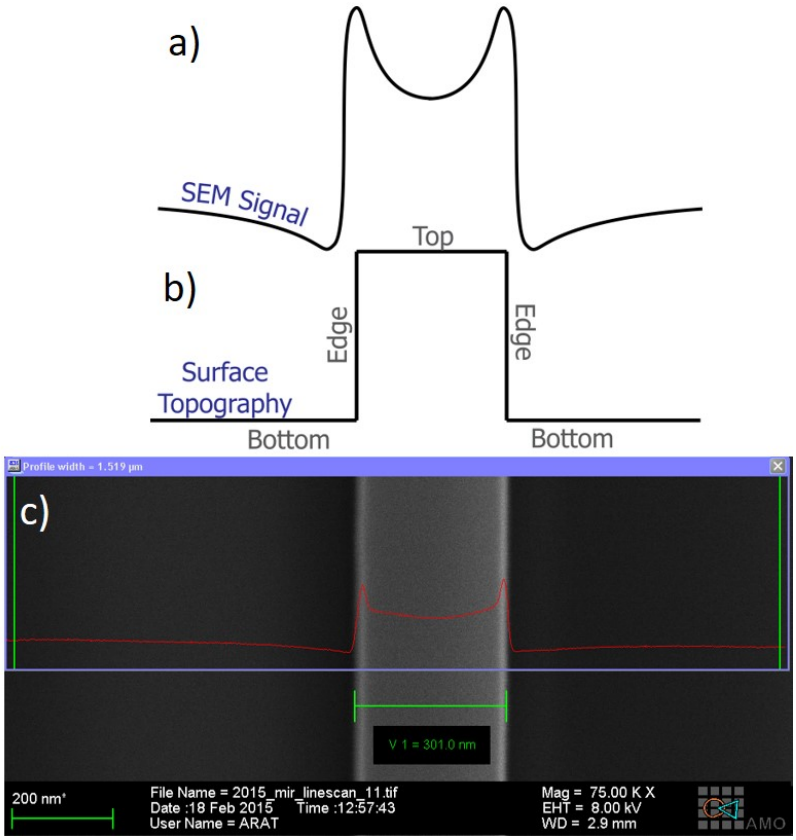


Figure 1.2: a) Typical SEM line scan signal over a line. b) The cross-sectional view of the line. c) Real top-down SEM image of the line. The signal increases near the top of an edge and decreases near the bottom. The surface topography can be measured as the width of the line with nanometer accuracy, e.g., between the peak maxima. However, the essential height information of the sample is hidden in compact grayscale images which are the result of a combination of electron-matter interaction, collection efficiency, detector response, and signal processing.

something or to do several test experiments. For instance, car-crash simulations help manufacturers to save on budgets for safety tests. For mask-makers, where the loss due to a defect on the mask can be as significant as the loss of a luxury car, the situation is similar.

Simulations can provide in-depth insights into the details of a process in a way that is often not possible in real life, because the models that describe the process can be easily changed. This allows one to investigate the effects of a phenomenon independently, and in much more detail.

Last but not least, it is an essential educational tool from which students and trainees can learn a lot. For example, airplane pilots have hundreds of hours of simulation training before they fly with real planes.

Semiconductor manufacturers also make use of various simulation tools. For exam-

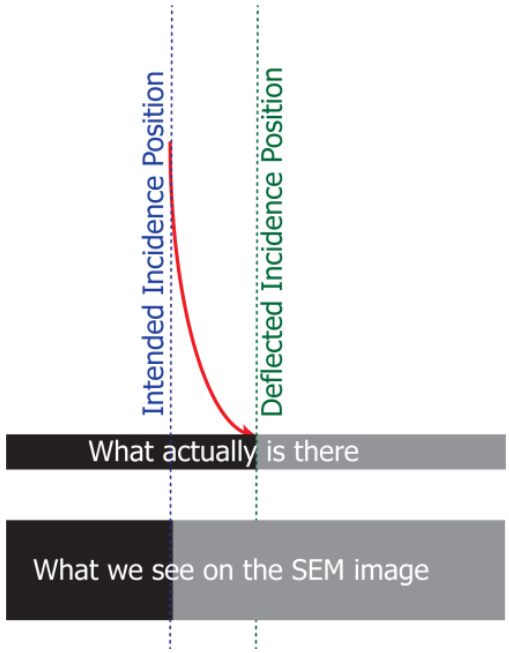


Figure 1.3: When a sample is charged, the detector in an SEM collects the data from the deflected position (red arrow), but assigns it to the intended location.

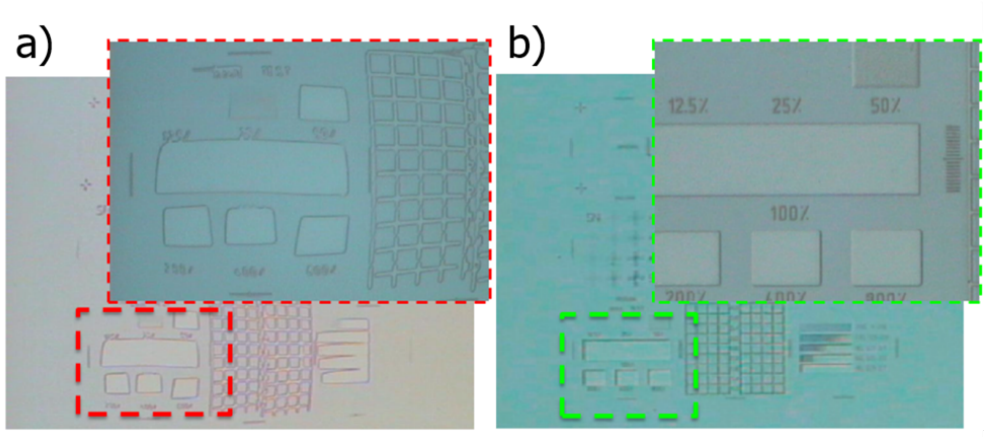


Figure 1.4: The charging effect has distorted a pattern defined by electron beam lithography. Optical images are shown of wafers with a) resist on insulator, and b) as a) but with an additional coating with a conductive polymer (espacer) [8]. The pattern fidelity clearly decreases without the conductive layer.

ple, computational lithography techniques such as e-beam proximity effect correction (PEC) or optical proximity correction (OPC) are already in use for more than a few decades.

In PEC, the effect of neighboring structures is calculated before the exposure is

being done, such that the measured CD's are the same as in the design, without costly experimental efforts. For instance, the spread of the electron beam in the material is an important parameter in these calculations, which can be obtained by using Monte Carlo simulation. Similar to this example, I will use Monte Carlo simulations to understand the 3D and charging effects in metrology and lithography, assuring that the simulators are accurate and fast, and that their limitations are well characterized.

1.5. Monte Carlo simulations

The first version of a Monte Carlo simulation was developed by Ulam et al. to investigate neutron scattering in materials as part of the Manhattan Project [9, 10]. The method is based on a statistical sampling of an event using random numbers, see Fig. 1.5. This is why it is called after a neighborhood in Monaco, well-known for its casinos.

Since then, several experimental, theoretical, and computational studies have contributed to the development of Monte Carlo simulations. I will continue with a brief coverage of the most prominent and relevant contributions.

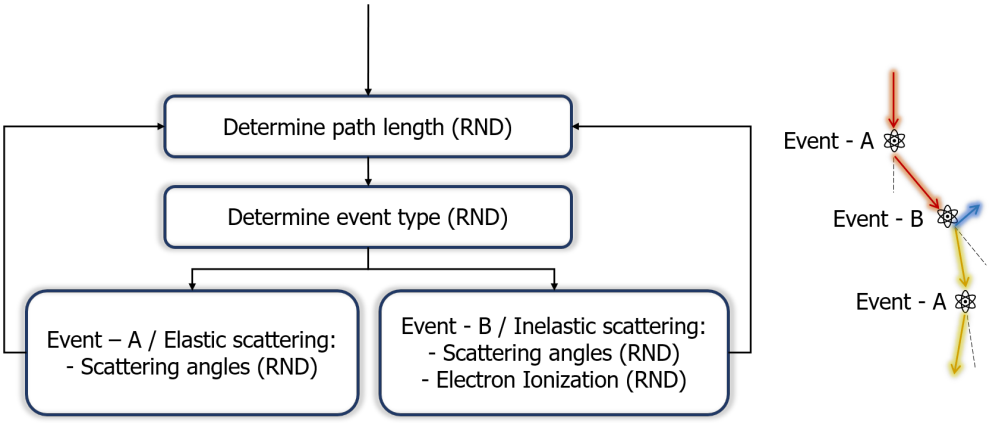


Figure 1.5: A generic flow diagram of a Monte Carlo process for electron – matter scattering. RND (random) indicates that the process involves random sampling.. The right-hand side cartoon visualizes what happens to an electron, which follows events in order of A, B, and A.

Monte Carlo simulations of electron-matter scattering require models such as elastic and inelastic scattering and boundary-crossing models. For instance, elastic scattering cross-sections have been calculated accurately by Mott [11] down to electron energies of a few hundred electronvolts (eV). Jablonski [12] compiled a database for elastic and transport cross-sections. However, Salvat developed a program (ELSEPA) [13], in which different atomic models can be chosen to calculate these cross-sections. In chapter 2 and chapter 3 of this thesis, we will see the effects of these options on backscattered electron (> 50 eV) emission and dimensional measurements.

Bethe's stopping power (SP) equation [14] is one of the most commonly used

expressions to model the inelastic phenomena. However, the model breaks down at very low energies, which is essential for us to simulate secondary electrons (< 50 eV). Rao-Sahib [15] and Joy [16] have modified the equation for those energies. While their CSDA-model (continuous slowing down approximation) is describing the energy loss per path length, it does not specify the inelastic channels, i.e., how the primary electron loses its energy. Lin[17] models and calibrates the electron generation based on empirical electron emission data. The advantage of this method and the pitfalls will be discussed in chapter 3 and chapter 4, respectively.

Differently, Gryzinski [18] described the inelastic atomic collisions in a discrete way. This approach can be used to model the inner-shell ionization[19] and can be integrated into the CSDA-model to simulate backscattering electrons more accurately [20]. A similar hybrid approach that also distinguishes fast secondary electrons, which is based on Moller cross-sections for light materials like resist, was proposed by Murata [21].

A more elaborate way of calculating inelastic scattering, especially for low energy electrons, is using the dielectric response of the material to an external perturbation. In this method, the primary electron's momentum and energy transfer to the medium have to be known. For example, Penn [22] calculated the inelastic scattering cross-sections based on the Lindhard dielectric function. Ashley [23] suggested a single-pole approximation to the calculation-heavy Penn model to connect the non-zero momentum energy loss function to the optical limit. However, the approximation is questionable for free-electron-gas-like materials at the energies comparable to the plasmon excitation energy [24]. However, the Lindhard-type dielectric function is itself questionable since it does not incorporate the finite lifetime of plasmons [25, 26]. This shortcoming is treated in the Mermin-type dielectric function [27]. Da proposed an extension to the Mermin theory with a better fit to the energy loss function by using an infinite number of positive and negative oscillators [28]. For most of the materials, optical constants and energy loss function can be found in Palik's book [29]. Alternatively, these can be calculated ab initio as performed by Sorini [30] and Werner [31].

Apart from the scattering models, surface effects are also very important since they directly influence the emission yield and energy spectrum. For instance, Kaneko [32] showed the effect of different transmission models (classical and quantum mechanical) on the emission spectra. And Cazaux [33] studied the effect of the work function on the secondary electron emission. The study highlights the impact of the surface condition in experiments, which are used to verify the Monte Carlo simulators. The emission data from ultra-high vacuum (UHV) experiments and the different surface treatments by Bronstein [34], Gineste [35], Hu [36], Walker [37], El Gomati [38], and Baglin [39] demonstrate the variation in yield values as reported in Joy's database [40]. In chapter 2 of the thesis, the value of good (well-described) experiments will be discussed. Another phenomenon that may affect electron emission is surface plasmons. These excitations mainly show up as another energy loss process in the energy spectra

of emitted electrons. Werner has studied the effect of bulk and surface plasmons on the energy spectra by REELS [31, 41] (reflective electron energy loss spectroscopy) and coincidence experiments [42, 43]. Gong has performed a Monte Carlo simulation study to show the effect of surface plasmons on the energy spectra for Silver [44]. In a recent simulation study by van Kessel [45] it is reported that the effect of surface plasmons may not be observable in the emission yield. In other words, a surface plasmon model is needed to simulate the energy spectra accurately, but to simulate an SEM image, the model is not essential. That tells us that the significance of the effect that details of a model, or even an entire model, have on a simulation result, depends on the particular application. This will be discussed throughout the thesis.

Powell [46], Tanuma [47], and Gergely [48, 49] reported valuable comparisons between calculated and experimental scattering cross-sections. A common conclusion is that, especially inelastic scattering cross-sections obtained from different theoretical and experimental works differ from each other at low energies. This variation causes an uncertainty in secondary electron emission. This will be discussed in chapter 2.

There are also full Monte Carlo studies done that analyse the effects of the various models on simulation results. For example, Dapor [50] studied the effect of assumptions for the instantaneous momentum of the secondary electron in the binary collision model. The effect of the same model assumption is studied on 3D structures in chapter 3 of this thesis. Dapor also compared the effects of single and multiple scattering inelastic models [51, 52]. Hovington developed the Monte Carlo program CASINO [53], which is one of the most commonly used ones. Demers [54] has extended the program to 3D. In chapter 3, in a model sensitivity analysis, this program is used to compare our own results too.

Furthermore, Salvat developed Penelope [55], which has first principle models for electron and photon transport, but secondary electron models are not included. Kuhr has developed a program based on first principle models that can trace the electrons till the vacuum level. Kuhr, Fitting, and Schreiber used Fröhlich theory to calculate [56–58] phonon scattering cross-sections for the quasi-elastic scattering of very low energy electrons. Kieft [59] developed a Monte Carlo program by combining several first principle models. For instance, he used Fitting's phonon scattering model, and Mott cross-sections as obtained by using ELSEPA. For inelastic scattering, he used Ashley's inelastic scattering cross-sections, which is physically superior to the continuous slowing down model [51]. In addition, they introduced refinements of their low energy electron scattering models in order to simulate secondary electron yields accurately.

Dapor [60] performed a Monte Carlo study on the secondary electron emission of resist lines, including a trapping cross-section [20]. However, neither his work nor the other works mentioned above do include a dynamic charging model, which is essential for insulators.

One of the most common approaches to explain charging is the so-called total yield approach [61]. In this approach, charging is positive if the emission yield is bigger than unity, otherwise negative. However, this approach falls short of explaining the

dynamics at a deeper level in the material, which makes it hard to predict experiments. Cazaux, in an early study [62], improved the total yield approach by including the effect of electrons interacting with traps, the irradiation time and a specimen bias. However, in a later study [63], he mentioned the simplicity of the total yield approach, realizing that one also needs to consider parameters such as sample geometry and the detector.

Another approach, dynamic double-layer (DDL), was used by Melchinger [64]. This approach assumes that there are separate positive and negative poles in a deeper region of the sample and time-dependent relaxation in these regions. However, the applicability of this 1D model is limited to a defocused beam and simple geometries. Besides, the availability of separate poles is questionable when the landing energy of electrons is very small. Davidson [65] questioned the validity of the DDL approach due to the weak conductivity between these regions. He assumes that the material's conductivity increases a lot due to beam-induced effects neutralizing the charging region deeper in the material. Therefore, he neglected the electrostatic fields inside the materials. However, this is quite an extreme assumption, considering that the induced conductivity should be dependent on dose and time [66, 67].

Some authors developed 3D simulations for charging. For instance, Grella [68] developed his simulation models in 3D based on a single scattering model without secondary electron generation. A similar study based on single scattering was also made by Kotera [67]. However, in this study, charging is limited to negative scenarios since there is no secondary electron model. A year later, Kotera [69] extended the scattering models allowing secondary electron generation, including the full cascade of electrons at energies below 100 eV. However, these extended models did not have any charging models. For charging, a more extensive Monte Carlo model was developed by Ko [70] based on a single scattering model, including secondary electrons, induced conductivity, and a double layer model for dimensional metrology of resist lines.

In addition, there are also some Monte Carlo studies of charging based on more elaborate first principle models. For instance, JMONSEL [71] discretely calculates elastic and inelastic scattering based on accurate Mott cross-sections and the Penn algorithm. Currently, it is the only publicly available program that can simulate charging based on the Finite Element Method (FEM). It has an empirical dielectric breakdown model, but it does not include a model for the induced conductivity.

From a computational perspective, unfortunately, Villarrubia states that JMONSEL is "much slower" [72] when charging models are enabled due to limited parallelization. But, İlgünsatiroglu [73] developed a massively parallelized charging simulator based on first principle models. However, these models do not include a charge redistribution model such as dielectric breakdown, induced conductivity, or a diffusion model.

As a master student, in a collaboration with GenISys-GmbH, I already developed an electric field solver based on a multigrid method [74] to boost the calculation times of charging simulations in virtualSEM [75] (a Monte Carlo simulator developed by GenISys-GmbH) based on empirical scattering models. At the same time, at TU Delft, Verduin [76] developed a graphical processing unit (GPU) accelerated Monte

Carlo program (e-scatter) based on Kieft's model [59] with the best possible electron-matter scattering models, but no electric field solver and charging model. Both simulators have different strong points both physics-wise and computation-wise. Therefore it makes sense to combine e-scatter, with its first principle scattering models, and virtualSEM, with its electric field solver, to obtain a better simulator which includes charging. As the charging phenomenon still remains very complex, there is still a lot of room for improvement, for instance in the dynamic recombination models. In a collaboration between TU Delft, GenISys GmbH, and RAITH B.V. we set ourselves the task to develop this combined Monte Carlo simulator and use it for applications in the fields of metrology and lithography.

1.6. Scope of the thesis

The first step was to further develop e-scatter [77], to fix bugs, and to study how sensitive simulated emission properties and SEM images are to the various model ingredients implemented in the simulator. The next step was to build the first principle and physically more sophisticated scattering models into virtualSEM, which already contained an advanced electric field solver and allowed for material charging. This way, a tool was obtained with accurate physics models and charging capability. Finally, the simulators developed were used to develop industry-driven applications involving complex geometries (3D) and charging effects in microscopy and lithography. These applications serve a three-fold purpose. They are leading to novel techniques for nanofabrication and inspection, they serve as very nice test cases of the simulation models and they serve as intuitive demonstrations of how Monte Carlo simulations can be used to solve semiconductor industry problems .

The thesis is organized in nine chapters, including this Introduction chapter 1.

In chapter 2, the physics background of electron transport and charging is treated. Following that, the models in the simulators are introduced, such that the reader will understand the model assumptions and their effects on the simulation results. To validate the simulation results they need to be compared with experimental data. However, it turns out to be hard to find trustworthy experimental data. Therefore, I will discuss the design of a well-defined experiment that can be used as a reference for Monte Carlo simulation work.

In chapter 3, a detailed sensitivity analysis is performed to understand the effects that different physics model ingredients have on critical dimension (CD) measurements of complex geometrical shapes in the semiconductor industry. This identifies the models with the most significant impact on dimensional metrology. Furthermore, the effect of the models on the calculation times has been studied with the purpose in mind of building an accurate and fast simulator.

The lessons learned in chapter 3 are used in chapter 4, to improve the electron-scattering models in virtualSEM, to obtain more realistic simulated charge distribution profiles. In addition, charge redistribution models are introduced and the electric field solver and the ray tracing are improved. The effects of the improvements are

demonstrated in three different realistic applications.

The charging effect in electron beam lithography is studied in chapter 5. A large set of experiments to understand the charge dynamics is conducted. On the one hand the simulations give insight in the complex charging behaviour, and on the other hand the experiments help to verify the simulation models. As a result, a smart scan-strategy is found out to minimize pattern distortions caused by charging.

In chapter 6 simulations are used to investigate a complex 3D problem in lithography. We show that, in nanofabrication on curved surfaces, a recalculation of the point spread function is required to achieve accurate proximity effect correction.

In chapter 7, by using simulations, a novel and practical technique is obtained to extract 3D information from 2D SEM images. Three different sets of experiments are used to verify the simulation models. In addition, this demonstrates how complex the quantification of signal amplitudes in SEM images really is.

In chapter 8 we will discuss the impact of the results in academia and industry, and the thesis will end with a chapter 9.

References

[1] G. E. Moore, *Cramming more components onto integrated circuits, Reprinted from Electronics, volume 38, number 8, April 19, 1965, pp.114 ff.* IEEE Solid-State Circuits Society Newsletter **11**, 33 (2009).

[2] TSMC, *TSMC Vision, Mission & Core Values TSMC's Vision,* (2020).

[3] W. Lambrechts, S. Sinha, J. A. Abdallah, and J. Prinsloo, *Extending Moore's Law through Advanced Semiconductor Design and Processing Techniques*, 1st ed. (CRC Press, Inc., USA, 2018).

[4] *INTERNATIONAL TECHNOLOGY ROADMAP FOR SEMICONDUCTORS 2.0 2015 EDITION EXECUTIVE REPORT,* ITRS **0**, 1 (2016).

[5] N. Balcon, D. Payan, M. Belhaj, T. Tondu, and V. Inguimbert, *Secondary electron emission on space materials: Evaluation of the total secondary electron yield from surface potential measurements,* IEEE Transactions on Plasma Science **40**, 282 (2012).

[6] L. Sanche, *Low Energy Electron Damage To DNA,* in *Radiation Induced Molecular Phenomena in Nucleic Acids. Challenges and Advances In Computational Chemistry and Physics*, edited by M. K. Shukla and J. Leszczynski (Springer, Dordrecht, 2008) pp. 531–575.

[7] N. G. Orji, M. Badaroglu, B. M. Barnes, C. Beitia, B. D. Bunday, U. Celano, R. J. Kline, M. Neisser, Y. Obeng, and A. E. Vladar, *Metrology for the next generation of semiconductor devices,* Nature Electronics **1**, 532 (2018).

[8] M. Pojar and A. Seabra, *Advanced resists for e-beam lithography: processing, exposure and characterization (Part III)*, Tech. Rep. (2015).

[9] R. Eckhardt, *Stan Ulam, John Von Neumann, and the Monte Carlo Method,* Los Alamos Science **15**, 131 (1987).

[10] N. Metropolis, *The Beginning of the Monte Carlo Method,* Los Alarnos Science Special Issue **15**, 125 (1987).

[11] Z. Czyżewski, D. O. N. Maccallum, A. Romig, D. C. Joy, and D. C. Joy, *Calculations of Mott scattering cross section,* **3066** (1990), 10.1063/1.346400.

[12] A. Jablonski, F. Salvat, and C. J. Powell, *NIST Electron Elastic-Scattering Cross-Section Database, Version 4.0*, Tech. Rep. (National Institute of Standards and Technology, Gaithersburg, MD, 2016).

[13] F. Salvat, A. Jablonski, and C. J. Powell, *ELSEPA—Dirac partial-wave calculation of elastic scattering of electrons and positrons by atoms, positive ions and molecules,* Computer Physics Communications **165**, 157 (2005).

[14] H. Bethe, *Bremsformel für Elektronen relativistischer Geschwindigkeit,* Zeitschrift für Physik **76**, 293 (1932).

[15] T. S. Rao-Sahib and D. B. Wittry, *X-ray continuum from thick elemental targets for 10–50 keV electrons,* Journal of Applied Physics **45**, 5060 (1974).

[16] D. C. Joy and S. Luo, *An Empirical Stopping Power Relationship for Low-Energy Electrons,* Scanning **11**, 176 (1989).

[17] Y. Lin and D. C. Joy, *A new examination of secondary electron yield data,* Surface and Interface Analysis **37**, 895 (2005).

[18] M. Gryziński, *Classical theory of atomic collisions. I. Theory of Inelestic collisions,* Physical Review **138**, 336 (1965).

[19] A. Jablonski, C. J. Powell, and S. Tanuma, *Monte Carlo strategies for simulations of electron backscattering from surfaces,* Surface and Interface Analysis **37**, 861 (2005).

[20] J. Ganachaud and A. Mokrani, *Theoretical study of the secondary electron emission of insulating targets,* Surface Science **334**, 329 (1995).

[21] K. Murata, *Monte Carlo simulation of fast secondary electron production in electron beam resists,* Journal of Applied Physics **52**, 4396 (1981).

[22] R. D. Penn, *Electron mean-free calculations using a model dielectric function,* Physical Review B **35**, 482 (1987).

[23] J. C. Ashley, *INTERACTION OF LOW-ENERGY ELECTRONS WITH CONDENSED MATTER: STOPPING POWERS AND INELASTIC MEAN FREE PATHS FROM OPTICAL DATA,* Journal of Electron Spectroscopy and Related Phenomena **46**, 199 (1988).

[24] S. F. Mao, Y. G. Li, R. G. Zeng, and Z. J. Ding, *Electron inelastic scattering and secondary electron emission calculated without the single pole approximation,* Journal of Applied Physics **104** (2008), 10.1063/1.3033564.

[25] I. Abril, R. Garcia-Molina, C. D. Denton, F. J. Pérez-Pérez, and N. R. Arista, *Dielectric description of wakes and stopping powers in solids,* Physical Review A - Atomic, Molecular, and Optical Physics **58**, 357 (1998).

[26] H. T. Nguyen-Truong, *Penn algorithm including damping for calculating the electron inelastic mean free path,* Journal of Physical Chemistry C **119**, 7883 (2015).

[27] N. D. Mermin, *Lindhard Dielectric Function in the Relaxation-Time Approximation,* Phys. Rev. B **1**, 2362 (1970).

[28] B. Da, H. Shinotsuka, H. Yoshikawa, Z. J. Ding, and S. Tanuma, *Extended mermin method for calculating the electron inelastic mean free path,* Physical Review Letters **113**, 1 (2014).

[29] E. D. Palik, *Handbook of Optical Constants of Solids, Volumes I, II, and III* (1985) p. 821.

[30] A. P. Sorini, J. J. Kas, J. J. Rehr, M. P. Prange, and Z. H. Levine, *Ab initio calculations of electron inelastic mean free paths and stopping powers,* Physical Review B - Condensed Matter and Materials Physics **74**, 1 (2006).

[31] W. S. M. Werner, K. Glantschnig, and C. Ambrosch-Draxl, *Optical constants and inelastic electron-scattering data for 17 elemental metals,* Journal of Physical and Chemical Reference Data **38**, 1013 (2009).

[32] T. Kaneko, *Energy distribution of secondary electrons emitted from solid surfaces under electron bombardment I. Theory,* Surface Science **237**, 327 (1990).

[33] J. Cazaux, *Calculated influence of work function on SE escape probability and Secondary Electron Emission yield,* Applied Surface Science **257**, 1002 (2010).

[34] I. M. Bronstein and B. S. Fraiman, *VTORICHNAYA ELEKTRONNAYA EMISSIYA. (Secondary Electron Emission).* Nauka Press .

[35] T. Gineste, M. Belhaj, G. Teyssedre, and J. Puech, *Investigation of the electron emission properties of silver: From exposed to ambient atmosphere Ag surface to ion-cleaned Ag surface,* Applied Surface Science **359**, 398 (2015).

[36] X. C. Hu, M. Cao, and W. Z. Cui, *Influence of surface topography on the secondary electron yield of clean copper samples,* Micron **90**, 71 (2016).

[37] C. G. H. Walker, M. M. El-Gomati, a. M. D. Assa'd, and M. Zadrazil, *The secondary electron emission yield for 24 solid elements excited by primary electrons in the range 250-5000 ev: a theory/experiment comparison.* Scanning **30**, 365 (2008).

[38] M. M. El Gomati, C. G. Walker, A. M. Assa'd, and M. Zadražil, *Theory experiment comparison of the electron backscattering factor from solids at low electron energy (250-5,000 eV),* Scanning **30**, 2 (2008).

[39] V. Baglin, J. Bojko, O. Gröbner, B. Henrist, N. Hilleret, C. Scheuerlein, and M. T. Cern, *THE SECONDARY ELECTRON YIELD OF TECHNICAL MATERIALS AND ITS VARIATION WITH SURFACE TREATMENTS,* Proceedings of EPAC , 217 (2000).

[40] D. C. Joy, *A DATABASE OF ELECTRON-SOLID INTERACTIONS,* A Database of Electron Solid Interactions , 334 (2008).

[41] W. S. M. Werner, W. Smekal, C. Tomastik, and H. Störi, *Surface excitation probability of medium energy electons in metals and semiconductors,* Surf. Sci. **486**, {L}461 (2001).

[42] W. S. M. Werner, A. Ruocco, F. Offi, S. Iacobucci, W. Smekal, H. Winter, and G. Stefani, *Role of surface and bulk plasmon decay in secondary electron emission,* Physical Review B **78**, 233403 (2008).

[43] W. S. Werner, F. Salvat-Pujol, W. Smekal, R. Khalid, F. Aumayr, H. Störi, A. Ruocco, and G. Stefani, *Contribution of surface plasmon decay to secondary electron emission from an Al surface,* Applied Physics Letters **99** (2011), 10.1063/1.3658455.

[44] J. Gong, L. Yang, K. Tőkési, and Z. Ding, *Surface and bulk plasmon excitations of silver by electron impact,* The European Physical Journal D **73**, 24 (2019).

[45] L. van Kessel, C. Hagen, and P. Kruit, *Surface effects in simulations of scanning electron microscopy images,* **18**, 29 (2019).

[46] C. J. Powell and A. Jablonski, *Evaluation of calculated and measured electron inelastic mean free paths near solid surfaces,* Journal of Physical and Chemical Reference Data **28**, 19 (1999).

[47] S. Tanuma, C. J. Powell, and D. R. Penn, *Calculations of electron inelastic mean free paths. IX. Data for 41 elemental solids over the 50 eV to 30 keV range,* Surface and Interface Analysis **43**, 689 (2011).

[48] G. Gergely, *Elastic peak electron spectroscopy,* Scanning **8**, 203 (1986).

[49] G. Gergely, *Elastic backscattering of electrons: Determination of physical parameters of electron transport processes by elastic peak electron spectroscopy,* Progress in Surface Science **71**, 31 (2002).

[50] M. Dapor, *A Monte Carlo investigation of secondary electron emission from solid targets: Spherical symmetry versus momentum conservation within the classical binary collision model,* Nuclear Instruments and Methods in Physics Research, Section B: Beam Interactions with Materials and Atoms **267**, 3055 (2009).

[51] M. Dapor, *Comparison between Energy Straggling Strategy and of Secondary Electron Emission of Insulating Materials,* **2**, 762 (2011).

[52] M. Dapor, *Secondary electron emission yield calculation performed using two different Monte Carlo strategies,* Nuclear Instruments and Methods in Physics Research, Section B: Beam Interactions with Materials and Atoms **269**, 1668 (2011).

[53] P. Hovington, D. Drouin, R. Gauvin, D. C. Joy, and N. Evans, *CASINO: A new monte Carlo code in C language for electron beam interactions-part III: Stopping power at low energies,* Scanning **19**, 29 (2006).

[54] H. Demers, N. Poirier-Demers, A. R. Couture, D. Joly, M. Guilmain, N. De Jonge, and D. Drouin, *Three-dimensional electron microscopy simulation with the CASINO Monte Carlo software,* Scanning **33**, 135 (2011).

[55] F. Salvat, J. Fernández-Varea, and J. Sempau, *PENELOPE-2011: A code system for Monte Carlo simulation of electron and photon transport,* Workshop Proceedings , 384 (2011).

[56] J.-C. Kuhr and H.-J. Fitting, *Monte-Carlo Simulation of Low Energy Electron Scattering in Solids,* Physica Status Solidi (a) **172**, 433 (1999).

[57] H. J. Fitting, E. Schreiber, J. C. Kuhr, and a. Von Czarnowski, *Attenuation and escape depths of low-energy electron emission,* Journal of Electron Spectroscopy and Related Phenomena **119**, 35 (2001).

[58] E. Schreiber and H.-J. Fitting, *Monte Carlo simulation of secondary electron emission from the insulator SiO2,* Journal of Electron Spectroscopy and Related Phenomena **124**, 25 (2002).

[59] E. Kieft and E. Bosch, *Refinement of Monte Carlo simulations of electron–specimen interaction in low-voltage SEM,* Journal of Physics D: Applied Physics **41**, 215310 (2008).

[60] M. Dapor, M. Ciappa, and W. Fichtner, *Monte Carlo modeling in the low-energy domain of the secondary electron emission of polymethylmethacrylate for critical-dimension scanning electron microscopy,* Journal of Micro/Nanolithography, MEMS, and MOEMS **9**, 23001 (2010).

[61] M. T. Postek and A. E. Vladár, *Does your SEM really tell the truth? How would you know? Part 4: Charging and its mitigation,* in *Proc. SPIE 9636*, Vol. 36, edited by M. T. Postek, D. E. Newbury, S. F. Platek, and T. K. Maugel (2015) p. 963605.

[62] J. Cazaux, *Some considerations on the secondary electron emission, δ, from e[sup −] irradiated insulators,* Journal of Applied Physics **85**, 1137 (1999).

[63] J. Cazaux, *On some contrast reversals in SEM: Application to metal/insulator systems,* Ultramicroscopy **108**, 1645 (2008).

[64] A. Melchinger and S. Hofmann, *Dynamic double layer model: Description of time dependent charging phenomena in insulators under electron beam irradiation,* Journal of Applied Physics **78**, 6224 (1995).

[65] M. P. Davidson and N. T. Sullivan, *Investigation of the effects of charging in SEM-based CD metrology,* in *Proc. SPIE*, Vol. 3050 (1997) pp. 226–242.

[66] N. Tanaka, Ryuichi; Sunaga Hiromi; Tamura, *The Effect of Accumulated Charge on Depth Dose Profile in Poly(Methylmethacrylate) Irradiated with Fast Electron Beam,* IEEE Transactions on Nuclear Science **NS-26**, 4670 (1979).

[67] M. Kotera and H. Suga, *A simulation of keV electron scatterings in a charged□up specimen,* Journal of Applied Physics **63**, 261 (1988).

[68] L. Grella, G. Lorusso, T. Niemi, and D. L. Adler, *Simulations of SEM imaging and charging,* Nuclear Instruments and Methods in Physics Research Section A: Accelerators, Spectrometers, Detectors and Associated Equipment **519**, 242 (2004).

[69] M. Kotera, *A Monte Carlo simulation of primary and secondary electron trajectories in a specimen,* Journal of Applied Physics **65**, 3991 (1989).

[70] Y. U. Ko and M. S. Chung, *Monte Carlo simulation of charging effects in linewidth metrology (II): On insulator substrate,* Scanning **20**, 549 (1998).

[71] J. Villarrubia, A. Vladár, B. Ming, R. Kline, D. Sunday, J. Chawla, and S. List, *Scanning electron microscope measurement of width and shape of 10 nm patterned lines using a JMONSEL-modeled library,* Ultramicroscopy **154**, 15 (2015).

[72] J. S. Villarrubia, A. E. Vladár, and M. T. Postek, *3D Monte Carlo modeling of the SEM: Are there applications to photomask metrology?* **9236**, 923602 (2014).

[73] E. Ilgünsatiroglu, *Synthesis of SEM images by means of High-Performance Computing*, Ph.D. thesis, ETH Zürich (2015).

[74] K. T. Arat, J. Bolten, T. Klimpel, and N. Unal, *Electric fields in Scanning Electron Microscopy simulations,* in *Proc SPIE*, Vol. 9778, edited by M. I. Sanchez and V. A. Ukraintsev (2016) p. 97780C.

[75] GenISys-Gmbh, *virtualSEM,* (2019).

[76] T. Verduin, S. R. Lokhorst, and C. W. Hagen, *GPU accelerated Monte-Carlo simulation of SEM images for metrology,* Proceedings of SPIE **9778**, 97780D (2016).

[77] T. Verduin, *Quantum Noise Effects in e-Beam Lithography and Metrology*, Ph.D. thesis, Delft University of Technology (2017).

2

Monte Carlo Simulators: Theory Models and Experimental Verification

2.1. Introduction

In simulation work, a fundamental question is to what extent simulation results can be trusted. This question is valid for the Monte Carlo simulations used in this thesis and understanding the models that describe the underlying physics will help to answer it. These models, however, can be very complicated depending on the level of detail. The goal of this chapter is to describe the physics of the models in the Monte Carlo simulators used in this study, e-Scatter and virtualSEM, in sufficient detail to understand the following chapters. In the first part, "Electron Scattering", we discuss what happens to the electrons inside and outside of the material from a physics point of view. In the next part, "Physics Models in Simulators", we discuss which models are used in the simulators to cover the phenomena mentioned in the previous chapter. We also discuss improvements made to these models and the models missing in the simulators. The improvements to the models required for virtualSEM are listed here but will be further explained in chapter 4. Subsequently, we address the important features of "good" experiments reported in the literature, to which the simulation results can be compared. Ultimately, we are going to verify how well the simulations can reproduce the electron emission and spatial extent of electrons in the material by comparing them with experiments. These properties were chosen specifically, as they can have a severe impact on electron image-formation and e-beam lithography.

2.2. Electron scattering

During electron exposure, high energy electrons are injected into the material. Let us try to understand what happens to them during the transport inside the material.

Electrons are charged particles, and they interact with the potential of the positive nucleus of the atom by the Coulomb force. This interaction mostly results in a trajectory change with no or a negligible amount of energy transferred to the nucleus, i.e. elastic scattering.

These electrons can also interact with the bound orbital electrons, which mostly results in a significant amount of momentum and energy being transferred to the bound electron, i.e. inelastic scattering.

In more detail, the bound electrons can be excited or, if the transferred energy is high enough, ionization can occur by the impact. In the impact-ionization process, one can distinguish inner-shell and outer-shell ionization events by the electron's binding energy. The binding energies of the inner-shell electrons are higher than the outer-shell electrons. Therefore, the inner-shell ionization events take place at higher incident energies, typically a high amount of energy is transferred in these events. Following an inner-shell ionization process, an electron from a higher orbital can fill the inner-shell vacancy and release the energy in the form of a photon, X-ray, or give rise to an Auger electron. On the other hand, if the energy transfer is lower, the loss process can be an impact ionization event of outer-shell electrons or, as we will later discuss, a collective perturbation of the electron gas.

As we have just mentioned, there are also collective phenomena with which the electrons may interact: the phonons, oscillations of the lattice and the plasmons, oscillations of the free electron gas created by the insertion of the electron.

In electron-phonon interaction, the electron can emit (lose energy to) or absorb (gain energy from) a phonon. The typical energy transfer is in the tens of milli-electronvolt (meV) range [1], much lower than the energy loss of an ionization event, such that we consider the interaction as quasi-elastic scattering.

In plasmon scattering processes, a free-electron polarizes the electron gas of the atoms, and these polarized electrons collectively oscillate. The oscillation damps with a finite lifetime [2] and mostly ends up with ionization of an electron from the valence band. This is an in-elastic scattering process and leads to the generation of the majority of secondary electrons.

So far, we have discussed the scattering and electron generation processes. However, when an ionization event occurs, not only is an electron promoted to the conduction band, but a hole is created where the electron was bound, i.e., electron-hole pair generation.

In metals, the hole will be filled by another freely moving electron since the conduction and valence bands overlap. In semiconductors and insulators, valence band electrons move to the conduction band during the ionization, generating a hole in the valence band and an electron in the conduction band which are separated by the band gap, see Fig. 2.1. The reverse process is the recombination process where the charge carriers annihilate each other. Some of the charge carriers get trapped in defect states in the band gap (vacancies, impurities, dislocations). The mobility of a trapped electron is dramatically reduced.

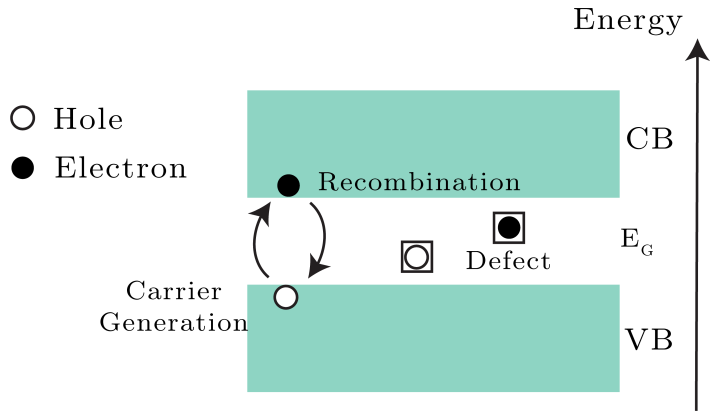


Figure 2.1: Charging in Insulators, band diagram perspective. CB: conduction band, VB: valence band, EG: band gap

The polarization of the medium can also reduce electron mobility. The induced polarization, together with these electrons with reduced mobility, are denoted as polarons. Similar to defects, polarons also lead to charge carriers staying in localized

states within the band gap.

These trapped charges create a strong electrostatic field in the surrounding media, i.e., charging. This field will influence the trajectories of scattering electrons. Understanding this effect is essential to interpret the, mostly undesired, effects on image formation, and lithography.

Not only the trajectories of the electrons drift due to the electric fields in the sample. Charge carriers, especially low energetic ones, move also due to the concentration differences induced by local electric fields. It is practical to explain this transport process by diffusion.

In some extreme cases, where the potential differences are very high, the bandgap does not function as before [3], and the conductivity increases dramatically until the potential differences normalize again by charge redistribution. This phenomenon is also known as dielectric breakdown, or breakdown for short, and governs the maximum allowed local potential difference in the material.

As in dielectric breakdown, the conductivity in semiconductors and insulators can increase in several ways such as thermal effects, field effects, and doping. The higher conductivity leads to more recombination events, in which electrons re-occupy valence band states. This leads to a de-charging process.

Similarly, under the electron irradiation of the sample free charge carriers are created. These carriers can move and recombine again. The increasing number of free charge carriers also increases the rate of recombination. This is explained by Rose as follows: the electron irradiation floods the shallow trapping sites in the bandgap and increases the recombination rate of free charge carriers in the deep trapping sites which are considered as recombination centers [4]. Macroscopically, this is another de-charging process.

When an electron reaches the physical boundaries of the medium, it interacts with the interface. The interface typically has a lot of trap states due to the abrupt termination of the lattice. As these trap sites can be a source of the charging process, they can increase the conduction, the trap-assisted conduction.

Lastly, the electrons that interact with the surface can be transmitted across the interface or be reflected depending on the electron's energy and incidence angle, and also the material's inner potential at both sides of the interface.

The general picture of electron-matter interaction is demonstrated in Fig. 2.2. In here, a high energy electron interacts with an atom elastically and changes its trajectory without losing energy. After that, it undergoes an inelastic scattering event and loses energy. As a result of the inelastic scattering, an electron-hole pair is generated. The low energy electron experiences quasi-elastic phonon scattering and loses energy gradually until it gets trapped in a trap site.

2.3. Physics models in simulators

After having sketched the general picture of electron-matter scattering, we now will describe the models used in the simulators e-Scatter [5] and virtualSEM [6].

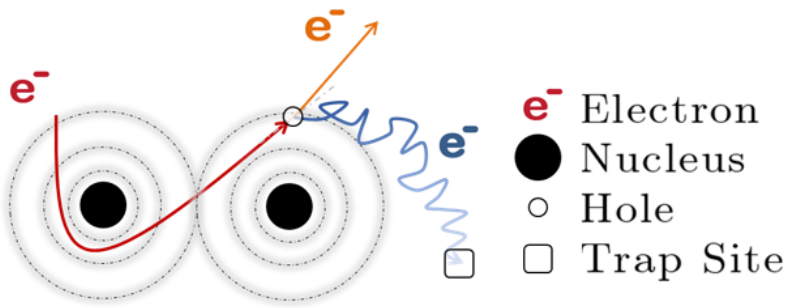


Figure 2.2: Electron-matter interaction. In this view, first, the high energy electron scatters elastically from the nucleus; then, scatters in-elastically with orbital electrons; creates charge carriers, a low energy electron and a hole; the low energy electron scatters quasi-elastically and suffers from a gradual energy loss and eventually gets trapped by the material. The high energy electron continues its path with reduced energy.

2.3.1. e-Scatter

This is our main simulator, which was developed in our research group by Verduin, based on the work of Kieft et al. [7]. The models in e-Scatter are described in detail in chapter 3 of Verduin's dissertation [8]. Here, we are only going to highlight some important points, describe bug fixes, and model changes, subdivided in the following sections: inelastic scattering, elastic scattering, and boundary-crossing models.

Inelastic scattering

The electron loses a considerable amount of energy when it undergoes inelastic scattering. e-Scatter uses dielectric function theory to calculate the inverse of the inelastic mean free path:

$$\lambda_i^{-1} = \frac{1}{\pi E} \int d\omega \int \frac{dq}{q} \operatorname{Im}\left(-\frac{1}{\epsilon\{q,\omega\}}\right) \tag{2.1}$$

where E is the kinetic energy of the electron, $\epsilon(q,\omega)$ is the dielectric function, and $\operatorname{Im}[-1/(\epsilon(q,\omega))]$ is the energy loss function (ELF). The parameters ω and q represent the energy and momentum transfer of the electron to the medium.

The ELF can be obtained from optical reflection and transmission data $\epsilon(0,\omega)$. The connection of the (zero-momentum) photons to (finite-momentum) electrons is made through Ashley's model using the Lindhard dielectric function [9]. This model is an approximation to the model described by Penn [10]. In these two models, the finite life time of the plasmons is not considered.

Verduin explains Ashley's model in detail in his thesis, between equation 3.59 and 3.80 [8], and obtains the final equation:

$$\lambda_i^{-1} = \frac{1}{2\pi E} \int_0^{E/2} \operatorname{Im}\left[-\frac{1}{\epsilon(0,\omega')}\right] L(E,\omega') d\omega' \tag{2.2}$$

where ω' is the zero-momentum energy transfer and

$$L(E,\omega') = \omega' \int_{\omega_{min}}^{\omega_{max}} \frac{1}{\omega(\omega-\omega')} d\omega \tag{2.3}$$

The kinematically allowed region of energy transfer is:

$$\omega_{min} < \omega < \omega_{max} \tag{2.4}$$

where

$$\omega_{min} = \frac{1}{2}(E + \omega' - E\sqrt{1-\frac{2\omega'}{E}}) \tag{2.5}$$

and

$$\omega_{max} = \frac{1}{2}(E + \omega') \tag{2.6}$$

Kieft [7] made the following refinements on Ashley's model:

- Restricting the energy loss to $\omega_{max} - E_F/2$, such that the primary electron does not end up below the Fermi level, where E_F is the Fermi energy.
- A distinction between inner-shell ionization and outer-shell ionization, including plasmon excitation.
- Neglecting exchange correction for plasmon excitation since the primary electron is distinguishable from the plasmon.
- Using a fudge factor (1.5) to match the mean free path with the literature data.
- Using an empirical expression L for ω'>50 eV that allows an additional region of energy transfer that is normally forbidden by rules of energy and momentum conservation.

These refinements led to $L(E,\omega')$ into its final analytical form (see Verduin [8] equation 3.80).

However, in the implementation of e-Scatter a bug was discovered. The integral in Eq. 2.3 uses the upper limit of the integral in Eq. 2.2 ($E/2$). A sub-section of this region should have been ruled out due to the upper limit (ω_{max}) of the kinematically allowed region. This extra sub-region abruptly decreases the mean free path around 50 eV, as shown in Fig. 2.3.

The bug created an artefact in the energy spectrum of the secondary electron emission, shown in Fig. 2.4. This artefact appears as a double-peak. The simulation with the corrected integration limit produces a single prominent peak similar to the experiment. Note that for the figure below and the graphs for electron yield, the

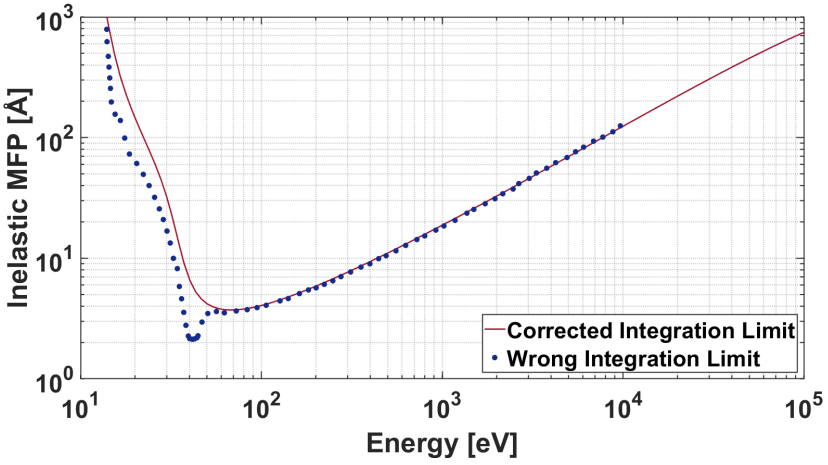


Figure 2.3: The effect of the wrong integration limit on the inelastic mean free path of silicon. The energy reference is the bottom of the band.

energy reference is the sample's vacuum level unless stated differently for particular figures or data.

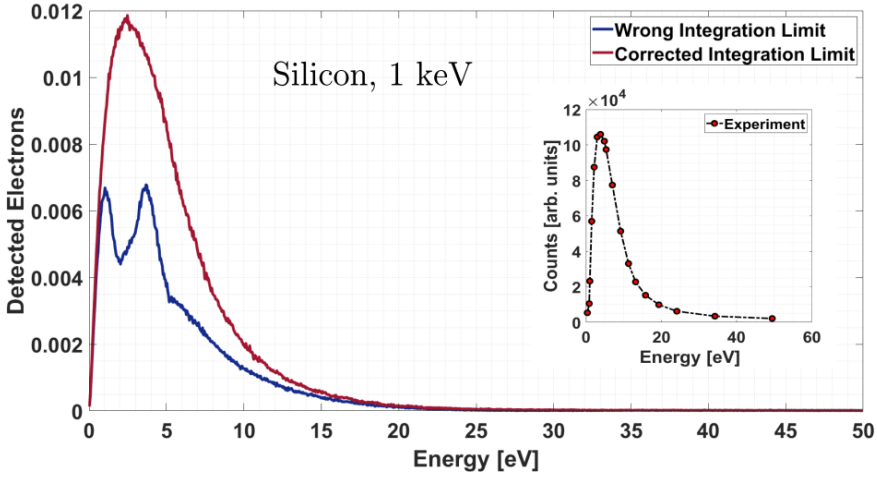


Figure 2.4: The effect of the wrong integration limit on secondary electron emission energy spectra of silicon and a primary electron energy of 1 keV. The spectrum is produced using 106 primary electrons and the result is binned in 1 eV intervals. The experimental data is obtained from Joy [11].

This bug also produces a secondary electron yield which nicely matched the experimental data as in Fig 4.8a in Verduin's thesis [8]. However, the corrected implementation leads to a much higher SE yield, see Fig. 2.5. Otherwise, the trends and the position of the maximum yield are the same.

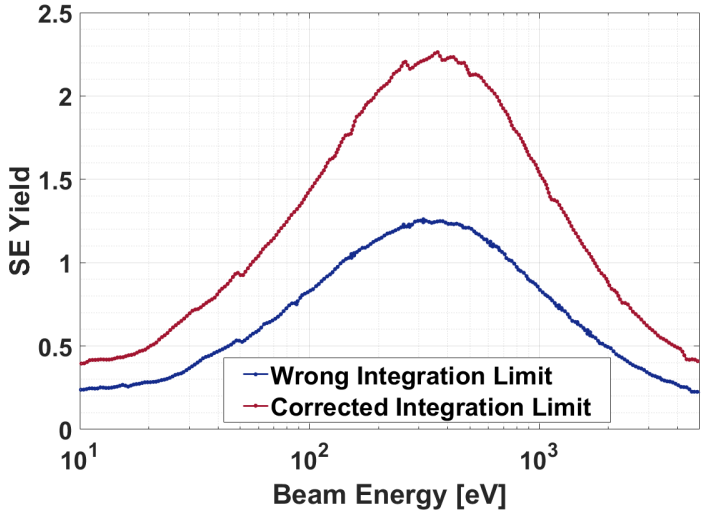


Figure 2.5: The effect of the wrong integration limit on SE Yield of Silicon.

The reader may notice from this comparison the sensitivity of the SE yield to the mean free path at very low energies, where a small difference in the MFP leads approximately to a factor of 2 difference in the SE yield.

Besides this correction, there are further model improvements made, which are discussed in Theulings' thesis [12]. There, it is explained that Kieft assumed that the exchange-correction can be neglected for plasmon events. However, they used the wrong equation from Ashley. Theulings [12] used equation 20 of Ashley [9] for the non-exchange corrected version with the integration boundaries as given below:

$$\omega_{min} = \frac{1}{2}(E + \omega' - E\sqrt{1 - \frac{2\omega'}{E}}) \tag{2.7}$$

and

$$\omega_{max} = \frac{1}{2}(E + \omega' + E\sqrt{1 - \frac{2\omega'}{E}}) \tag{2.8}$$

We adopted this modification in the latest version of inelastic mean free path calculations. All together these models are called "Improved Models" further in the text. After this modification, the fudge factor (1.5) in Kieft's model is no longer needed (and is therefore omitted) since the mean free path compares well with experiments at high energies.

In Fig. 2.6, inelastic mean free paths from experimental and theoretical sources are compared. The experimental data match well with each other at energies down

to ≈100 eV. The values calculated with the "Improved Models" match with the experimental data at those energies as well. However, at lower energies, it is seen that the agreement among the data is poor including the experiments (e.g. Khalid [13] and Kane as reported in Pierron [14]). In the measurements, different techniques are used such as measuring the coincidence of secondary electrons and backscattered electrons [13], or measurement of phenomenological properties (energy distribution, position, intensity, etc.) of the elastic reflection peak in inelastic peak electron spectroscopy (EPES) [15–17]. However, these techniques deduce the mean free paths instead of directly measuring it. Furthermore, they are significantly influenced by experimental conditions such as e.g. the surface condition of the sample [18] which complicates the determination of the inelastic mean free path at low energies (< 100 eV).

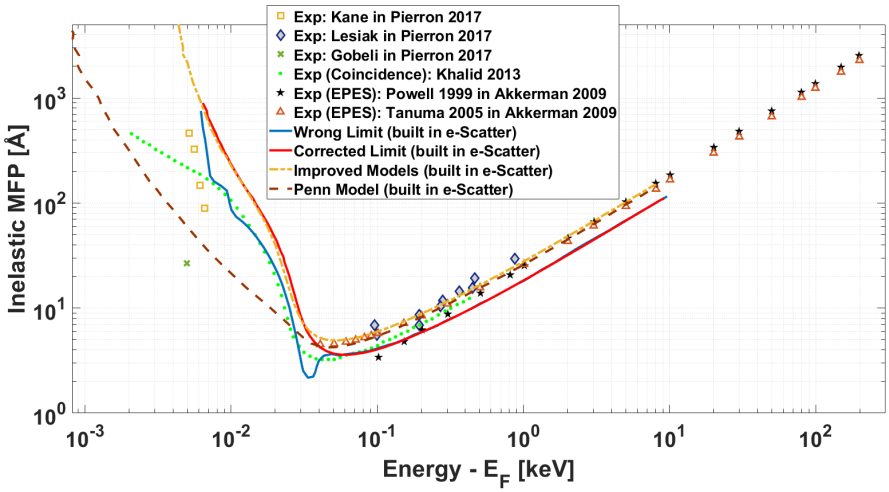


Figure 2.6: Comparison of the inelastic mean free paths (MFP) of silicon from various sources. The experimental data from Kane, Lesiak, and Gobeli (reported in Pierron 2017 [14]), Khalid 2013 [13], and Akkerman 2009 [19] are plotted with markers. The curves are calculated data used in the simulators. These data are calculated using the models by Ashley [9] and Penn [10]. The zero of energy is the Fermi energy (E_F).

As in the previous figure, the inelastic mean free paths of copper from various sources are compared in Fig. 2.7. The "Improved Models" agrees well with the others down to 100 eV. The mean free paths at lower energies are overestimated compared to all others sources. At very low energies (≈1 eV), the general agreement between experimental sources is better than for silicon at these energies except for the X-ray absorption fine structure spectroscopy (XAFS) results by Bourke et. al., reported in Ridzel's dissertation [20]. The other experimental methods reported in this figure are angle-resolved photoemission spectroscopy (ARPES), and time-resolved two-photon photoemission spectroscopy (TR-2PPE).

Worth mentioning, the ab-initio calculation at low energies by Campillo et al. [21] agrees well with experimental data at energies below 10 eV. Besides that, the calcu-

lations of Ridzel using Mermin's model, where the finite life time of the plasmons is considered show a good qualitative agreement with experiment over all energies [20].

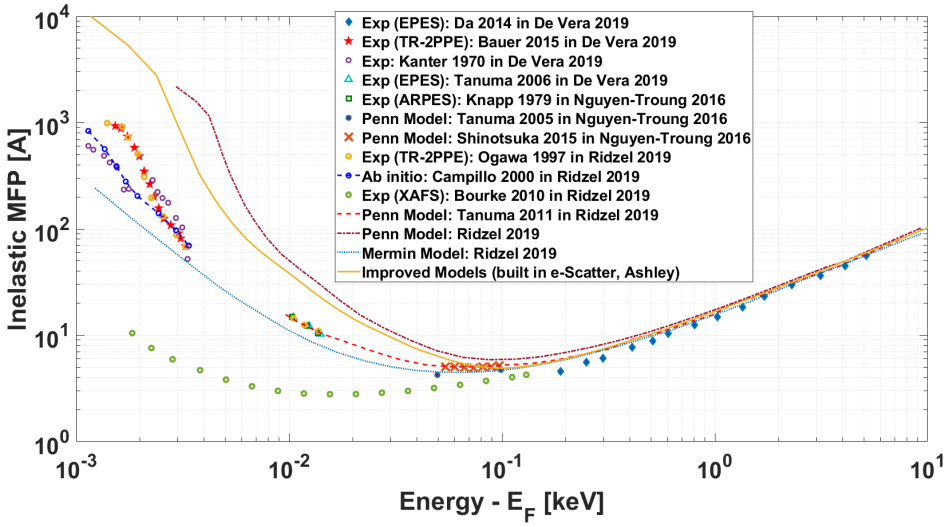


Figure 2.7: Comparison of the inelastic mean free paths of copper from various sources. The experimental data are plotted with markers. The curves are calculated data from various sources. The data are obtained from De Vera 2019 [22], Nguyen-Troung 2016 [23], Ridzel 2019 [20]]. See text for further description. The zero of energy is the Fermi energy (E_F).

There is another issue in Verduin's model [8] related to the electron-ionization cross-sections. This is not mentioned in Theulings' thesis, where the photo-ionization cross-sections were used, as Kieft did [7]. In Verduin's code, the cross-sections were multiplied by shell occupancies. For the inner-shells of the silicon atom, these values are 2, 2, 2, and 4 for K, L1, L2, and L3 shells, respectively. However, these cross-sections were already given for the entire shell in the Lawrence Livermore National Lab evaluated electron data library [24]. Therefore, we fixed this issue and used the inner-shell cross-section, as shown in Fig. 2.8.

For the outer-shell, when the energy transfer is smaller than 100 eV, an empirical model (as follows Kieft and Verduin's code) is used. In this model, the electron binding energy is chosen as the maximum binding energy value which is smaller than the energy transfer in the material data file in Kieft's code (e.g. in the df_Si.dat file).

For light atoms such as silicon, the effect of this modification on electron emission yields is negligible because the ratio of the cross-sections (probability of the shell ionization is determined after normalization) does not change a lot, since the inner shell occupancy numbers are mostly the same value.

In the database, the x-axis is the kinetic energy of the electron. However, Verduin treats the x-axis as zero-momentum energy transfer. That would be a valid assumption if the projectile would be a photon, however, it is an electron. This decision is not

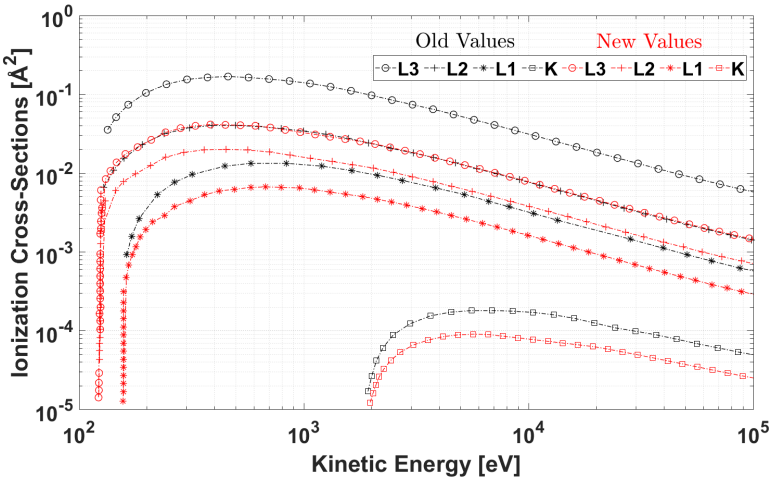


Figure 2.8: Electron ionization cross sections for a free silicon atom from the Lawrence Livermore National Lab (LLNL) evaluated electron data library[24].

discussed explicitly in Verduin's thesis [8].

Another assumption for the determination of binding energy (as the x-axis), in the other extreme, can be using the electron kinetic energy, since the x-axis is defined as the kinetic energy of the electron. However, this assumption is also flawed since it does not check the energy transfer in the event. Therefore, it overestimates the ionization probability of inner-shells.

Fig. 2.9 demonstrates the sensitivity of SE and BSE yields for silicon to these two assumptions. The SE yield drops slightly after the edge energy of the first inner-shell around 100 eV and the gap gets bigger as the other inner-shells get involved at higher energies. However, the effect on the SE yield is less than 10 % since the outer-shell ionization is the dominant process in both approaches. It is also negligible on the BSE yield since the dominant scattering events are elastically scattered ones. Nevertheless, we proceed with Verduin's model but without the wrong occupancy multiplication. Ideally, using the electron energy loss function instead of the optical energy loss function with electro-ionization cross-section would be the proper model for the determination of binding energies.

The dielectric function theory uses the ELF to calculate the inelastic mean free path (Eq. 2.1). The inelastic events are observable on the ELF, which describes the probabilities of the material's energy absorption (see Fig. 2.10). The maximum, approximately at 20 eV, is the bulk plasmon peak which is the most dominant energy loss mechanism. The sudden jumps on the ELF show that L- and K-shell electron ionization channels are enabled by energy transfers higher than 100 eV and 1800 eV, respectively. However, some features such as surface plasmons do not exist on the optical ELF in Fig. 2.10, because photons at those energies do not couple to surface

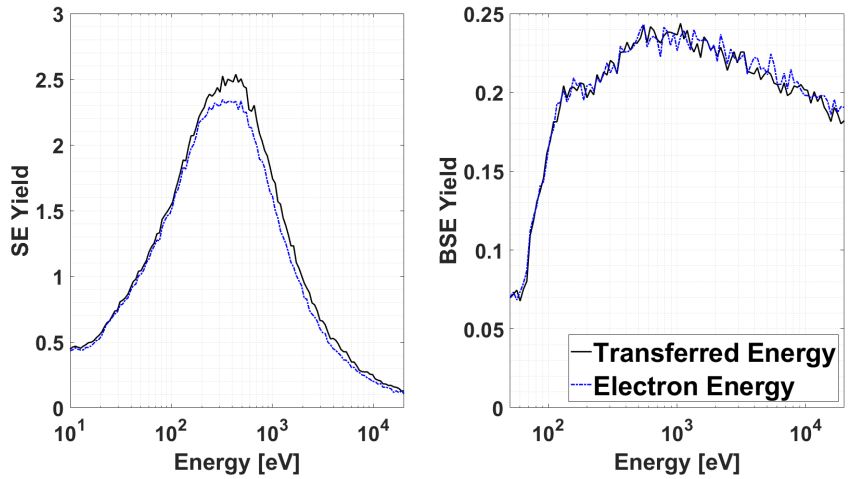


Figure 2.9: The effect of ionization models on SE and BSE yields as a function of transferred energy or incident electron kinetic energy.

plasmons, but electrons do.

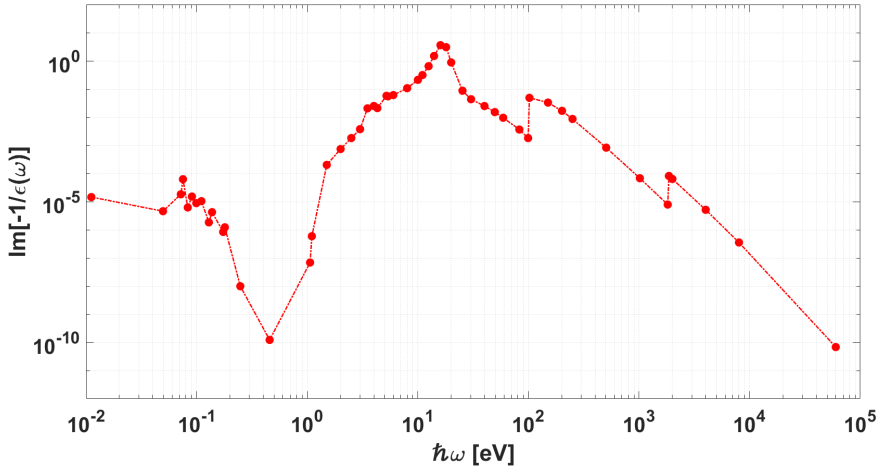


Figure 2.10: Optical Energy Loss Function for silicon [8]. The energy reference is the sample's vacuum level.

Verduin has calculated the ELF for surface plasmon losses using a simple model through Kramers-Kronig analysis [8]. The model assumes a fixed depth for surface plasmons coupling. Recently, van Kessel included surface plasmons with a more sophisticated model [25]. In this model, the coupling depth to surface plasmons is a function of energy instead of a fixed depth. The latter study has shown that surface

plasmons are important when simulating electron emission energy spectra, but their effect on the SE yield can be neglected. Therefore, we are not going to include it here since the model is computationally expensive.

Elastic scattering

An overview of the elastic scattering models used in the simulators is depicted in Fig. 2.11.

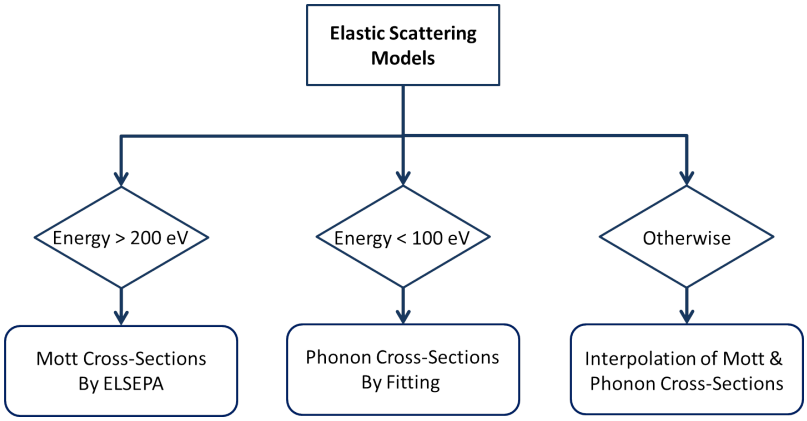


Figure 2.11: Schematic overview of elastic scattering models.

At energies higher than 200 eV, the accurate way of calculating the elastic mean free path is solving the Dirac equation [26] including the screening effects of the orbital electrons and relativistic effects [27]. The solution leads to Mott cross-sections [28] where the mean free path can be calculated from Eq. 9:

$$\lambda = \frac{1}{\sigma} \cdot \frac{M}{\rho_m N_A} \tag{2.9}$$

where σ is the scattering cross-section, M is the molar mass, ρ_m is the mass density and N_A is Avogadro's number.

The Mott cross-sections are calculated and tabulated previously by different authors for various atomic potentials [29–31]. The state of the art way of calculating these cross-sections is available in a program called ELSEPA [32].

In ELSEPA different electron density models are employed: Thomas-Fermi-Molière (TFM), Thomas-Fermi-Dirac (TFD), Dirac-Hartree-Fock-Slater (DHFS), and numerical Dirac-Fock (DF). The latter is claimed to be the most accurate model for the free atom model in the program [32]. However, we are interested in the solid-state form of materials. To include the solid-state effects, a muffin-tin model is used. The muffin-tin radius has to be provided as input. The radius is readily available in the program for elements that can be found in elemental form in nature. For elements such as Nitrogen and Oxygen one needs to provide the radius. In our calculations, we have

adapted the values from silicon (11.75x1e-11 m).

A comparison of the elastic MFP in silicon for the various electron density models is given for the free atom and muffin-tin potentials in Fig. 2.12. The deviation between the models is smaller for the muffin-tin potential than for the free atom potential. We think that this is due to the shielding effect of the muffin-tin model. Since the effect is very small, we assume that the choice between these densities would not have a significant impact on the emission results. Therefore, we proceed with the Dirac-Fock densities for the muffin-tin model.

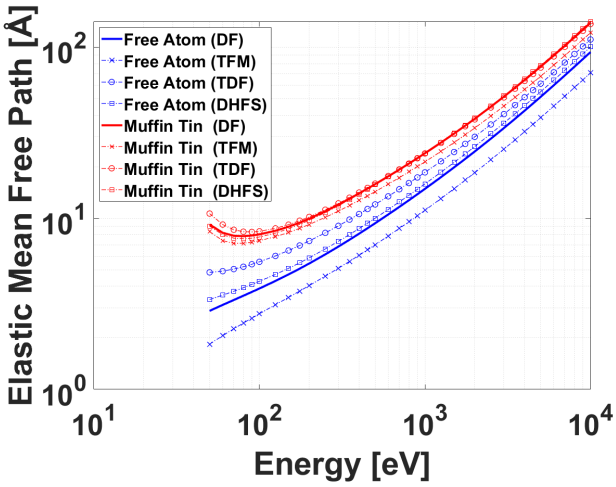


Figure 2.12: Comparison of the elastic mean free path of silicon for various electron density models in ELSEPA, and two potential models. The energy reference is the sample's vacuum level.

The difference between the mean free paths calculated using the free atom and the muffin-tin potentials is more than a factor of 1.5. ELSEPA also offers several options for refinement of the atomic potential such as exchange correction, correlation polarization potential, and the absorption coefficient. The effect of these refinements on the elastic mean free path is very limited compared to the effect of the atomic potential for energies higher than 100 eV but significant at very low energies (≈10 eV) as seen in Fig. 2.13.

The mean free paths used in virtualSEM (2016) are based on work by Czyzewski [30]. These results agree well with the ELSEPA calculations for the free atom potential (see Fig. 2.13). Another calculation done by Kuhr [33] agrees with the muffin-tin potential one only above 100 eV.

The mean free path difference between the free atom and muffin-tin potential models is a factor of ≈1.5 (see Fig. 2.13 above) for energies above 100 eV. However, the transport length (the mean displacement of a particle after so many elastic scattering events) is similar for these two potentials, for energies above 100 eV (Fig. 2.14). ELSEPA calculates it as reported in [32] (equation 10 in the reference). Although the

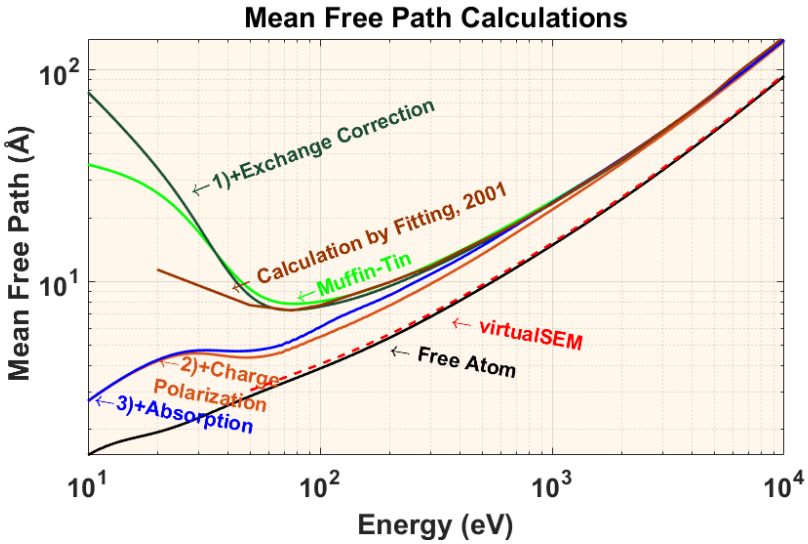


Figure 2.13: Sensitivity of the elastic mean free path of silicon to several model refinements. VirtualSEM (2016) uses the mean free path calculations based on Czyzewski [30]. The energy reference is the sample's vacuum level.

free atom potential results in a shorter mean free path than the muffin-tin potential, the average displacement of the electron is the same for both potentials.

None of the model refinements significantly impacts the elastic mean free path for energies above 200 eV. However, the absorption potential (referred to as "absorption" in Fig. 2.13 and 2.14) results in a slightly different transport length than the other models do (2.5 nm larger at 300 eV). It indicates that this refinement changes the scattering angles towards the forward direction. The electron yield sensitivity to these models will be given later in this section (Fig. 2.17). First, the electron-phonon scattering model will be introduced as the electron-phonon cross-sections will substitute the Mott cross-sections at energies below 200 eV with a smooth transition.

Fundamentally, the Mott cross-sections describe the elastic scattering of a projectile, i.e. electron, with a single atomic target. At low energies, however, the electron couples stronger with the lattice interactions since its wavelength becomes comparable to the interatomic distances. Therefore, we will follow the approach by Kieft [7], and later by Verduin [8] to use the Mott cross-sections for energies above 200 eV, electron – acoustic (AC) phonon cross-sections [2, 21] for energies below 100 eV and a linear interpolation between these two cross-sections for energies between 100 and 200 eV, as was schematically summarized in Fig. 2.11.

We calculate the electron-phonon mean free path with the model developed by Verduin for three acoustic phonon modes [8]. However, as the source of parameters used in these models was not properly referenced, we replaced the values with different values which are reported in reliable sources. These parameters are reported in

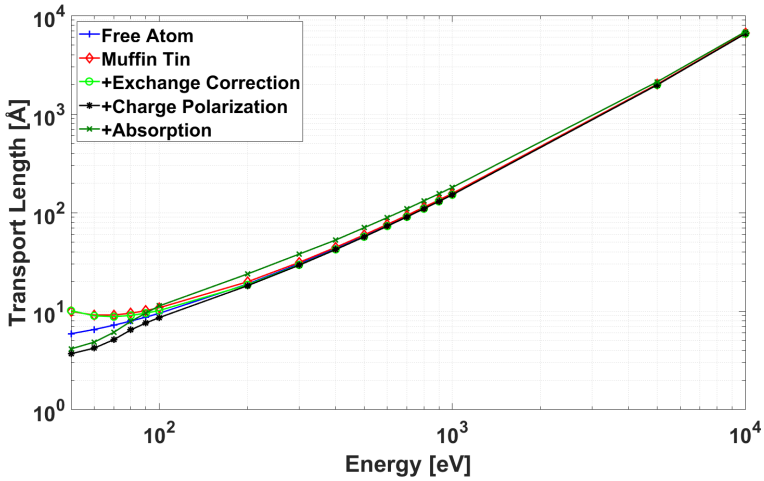


Figure 2.14: Effect of different ELSEPA options on the Transport Length. The energy reference is the sample's vacuum level.

chapter 4 (Table 4.1).

The effect of these new parameters on the mean free path compared to those reported in Verduin's thesis [8] is demonstrated in Fig. 2.15. The mean free path has two limits at low (red) and high (blue) energy. The high-energy part will not be affected since Mott theory is used in that regime. At low energy, the mean free path is lower than before which increases the frequency of elastic events.

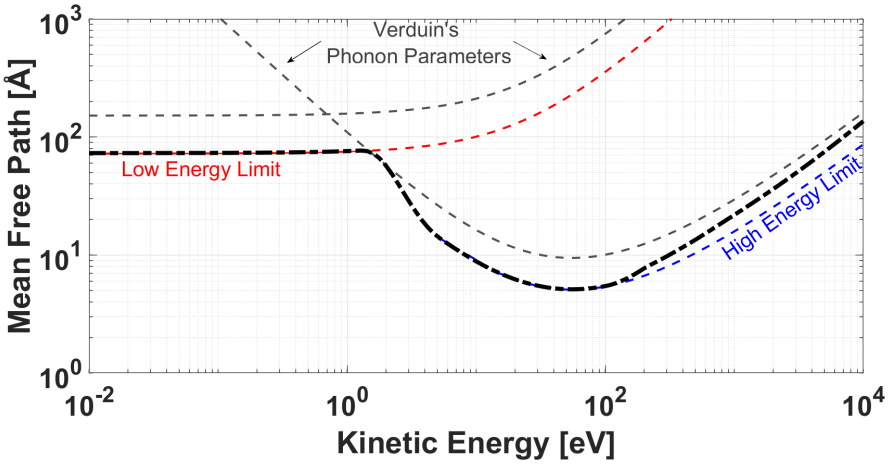


Figure 2.15: Change in the AC phonon MFP due to the new phonon parameters. The black dashed line is the final elastic MFP merging the two limiting cases. The MFP below 200 eV is clearly affected by the parameter update. The energy reference is the bottom of the band.

The effect of the parameter changes on the SE and BSE yields is presented in Fig. 2.16. The smaller mean free path at low energies increases the emission for both the SE and BSE yield at low energies. At higher energies the BSE yield is not affected but the SE yield decreases. This can be explained considering the creation depth of the electrons. At low primary energies, the SEs near the surface are subject to more elastic scattering than inelastic scattering due to the shorter electron-phonon mean free path. Therefore, their escape probability is larger. At high primary energies, the beam penetrates deeper in the material subject to Mott scattering, thus the SEs are created deeper in the material and suffer more energy losses due to the shorter electron-phonon mean free path before they come to the surface. As a consequence, the SE yield drops. A similar effect occurs for the low energy part of the BSE yield and the yield increases, but the high energy part of the yield curve is not affected since the electrons are still scattered by Mott scattering.

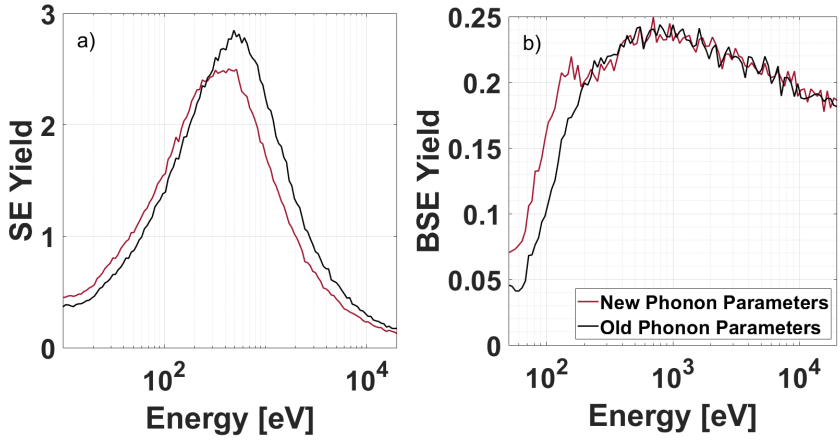


Figure 2.16: The effect of new phonon parameters on the SE and BSE yield.

Now, we compare the impact of the model refinements of the elastic MFP on the SE and BSE yields. Since the Mott cross-sections are substituted with the electron-phonon scattering cross-sections at low energies, the effect of model refinements below 100 eV are not present in this comparison.

The sensitivity of the secondary and backscattered electron emission to the various elastic MFP model choices is demonstrated in Fig. 2.17. The difference is negligible, although the mean free paths are different.

The results demonstrated that SE and BSE yields are not sensitive to the changes in mean free paths for energies > 200 eV, but they are sensitive to mean free path changes at energies lower than 200 eV (Fig. 2.16), which makes the electron-phonon mean free paths important. For these low energy quasi-elastic scattering events, we are going to use the model developed by Kuhr [33], Fitting [34], and Schreiber [35] as implemented in Verduin [8] with updated material parameters for silicon, copper,

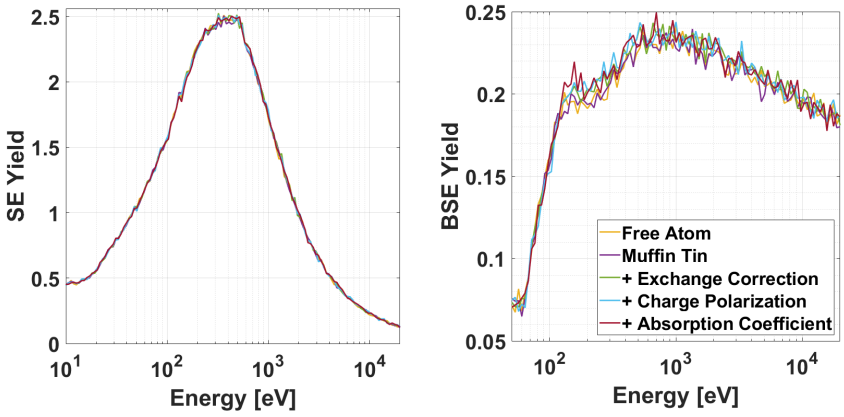


Figure 2.17: Sensitivity of SE and BSE yields to Mott Cross - Section Options

and silicon dioxide (chapter 4 - Table 4.1).

Boundary crossing

Classically, when an electron interacts with a boundary, it can be transmitted to the other medium or be reflected. If the perpendicular component (to the surface) of the electron's kinetic energy K is larger than the surface barrier ΔU, it is transmitted. After the transmission, the electrons new energy K' is equal to K-ΔU. The barrier height is:

$$\Delta U = Barrier@Destination - Barrier@Departure \tag{2.10}$$

where Barrier (to reach the vacuum level) is the sum of the Fermi Energy and the Work Function for metals, and the sum of the Electron Affinity, Fermi Level, and half the Band Gap for semiconductors and insulators [12]. This equation is valid for both sample-sample, and sample-vacuum interfaces. In case, one side of the interface is vacuum, then the term for the vacuum equals to 0, and ΔU equals to a single term.

If the electron is not perpendicularly incident on the surface, the electron direction will change upon transmission due to the change in energy, which is known as refraction.

The refraction angle θ' can be calculated by conservation of momentum in the direction parallel to the surface. The final equation [8] is given below:

$$sin\theta' = \sqrt{\frac{1}{1+\frac{\Delta U}{K}}} \cdot sin\theta \tag{2.11}$$

where θ is the incidence angle.

Quantum mechanically, part of the amplitude of the electron wave can still be

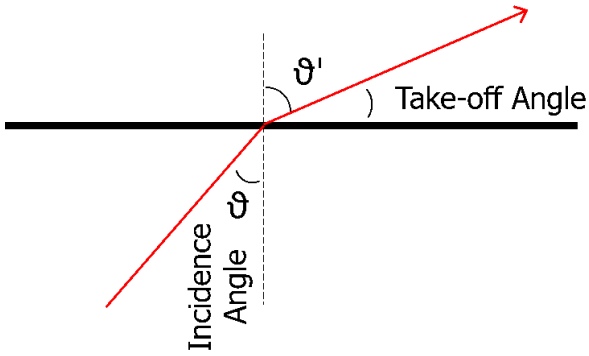


Figure 2.18: The sketch for the refraction when an electron is crossing an interface. The horizontal solid line is the material interface; the orthogonal dashed line is the surface normal. The electron depicted with the solid red lines is approaching the interface with an incidence angle of ϑ, and refracts in the direction of ϑ′ after the interface. The take-off angle is the angle between the emitted electron and the interface.

reflected even though it is transmitted. The probability of transmission, T is given in Eq. 2.12:

$$T = \frac{4\sqrt{1+\frac{\Delta U}{Kcos^2\theta}}}{(1+\sqrt{1+\frac{\Delta U}{Kcos^2\theta}})} \tag{2.12}$$

The quantum mechanical model decreases the low energy electron emission since the denominator gets bigger than the numerator as the electron's energy decreases. The sensitivity of critical dimension measurements to the quantum mechanical interface transmission model is going to be discussed in chapter 3.

2.3.2. virtualSEM

The models used in virtualSEM (version February-2016) were previously published in Arat et al. [6]. For convenience, we describe the models and highlight the differences from the ideal picture given in the beginning of this chapter.

Inelastic scattering

For inelastic scattering losses, the continuous slowing down approximation (CSDA) was employed [36, 37]. In contrast to discrete energy loss channels, as employed in e-scatter CSDA assumes an average energy loss of all inelastic channels per distance traveled.

Remember that the dielectric function model provides the energy and momentum transfer for an inelastic event. CSDA does not specify those for a particular event, and the secondary electron generation is poorly defined within this model. Therefore, another model is needed to define SE generation and its properties.

For fast (> 50 eV) secondary electron generation, virtualSEM uses Møller cross-sections as proposed by Murata [38]. This is a hybrid CSDA model.

In this model, the inner-shell ionization is defined discretely up to a cut-off energy, and the stopping power of the inner-shell ionization models is subtracted from the total stopping power. For slow (< 50 eV) secondary electrons virtualSEM uses a model proposed by Lin et al. [37]. In the model, the energy loss between two elastic scattering events is assigned to the secondary electrons based on the (remaining) stopping power:

$$-\frac{dE}{ds} \tag{2.13}$$

where dE is energy change and ds is traveling distance.

The stopping power (SP) used in virtualSEM is a modified version [36] of Bethe's equation since the original equation results in negative values at low energies (Fig. 2.19). The cut-off energy for the fast SE is approximately at 1 keV. Below this energy, fast SEs are not produced (red line in Fig. 2.19). The modified version is comparable with the other SP (Denton and Nguyen-Truong [39]), which are calculated with the full Penn algorithm.

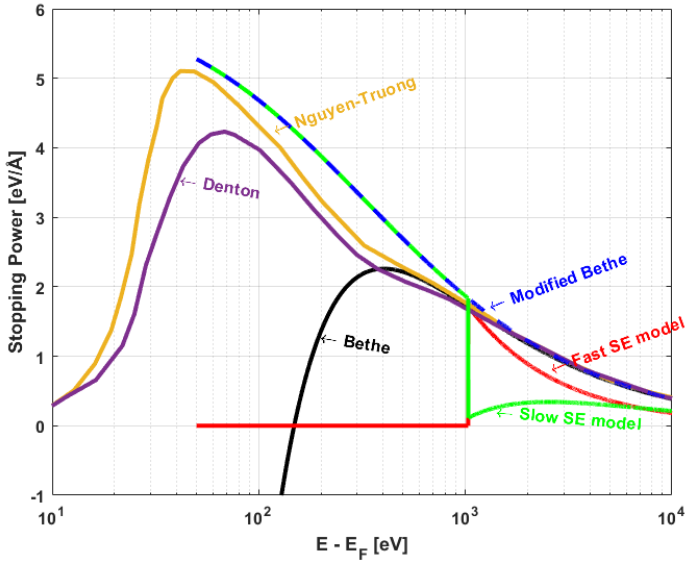


Figure 2.19: Stopping power (SP) comparison for silicon: the dashed blue line is the SP of the CSDA model by modified Bethe, which has only elastic scattering. The impact-ionization mechanism is the explicit inelastic scattering mechanism named as fast SE model, which is drawn by the solid red line. The remaining SP from the modified Bethe model is given by the solid green curve. This is the SP used for slow SE generation. The Bethe [36], Denton (in [39]) and Nguyen-Truong [39] are benchmarks from the literature. The zero of energy is the Fermi energy (E_F).

However, as we mentioned earlier, an additional model is required to convert the

energy lost to SEs. The SE generation rate, n(z,E) is defined by using the stopping power as follows:

$$n(z,E) = -\frac{1}{\varepsilon}\frac{dE}{ds} \tag{2.14}$$

where ε is effective energy to generate a SE. However, ε is an unknown.

The emission probability of the generated SE, p(z) is given by:

$$p(z) = \frac{1}{2}e^{-\frac{z}{\lambda}} \tag{2.15}$$

λ is an effective escape depth, and z is the depth. The fraction (0.5) corresponds to the half of the electrons which are generated towards the surface.

SE yields can be found by taking the integral of n(z,E) times p(z) over the depth [37]:

$$\delta(E_{primary}) = \int n(z,E)\cdot p(z)dz \tag{2.16}$$

Following a reverse approach, i.e. fitting the simulated yield to experimental SE yield data, ε and λ can be found.

From the relation of the stopping power (Eq. 14) and ε, the number of generated SEs between two elastic events is calculated. The energies of slow SEs are determined at their generation by inverse distribution of number of generated electrons $S(E')$ where E' is the generation energy. The function is based on the Streitwolf's equation reported in equation 4.28 in Reimer [27] and given below:

$$S(E') = C\cdot\frac{1}{(E'-E_F)^2} \tag{2.17}$$

where E_F is the Fermi energy. The pre-factor, C is determined such that we can draw a random energy (between Fermi level + work function and 50 eV + work function) from that distribution function where the integral from the lower bound (the smallest energy such that SE can escape) to the upper bound (50 eV + work function, i.e., such that the highest energy after surface crossing is 50 eV) gives exactly 1.

From the relation of the stopping power (Eq. 2.14) and ε, the number of generated SEs between two elastic events is calculated. The energies of slow SEs are determined at their generation based on the calculations of Streitwolf and the analytical distribution function (Eq. 4.30 given in Reimer [27]). However, as Reimer explained, this model does not consider the events excitation of core & conduction electrons, elastic & inelastic scattering, and the interface effects discretely. Therefore, it may fall short of reproducing the emission spectrum if not calibrated.

The scattering angles of slow SEs at generation are randomly decided from a uniform (isotropic) distribution. Our own tests and the literature [40] demonstrated that this is a suitable approximation since the low energy electrons lose the initial scattering angle information after multiple scattering. In other words, they are memoryless in terms of scattering angles.

The electron scattering is stopped at 100 eV or below since the stopping power below 100 eV has considerable uncertainty. In addition, it is assumed that these low energy electrons do not travel a big distance. The residual energy is converted to SEs with the same two-parameter (λ, ε) model and distributed throughout the material with the mean free path of λ. They are either emitted from the surface or absorbed by the material at this final location. The model described here has particular advantages such as producing the desired SE yield. However, it overlooks the electron scattering cloud and the energy distribution of electrons since there is no low energy scattering model.

Elastic scattering

For elastic scattering, the Mott cross-sections are used from Czyzewski's calculation [30] for a free atom model down to 100 eV (see Fig. 2.13) instead of a muffin-tin model. In e-Scatter, this limit was set to 200 eV, replaced with electron-phonon scattering cross-sections below 100 eV, and from 100 eV to 200 eV these two cross-sections are interpolated.

Stopping the electron scattering at 100 eV is a very crude assumption that can impact the electrons' spatial distribution in the material. VirtualSEM results in 50 % of the emission current being within a radius of 1 nm around the point of incidence for a 0-nm diameter beam. This value is 4.5 nm for e-Scatter.

Fig. 2.20 compares the normalized SE emission current of virtualSEM and e-Scatter for silicon with 0-diameter spots. The emission is defined as (equation 3.10 in Silvis-Cividjian [41]):

$$N_{\sum}(r) = \sum_{0}^{r} N(r') \tag{2.18}$$

where $N(r')$ is the number of secondary electrons emitted in a ring between [r', $r' + dr'$].

The sensitivity of the emission and critical dimension measurements to the elastic cross-sections will be described in chapter 3.

Boundary crossing

In virtualSEM, electrons cross the boundary based on the classical refraction effect, and quantum mechanical treatment is not performed. Fig. 2.21 compares the angular emission properties of virtualSEM and e-Scatter, where the quantum mechanical model is used only in the latter. Assuming the electrons' angular distribution is the same in the material for both models, let's try to understand the curves more in detail. The emission angle is the angle between the surface and the electron emission direction, which we call the take-off angle (see Fig. 2.18). The incidence angle is the angle between the surface normal and the electron.

For vacuum-sample interfaces, an emitted electron's take-off angle can be 90° only

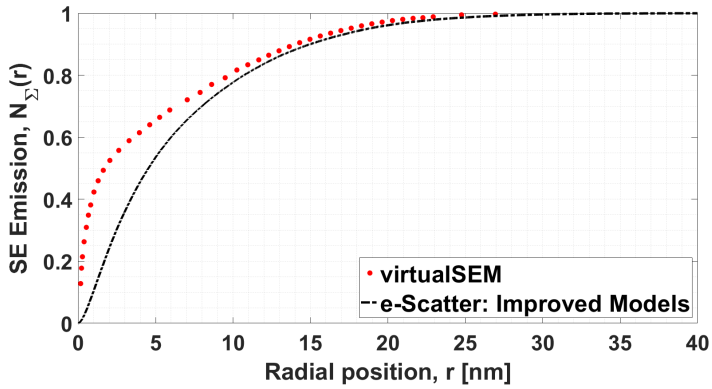


Figure 2.20: Normalized SE emission from a disk of radius, r for silicon.

if its incidence angle to the surface is 0°. Otherwise, it will be refracted towards the surface when it is transmitted to the vacuum. At those high emission angles, the solid angle is tiny. Therefore, the probability distribution function (PDF) is small. At the lower take-off angles the solid angle increases, therefore the PDF increases (45°). Although the solid angle increases at even smaller take-off angles (< 45°), the emission decreases because the perpendicular component of the electron energy becomes too small to overcome the surface barrier. Therefore, the small emission angles (0°) are expected to be less present in the angular spectrum. So far, this explains the behavior of the orange curve in Fig. 2.21 (virtualSEM), but not the asymmetry in the blue curve (e-Scatter). The quantum mechanical probability of reflection increases when the incidence angle increases. This additional effect decreases the presence of the low take-off angles (0°). This is the explanation of the suppression at low angles and the asymmetry of the blue curve.

The effect of this difference on SEM imaging and critical dimension (CD) measurement will be investigated in a sensitivity analysis in chapter 3.

Charging model

Previously, a multigrid based electrostatic field solver was implemented into virtualSEM [6]. This allows virtualSEM to calculate the induced fields and trace the electron trajectories within these fields.

The Monte Carlo kernel (scattering models) calculates the electron distribution within the material. Once the distribution is known, the Poisson solver calculates the electrostatic potential for a non-uniform quadrilateral mesh. When the field is known for the entire domain, the Monte Carlo kernel is able to calculate another batch of electron trajectories in the electric field. The electron scattering and the electric field update follow each other in a dynamic feedback loop.

The charging model in virtualSEM (2016) allows for the electron-hole recombination during the Monte Carlo part, i.e. the scattering. However, it does not include any

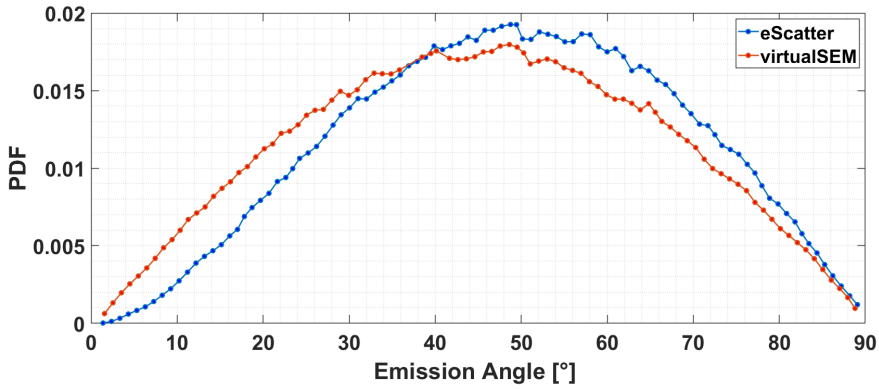


Figure 2.21: Distribution of angular emission of SE electrons. Probability density function (PDF) versus emission angle. The emission angle is the take-off angle, which is the angle from the sample surface to the electron direction.

dynamic redistribution model, as mentioned in the introduction.

As explained, virtualSEM has some crude approximations and some missing models for both the electron scattering and charging parts. But, the accuracy of the charge carrier generation and their distribution is essential to simulate charging. We will investigate the model details in chapter 3 and chapter 4, and explain the model improvements to simulate charging in chapter 4.

2.4. Description of a ”good” experimental reference

To verify the SEM simulators, the results should be compared with real experiments. What happens if the results agree well with particular experiments? Should they be trusted fully? If the results do not compare favourably, does this mean the simulation is completely untrustworthy? What happens if both the experiment and simulation are flawed and they both look similar but don’t show the reality? For these reasons, it is essential to have ”trustworthy” references for the verification of simulations. In a trustworthy experiment, insight has to be given in all parameters that may affect the measured data.

Ideally, we would like to know as many details as possible from the ”good” experimental data to set up the simulation properly. On the other hand, controlling and reporting all the details of the experiment is a demanding task. And papers in literature often fail from this perspective.

For instance, literature reports secondary electron (SE) yields but falls short of reporting sample properties, surface treatments, and vacuum conditions. One should be aware of the effects that several parameters have on the detected signal to reproduce the published results by simulation.

Here, we will analyse the experimental factors that may influence electron emission yield measurements. As a result, we can evaluate the reliability of data to serve as a reference for simulations and assess the sources of possible mismatches in comparisons.

Below, we describe the most critical parameters for electron emission yield and energy spectra measurements. In each item, first we discuss static experimental setups where time-dependent (dynamic) effects such as charging effects are not observed. Then we extend the discussion of these items to cover the charging effect.

In the checklist of 2.1, the required information is listed that ideally is included in every study reporting electron emission yields. The right-hand side contains information that is required for charging samples, in addition to the information required for non-charging samples on the left-hand side.

2.4.1. Literature examples for yield measurements with charging

Reproducing experimental SE yields is one of the most frequently used test methods for simulations. However, there is a considerable spread in the experimentally reported results [55], which increases the uncertainty. The spread is due to the different experimental conditions and parameters covered in the section above. Ideally, we would like to know all the parameters that can affect the results. The simulation can still represent the setup properly if the essential parameters are reported. Hence, we should look at the description of the experiment, whether it gives enough detail. As an example, we evaluated two papers from this perspective.

Dionne reports the SE yield of SiO_2 [56]. This data is also reported in the widely used database of electron-solid interactions compiled by Joy [53]. The reported information in the original study contains external fields, the description of the method, the detection mechanism, the surface state after cleaning (argon-sputter etching), and the beam energy. However, details about the sample such as the type of oxide, and the crystal structure are missing. In addition, the properties of the probe (current/dose/dwell time) are not reported and the vacuum condition is not reported.

Another example of SE yield data is reported for Al_2O_3 by Belhaj [52]. In this study, the reported information is: the type of material (polycrystalline Al_2O_3), the exact geometry (the thickness and the size), the vacuum condition, the temperature, the detailed information about the experimental tools (pump types, the electron gun and detectors), the probe features (the diameter, current/charges per pulse), the detection sensitivity, the evolution of the surface potential, the cleaning of the charged region, the number of incident charges, the pulse duration, and the external field. Although, the contamination analysis of the surface was not reported, this study provides great detail. This example also shows that it is not as straightforward to report the SE yield of insulators as it is for conductors since the yield significantly depends on many additional parameters.

Parameter	Description
Sample:	The electron emission properties significantly depend on the type and condition of the inspected sample. The surface condition of the sample is one of the most critical parameters that affect the SE emission. For instance, the effects of a native oxide [42], water vapor [43, 44], hydrocarbons [42, 45], physisorbed [46] or induced carbon deposition during the measurement [47] have been demonstrated experimentally. On the other hand, the effect on the BSE yield measurements is minor. It is essential to compare simulation results and data from clean samples to determine the ideal electron yield of the material. It is important to use data from ultra-high vacuum (UHV) setups and cleaned samples. However, it should also be noted that surface treatments such as ion sputter cleaning alters the surface roughness, which also changes the SE yield [48]. This is one of the most overlooked parameters in yield measurements. In case the measurand is an insulator, the details of the material properties are very important. For example, the number of trapping sites often differ considerably for different crystal structures [49].
Detector:	The detector and detection method can have a significant effect on both SE and BSE signals [50]. The details of the detector design and collection efficiency are often missing. For example, the sensitivity of the measurements to the grid transparency in hemispherical collectors is not known [51].
Beam:	Yield measurements are mostly reported as normalized data. Therefore, it is important to determine the probe current accurately since it will determine the yield. It is usually measured by a Faraday cup with good accuracy, but at very low energies, it can be a source of error [52]. When measurements on insulating materials are performed, the details of the probe become more important. The incident charge, pulse duration, dynamically changing beam energy, become very important parameters since they affect the SE yield significantly [53, 54].

Table 2.1: Required information for a "good" experimental determination of electron emission yield for non-charging and charging samples. For the charging samples the information for non-charging samples is required too.

Non-Charging Samples		Charging Samples	
Vacuum condition		Trap densities	
Sample (purity, crystal structure)		External fields	
Sample thickness (if not bulk)		Dwell time	
Surface roughness		Probe pulse duration (if applicable)	
Detector collection efficiency		Probe diameter	
Surface contamination analysis (before and after the measurement)		Cleaning of the charged region in terms of charged contamination	
Probe current			
Error analysis			

2.5. Emission properties

In this section, we compare our own basic simulation outputs with various experimental data and other simulated data. The data contain: SE yield, BSE yield, angular emission distribution, energy spectra, and penetration depth.

2.5.1. SE yield

We start with comparing SE yields for silicon and copper with various experimental and simulation data. As emphasized in the previous section, we paid attention to "good" experimental data. The data markers of more reliable experiments (in UHV, surface treatment) are exaggerated in Fig. 2.22 and Fig. 2.24.

Fig. 2.22 shows the simulated SE yield curve by e-Scatter and compares it with various experimental data. Among these experiments, the data from Walker [55] and Bronstein [56] are reliable because a UHV setup is used and the sample is cleaned. The original source of Bronstein [56] is hard to find, (in Russian), but the data is reported in several sources such as the database of Joy [53] (ref. 106), Walker [55], Demers [57], and Pierron [14].

The data for as inserted and cleaned samples from Walker [55] shows the effect of the sample surface condition. The data from Joy's database [53] are also plotted here since they are frequently used as a source. However, these data (except ref. 106 in the database) are either poorly explained or not obtained in a UHV setup. For example, the data from ref. 2 in this database are obtained under SEM conditions where the sample surface is generally dirty (contaminants, oxide, and carbon). Similarly, ref. 25 (in this database) does not use a UHV setup for the measurements [54]. Additionally, ref. 17 does not mention about silicon in the paper at all [58]. Therefore, these data are not recommended to use.

The calculated yield value by e-Scatter is approximately a factor of two larger than the experimental values. The energy where the yield reaches its maximum does agree well with the experimental values. This high yield is less of a problem when doing

relative comparisons, and SEM images are scaled anyway during acquisition.

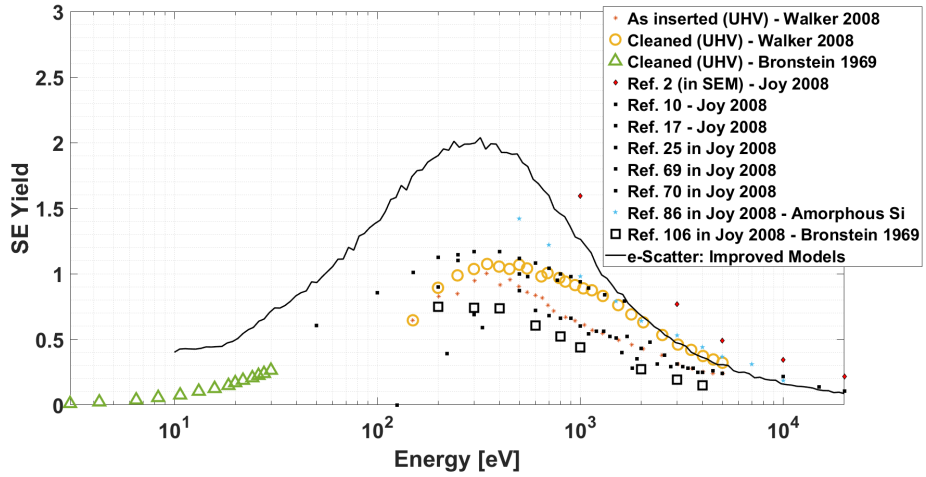


Figure 2.22: SE yield comparison of experiments and e-Scatter simulations for Si. The data is from Walker [55], Bronstein [56] (at low energies), and Bronstein [53] (at high energies). The data from Joy's database [53] is tagged as it is cited.

Fig. 2.23 shows a compilation of simulated SE yield curves from several sources [6, 14, 33, 57, 59–64]. The purpose of this comparison is to give a general idea of other simulation work in literature.

In general, the simulations that are based on or involve Penn's algorithm (Ding 2011 [55], Renschler 2011 [59], Pierron 2017 [14], Li 2013 [60]: Full Penn, JMONSEL, Nebula) produce a yield where its maximum yield occurs at lower energy than for yields produced by other models. For example, the data based on the Mermin dielectric function by Kuhr [33] reaches its peak at a slightly higher energy, and data based on Ashley's model (Li 2013 [60]: Single Pole, and e-Scatter) peaks at even higher energy (up to 150 eV). Lastly, the yields from the simulations (CASINO, virtualSEM 2016) based on the CSDA model follow a very different trend.

In Fig. 2.24 several experimental sources [42, 48, 50, 53, 63, 64, 66, 67] are compared for copper. Here, we exaggerated the markers from reliable sources which use clean samples and UHV systems. These data still show a considerable spread in yield, but the maximum yield occurs at the same energy. Although the simulated yield value is approximately a factor of two higher than the experimental values, the energy of the peak position matches well.

Also, there are data from as inserted (dirty) samples or measurements under poor vacuum conditions. The measurements (Ref. 2 and Ref. 3 in Joy's database [53]) in SEM conditions are examples. These data show a bigger spread than the mean of the other experiments and their maximum yields occur at lower beam energies.

In this comparison, there is an uncommon rise at very low energies (4.65 eV). This is due to the author's definition of energy reference. They used the Fermi level as the

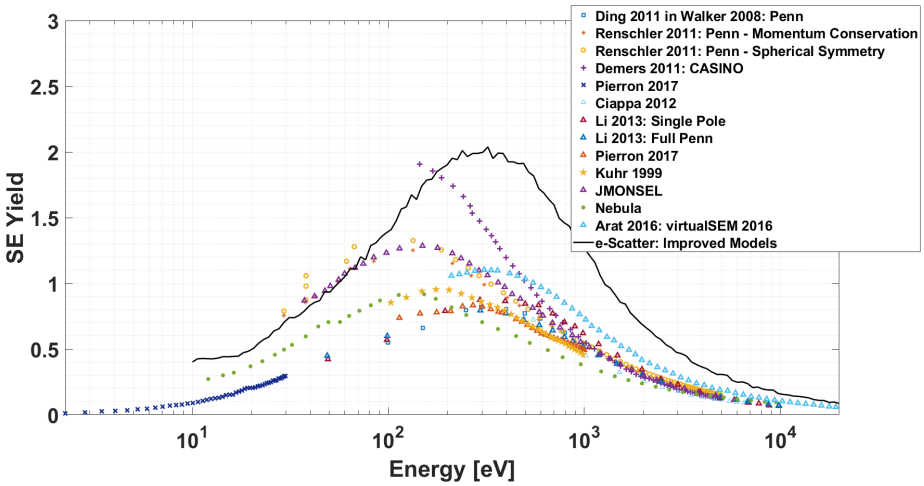


Figure 2.23: The SE yield comparison of different simulations and e-Scatter for Si. The simulated data is from Ding 2011 [55], Renschler [59], Demers 2011 [57], Pierron 2017 [14], Ciappa 2012 [65], Li 2013 [60], Kuhr 1999 [33], JMONSEL [61], Nebula [62], and Arat [6].

zero of energy instead of the vacuum level. Therefore, they can measure the sample's work function. The smooth drop is due to the energy spread of the electron source. For a one-to-one comparison with other data, these should be shifted to the left by the work function (4.65 eV).

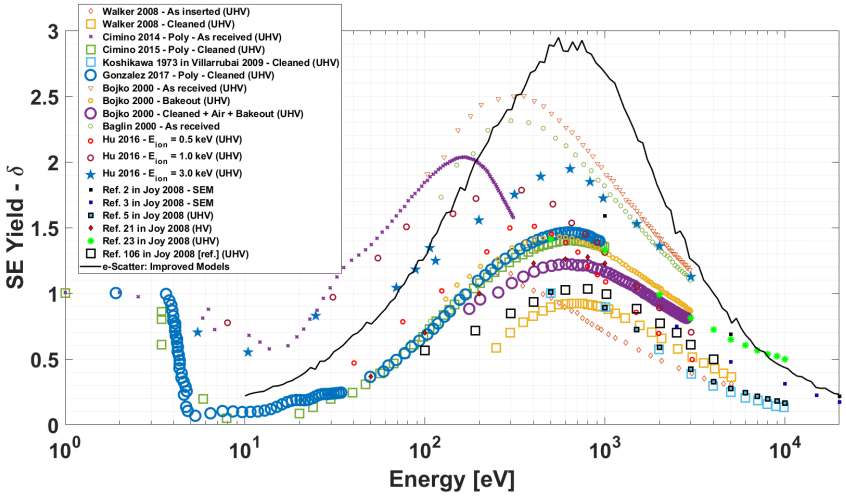


Figure 2.24: The SE yield comparison of experiments and e-Scatter for Cu. The data is from Walker 2008 [55], Cimino 2014 [63], Cimino 2015 [50], Koshikawa 1973 [68], Gonzalez 2017 [66], Bojko 2000 [42], Baglin 2000 [67], Hu 2016 [48]. The data from Joy's database [53] no data tagged as it is referred at there. The zero of energy is the vacuum level except for Gonzalez [66] and Cimino [50, 63]. For those, it is the fermi level (vacuum level – work function, 4.65 eV).

In Fig. 2.25, simulated SE yields of Cu are compared with e-Scatter. The data from [49, 64, 69–71] are based on the Full Penn algorithm, except "Mao 2008 – SPA" which is based on the Single Pole Approximation of the Penn Algorithm [71]. Ashley's model used in e-Scatter is close to this approximation, in terms of inelastic scattering model, but still there is a considerable difference due to Kieft's refinements and the electron-phonon models which influence the SE yield.

In most of these simulations (Ding 2001 [69], Villarrubia 2009 [64], Ding 2004 [70], Mao 2008-FPA [71]), the Full Pen algorithm is used. This algorithm describes the transferred energy in an inelastic scattering event but not the initial kinetic energy of the SE. If it is an inner shell ionization event, the SE's energy is the transferred energy after subtracting the binding energy. Otherwise, different assumptions were used as noted in the legend of Fig. 2.25. "Fermi Level" refers to the simulation assumption that the initial kinetic energy of the SE is equal to the Fermi Energy. "Fermi Sea" refers to the case that this initial energy is determined from the Fermi sea where the probability distribution function is proportional to the density of states of the free electron gas [70]. "Distinction" refers to the situation when ionization is distinguished for plasmon decay and impact ionization of valence band electrons. In e-Scatter, the electron energy for outer-shell ionization is determined from the "Fermi Sea" model.

The SE yield can differ significantly depending on how one determines the initial energy of the SEs. However, the beam energy where the yield reaches its maximum is approximately the same for all Penn models. The maximum energy value is slightly lower than for e-Scatter.

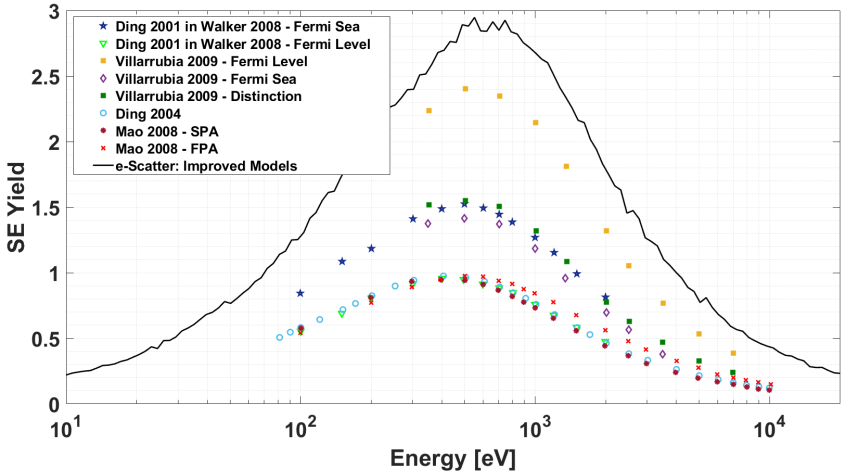


Figure 2.25: The SE yield comparison of different simulations and e-Scatter for Cu. The data is from Ding 2001 [49], Villarrubia 2009 [64], Ding 2004 [70], and Mao 2008 [71].

Let's wrap up what we have demonstrated so far. The absolute value of the SE yields from e-Scatter simulations for silicon and copper is roughly 2 to 3 times higher

than the experimental yields. For the analysis of SEM images, this may not have a significant effect when the detection signal is scaled, such that e-Scatter can reproduce qualitatively well the features of experimental SEM images.

We have seen the effect of experimental conditions too. Surface contamination has a significant effect on the SE yield. For instance, the data from UHV setups and cleaned samples is more consistent than the ones from HV conditions. For clean samples, the SE yield difference is within a factor of 2, where it is up to a factor of 4 for uncleaned samples. If the sample is cleaned with a bakeout and/or a sputtering process, the experimental data agree better (within 80 %).

Sample cleaning also influences the peak position of the yield curves. The experimental curves peak at ≈300 eV for uncleaned copper samples. After the cleaning process, the yields peak at ≈650 eV. This is the same value as simulated by e-Scatter.

Regarding the comparison of e-Scatter with other simulators, generally, other simulators produce lower yields which are closer to the experimental values. However, their peak positions are at a few hundred eV lower than e-Scatter and the experimental data, noticeably the ones using the Full Penn algorithm.

2.5.2. BSE yield

Here, we compare BSE yields of silicon and copper samples with several experimental and simulation data. In contrast to the SE yield, the BSE yield should not be as sensitive to surface contamination because high energy electrons are not very sensitive to surface contamination. Therefore, the difference between HV (high vacuum) and UHV experiments is not expected to be significant. Nevertheless, UHV setups are represented with bigger markers [49, 53] in Fig. 2.26 and Fig. 2.28.

El Gomati [49] published BSE yields measured in a UHV tool for a silicon sample before and after (sputter) cleaning. In Fig. 2.26, this data is marked as ”As Inserted” and ”Cleaned”. The comparison shows that the number of high energy electrons, i.e. the BSE yield is not affected by the surface condition. There is still some variation in the data from different sources. This can be ascribed to different material properties such as crystal structure. For instance, the data from El Gomati [49] is for a single crystal sample and the data from Ref. 86 in Joy [53] is for an amorphous sample. Overall, the simulated data agree well with the experiments for energies higher than 500 eV.

Simulated BSE yields from literature [39, 49, 57, 59] are compared with e-Scatter in Fig. 2.27. At low energies (200 eV – 500 eV), our data agrees well with most of the simulated data. At high energies, e-Scatter yields deviate from all other simulated data. This shows that simulated data underestimate the BSE yield compared to e-Scatter and the experiments shown in Fig. 2.26.

Similar to the comparison for silicon, the BSE yield of copper simulated using e-Scatter is compared with experiments (Fig. 2.28) and with other simulations (Fig. 2.29) from literature.

The spread of experimental data is bigger for copper than for silicon, where the

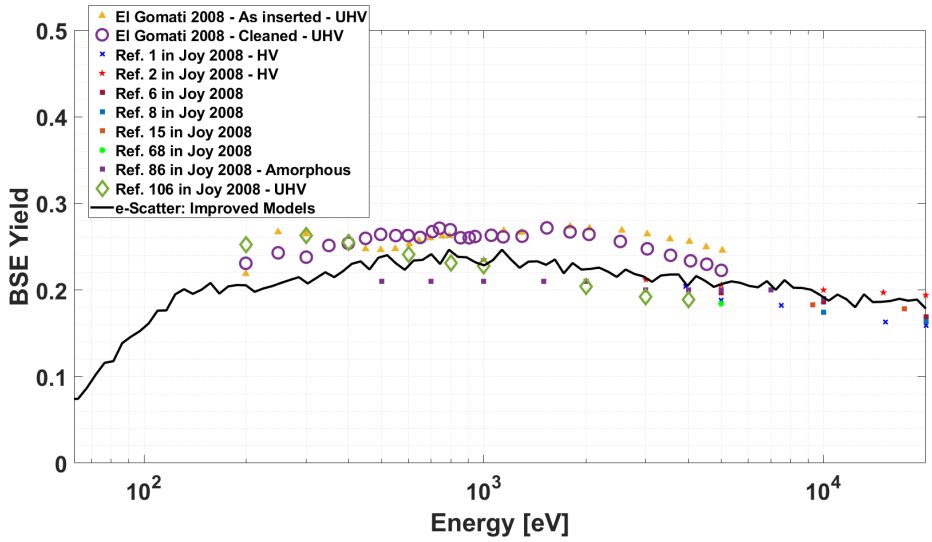


Figure 2.26: The BSE yield of silicon from e-Scatter simulations compared to experimental data: El Gomati [49] and Joy [53].

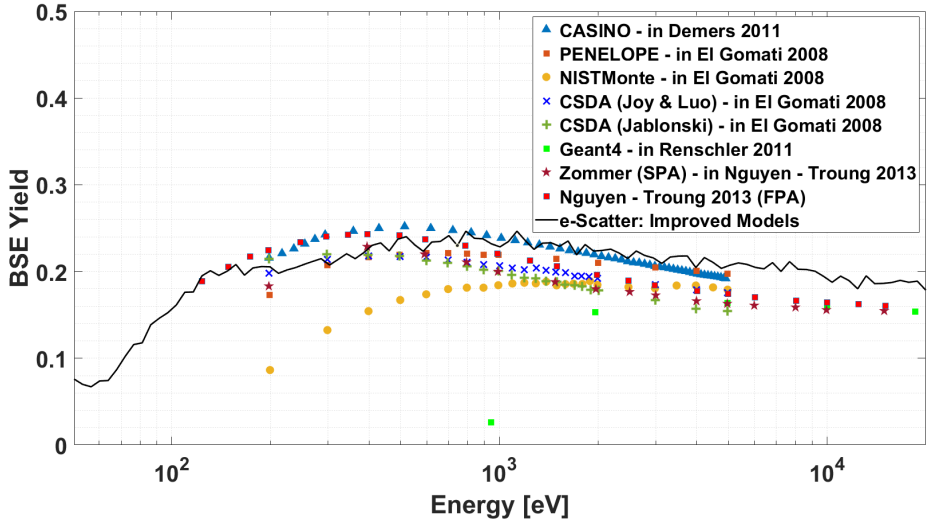


Figure 2.27: The BSE yield of silicon from e-Scatter simulations compared with other MC simulation results [39, 49].

variation of sample properties plays an important role. For silicon, samples are mostly single crystal wafers. However, for copper, samples are mainly polycrystalline or technical materials. Therefore, the properties and also the yields show bigger differences.

In addition, El Gomati's experiments [49] show that the sample cleaning does affect

the BSE yield significantly. For copper, the BSE yield from "As inserted" samples is very different after the ion sputter cleaning at low energies (≈500 eV). At high energies (> 10 keV), we see that the data from different experiments converge irrespective of whether they were performed in UHV setups [49, 72] or under SEM conditions [73, 74]. Overall, the yield produced by e-Scatter agrees well with the experiments, especially with the data from Koshikawa et al.[68].

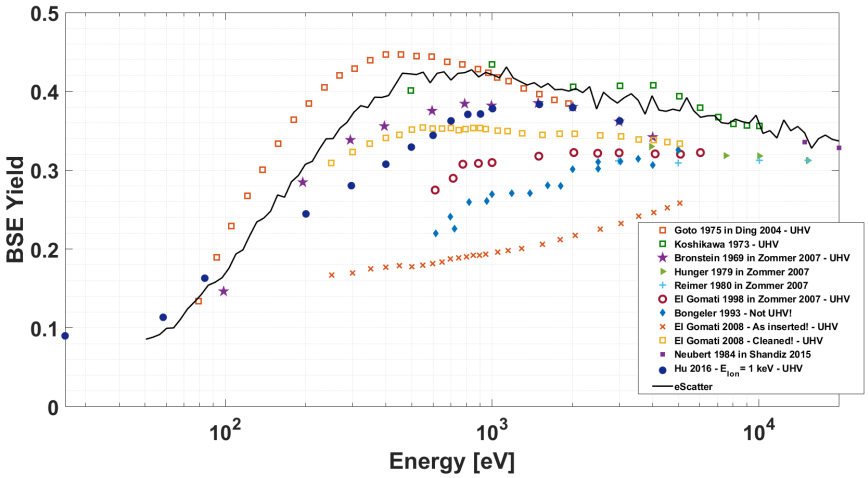


Figure 2.28: The BSE yield of copper from e-Scatter simulations compared to experimental results in literature[48, 49, 68, 70, 72, 74, 75]. Ultra-high vacuum (UHV) setups are indicated in the legend.

The spread in simulated data is also bigger for copper than for silicon at low energies and converges to the same value at high energies. Perhaps, this is related to the sample's purity. Otherwise, we do not expect that small changes in surface work function change the BSE yield significantly.

Simulations have very similar elastic and inelastic mean free paths at high energies. However, the mean free paths differ significantly at lower energies depending on the models used and this changes the BSE yield significantly at low energies as seen in Fig. 2.29.

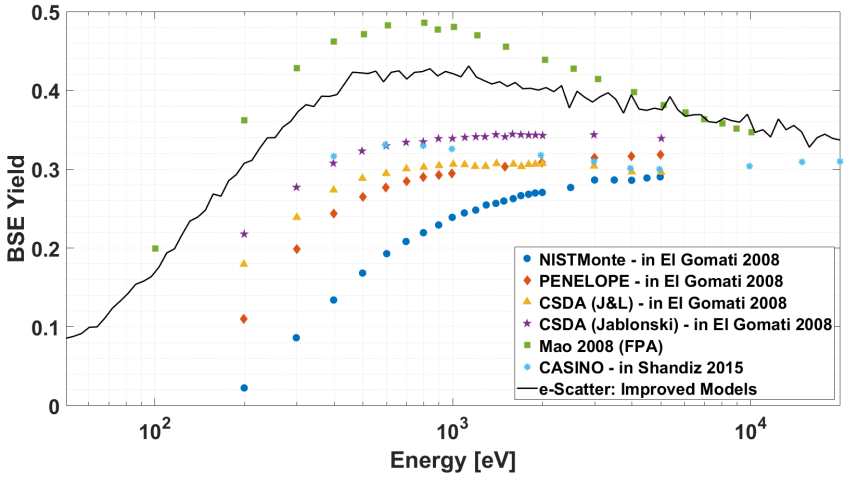


Figure 2.29: The BSE yield of Cu from e-Scatter simulations compared with other Monte Carlo simulation results [49, 71, 75].

2.5.3. BSE yield vs. incidence angle

To obtain some idea about the scattering volume of electrons in the sample, we compare the BSE yield as a function of the incidence angle. This method allows us to get more information about the scattering volume since different portions of the volume will contribute to the emission at different incidence angles.

In Fig. 2.30, the BSE yield from e-Scatter is compared to experimental and simulated data from the literature for silicon [59].

The incidence angle is defined as the angle between the beam and the surface normal. At low incidence angles (< 40°), e-Scatter and the experimental data quantitatively match well. At higher angles, both simulation data only slightly overestimate the experimental emission data.

In general, the measurements at grazing angles are more complicated. The electron probe lands at a larger area on the sample. A tail of the Gaussian probe can interact with the sample holder. In addition, the electron scattering volume intersection with the sample surface is larger. The measurement could be more prone to surface conditions such as roughness and contamination. Since the sample is rotated, the crystal orientation of the sample is not the same anymore. In the Monte Carlo simulation, this effect is not included. Last but not least, the detection efficiency can be different for a tilted sample. Considering that all these factors may contribute to the observed difference, the agreement is still remarkably good.

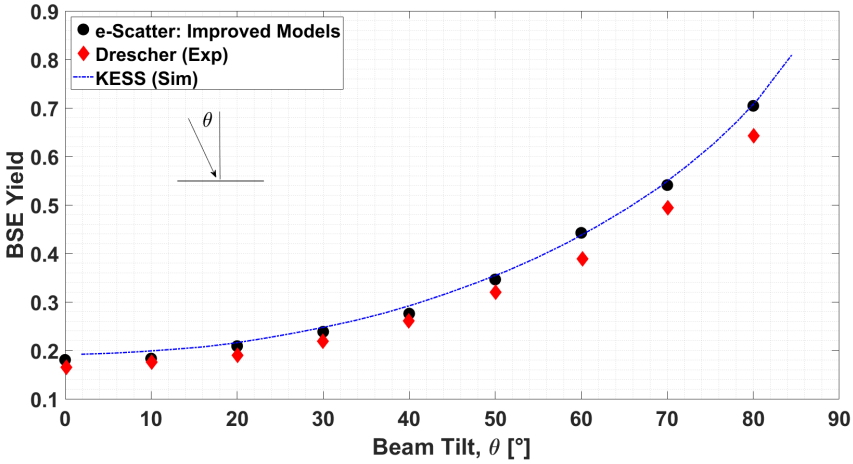


Figure 2.30: The BSE yield for silicon, from experiments and e-Scatter simulations, versus incidence angle θ. The beam energy is 25 keV.

2.5.4. Angular emission

The angular spectra of the simulated SE data are compared to experiments [76] in Fig. 2.31. The sample is copper. The beam energy is 800 eV and the incidence angle is 0°, which is indicated by an arrow. The emission is compared in four different energy ranges. The simulated data are corrected for the solid-angle (1/sin(ϕ)) and scaled such that the maximum of the 0.5 eV - 5.5 eV signal matches the experimental value. The same scaling constant is applied for the other ranges too.

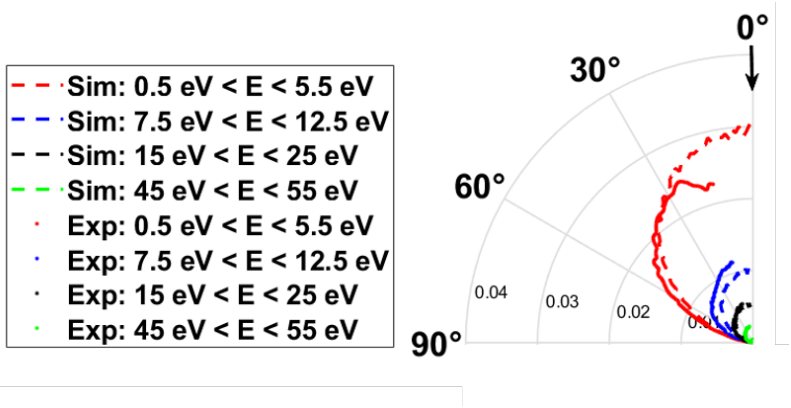


Figure 2.31: Comparison of the angular spectrum of the secondary electrons from a Cu sample. The primary energy is 800 eV. The experimental data is from Appelt et. al.[76]. The radial values are the intensity of the signal.

The experimental data is not available below 15° due to the column opening for

the beam. At angles lower than 30° in the first region (0.5 eV – 5.5 eV), it shows a sharp drop due to the design of the tool. At high angles in this region, the match is relatively poor compared to the second (7.5 eV to 12.5 eV) and the third region (15 eV to 25 eV). At the fourth region (45 eV to 55 eV), the match is qualitatively even better, however, the yield of the simulated signal is much lower than the experimental data.

2.5.5. Energy spectra

In Fig. 2.32, the energy spectra of emitted electrons are given for copper[63]. The primary electron energy is 112 eV. The simulated data are scaled such that its low energy peak matches with the experiment's low energy peak. The curves match very well over the entire spectrum. The peak positions and the slope of the exponential decay are matching well. The simulation gives a sharp peak at the primary energy which is caused by low-loss electrons. On the other hand, the experimental peak is relatively broad. This is due to the energy spread in the primary electron beam which is not included in the simulation.

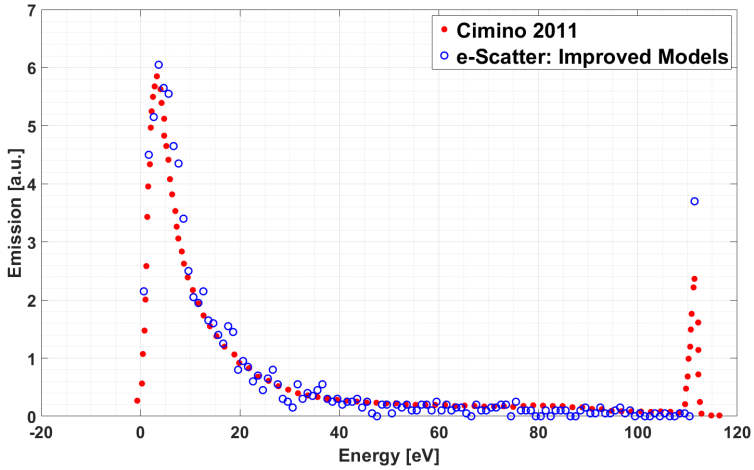


Figure 2.32: The energy spectrum of the emitted electrons from a Cu sample for a 112 eV beam, compared to the experimental energy spectrum obtained by Cimino et al.[63]

2.6. Conclusions

In this chapter, we discussed the physics of electron-matter interaction. The models used, the issues to be repaired, and the improvements made in e-Scatter were explained. The results were compared with experimental and simulated data from literature.

It was discovered that e-Scatter produces as an artefact a double-peak in the en-

ergy spectrum of the emitted SEs. This was fixed by correcting a bug in the calculation of the low energy part (< 50 eV) of the inelastic mean free path. As a result, the SE yield also changed and increased approximately by a factor of 2 for conductors and semiconductors such as gold and silicon, respectively. This change shows that the SE yield is very sensitive to the inelastic mean free path.

Another correction made to the inelastic scattering model was using Ashley's non-exchange corrected version instead of Ashley's exchange corrected version since it is possible to distinguish primary and secondary electron in the plasmon decay events. The inelastic mean free path increased approximately by a factor of 1.5 at energies above 50 eV.

After these modifications, the inelastic mean free path was also compared with the literature data (experimental and from simulations). The agreement at energies above 1 keV is within 5 %. This is the same for some experimental data down to energies of 50 eV, and for some other experimental data is within a factor of 2. Below 50 eV, the variation among the compared data (both experimental and from simulations) can be a few orders of magnitude. This can result in a significant difference in SE yields. Although the inelastic scattering models are now more accurate in e-Scatter, the absolute value of the SE yield is approximately 2 times higher than the experimental yield values. However, this absolute difference may still do not have any impact on the analysis of SEM images, where the signal is always scaled, such that e-Scatter can reproduce the features of experimental SEM images qualitatively well.

We have also investigated various model choices for the elastic scattering model. In ELSEPA, there are several model choices for Mott cross-sections. For example, the elastic mean free path is 1.5 times higher if the muffin-tin model is used instead of the free atom model. This difference can be as high as 3 times due to the different electron distribution models. However, we have shown that these don't have a significant effect on SE and BSE yields when using these models for energies above 100 eV.

For energies below 100 eV, an electron-phonon scattering model is used. We have demonstrated that both the absolute value and the shape of the SE yield curve are sensitive to the phonon model parameters. For instance, the curve's peak position has shifted to 300 eV from 500 eV for silicon when the parameters are updated with the ones from more reliable sources. This peak is at 300 eV in experimental SE yield curves. This leads to a qualitatively and quantitatively better agreement between e-Scatter and experiments.

To verify the models in e-Scatter, we have compared simulation results with experimental data for silicon and copper. These comparisons contain SE yields, BSE yields, the BSE yield as a function of incidence angle, the emission energy spectrum, and the angular spectrum of the SE emission. However, the experimental data has a big spread. For instance, the spread in SE yield from different sources can be as big as a factor of 4. Part of this due to experimental conditions such as surface contamination in HV or SEM conditions. We recognized that the data from UHV setups and cleaned samples is more consistent than the ones taken under HV conditions. The variation is

smaller (within a factor 2). A similar effect is seen for copper too. The SE yield data for as received copper samples (even in UHV setups) vary within a factor of 3. If the sample is cleaned with a bakeout and/or a sputtering process, the variation is within 80 %. This difference is related to parameters such as the sample itself and the effect of the cleaning process, such as induced surface roughness during sputtering. Also, we found that e-Scatter can reproduce trends well. The experimental SE yield curves peak at around 300 eV for as received copper samples. After the cleaning process, the data from multiple sources peak at about 650 eV. This is the same value for the simulated data by e-Scatter.

The experimental data is more consistent for BSE yields than for SE yields. The variation is less than 20 % for silicon. The effects of sample cleaning and the vacuum condition are negligible, and the simulated data by e-Scatter represent the average values of the experimental data. However, for copper, we have observed a deviation between two groups of data (group-1: cleaned and UHV setups; group-2: as received and HV setups). This deviation is as large as a factor of 2. In addition, as received samples do not have a peak value, where the data from clean samples peak at energies between 400 eV to 1 keV. This value is at 650 eV for the data simulated by e-Scatter, corresponding to the mean value of the experimental data. The amplitude of the signal also agrees well. It is within 20 % of all data from cleaned samples and 5 % of the data published by Koshikawa 1973 [68] (also a cleaned sample). The BSE yield as a function of tilt angle has a good agreement with the experimental data (within 10 %). After the model changes, we found that the energy spectrum of the simulated data has a very good agreement with experimental data for copper.

These comparisons have shown that the experimental data from UHV setups and cleaned samples have better agreement with each other and with simulated data by e-Scatter than those obtained in SEM or HV conditions. We have promoted the first category in our comparisons. However, the experimental uncertainties should be minimized for yield measurements. We have further discussed the ideal features of an experiment, such as sample preparation and signal detection. In other words, delicate experimental procedures and detailed reporting for these experiments are required for simulator developers, who are depending on the details of these data. We also gave a recipe for a "good" experimental yield determination. This recipe summarises essential parameters to be given by researchers who publish electron yield measurements.

We have also compared the yield curves from other simulators to the ones from e-Scatter. In general, other simulators produce lower yields. For SEs, these results are closer to the experimental values. However, their qualitative shapes, i.e., the peak position of the curves, are a few 100 eV lower than e-Scatter and the experimental data, notably those using the Full Penn algorithm. For BSE yields, the agreement is better than for the SEs. This is within 10 % for silicon and 30 % for copper.

In addition, we have explained the models in virtualSEM and highlighted issues such as the electron scattering volume in the sample and the emission due to the assumptions in inelastic, elastic, and models used for elastic scattering. Moreover, the

interface transmission model is compared to the one in e-Scatter. The result of that will be presented in chapter 3 when we further investigate the sensitivity of the yields and critical dimension measurements to the model ingredients. The models are going to be further tested in chapters 3-7 with 3D and charging applications. The comparisons shown here are already giving confidence in a qualitative agreement between simulated and experimental results for those tests, and an expected quantitative agreement within a factor of 2-3.

Acknowledgements

We are grateful to Luc van Kessel for reading and correcting the manuscript. We are thankful to Thomas Klimpel for the discussion on the model in virtualSEM, and Dr. Robert Polster for the discussions on scattering physics.

References

[1] H.-J. Fitting and J.-U. Friemann, *Monte-Carlo Studies of the Electron Mobility in SiO2,* Physica Status Solidi (a) **69**, 349 (1982).

[2] C. T. Chantler and J. D. Bourke, *Electron Inelastic Mean Free Path Theory and Density Functional Theory Resolving Discrepancies for Low-Energy Electrons in Copper,* The Journal of Physical Chemistry A **118**, 909 (2014).

[3] X. Li, C. H. Tung, and K. L. Pey, *The nature of dielectric breakdown,* Applied Physics Letters **93**, 072903 (2008).

[4] A. Rose, *Recombination Processes in Insulators and Semiconductors,* Physical Review **97**, 322 (1955).

[5] T. Verduin, S. R. Lokhorst, J. Hidding, L. van Kessel, K. T. Arat, and C. W. Hagen, *e-Scatter: Fast simulator for Physical Scattering Processes in Materials,* (2019).

[6] K. T. Arat, J. Bolten, T. Klimpel, and N. Unal, *Electric fields in Scanning Electron Microscopy simulations,* in *Proc SPIE*, Vol. 9778, edited by M. I. Sanchez and V. A. Ukraintsev (2016) p. 97780C.

[7] E. Kieft and E. Bosch, *Refinement of Monte Carlo simulations of electron–specimen interaction in low-voltage SEM,* Journal of Physics D: Applied Physics **41**, 215310 (2008).

[8] T. Verduin, *Quantum Noise Effects in e-Beam Lithography and Metrology*, Ph.D. thesis, Delft University of Technology (2017).

[9] J. Ashley, *Interaction of low-energy electrons with condensed matter: stopping powers and inelastic mean free paths from optical data,* Journal of Electron Spectroscopy and Related Phenomena **46**, 199 (1988).

[10] D. R. Penn, *Electron mean-free-path calculations using a model dielectric function,* Physical Review B **35**, 482 (1987).

[11] D. C. JOY, M. S. PRASAD, and H. M. MEYER, *Experimental secondary electron spectra under SEM conditions,* Journal of Microscopy **215**, 77 (2004).

[12] A. M. Theulings, *Optimisation of photon detector tynode membranes using electron-matter scattering simulations*, Ph.D. thesis, Delft University of Technology (2020).

[13] R. Khalid, F. S. Pujol, and W. S. M. Werner, *Secondary electron energy loss coincidence (e,2e) spectroscopy on Ag and Si surfaces,* Journal of Physics: Conference Series **439**, 012003 (2013).

[14] J. Pierron, C. Inguimbert, M. Belhaj, T. Gineste, J. Puech, and M. Raine, *Electron emission yield for low energy electrons: Monte Carlo simulation and experimental comparison for Al, Ag, and Si,* Journal of Applied Physics **121**, 215107 (2017).

[15] G. Gergely, *Elastic peak electron spectroscopy,* Scanning **8**, 203 (1986).

[16] W. S. M. Werner, *Electron transport in solids for quantitative surface analysis,* Surface and Interface Analysis **31**, 141 (2001).

[17] S. Tanuma, T. Shiratori, T. Kimura, K. Goto, S. Ichimura, and C. J. Powell, *Experimental determination of electron inelastic mean free paths in 13 elemental solids in the 50 to 5000 eV energy range by elastic-peak electron spectroscopy,* Surface and Interface Analysis **37**, 833 (2005).

[18] G. Gergely, *Elastic backscattering of electrons: determination of physical parameters of electron transport processes by elastic peak electron spectroscopy,* Progress in Surface Science **71**, 31 (2002).

[19] A. Akkerman, M. Murat, and J. Barak, *Monte Carlo calculations of electron transport in silicon and related effects for energies of 0.02–200 keV,* Journal of Applied Physics **106**, 113703 (2009).

[20] O. Ridzel, *Interaction of slow electrons with matter for nanoscale characterisation of solids*, Ph.D. thesis, TU Wien (2019).

[21] I. Campillo, A. Rubio, J. M. Pitarke, A. Goldmann, and P. M. Echenique, *Hole Dynamics in Noble Metals,* Physical Review Letters **85**, 3241 (2000).

[22] P. de Vera and R. Garcia-Molina, *Electron Inelastic Mean Free Paths in Condensed Matter Down to a Few Electronvolts,* The Journal of Physical Chemistry C **123**, 2075 (2019).

[23] H. T. Nguyen-Truong, *Low-energy electron inelastic mean free path in materials,* Applied Physics Letters **108**, 172901 (2016).

[24] S. Perkins, D. Cullen, and S. Seltzer, *Uclr–50400*, Tech. Rep. (Lawrence Livermore National Laboratory (LLNL), Livermore, CA, 1991).

[25] L. van Kessel, C. Hagen, and P. Kruit, *Surface effects in simulations of scanning electron microscopy images,* in *Metrology, Inspection, and Process Control for Microlithography XXXIII*, Vol. 18, edited by O. Adan and V. A. Ukraintsev (SPIE, 2019) p. 29.

[26] P. A. M. Dirac, *The quantum theory of the electron,* Proceedings of the Royal Society of London. Series A, Containing Papers of a Mathematical and Physical Character **117**, 610 (1928).

[27] L. Reimer, *Scaning Electron Microscopy*, 2nd ed., Vol. 45 (Springer, Heidelberg, 1998).

[28] N. F. Mott, *The Scattering of Fast Electrons by Atomic Nuclei,* Proceedings of the Royal Society of London. Series A, Containing Papers of a Mathematical and Physical Character **124**, 425 (1929).

[29] L. Reimer and B. Lödding, *Calculation and tabulation of mott cross-sections for large-angle electron scattering,* Scanning **6**, 128 (1984).

[30] Z. Czyżewski, D. O. MacCallum, A. Romig, and D. C. Joy, *Calculations of Mott scattering cross section,* Journal of Applied Physics **68**, 3066 (1990).

[31] A. Jablonski and S. Tougaard, *Database of relativistic elastic scattering cross-sections for calculations of photoelectron and Auger electron transport,* Surface and Interface Analysis **22**, 129 (1994).

[32] F. Salvat, A. Jablonski, and C. J. Powell, *elsepa—Dirac partial-wave calculation of elastic scattering of electrons and positrons by atoms, positive ions and molecules,* Computer Physics Communications **165**, 157 (2005).

[33] J.-C. Kuhr and H.-J. Fitting, *Monte Carlo simulation of electron emission from solids,* Journal of Electron Spectroscopy and Related Phenomena **105**, 257 (1999).

[34] H.-J. Fitting, E. Schreiber, J.-C. Kuhr, and A. von Czarnowski, *Attenuation and escape depths of low-energy electron emission,* Journal of Electron Spectroscopy and Related Phenomena **119**, 35 (2001).

[35] E. Schreiber and H.-J. Fitting, *Monte Carlo simulation of secondary electron emission from the insulator SiO2,* Journal of Electron Spectroscopy and Related Phenomena **124**, 25 (2002).

[36] D. C. Joy and S. Luo, *An empirical stopping power relationship for low-energy electrons,* Scanning **11**, 176 (1989).

[37] Y. Lin and D. C. Joy, *A new examination of secondary electron yield data,* Surface and Interface Analysis **37**, 895 (2005).

[38] K. Murata, D. F. Kyser, and C. H. Ting, *Monte Carlo simulation of fast secondary electron production in electron beam resists,* Journal of Applied Physics **52**, 4396 (1981).

[39] H. T. Nguyen-Truong, *Determination of the maximum energy loss for electron stopping power calculations and its effect on backscattering electron yield in Monte-Carlo simulations applying continuous slowing-down approximation,* Journal of Applied Physics **114**, 163513 (2013).

[40] M. Dapor, *A Monte Carlo investigation of secondary electron emission from solid targets: Spherical symmetry versus momentum conservation within the classical binary collision model,* Nuclear Instruments and Methods in Physics Research Section B: Beam Interactions with Materials and Atoms **267**, 3055 (2009).

[41] N. Silvis-Cividjian, *Electron Beam Induced Nanometer Scale Deposition*, Ph.D. thesis, Delft University of Technology (2002).

[42] I. Bojko, N. Hilleret, and C. Scheuerlein, *Influence of air exposures and thermal treatments on the secondary electron yield of copper,* Journal of Vacuum Science & Technology A: Vacuum, Surfaces, and Films **18**, 972 (2000).

[43] H.-B. Zhang, X.-C. Hu, M. Cao, N. Zhang, and W.-Z. Cui, *The quantitative effect of thermal treatment on the secondary electron yield from air-exposed silver surface,* Vacuum **102**, 12 (2014).

[44] X.-c. Hu, H.-B. Zhang, M. Cao, N. Zhang, and W.-z. Cui, *Heating-induced variations of secondary electron emission from ion-cleaned copper samples,* Micron **64**, 52 (2014).

[45] N. Hilleret, C. Scheuerlein, and M. Taborelli, *The secondary-electron yield of air-exposed metal surfaces,* Applied Physics A: Materials Science & Processing **76**, 1085 (2003).

[46] A. Kuzucan, H. Neupert, M. Taborelli, and H. Störi, *Secondary electron yield on cryogenic surfaces as a function of physisorbed gases,* Journal of Vacuum Science & Technology A: Vacuum, Surfaces, and Films **30**, 051401 (2012).

[47] T. Gineste, M. Belhaj, G. Teyssedre, and J. Puech, *Investigation of the electron emission properties of silver: From exposed to ambient atmosphere Ag surface to ion-cleaned Ag surface,* Applied Surface Science **359**, 398 (2015).

[48] X.-C. Hu, M. Cao, and W.-Z. Cui, *Influence of surface topography on the secondary electron yield of clean copper samples,* Micron **90**, 71 (2016).

[49] M. M. EL Gomati, C. G. H. Walker, A. M. D. Assa'd, and M. ZadraŽil, *Theory Experiment Comparison of the Electron Backscattering Factor from Solids at Low Electron Energy (250-5,000 eV),* Scanning **30**, 2 (2008).

[50] R. Cimino, L. A. Gonzalez, R. Larciprete, A. Di Gaspare, G. Iadarola, and G. Rumolo, *Detailed investigation of the low energy secondary electron yield of technical Cu and its relevance for the LHC,* Physical Review Special Topics - Accelerators and Beams **18**, 051002 (2015).

[51] M. Belhaj, T. Tondu, and V. Inguimbert, *Experimental investigation of the effect of the internal space charge accumulation on the electron emission yield of insulators submitted to e-irradiation: application to polycrystalline MgO,* Journal of Physics D: Applied Physics **42**, 145306 (2009).

[52] M. Belhaj, T. Tondu, and V. Inguimbert, *Effect of the incident electron fluence on the electron emission yield of polycrystalline Al2O3,* Applied Surface Science **257**, 4593 (2011).

[53] D. C. Joy, *A DATABASE OF ELECTRON-SOLID INTERACTIONS,* (2008).

[54] G. F. Dionne, *Origin of secondary□electron□emission yield□curve parameters,* Journal of Applied Physics **46**, 3347 (1975).

[55] C. Walker, M. El-Gomati, A. Assa'd, and M. Zadražil, *The secondary electron emission yield for 24 solid elements excited by primary electrons in the range 250-5000 ev: a theory/experiment comparison,* Scanning **30**, 365 (2008).

[56] I. M. Bronstein and B. S. Fraiman, *Vtorichnaya Elektronnaya Emissiya (in Russian),* Nauka (1969), 10.5445/IR/1000024959.

[57] H. Demers, N. Poirier-Demers, A. R. Couture, D. Joly, M. Guilmain, N. de Jonge, and D. Drouin, *Three-dimensional electron microscopy simulation with the CASINO Monte Carlo software,* Scanning **33**, 135 (2011).

[58] W. Czaja, *Response of Si and GaP p□n Junctions to a 5□ to 40□keV Electron Beam,* Journal of Applied Physics **37**, 4236 (1966).

[59] P. Renschler, *KESS - A new Monte Carlo simulation code for low-energy electron interactions in silicon detectors*, Ph.D. thesis, Karlsruher Institut für Technologie (KIT) (2011).

[60] Y. G. Li, P. Zhang, and Z. J. Ding, *Monte Carlo Simulation of CD-SEM Images for Linewidth and Critical Dimension Metrology,* Scanning **35**, 127 (2013).

[61] J. Villarrubia, A. Vladár, B. Ming, R. Kline, D. Sunday, J. Chawla, and S. List, *Scanning electron microscope measurement of width and shape of 10 nm patterned lines using a JMONSEL-modeled library,* Ultramicroscopy **154**, 15 (2015).

[62] L. van Kessel and C. Hagen, *Nebula: Monte Carlo simulator of electron–matter interaction,* SoftwareX **12**, 100605 (2020).

[63] R. Cimino and T. Demma, *Electron cloud in accelerators,* International Journal of Modern Physics A **29**, 1430023 (2014).

[64] Z. J. Ding, *Sensitivity of scanning electron microscope width measurements to model assumptions,* Journal of Micro/Nanolithography, MEMS, and MOEMS **8**, 033003 (2009).

[65] M. Ciappa, E. Ilgünsatiroglu, and A. Y. Illarionov, *Monte Carlo simulation of emission site, angular and energy distributions of secondary electrons in silicon at low beam energies,* Microelectronics Reliability **52**, 2139 (2012).

[66] L. A. Gonzalez, M. Angelucci, R. Larciprete, and R. Cimino, *The secondary electron yield of noble metal surfaces,* AIP Advances **7**, 115203 (2017).

[67] V. Baglin, J. Bojko, O. Gröbner, B. Henrist, N. Hilleret, C. Scheuerlein, and M. T. Cern, *THE SECONDARY ELECTRON YIELD OF TECHNICAL MATERIALS AND ITS VARIATION WITH SURFACE TREATMENTS,* Proceedings of EPAC , 217 (2000).

[68] T. Koshikawa and R. Shimizu, *Secondary electron and backscattering measurements for polycrystallıne copper woth a spherical retarding-field analyser.pdf,* J. Phys. D: Appl. Phys. **6**, 1369 (1973).

[69] Z. J. Ding, X. D. Tang, and R. Shimizu, *Monte Carlo study of secondary electron emission,* Journal of Applied Physics **89**, 718 (2001).

[70] Z. Ding, H. Li, X. Tang, and R. Shimizu, *Monte Carlo simulation of absolute secondary electron yield of Cu,* Applied Physics A: Materials Science & Processing **78**, 585 (2004).

[71] S. F. Mao, Y. G. Li, R. G. Zeng, and Z. J. Ding, *Electron inelastic scattering and secondary electron emission calculated without the single pole approximation,* Journal of Applied Physics **104**, 114907 (2008).

[72] L. Zommer, A. Jablonski, G. Gergely, and S. Gurban, *Monte Carlo backscattering yield (BY) calculations applying continuous slowing down approximation (CSDA) and experimental data,* Vacuum **82**, 201 (2007).

[73] L. Reimer and C. Tollkamp, *Measuring the backscattering coefficient and secondary electron yield inside a scanning electron microscope,* Scanning **3**, 35 (1980).

[74] R. Böngeler, U. Golla, M. Kässens, L. Reimer, B. Schindler, R. Senkel, and M. Spranck, *Electron-specimen interactions in low-voltage scanning electron microscopy,* Scanning **15**, 1 (1993).

[75] M. Attarian Shandiz, F. Salvat, and R. Gauvin, *Detailed Monte Carlo Simulation of electron transport and electron energy loss spectra,* Scanning **38**, 475 (2016).

[76] G. Appelt, *Fine Structure Measurements in the Energy Angular Distribution of Secondary Electrons from a (110) Face of Copper,* Physica Status Solidi (b) **27**, 657 (1968).

3

Model Sensitivity Analysis of Monte Carlo Based SEM Simulations

The sensitivity of simulated scanning electron microscopy (SEM) images to the various physical model ingredients is studied using an accurate, but slow simulator, to identify the most important ingredients to include in a reliable and fast SEM image simulator. The quantum mechanical transmission probability (QT) model and the electron-acoustical phonon scattering model are found to have the most significant effect on simulated 2D and 3D metrology results. The linewidth measurement error caused by not including these models in the simulation is less than 2 nm. Specifically, it was found from a comparison to experimental data that the QT model is essential in accurately predicting particular signal features in line scans such as "shadowing". The simulator is compared with two other publicly available simulators, JMONSEL and CASINO, where the first one is also based on first-principle physics models and the latter one is using phenomenological models. CASINO is the fastest simulator on CPU, but Nebula on GPU is two orders of magnitude faster compared to a single threaded CPU simulation. Only up to 6% speed increase has been achieved by different model choices.

This chapter is published as a journal paper:
Kerim T. Arat, Cornelis W. Hagen; Model sensitivity analysis of Monte-Carlo based SEM simulations,*Results in Physics*, Volume 19, 12/2020, 103545,DOI:10.1016/j.rinp.2020.103545

3.1. Introduction

As semiconductor devices shrink in size, it becomes crucial to inspect with optimized system parameters to minimize measurement errors [1, 2]. For example, for high-end transistors accurate edge positioning [3–5] becomes essential when structure sizes approach a few nanometers. In addition, the dramatically changing height/width (aspect) ratio of lines [6] requires full 3D metrology [7–9]. Synthetic scanning electron microscope (SEM) images produced by Monte Carlo simulations can be a great aid in analyzing such complex metrology tasks [10–12]. But, the resulting images will depend on the physical models included in the simulator. Therefore, it is essential to know what their influence is on the results.

Typically, Monte Carlo simulators contain models for electron generation (inelastic scattering), electron transport (elastic and inelastic events) and boundary-crossing events. Simulators based on phenomenological models can provide fast solutions, but their accuracy is not guaranteed unless they are carefully calibrated for particular purposes. On the contrary, simulators based on first principle physics models should lead to accurate results without any calibration, but they can be impractically slow. The question is whether all model ingredients in such accurate, but slow, simulators have a noticeable influence on the results. Some of them may well be left out, or can be approximated, to speed up the simulations. This way, a fast simulator can be obtained which may still be quite accurate. The goal of this study is to study how sensitive the results are to the various model ingredients and identify those which are essential to keep in a fast and accurate simulator of SEM images for 2D and 3D metrology.

Previously, Villarrubia et al. have reported a detailed sensitivity analysis of the effects of inelastic scattering models and surface potential barrier models on 2D linewidth measurements [13]. They considered inelastic scattering models such as continuous slowing down approximation (CSDA), a phenomenological model, and the dielectric function theory (DFT), a first-principle physics model, and concluded that the edge positioning error due to the model differences is at most 3 nm.

Verduin et al. have done a model sensitivity analysis by artificially changing the elastic and inelastic scattering cross-sections in line edge roughness (LER) simulations [14]. They concluded that the cross- sections do have an impact on SEM image contrast, but not on the determination of LER.

To obtain 3D information from top-down SEM images, Arat et al. developed a method to deduce step heights from signal contrast in SEM images [15]. They used simulations to show that part of the secondary electron signal, when scanning over a step edge, is determined by the step height rather than the geometry of the step edge (see Fig. 3.1). In the figure, $f_s(x)$ is the line scan signal where x is the beam position, f_b is the baseline level determined by the SE yield at the particular beam energy and the brightness level setting of the SEM, a_1 and a_2 are the integration boundaries between which the signal is most sensitive to height as discussed in [15]. The integrated area is used to quantify the height. They also demonstrated this experimentally. To accurately predict step heights from simulations, it is important to identify those models that

influence the signal contrast most (the green area in Fig. 3.1).

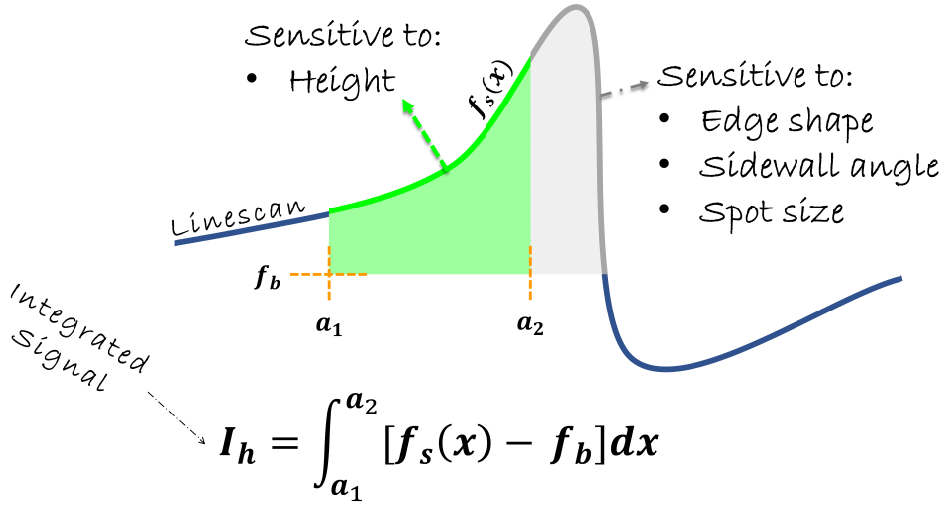


Figure 3.1: Line scan over a step height. The green area is sensitive to the step height.

This study will focus on the simulation of line scans over a Si line of rectangular cross-section, and the influence of the various first principle physics models of the simulator on the line scan secondary electron (SE) signals. The primary energy dependence of the line scans will be studied, and visualized such that one can easily judge the importance of each model ingredient for the prediction of a certain property such as linewidth, or LER or step height. Furthermore, the calculation times will be taken into consideration, and the results will be compared with results from two well-known other simulators, JMONSEL [10] and CASINO [16]. The essential models for an accurate and fast simulator will be identified and the possibility to speed-up the simulator without changing the accuracy will be discussed. In the next section the various model ingredients will be introduced and briefly discussed.

3.2. Models

Primary electrons incident on a material sample interact with the material and will be scattered (Fig. 3.2). The scattering events in which the energy loss is negligible are termed elastic scattering events. In these events, electrons mostly experience trajectory changes. On the other hand, the events in which there is a considerable energy loss are termed inelastic scattering events. In those events, electrons transfer energy to other electrons and experience both energy loss and trajectory change, or they can be trapped. The event in which an electron is incident on an interface, e.g. between sample and vacuum, requires a boundary-crossing model to determine the probability for transmission or reflection.

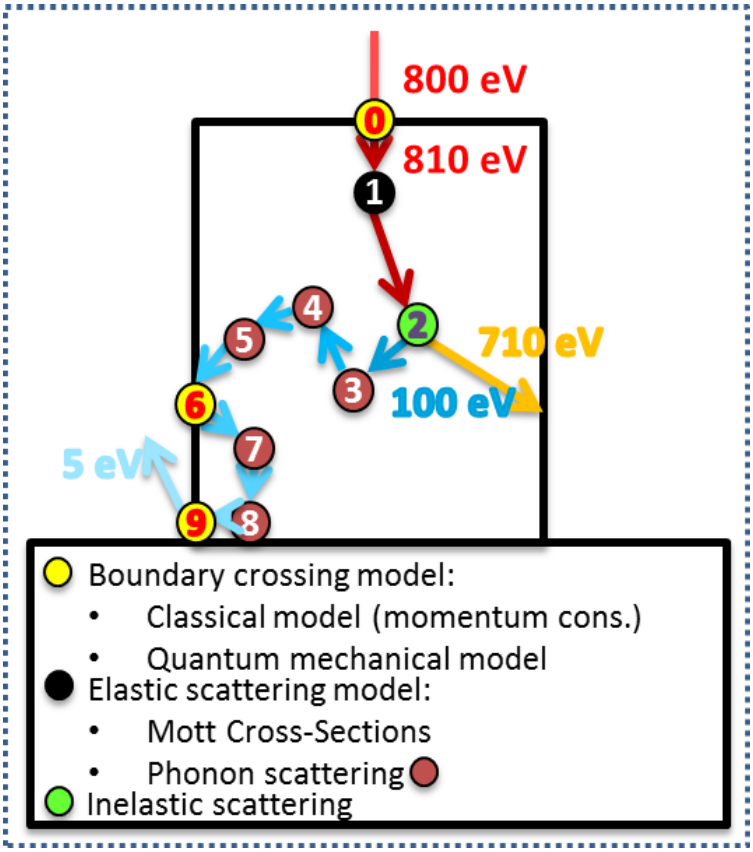


Figure 3.2: An 800 eV primary electron interacts with a silicon line (cross-sectional view). The scattering events (elastic and inelastic) are depicted as well as the boundary crossing when an electron leaves the wire.

3.2.1. Elastic scattering models

The sensitivity of simulated SE signals to the elastic scattering models has not been investigated in the literature as much as the sensitivity to inelastic scattering models.

Elastic scattering occurs when an electron is deflected by the nuclear potential of a specimen atom without any exchange of kinetic energy. The frequency of the events and the probability distribution of deflection angles can be modeled by the Mott cross-sections, which are obtained using a computer program ELSEPA based on relativistic partial-wave calculations of elastic scattering of electrons by atoms [17]. The program also allows us to include solid-state effects, using a muffin-tin potential as a representation of the potential well in a densely packed crystal lattice, which influences the total cross-section.

At low energies the electron couples stronger with the lattice as its wavelength becomes comparable to the lattice distance. Therefore, modeling the electron–phonon

interaction is essential for the completeness of the physical picture at low energies. The elastic scattering approach by [18] and [19] is followed, using the Mott cross-section model for energies above 200 eV, quasi-elastic acoustic (AC) phonon [20] scattering cross-sections below 100 eV and an interpolation between the two cross-sections for energies in between 100 and 200 eV.

In Fig. 3.3, the effect of different elastic scattering model choices on the mean free path (MFP) is shown for silicon (Si). The best model choice, from a physics point of view, is Mott cross-sections with muffin–tin potential, including AC phonons for low energies (shown by the red line with crosses). The default model in ELSEPA is Mott cross-sections for free atoms, i.e. not taking the muffin-tin potential into account. Combining this with AC phonon scattering cross sections results in the dashed blue line in Fig. 3.3. The MFP is roughly 1.5 times smaller at high energies. For example, the MFP of a 10 keV electron is 10 nm (free atom) instead of 15 nm (muffin-tin).

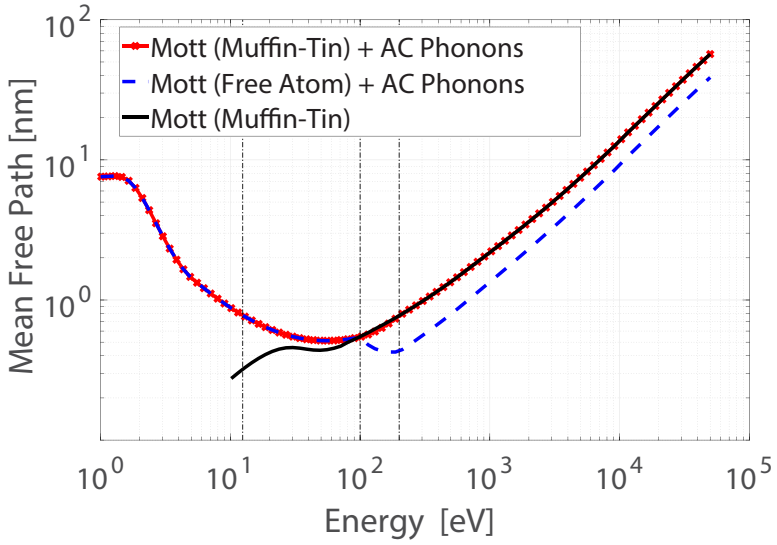


Figure 3.3: The elastic mean free path for silicon and different scattering models as indicated in the legend. The vertical lines indicate, from left to right: the vacuum barrier energy (12.44 eV), electrons below the barrier energy can be discarded; in between the lines at 100 eV and 200 eV the MFP is interpolated (see text). The energy axis denotes the kinetic energy of the electron in the material with respect to the bottom of the valence band.

Mott cross-sections with the muffin-tin potential, but excluding the AC phonon scattering, leads to the MFP depicted by the black solid line in Fig. 3.3, at very low energies a factor of 2 lower than the AC cross-sections.

It is worth noting that the energy scale adopted in the simulations refers to the kinetic energy of an electron in the material taken with respect to the bottom of the valence band. This means that the kinetic energy of an electron should at least be equal to the barrier energy (12.44 eV for Si) to escape from the material to the vacuum.

Therefore, the simulator stops tracing electrons with energy below the barrier energy. These electrons are trapped, which has no consequences for conducting materials, but it may have for insulators leading to charging effects. The latter are not considered in this study.

3.2.2. Inelastic scattering models

In contrast to elastic events, an electron loses energy and momentum in an inelastic event. These events play a significant role in SE generation. Energy loss processes include interaction with outer-shell electrons and plasmons, inner-shell electrons, and longitudinal optical (LO) phonons. The energy loss of an electron can be modeled discretely for each event, or as an average energy loss per distance traveled, i.e. using the stopping power. The two conventional approaches to model inelastic scattering are dielectric function theory (a first-principle physics model) and continuous slowing down approximation (a phenomenological model).

Villarrubia et al. studied the sensitivity of CD measurements to eight different inelastic scattering models, such as variants of the dielectric function theory (based on the Penn [21] algorithm) and phenomenological models based on fitting experimental SE yield versus energy curves [13]. In the third variant of the dielectric function model, DFT3 in their notation, they followed the approach of Mao et al. [22] and separated electron–electron and electron-plasmon types based on momentum transfer. In case the momentum is conserved, it is assumed that the event is electron–electron scattering and the initial momentum of the SE is randomly sampled from the Fermi Sphere. Otherwise, it is an electron-plasmon event and the SE energy is randomly sampled from the Fermi sea electrons based on the free electron density of states.

The inelastic model used here is similar to DFT3. We use the full Penn algorithm (FPA) as described by Shinotsuka [23]. However, we restrict the energy transfer such that the primary electron cannot end up with energy below the Fermi level. For the outer-shell electron excitation, we follow the approach described by Mao et al. [22] as in the DFT3 model. In the electron-plasmon event, the instantaneous (non-zero) momentum of the secondary electron is randomly chosen in an isotropic direction, as in DFT3. This has also been suggested by Dapor [24].

For the inner-shell electron excitation, the model is followed as described by Kieft et al. [18], where the energy transfer is larger than 100 eV. For energy transfers lower than the bandgap energy, again the approach by Kieft et al. [18] is followed, treating them as LO phonons [25]. These losses are about 100 meV [25].

In an elastic event, it is assumed that there is no energy loss. However, when an electron is deflected by the nucleus it does lose some energy due to the conservation of momentum [26]. Although these losses are very small (<1 eV) for light materials and low beam energies, they will still be modeled as “atomic recoil losses”.

3.2.3. Boundary crossing models

When an electron is incident on an interface between two materials, e.g. the specimen-vacuum interface, it can either be reflected or transmitted. When it is transmitted the electron energy changes as a result of the different potential energy on both sides of the interface, and due to conservation of momentum its direction also changes, i.e. the electron is refracted. Quantum mechanically, part of the incident electron wave can be transmitted, and part of it can be reflected. This quantum mechanical transmission probability with a single barrier height model [19] has been implemented in the present simulator Nebula, which is available on Github [27].

3.3. Methods

The simulation code has been written such that individual parts of the physics models can be included or ignored; in other words, "knobs" were implemented, which can switch model parts on and off. To judge the model effects on topographic features, a silicon line of 32 nm × 32 nm cross-section was chosen as the specimen, shown schematically in Fig. 3.4a. An incident electron beam, of 0.1 nm (FW50) Gaussian beamwidth, is scanning an area of 64 nm × 8 nm with 500 electrons per 0.5 nm pixel. Each scanline is taken at a different energy, 16 energies in total. All electrons emitted from the specimen per pixel are collected by a detector above the specimen, and those with energy less than 50 eV (the SE's) are taken as the signal. The 16 scanlines are shown in Fig. 3.4b, stretched in width for visualization purposes, and stitched together for increasing energy ordered from top to bottom, basically a multi-energy SEM image. The detected signal is normalized to the number of primary electrons per pixel and shown on a color scale.

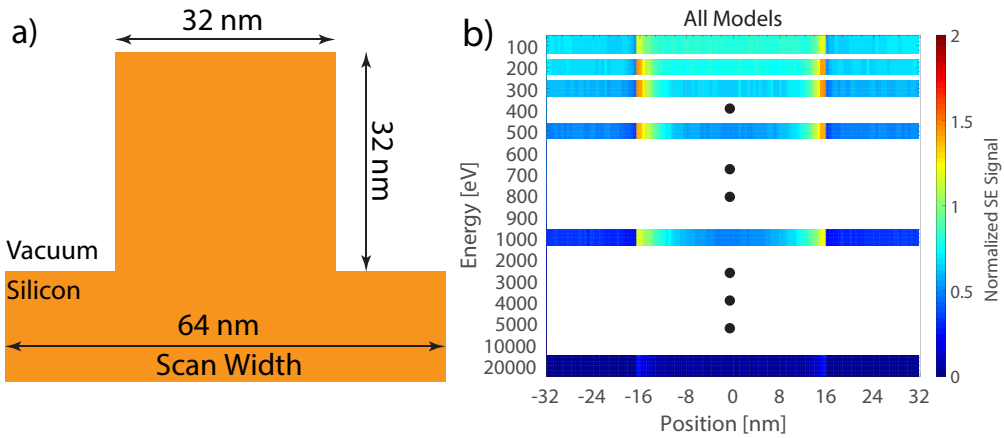


Figure 3.4: (a) Multi-energy SEM image for a silicon line. (b) Scanlines, stretched in width for visibility, taken at increasing energy from top to bottom. The scanwidth is 64 nm and the SE detector is located above the line.

The physics models to be switched on and off in the simulator are summarized in Table 3.1. The first column lists all models which are assumed to describe the physics of the problem in the best possible way, the first-principle models. By default they are all switched on, i.e. they are included in the simulator. The second column describes the model status of the simulator when the first-principle model of the first column is switched off, i.e. not implemented.

The effects that these models are expected to have on the simulated images will be discussed first.

Disabling the muffin-tin model means that the simulator uses a free-atom model, resulting in a corresponding decrease of the elastic MFP. This causes high energy electrons to scatter and change direction more frequently. The effect of this is not expected to be significant for the SE emission since the cross-sections at low energies are not affected.

Switching from AC phonon cross-sections to Mott cross-sections decreases the mean free path at low energies by a factor of ≈2. As a direct result, the total mean free path decreases and the first expectation is a smaller scattering volume. However, the scattering probabilities of different types of events (inelastic & trapping) change as well. It is therefore not straightforward to estimate the scattering volume without running the Monte Carlo process.

When acoustic phonon energy losses are switched off the scattering becomes purely elastic. This may lead to an increased emission. Because there are not many energy loss channels for low energy electrons deep in the material, their scattering lifetime will be long before they get trapped. Therefore, the simulation time is expected to be higher.

The effect of the LO phonon losses is similar to that of the AC phonon losses. However, the energy loss functions (ELFs) show that these events are less frequent than the AC phonon losses. Therefore, the effect should be small. Similarly, atomic recoil events [26] should have not an important effect for typical CD-SEM energies of 300–500 eV since the loss is a few orders of magnitude lower than the energy of the electron. For instance, the loss is about 100 meV for a 300 eV electron.

When the instantaneous momentum of the SE's is switched off, electrons are modeled as being stationary before the collision. Although this physically does not make sense, the electron will lose its initial momentum any way after several collisions. Therefore, it is expected to have no effect on the results. Switching off this model should speed-up the simulator.

In the default model momentum is conserved after collision with an inner-shell electron. However, the initial momentum of the inner-shell electron is not known. The model assumes it is zero. The other extreme would be that the primary electron does not change direction after inelastic scattering. Although this is not a valid assumption, it will provide insight into how these two extremes influence the SE image.

Similarly, switching off momentum conservation during boundary crossing, i.e. refraction, is not physically correct. But its effect will show the sensitivity of the results

to emission angles. It is expected that the SE signal will change, especially at the shadow regions next to the sidewalls of the line.

Finally, switching off the quantum mechanical transmission probability will lower the emission yield because electrons then have a higher probability to be reflected from the interface. It is expected that the effect is stronger in the shadow regions next to the line because there will be a lower detection probability for the electrons which escape from the surface and then scatter from the sidewall and finally hit the detector.

How to analyze the effect of switching off a model component is best illustrated with an example. Fig. 3.5a shows the multi-energy image of the silicon line when all models are switched on. This way of visualization provides a nice overview of what a top-down SEM image of a rectangular line will look like at various energies. Fig. 3.5b shows the line scan results when the quantum mechanical transmission model is switched off, and Fig. 3.5c shows the difference, i.e. Fig. 3.5b subtracted from Fig. 3.5a. The shape of the line appears in Fig. 3.5c especially at low energies, which indicates that the topographic features are sensitive to the disabled model.

Table 3.1: Overview of the simulation models

1st Principle Models ("knobs")	The simulator status, excluding the model on the left
• Muffin-Tin Model	• Free Atom Model
• Acoustic Phonon Model	• Replaced by Mott cross-sections (Muffin-Tin model)
• Acoustic Phonon Energy Loss	• Low energy (<200 eV) elastic scattering becomes purely elastic
• Optical Phonon Energy Loss	• Energy losses lower than the band-gap energy are neglected
• Atomic Recoil Loss	• High energy (>200 eV) elastic scattering becomes purely elastic
• Instantaneous Momentum of SE	• SEs are treated as stationary before the collision
• Momentum Conservation of Inner Shell Scattering	• Primary electrons undergo forward scattering when creating a fast SE electron
• Interface Effect - Refraction	• Electron pass boundaries without changing their direction
• Quantum Mechanical Transmission Probability	• Electrons interact with the boundaries only classically

3.4. Results

A sensitivity analysis was performed with the nine different models listed in Table 3.1 using the aforementioned method. The resulting difference images are shown in Fig. 3.6. It is seen that the line profiles are influenced most by the exclusion of the acoustic phonon model, refraction, and the quantum mechanical transmission of an electron through interfaces (Fig. 3.6b, h and i, resp.).

3.4.1. Consequences for 2D measurements

To quantify the impact of excluding these models on 2D metrology, linewidths were measured. The measurement method employed turns out to be crucial. The 50 % threshold method is chosen here because of its accuracy and simplicity [28, 29]. Although it is a relatively simple method, the exact definition should still be clarified. Two different definitions of the threshold method were found in the literature. The first one assumes that the edge position is where the signal is halfway between the global max-

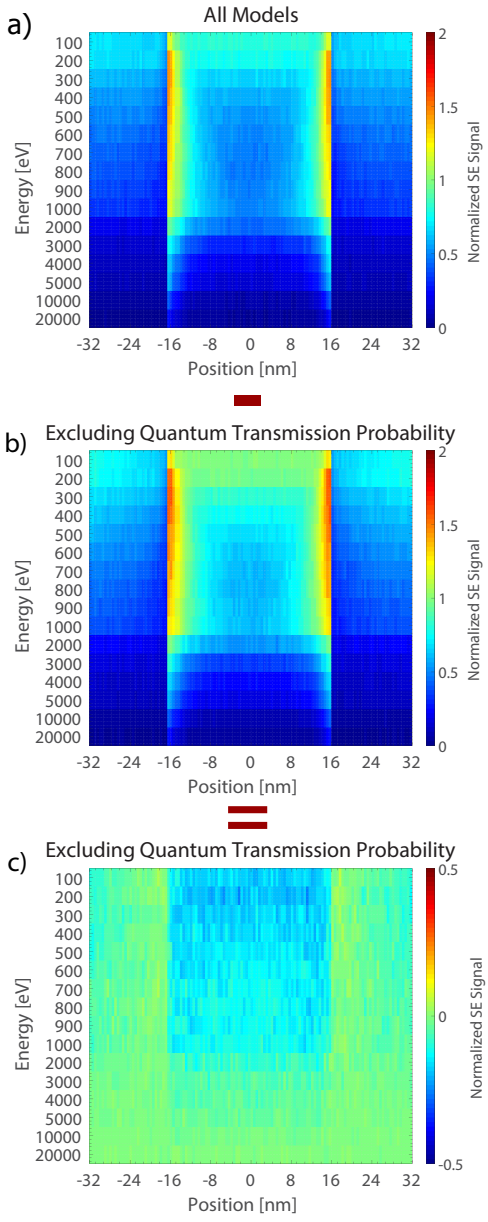


Figure 3.5: Illustration of the analysis method. a) the multi-energy SE image with all models switched on, b) switching off quantum mechanical transmission probability, and c) the difference, b) subtracted from a). It is observed that the switched-off model has a significant impact on the SE signal at low beam energies. The contrast clearly reveals the line shape.

imum and the global minimum of the edge profile, as implemented by Shishido et al. [28]. The second one estimates the edge position where the signal is halfway between

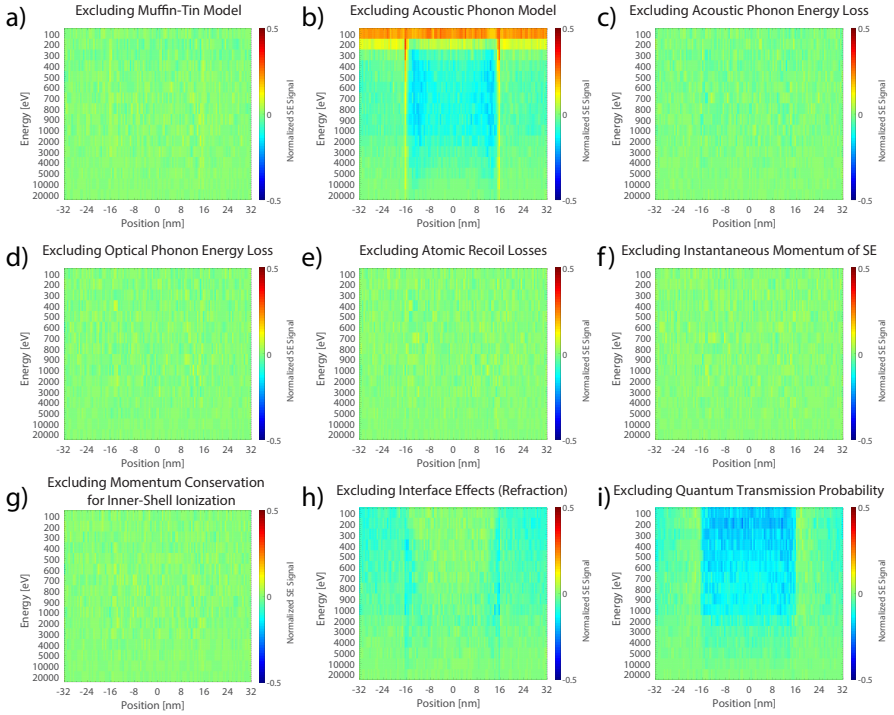


Figure 3.6: The sensitivity analysis at a glance. The difference images are shown between all models included and one of the following models excluded (a) muffin-tin potential, (b) electron acoustic phonon scattering, (c) energy loss at electron acoustic phonon scattering, (d) energy loss at electron-optical phonon scattering, (e) energy loss due to atomic recoil effect, (f) instantaneous momentum of secondary electrons, (g) momentum conservation for inner-shell ionization, (h) refraction, (i) quantum mechanical transmission probability.

the global maximum of the edge profile and the signal baseline, as used by Villarrubia et al. [30]. The former is easy to apply to signals where the global minimum of the signal is easily identified. The latter technique can be more robust for signals where the shadowing effect is not that apparent, as in high energy or noisy experiments.

For this study, at higher energies (>2 keV), the uncertainty in the determination of the signal minimum increases (as large as 4 nm) and measurements using the first method show variations up to 10 nm. The second method predicts the linewidth with a much better overall performance (error <2 nm) at all energies. The measurement quality could be improved by fitting the signal to a more complex function such as a sigmoidal [31, 32] or a double-Gaussian function [14, 33].

The comparison here is focused on the energy range between 100 eV and 1 keV which is relevant for CD-SEMs. Fig. 3.7 shows that the CD deviation from its nominal value is least when all models are switched on and larger when quantum mechanical transmission probability or electron-acoustic phonons cross-sections are switched-off, although almost all measurements are within pixel uncertainty (±0.5 nm). The same

comparison is given for the second method in Fig. 3.8. These measurements are slightly less accurate but qualitatively very similar.

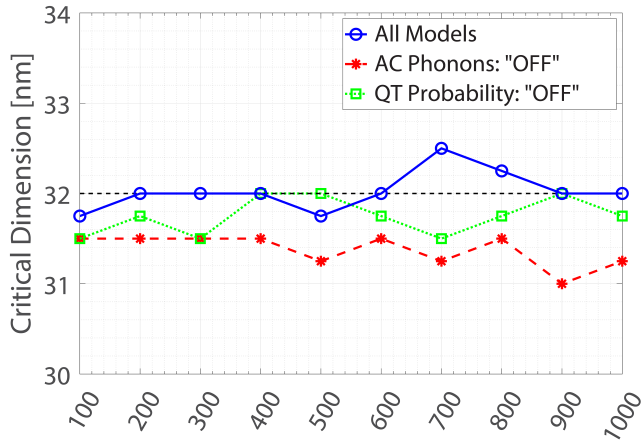


Figure 3.7: CD measurement and the effect of switching off different model ingredients. The nominal CD is 32 nm. The threshold (50 %) method was applied between global maximum and minimum.

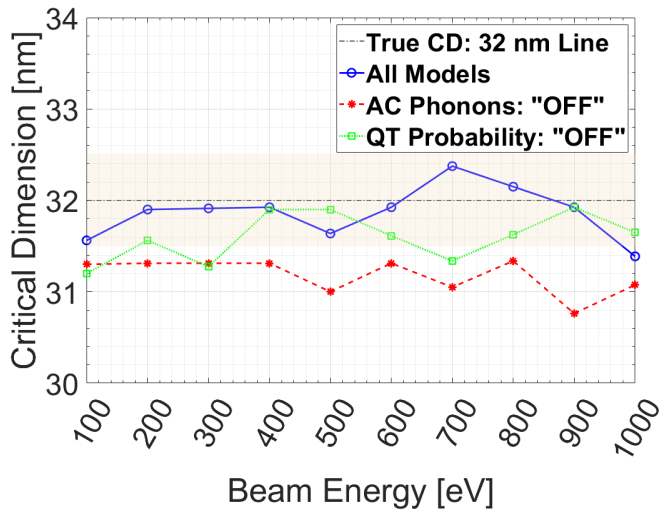


Figure 3.8: CD measurement as in Fig. 3.7, but the threshold (50 %) method was applied between the global maximum and the baseline.

From this comparison, it is concluded that the AC phonon model has a bigger effect on the CD than any other model and the measurement bias is less than 2 nm. The conclusion is that switching off the model ingredients shown to be relevant in

the SE images does not have a significant effect on 2D measurements such as the critical dimension, in agreement with what has been observed before by Villarrubia [34] and Verduin [14]. Furthermore, at CD-SEM energies, the measurement method based on global maximum and minimum leads to slightly more precise results. However, this difference is within the uncertainty of discretization. Therefore, the effect is insignificant.

3.4.2. Consequences for 3D measurements

As an example of 3D measurements determination of step height is chosen. In Fig. 3.1 it was argued that step height can be estimated from a top-down SEM image using the scanline profile [15]. To evaluate the impact of model ingredients on 3D metrology applications the attention has to be on contrast changes in signals. For instance, the effect on a line scan profile at 300 eV of switching off acoustic phonon cross-sections is plotted in Fig. 3.9. The baseline signal has not changed in the intervals −32 to −16 nm and 16 to 32 nm. But the signal from the top of the line is significantly altered since the Mott MFP's (replaced model) are much smaller than the electron-acoustic phonon MFP's. In the low energy regime, electrons undergo more elastic scattering before they are trapped and spread over a larger area in the material. When the electron beam scans over the line, this leads to more SEs escaping from the sidewalls of the line. The magnitude of the signal has increased as well as the slope of the "edge blooming" part of the signal. Both are important changes that seriously influence model-based 3D measurements such as step heights [15].

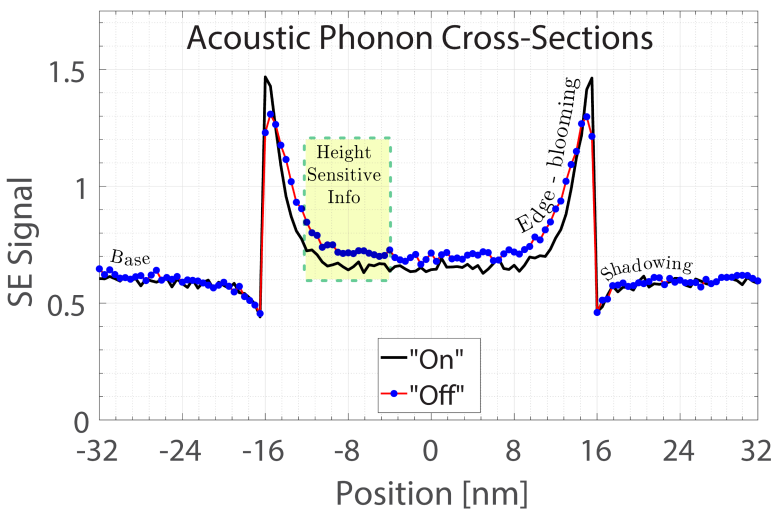


Figure 3.9: Effect of the electron-acoustic phonon scattering model on a line scan over the Si line at 300 eV. Line scans with model on and off are drawn.

Similarly to the AC phonon model, the quantum mechanical transmission (QT) model has an essential impact on the signal profile (Fig. 3.10). Switching off the QT model results in more electron emission from both the line and the substrate, be it with different ratios. In this case, electrons which would usually be reflected are now allowed to cross the interface. It is observed that the SE signal increases more on top of the line (from 0.7 to 0.85) than at the substrate level (from 0.6 to 0.65). The reason for this is the topography, allowing electrons to escape from both sidewalls of the line as well. For the same reason, the substrate signal increase is more, further away from the line. Although at each position next to the line the same number of electrons escapes from the substrate, the ones emitted close to the line end up in the line again and are not detected.

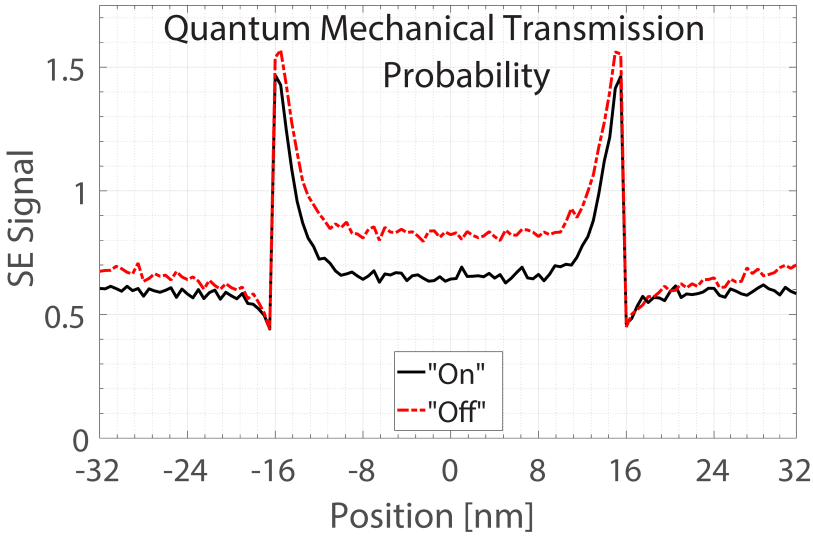


Figure 3.10: Effect of the quantum mechanical transmission probability model on a line scan over a Si line at 300 eV. Line scans with model on and off are drawn.

The conclusion is that the implementation of the QT model is important for the correct simulation of signal contrast.

3.5. Comparison with CASINO and JMONSEL

To put the results, obtained with Nebula and presented here, in perspective a comparison is done with two other widely used Monte Carlo simulators: JMONSEL [10] and CASINO (version 3.2.0.4). These packages include different scattering models or model assumptions. It is assumed that the default options provide the most accurate results to a basic user. Understanding and comparing the effects of model assumptions

in these packages is beyond the context of this study. The present goal is to obtain results from these packages, as used with the default physics models they come with, and compare them to results obtained with Nebula such that we can understand the overall effect of the different models.

The CASINO simulations are used with the "MONSEL Defaults", a default user option in the program [16]. That means Mott cross-sections by Browning [35] for elastic scattering and inelastic scattering based on the stopping power as modeled by Joy and Luo [36], and modified by Lowney [37]. It is not stated in any of the publications on CASINO whether the quantum mechanical transmission probability has been included in the models. Therefore, it is assumed that it is not included.

The default version (the example script "LinesOnLayers.py") of JMONSEL makes use of the Mott cross-sections for elastic scattering, the full Penn algorithm for inelastic scattering and classical boundary transmission based on momentum conservation. In more detail, for elastic scattering the Browning empirical cross-sections were used for $E < 50$ eV, tabulated Mott cross-sections for 50 eV $< E <$ 20 keV, and Screened Rutherford cross-sections for $E >$ 20 keV, where E is the energy of the electron. The elastic scattering model is very similar to the one in CASINO. For inelastic scattering, there are two options: electron–electron scattering and electron-plasmon scattering. Electron-electron scattering has been modeled as described by Mao et al. [22]. In an electron-plasmon event, if the energy loss of the primary electron ΔE is larger than the binding energy (Eb) of an inner-shell, then the energy of the SE is ΔE - Eb [38]. Otherwise, it is determined probabilistically based on electron densities between Ef - ΔE and Ef where Ef is the Fermi energy [39]. The inelastic scattering model is similar to the model in Nebula.

The silicon line of Fig. 3.4a is used for the comparison. The signal profiles of a line scan at 300 eV are compared in Fig. 3.11. The signals are normalized to the number of primary electrons (80,000 for CASINO, 10,240 for JMONSEL, and 20,000 for Nebula). The electron beam, a Gaussian beam with 0.1 nm diameter (full width 50 – FW50), was scanned over 64 nm with a step size of 0.5 nm.

As seen from Fig. 3.11a the simulators give very different values for the SE yield at 300 eV. When the SE signals are normalized to the signal value from Nebula in the middle of the line, the results from CASINO and JMONSEL agree surprisingly well (Fig. 3.11b), at the edge-blooming region and especially at the shadowing region, although very different inelastic scattering models were used. In contrast to the Nebula result, the signals obtained from the two other simulators, continue to rise between 20 nm and 32 nm although they should have reached their nominal emission value already. Fig. 3.12 now also shows the comparison to Nebula excluding the QT model, revealing the same signal rise as observed from CASINO and JMONSEL in Fig. 3.11.

The final results are very similar although the exact scattering cross-sections are different. Apparently the different scattering models converge to similar results after several scattering events. But, based on this comparison, we conclude that including the QT-model makes a significant difference. So, perhaps there is no need to improve

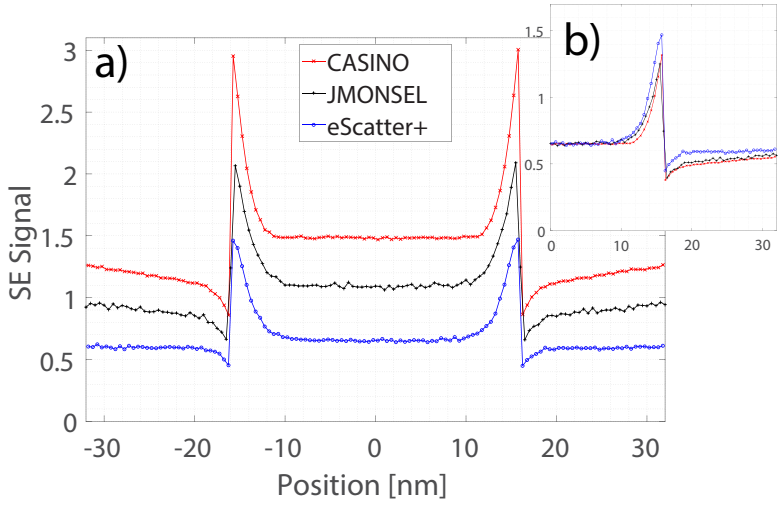


Figure 3.11: Three simulators compared on a Si line line scan at 300 eV. a) absolute SE signal, b) normalized SE signal.

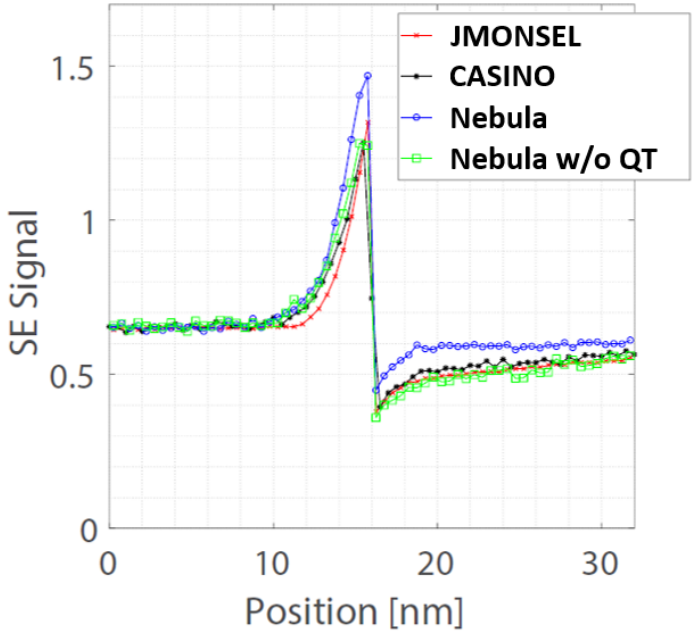


Figure 3.12: Effect of excluding the quantum mechanical transmission probability (QT) model from e-Nebula, compared to the signals shown in Figure 3.11b.

the accuracy of the cross-sections and phenomenological models work just as well for 2D and 3D metrology purposes. However, a QT-model should be included.

3.6. Comparison with experiments

For a final verification, the model effects were also compared with an experiment. Results were used from RM8820 [40], an industry-level calibration sample for metrology tools. The data were obtained from Fig. 3.2 in Postek et al. [41]. An integrated line scan of the middle poly-silicon line is plotted in Fig. 3.13.

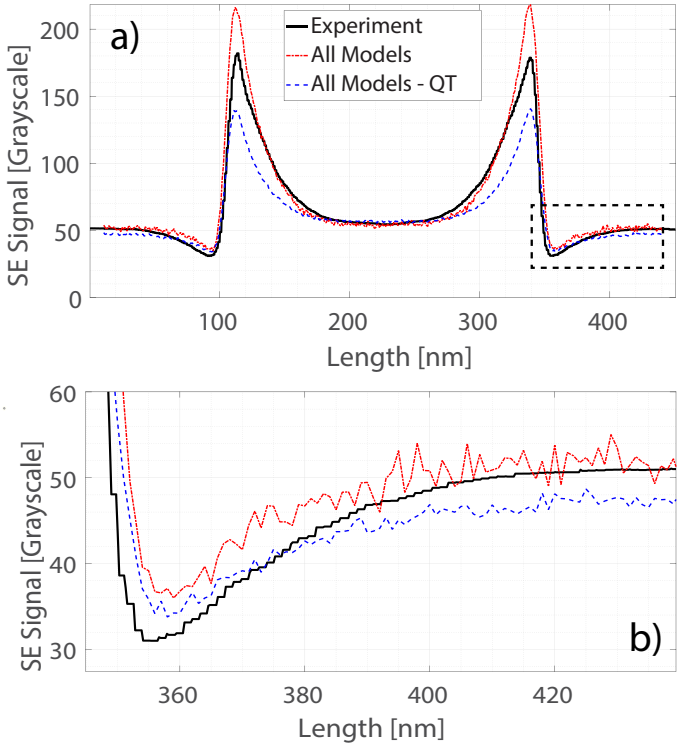


Figure 3.13: a) Experiment vs. simulation of a line scan over benchmark sample RM8820. The simulation either included all models or had quantum mechanical transmission probability switched off. b) zoom-in of the rectangular area in a).

Many details about the inspection are given in the paper. For example, the sample geometry is described well and line cross-sections are also given. However, performing a quantitative comparison between experiment and simulation is an extremely challenging task. Many other parameters should also be known, such as beam spot size, or whether the region is imaged for the first time [42]. Besides, there are also details that are very hard to know such as detector collection efficiency and the surface condition of the sample. Last but not least, lack of knowledge of the detection settings such as brightness (voltage offset) and contrast (voltage gain) makes it very complicated to compare experimental data to simulated data quantitatively. Therefore, the best attempt to a qualitative comparison is performed here, to give an idea of the model effect on the signal trends.

The following parameters were used. The top and bottom CDs are modeled as 228 nm and 240 nm, respectively. The beam energy is 2 keV and 10,000 electrons are scanned over 430 nm with 1 nm pixel size. The spot size is 12 nm, which seems overestimated, but leads to a better match. Offset (brightness) and gain (contrast) have been arranged such that simulated signals match in the middle of the line and at the substrate baseline. As before, a comparison was done to a simulation with all models included and one with the QT model excluded. From Fig. 3.13 it is clearly seen that the quantum mechanical transmission probability has a significant impact on the signal. Only with the QT model included the experimental signal trend can be reproduced, especially in the shadowing area.

3.7. Model-affected simulation time

In literature, it is very hard to find explicit information on Monte Carlo simulation times. That is understandable because the computer system used, and the programming techniques, and such kind of non-model related issues, influence the results. To have a rough idea of how long a typical calculation can take with the packages used in this work, a timing benchmark was performed. For this comparison, doing any user-level optimization was deliberately avoided, such as e.g. switching-off tracing secondary electrons which are far from the surface. Therefore, the results can be regarded as upper bounds to the calculation times.

A line scan of the same silicon line as above, of 128 pixels scan length, is simulated with 10,240 electrons/pixel for JMONSEL, and 80,000 electrons/pixel for CASINO and Nebula. It is worth mentioning that JMONSEL is a single-threaded program, whereas CASINO can utilize CPU parallelism, and Nebula can use both CPU and GPU parallelism. The CPU versions were run on a Windows 7 platform with Intel Xeon CPU E5-1620 v3 @3.5 GHz (8 threads), and the GPU version of Nebula was run on NVIDIA GeForce GTX 1080 with 8 GB memory. The CPU timings are normalized to the number of CPU cores for the comparison in Fig. 3.14. The Nebula GPU version timing was reported without any normalization to the number of threads because the number of active threads is changing during the runtime.

The comparison shows that CASINO is the fastest program running on a CPU. Assuming all the simulators were coded at a similar level of expertise, the phenomenological model leads to faster simulation times. However, Nebula has a very comparable speed and includes first-principle inelastic models. The GPU version of Nebula is almost two orders of magnitude faster than the CPU version and CASINO.

In Fig. 3.6, the effect that the model ingredients have on the line scans was shown. To speed-up the simulator, one could switch-off model ingredients that were shown to have no influence on the line scans. For instance, one could switch off acoustic phonon loss (Fig. 3.6c), optical phonon loss (Fig. 3.6d), atomic recoil losses (Fig. 3.6e), and instantaneous momentum of SEs (Fig. 3.6f). The GPU version of Nebula then becomes slower by 3% at 0.3 keV, 1 keV, and 20 keV, instead of becoming faster. In fact, switching off various loss mechanisms causes low energy electrons to scatter

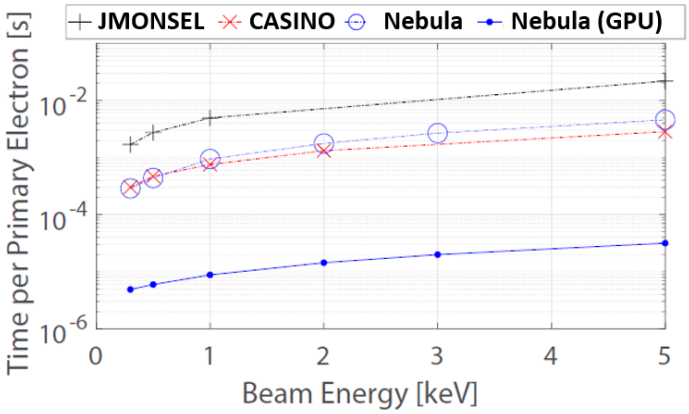


Figure 3.14: Timing comparison between JMONSEL, CASINO, and Nebula (CPU and GPU versions).

without losing much energy, such that they exist for long times at the expense of an increased computational load. Instead of completely switching off low energy electron loss mechanisms, approximating their net effect by a single energy loss value (50 meV in Fig. 3.15) in the AC phonon energy loss model, can speed up the simulations by 2% for 0.3 keV, 5% for 1 keV and 6% for 20 keV without significantly affecting the signal. The conclusion is that one has to be careful with switching off model components that do not seem relevant. It may even slow down the simulations, in which case it would be better to keep the models and optimize the simulation time in different ways.

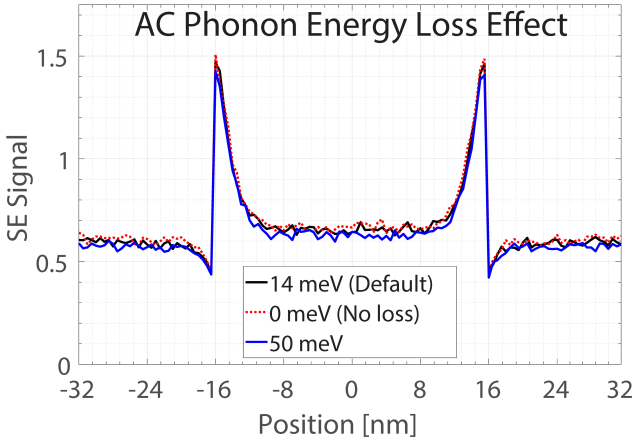


Figure 3.15: Effect of two fixed energy loss values in the electron-acoustic phonon scattering model on a line scan at 300 eV. The line scan signals are hardly affected by this.

3.8. Discussion

The results have shown that the scattering models have an impact on 2D and 3D metrology tasks. For instance, the linewidth measurement error due to the model variations presented here is less than 2 nm for a 32 nm line. This might still be acceptable but today, the semiconductor industry already targets sub-10 nm features [7, 43]. In that size range a 2 nm error would not be acceptable as it would have a serious influence on the physical properties of devices, for instance on the thermal conductivity [44, 45], or on the optical and electronic properties such as the dielectric function [7] or band-gap [46].

One may wonder whether phenomenological models can be used for dimensional metrology. So far, phenomenological inelastic scattering models were calibrated using experimental SE emission yields from semi-spherical surfaces [47]. But then still, a correct value of the SE yield does not necessarily mean that the electron scattering volume in the material is calculated properly. The scattering cloud of these models can be very misleading, as pointed out in literature [48]. Re-calibration, using more complex procedures, would then be required to make the simulation tool suitable for dimensional metrology tasks. In any case, as demonstrated in this work, the phenomenological simulation tools do need to include a quantum mechanical transmission probability model.

Dynamic effects were not investigated in this study. For example, if the material is not sufficiently conductive, the accumulated charge will lead to different signal contrast and critical dimension measurements. In that case, the impact of the model ingredients can be different. This should be investigated separately in a future study.

3.9. Conclusion

We studied the sensitivity of simulated SEM images to various first-principle physics models. For this purpose multi-energy SEM images were introduced, a very powerful visualization technique that allows a quick analysis over a broad energy range. The quantum mechanical transmission probability model (QT) was found to have an essential impact on images at low energies (up to 1 keV). It is also found that this model is essential in reproducing the "shadowing" features of the signal.

Including acoustic phonon (AC) cross-sections instead of Mott cross-sections at low energies, yields significantly different results. A smaller (AC phonon) elastic mean free path leads to a smaller scattering volume for silicon. It affects the linewidth measurement error by less than 2 nm. We found that the difference between the two CD measurement methods based on 50% threshold is insignificant for beam energies up to 1 keV.

Both AC phonon and QT models are found to change the emission in a topography dependent way. This will affect 3D measurements based on signal intensities, such as height measurements from top-down SEM images.

Concerning simulation times, different model choices did not lead to a significant

speed-up. For the effect of inelastic scattering model on CD, we compared two different simulators, JMONSEL and CASINO. The comparison between these simulators shows that phenomenological inelastic scattering models are the fastest, but they often lead to different results. In a future study, it would be more accurate to implement these different models into the same simulator to analyze their effect on simulation times.

Comparing CASINO and JMONSEL to Nebula only led to similar results when the QT model was excluded. However, good agreement was found between experimental results and Nebula simulations with the QT model included. This demonstrates the relevance of the QT model and, assuming that no QT model has been included yet in CASINO or JMONSEL, if it would be included, both simulators would do much better in reproducing results from simulators based on first-principle physics models.

Acknowledgements

We acknowledge GenISys-GmbH and Raith B.V. for funding this project.

References

[1] N. G. Orji, M. Badaroglu, B. M. Barnes, C. Beitia, B. D. Bunday, U. Celano, R. J. Kline, M. Neisser, Y. Obeng, and A. E. Vladar, *Metrology for the next generation of semiconductor devices,* Nature Electronics **1**, 532 (2018).

[2] G. F. Lorusso, N. Horiguchi, J. Bömmels, C. J. Wilson, G. V. den Bosch, G. S. Kar, T. Ohashi, T. Sutani, R. Watanabe, Y. Takemasa, and M. Ikota, *Electron beam metrology for advanced technology nodes,* Japanese Journal of Applied Physics **58**, SD0801 (2019).

[3] J. Mulkens, M. Kubis, W. Tel, M. Maslow, E. Ma, K. Chou, X. Liu, W. Ren, X. Hu, F. Wang, K. Liu, B. Slachter, H. Dillen, and P. Hinnen, *Holistic approach for overlay and edge placement error to meet the 5nm technology node requirements,* in *Metrology, Inspection, and Process Control for Microlithography XXXII*, May, edited by O. Adan and V. A. Ukraintsev (SPIE, 2018) p. 55.

[4] A.-L. Charley, T. Sutani, Y. Takemasa, G. F. Lorusso, and P. Leray, *Advanced CD-SEM solution for edge placement error characterization of BEOL pitch 32nm metal layers,* in *Metrology, Inspection, and Process Control for Microlithography XXXII*, Vol. 1058519, edited by O. Adan and V. A. Ukraintsev (SPIE, 2018) p. 44.

[5] K. Bhattacharyya, *Tough road ahead for device overlay and edge placement error,* in *Metrology, Inspection, and Process Control for Microlithography XXXIII*, Vol. 1095902, edited by O. Adan and V. A. Ukraintsev (SPIE, 2019) p. 1.

[6] ITRS, *ITRS*, Tech. Rep. (2015).

[7] B. Bunday, *HVM metrology challenges towards the 5nm node,* in *Metrology, Inspection, and Process Control for Microlithography XXX*, Vol. 9778, edited by M. I. Sanchez and V. A. Ukraintsev (2016) p. 97780E.

[8] J. S. Villarrubia, V. N. Tondare, and A. E. Vladár, *Virtual rough samples to test 3D nanometer-scale scanning electron microscopy stereo photogrammetry,* (2016) p. 977809.

[9] E. Solecky, A. Rasafar, J. Cantone, B. Bunday, A. Vaid, O. Patterson, A. Stamper, K. Wu, R. Buengener, W. Weng, and X. Dai, *In-line E-beam metrology and defect inspection: industry reflections, hybrid E-beam opportunities, recommendations and predictions,* in *Proceedings of SPIE*, March 2017, edited by M. I. Sanchez and V. A. Ukraintsev (2017) p. 101450R.

[10] J. Villarrubia, A. Vladár, B. Ming, R. Kline, D. Sunday, J. Chawla, and S. List, *Scanning electron microscope measurement of width and shape of 10 nm patterned lines using a JMONSEL-modeled library,* Ultramicroscopy **154**, 15 (2015).

[11] V. N. Tondare, J. S. Villarrubia, and A. E. Vladár, *Three-Dimensional (3D) Nanometrology Based on Scanning Electron Microscope (SEM) Stereophotogrammetry,* Microscopy and Microanalysis **23**, 967 (2017).

[12] Y. Zou, M. Khan, H. Li, Y. Li, W. Li, S. Gao, L. Liu, and Z. Ding, *Use of model-based library in critical dimension measurement by CD-SEM,* Measurement **123**, 150 (2018).

[13] J. S. Villarrubia and Z. J. Ding, *Sensitivity of scanning electron microscope width measurements to model assumptions,* Journal of Micro/Nanolithography, MEMS, and MOEMS **8**, 033003 (2009).

[14] T. Verduin, S. Lokhorst, C. Hagen, and P. Kruit, *Sensitivity of secondary electron yields and SEM images to scattering parameters in MC simulations,* Microelectronic Engineering **155**, 114 (2016).

[15] K. T. Arat, J. Bolten, A. C. Zonnevylle, P. Kruit, and C. W. Hagen, *Estimating Step Heights from Top-Down SEM Images,* Microscopy and Microanalysis **25**, 903 (2019).

[16] H. Demers, N. Poirier-Demers, A. R. Couture, D. Joly, M. Guilmain, N. de Jonge, and D. Drouin, *Three-dimensional electron microscopy simulation with the CASINO Monte Carlo software,* Scanning **33**, 135 (2011).

[17] F. Salvat, A. Jablonski, and C. J. Powell, *ELSEPA—Dirac partial-wave calculation of elastic scattering of electrons and positrons by atoms, positive ions and molecules,* Computer Physics Communications **165**, 157 (2005).

[18] E. Kieft and E. Bosch, *Refinement of Monte Carlo simulations of electron–specimen interaction in low-voltage SEM,* Journal of Physics D: Applied Physics **41**, 215310 (2008).

[19] T. Verduin, *Quantum Noise Effects in e-Beam Lithography and Metrology*, Ph.D. thesis, Delft University of Technology (2017).

[20] E. Schreiber and H.-J. Fitting, *Monte Carlo simulation of secondary electron emission from the insulator SiO2,* Journal of Electron Spectroscopy and Related Phenomena **124**, 25 (2002).

[21] D. R. Penn, *Electron mean-free-path calculations using a model dielectric function,* Physical Review B **35**, 482 (1987).

[22] S. F. Mao, Y. G. Li, R. G. Zeng, and Z. J. Ding, *Electron inelastic scattering and secondary electron emission calculated without the single pole approximation,* Journal of Applied Physics **104**, 114907 (2008).

[23] H. Shinotsuka, S. Tanuma, C. Powell, and D. Penn, *Calculations of electron stopping powers for 41 elemental solids over the 50eV to 30keV range with the full Penn algorithm,* Nuclear Instruments and Methods in Physics Research Section B: Beam Interactions with Materials and Atoms **270**, 75 (2012).

[24] M. Dapor, *A Monte Carlo investigation of secondary electron emission from solid targets: Spherical symmetry versus momentum conservation within the classical binary collision model,* Nuclear Instruments and Methods in Physics Research Section B: Beam Interactions with Materials and Atoms **267**, 3055 (2009).

[25] H.-J. Fitting, E. Schreiber, J.-C. Kuhr, and A. von Czarnowski, *Attenuation and escape depths of low-energy electron emission,* Journal of Electron Spectroscopy and Related Phenomena **119**, 35 (2001).

[26] R. Egerton, P. Li, and M. Malac, *Radiation damage in the TEM and SEM,* Micron **35**, 399 (2004), arXiv:arXiv:1011.1669v3 .

[27] L. van Kessel, *Nebula,* (2018).

[28] C. Shishido, M. Tanaka, and M. Osaki, *CD-bias reduction in CD-SEM line-width measurement for the 32-nm node and beyond using the model-based library method,* in *Proceedings of SPIE*, Vol. 7272, edited by J. A. Allgair and C. J. Raymond (2009) p. 72722C.

[29] J. S. Villarrubia, A. E. Vladár, and M. T. Postek, *3D Monte Carlo modeling of the SEM: Are there applications to photomask metrology?* (2014) p. 923602.

[30] J. S. Villarrubia, R. G. Dixson, and A. E. Vladár, *Proximity-associated errors in contour metrology,* in *Metrology, Inspection, and Process Control for Microlithography XXIV*, Vol. 7638, edited by C. J. Raymond (2010) p. 76380S.

[31] J. S. Villarrubia, A. E. Vladar, J. R. Lowney, M. T. Postek, Jr., R. A. Allen, M. W. Cresswell, and R. N. Ghoshtagore, *Linewidth measurement intercomparison on a BESOI sample John,* in *Metrology, Inspection, and Process Control for Microlithography XIV*, Vol. 3998, edited by N. T. Sullivan (2000) pp. 84–95.

[32] P. Zhang, *Monte Carlo study for correcting the broadened line□scan profile in scanning electron microscopy,* Journal of Microscopy **277**, 23 (2020).

[33] S. Hari, T. Verduin, P. Kruit, and C. W. Hagen, *A study of the reproducibility of electron beam induced deposition for sub-20 nm lithography,* Micro and Nano Engineering **4**, 1 (2019).

[34] J. S. Villarrubia, *Simulation study of repeatability and bias in the critical dimension scanning electron microscope,* Journal of Micro/Nanolithography, MEMS, and MOEMS **4**, 033002 (2005).

[35] R. Browning, T. Z. Li, B. Chui, J. Ye, R. F. W. Pease, Z. Czyżewski, and D. C. Joy, *Empirical forms for the electron/atom elastic scattering cross sections from 0.1 to 30 keV,* Journal of Applied Physics **76**, 2016 (1994).

[36] D. C. Joy and S. Luo, *An empirical stopping power relationship for low-energy electrons,* Scanning **11**, 176 (1989).

[37] J. R. Lowney, *Monte Carlo simulation of scanning electron microscope signals for lithographic metrology,* Scanning **18**, 301 (2006).

[38] Z.-J. Ding and R. Shimizu, *A Monte Carlo modeling of electron interaction with solids including cascade secondary electron production,* Scanning **18**, 92 (2006).

[39] Z. J. Ding, X. D. Tang, and R. Shimizu, *Monte Carlo study of secondary electron emission,* Journal of Applied Physics **89**, 718 (2001).

[40] M. T. Postek, A. E. Vladar, W. Keery, M. Bishop, B. Bunday, and J. Allgair, *Reference material (RM) 8820: a versatile new NIST standard for nanometrology,* in *Proc SPIE*, Vol. 7638, edited by C. J. Raymond (2010) p. 76381B.

[41] M. T. Postek, A. E. Vladár, J. S. Villarrubia, and A. Muto, *Comparison of Electron Imaging Modes for Dimensional Measurements in the Scanning Electron Microscope,* Microscopy and Microanalysis **22**, 768 (2016).

[42] B. Cai, Y.-S. Lin, Q. Wu, Y. Huang, S. Yang, W.-H. Li, and M. Hao, *Characterization of a 'first measurement effect' in CD-SEM measurement,* in *Metrology, Inspection, and Process Control for Microlithography XXVII*, Vol. 8681, edited by A. Starikov and J. P. Cain (2013) p. 868131.

[43] A. E. Vladár, J. S. Villarrubia, J. Chawla, B. Ming, J. R. Kline, S. List, and M. T. Postek, *10nm three-dimensional CD-SEM metrology,* in *Metrology, Inspection, and Process Control for Microlithography XXVIII*, Vol. 9050, edited by J. P. Cain and M. I. Sanchez (2014) p. 90500A.

[44] S. Gireesan, P. Torres, F. X. Alvarez, and P. A. Bobbert, *Diameter-dependent thermal conductivity of ultrathin GaP nanowires: A molecular dynamics study,* Physical Review B **101**, 024307 (2020).

[45] S. Mousavi, S. Davatolhagh, and M. Moradi, *Effects of thickness, impurity, surface roughness, and temperature on transport and thermoelectric coefficients of ultrathin silicon nanowires: An analytic study,* Physica E: Low-dimensional Systems and Nanostructures **118**, 113889 (2020).

[46] M. K. Sahoo and P. Kale, *Integration of silicon nanowires in solar cell structure for efficiency enhancement: A review,* Journal of Materiomics **5**, 34 (2019).

[47] K. T. Arat, J. Bolten, T. Klimpel, and N. Unal, *Electric fields in Scanning Electron Microscopy simulations,* in *Proc SPIE*, Vol. 9778, edited by M. I. Sanchez and V. A. Ukraintsev (2016) p. 97780C.

[48] K. T. Arat, T. Klimpel, and C. W. Hagen, *Model improvements to simulate charging in scanning electron microscope,* Journal of Micro/Nanolithography, MEMS, and MOEMS **18**, 1 (2019).

4

Model Improvements to Simulate Charging

Charging of insulators is a complex phenomenon to simulate since the accuracy of the simulations is very sensitive to the interaction of electrons with matter and electric fields. Aim: In this study, we report model improvements for a previously developed Monte-Carlo simulator to more accurately simulate samples that charge. The improvements include both modeling of low energy electron scattering by first-principle approaches and charging of insulators by the redistribution of the charge carriers in the material with an electron beam-induced conductivity and a dielectric breakdown model. The first-principle scattering models provide a more realistic charge distribution cloud in the material and a better match between non-charging simulations and experimental results. The improvements on the charging models, which mainly focus on the redistribution of the charge carriers, lead to a smoother distribution of the charges and better experimental agreement of charging simulations. Combined with a more accurate tracing of low energy electrons in the electric field, we managed to reproduce the dynamically changing charging contrast due to an induced positive surface potential.

This chapter is published as a journal paper:
Kerim T. Arat, Thomas Klimpel, Cornelis W. Hagen: Model improvements to simulate charging in scanning electron microscope. *Journal of Micro/Nanolithography, MEMS, MOEMS*. 12/2019; 18(04):1. DOI:10.1117/1.JMM.18.4.044003

4.1. Introduction

Electron beam-based inspection techniques have become a standard, where nanometer resolution imaging is required for state of the art semiconductor devices. However, when nonconductive materials are involved, charging occurs and issues are reported, such as image distortion due to primary beam deflection [1–5] and image contrast changes due to the changing secondary electron (SE) emission [6–8]. As a consequence, measurements of critical dimensions will be less accurate [9–11]. Therefore, a better understanding of the charging effects on electron imaging becomes crucial for metrology.

Several Monte Carlo studies were reported that included charging effects, but they rather focused on simulations for simplified geometries, such as semi-infinite surfaces [12–14]. Besides that, some Monte Carlo simulators were developed to simulate full 3D geometries and charging models were also incorporated [15–19]. However, the long calculation times of these simulators render them quite impractical for realistic scenarios.

In an earlier study, we reported a Monte Carlo simulator that included charging effects, making use of a multigrid-based electric field solver to decrease the electric field computation time [20]. Combining the electric field solver with a semi-empirical electron-matter interaction model, we were able to simulate a scanning electron microscope (SEM) image of an area of ≈1.5 μm^2 of grating couplers, as shown in Fig. 4.1a, in about 1 h [20]. However, the shadowing phenomenon (bright-to-dark transition) on the oxide pads, seen in Fig. 4.1, could not be reproduced in the simulation Fig. 4.1c. Including the charging model only led to a blur of the edges due to beam deflection, see Fig. 4.1b and 4.1c.

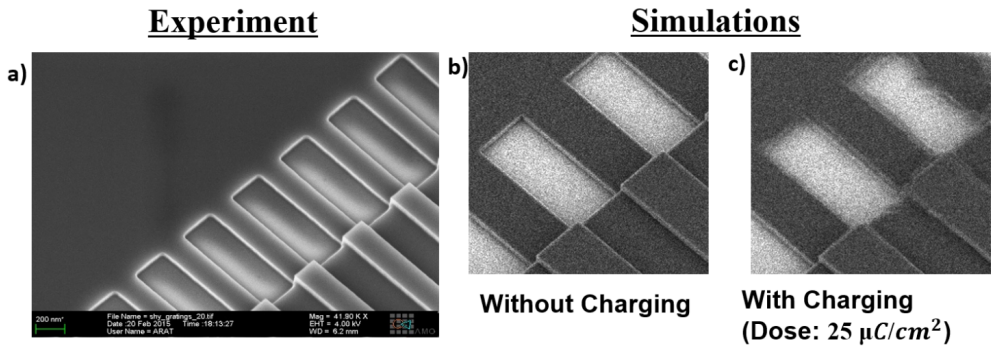


Figure 4.1: (a) Experimental SEM image of a grating coupler [20] compared with (b) the simulated image without charging, and (c) the simulated image with charging taken into account. Simulated areas [in panels (b) and (c)] are 1.2 × 1.2 μm^2.

To properly include the charging effects, it is important to accurately model the electron-matter interaction, especially for low energetic electrons, which are very sensitive to the local electric fields. Therefore, improvements are needed for both the

electron scattering models and the charging models. In this work, we report our attempts to improve both.

First, we improved the electron scattering models by incorporating discrete scattering of electrons instead of the continuous slowing down approximation (CSDA). Inelastic scattering is modeled using the dielectric function. Also, electron-phonon scattering and quantum mechanical transmission through boundaries are implemented. Moreover, solid-state effects on the atomic potential are taken into account in modeling the elastic scattering. All electrons are traced until their energy is below the surface barrier of ≈10 eV, measured with respect to the bottom of the band.

Second, we addressed issues exclusively relevant for insulators, namely charge redistribution to include effects, such as electron beam-induced conductivity (EBIC). The most straightforward approach would be to completely ignore charge redistribution in insulators, as was done in our previous study [20], or only consider catastrophic effects like dielectric breakdown. The other extreme would be modeling from first principles, including effects like electron-hole recombination and trapping. We chose a midway and modeled the charge redistribution effects using phenomenological models with a limited number of calibration parameters [21].

After that, the effect of charging on the electron emission from a bulk oxide sample during a line scan, for different doses, is demonstrated. Subsequently, a top-down view of the grating couplers is simulated where the charging (bright-to-dark) contrast is present. Finally, the impact of the charge redistribution model is shown on a test sample with four metal contact pads embedded in a thin silicon dioxide (SiO_2) layer on top of a silicon (Si) wafer. Three pads are electrically floating (no contact with the underlying Si wafer), and the fourth one is connected to the underlying Si wafer. The effect on the simulated SEM images is shown when the charging and/or EBIC model is switched on. The models lead to more realistic images and can reproduce phenomena that were not possible to reproduce with the previous models.

4.2. Scattering model

We will now first describe the scattering model improvements and assume that the scattering cross-sections do not change due to charging. The electron trajectories are influenced by the charge clouds in the materials, which are formed by electrons getting trapped (negative charge) or electrons generating new electrons (both negative and positive charge). Hence, accurate modeling of electron generation, transport, and boundary-crossing is essential to understand the charge distribution in the material and the electron emission.

In our previous study [20], the semi-empirical scattering models were designed to get an accurate value of the SE yield for a semi-infinite surface. However, an accurate SE yield does not guarantee a realistic scattering cloud inside the material, as shown in Fig. 4.2a. The very different scattering cloud will not only affect charge distribution but also the detected signal from topographical structures. It is still possible to generate a more realistic scattering cloud using CSDA, similar to Fig. 4.2b, by allow-

ing the generation and scattering of electrons in deeper regions of the material, but any inaccuracy due to the approximate model will lead to a deviation of the charging phenomenon. Therefore, we preferred to use first principle modeling to determine the charge distribution.

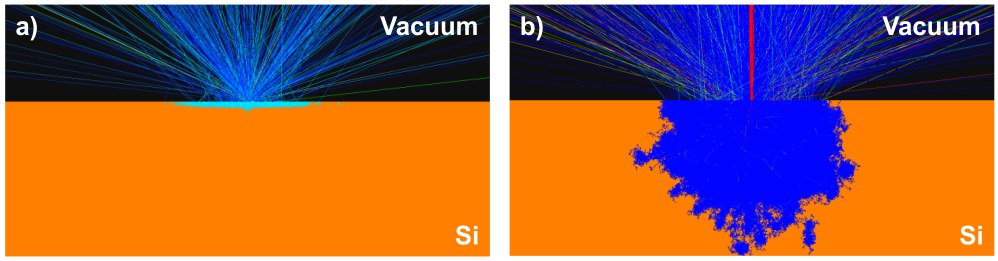


Figure 4.2: Scattering cloud of SEs: the generic shape of the cloud obtained with (a) the approximate (former) models and (b) first principle (current) models. In panel (a), only SEs that can escape are generated and in (b), all SEs are generated and traced.

4.2.1. Improvements on elastic scattering cross-sections

In our earlier work, Mott cross-sections were used to calculate the elastic scattering mean free paths and the scattering angles. However, the calculations were done for a "free atom" potential, which is not quite appropriate for our application because solid-state effects are not included. Instead, a "muffin-tin" potential is more realistic. Furthermore, the indistinguishability of the incident electron from the bound electrons, "exchange-correction," and the polarization of the target atom due to incident electrons, "correlation-polarization" are also included. All these options are offered by the ELSEPA package [22]. For Si, the "muffin-tin" potential results in ≈1.5 times larger mean free paths, as shown in Fig. 4.3. At low energies, below a few hundred electron volts (eV), the Mott cross-sections turn out to become very sensitive to the atomic potential [23]. Because at these low energies (the quasi-elastic), electron-phonon interaction becomes dominant, we followed the approach suggested by Verduin [24] and use the electron-phonon scattering model for low energies. Therefore, in the present study, the elastic scattering cross-section consists of

- Mott cross-section (muffin-tin + "exchange correction" + "correlation-polarization") for energy > 200 eV
- Acoustic phonon scattering cross-section for energy < 100 eV.

For energies between 100 and 200 eV, the cross-section is interpolated between the two.

Material parameters, especially related to acoustic phonons, are not easy to find. To serve the interested reader, we list the parameters used in this work in Table 4.1.

Density ρ_m, Fermi energy E_F, W, electron affinity χ, bandgap E_g at 300 K, density of state mass m_{dos}, effective mass of electron m_{eff}, screening parameter A_{ac}, speed

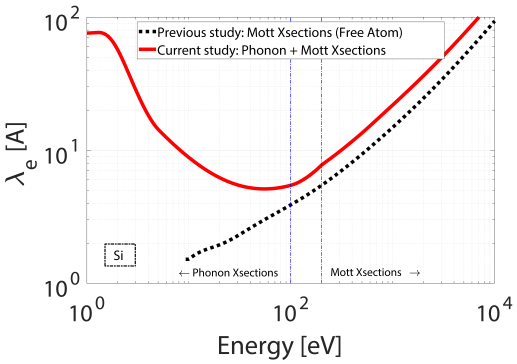


Figure 4.3: Elastic mean free path versus energy for Si: it consists of an interpolation between the Mott cross-section (energy > 200 eV) and phonon cross-sections (energy < 100 eV). The Mott cross-sections were calculated by ELSEPA [22], assuming the muffin-tin approximation, exchange correction, and correlation-polarization effects.

Table 4.1: Material parameters for Si, Cu, and SiO2

		Si	Cu	SiO2
ρ_m		2.329[25]	8.96[26]	2.648[27]
E_F		7.83	7.0[28]	-
W or χ		4.05	4.65[28]	0.9[29]
E_g		1.12	-	9.0[29]
m_{dos}		1.08[30]	1.0[24]	1.0^+
m_{eff}		0.26[30]	1.01[28]	1.0^+
A_{ac}		5^+	5^+	7[31]
E_{Ph}		14^*	12.6^*	6.8^*
u_s	*Longitudinal*	9130[32]	4760[28]	3560[31]
	Transversal	5842[32]	2325[28]	3560^+
ε_{ac}	*Longitudinal*	9.2[33]	4.76^*	3.4[31]
	Transversal	5.0[33]	3.72^*	3.4^+

of sound in solid u_s, and acoustic deformation potential ε_{ac} are given in Table 4.1. [*] are calculated values and [+] are assumed values. The net-average energy loss in the phonon scattering, E_{Ph}, is calculated by Eq. 3.116 in Verduin [24].

4.2.2. Improvements on inelastic scattering cross-sections

In the previous study [20], an algorithm based on CSDA was used to model the energy transfer of the primary electrons [34]. Although CSDA is a good approximation to estimate stopping power (SP) at high energies, it overestimates the SP at very low energies. Furthermore, it does not describe the SE generation. Therefore, we have employed the first principle modeling to simulate the low energetic electrons as accurately as possible. In this study, energy and momentum transfer of an electron to the material is modeled by the dielectric function formalism using optical data [35]. It allows the calculation of inelastic events discretely, as depicted in Fig. 4.4.

To calculate inelastic cross-sections, we take Ashley's (simple) model [35] and adopted the refinements suggested by Kieft and Bosch [23], i.e., no exchange cor-

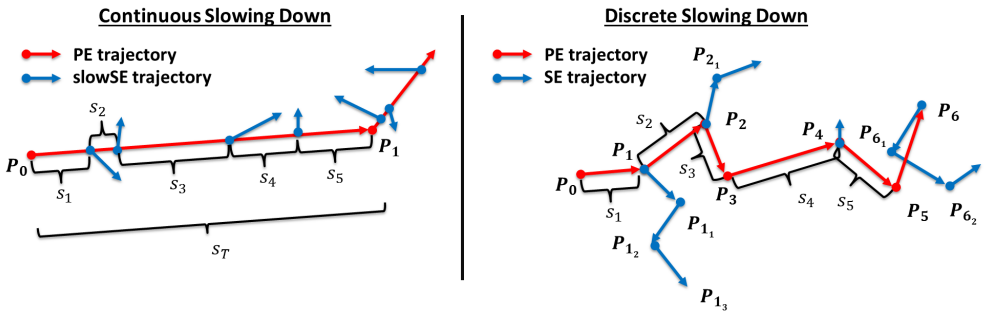


Figure 4.4: Inelastic scattering: (a) a semiempirical model is used in the previous study, which is based on the CSDA. It estimates the number of (slow) SEs and their energies for a path length (ST) from the stopping power; (b) first principle modeling is used in the current study, which is based on dielectric function formalism. It estimates the inelastic mean free path, energy and momentum transfer for each inelastic event (P1, P2, P4, and P6) based on the energy loss function.

rection for energies < 50 eV, and restrict energy losses, such that electrons cannot end up with an energy lower than the Fermi level. We have used the density per atom for elements, such as Si and copper (Cu), and the density per molecule for molecules and compounds, such as SiO_2, when calculating the mean free paths.

The SP from the previous study is compared to the powers, as obtained from the refined Ashley model for Si in Fig. 4.5a. It is seen to be identical for energies above 1 keV but deviates at lower energies. The elastic and inelastic mean free paths are also given in Fig. 4.5b.

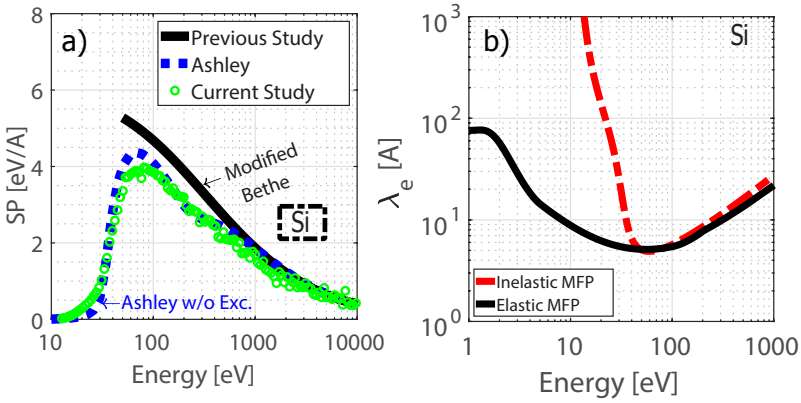


Figure 4.5: Modelling inelastic scattering: (a) stopping power and (b) comparison of mean free paths of Si in the current study.

We obtain the energy transfer using the dielectric function formalism. This, however, does not provide the initial (binding) energy of the SE prior to a scattering event. We model that following the approach suggested by Kieft and Bosch [23].

For insulators like SiO_2, electron trapping due to polaronic effects has been reported

by several authors [12, 36, 37], but none of them is based on a first principle physics model. In this study, the nominal SE emission is unrealistically high (7 at its maximum) without explicit implementation of trapping cross-sections (Fig. 4.6). Therefore, we also implemented an empirical model [12] for trapping cross-sections for SiO_2 to not neglect the trapping phenomenon in insulators and to lower the nominal (theoretical) SE yield to values in agreement with those reported by Schreiber and Fitting [31] and Ohya et al. [36]. We have used $S_{trap} = 0.2(1/nm)$ and $\gamma_{trap} = 0.2(1/eV)$ when calculating the trapping cross-sections from Eq. 13 of Ref. [12]. The SE and backscattered electron (BSE) yields of SiO_2 with and without trapping cross-sections are given in Fig. 4.6. The inclusion of the trapping cross-sections hardly affects the BSE yield because trapping only has an effect on very slow electrons.

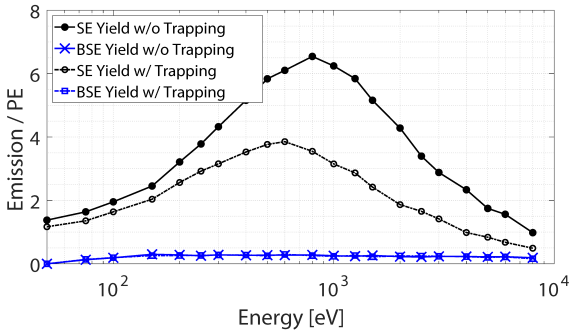


Figure 4.6: Comparison of emission yields with (w/) and with (w/o) trapping cross-sections.

4.2.3. Improvements on boundary cross-sections

The lower the electron energy, the more its path is affected when it interacts with a boundary and as a result, it can be reflected or transmitted. Modeling the boundary-crossing correctly is crucial for SE emission. In the previous study, the probability of crossing the surface barrier was modeled using momentum conservation only. That is, if the electron approaches the surface under an angle bigger than the critical angle (α_c, see Fig. 4.7), then it will be reflected (total internal reflection).

In this study, the probability of transmission is determined quantum mechanically [38]. When the electron is considered as a wave, there is a probability that part of the wave is transmitted through the boundary and part of it is reflected.

$$P(\alpha') = \frac{4\sqrt{1 + \frac{-\Delta U}{E\cos^2\alpha'}}}{(1 + \sqrt{1 + \frac{-\Delta U}{E\cos^2\alpha'}})^2} \tag{4.1}$$

where ΔU is the net change in kinetic energy, E is the kinetic energy of the electron, and α' is the angle of incidence.

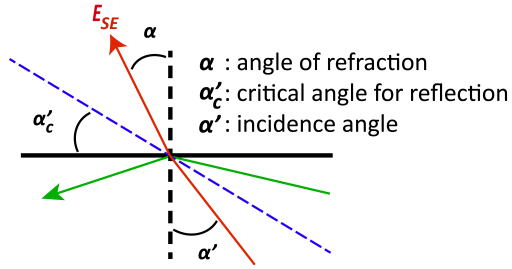


Figure 4.7: Transmission of an electron from the surface.

4.3. Charging Model

The basic principle of the Monte Carlo simulation of the interaction of individual electrons and the continuously changing electric fields and accompanying charging effects is simple: a certain number of PEs is simulated, and then, the field solver updates the field and redistributes the charge as needed. This procedure is repeated many times, typically at least once per simulated pixel. Updating multiple times for a single pixel is not unreasonable either, say after every 200 PEs. The detailed-level interaction between the field solver, the Monte Carlo simulation, and the charge redistribution models is more complicated. The numerical discontinuities of the electric field solution must be handled by the Monte Carlo simulation, and the charge redistribution models tend to make the solution of the field equation more difficult and time-consuming.

4.3.1. Electric field solver

The electric field solver uses the Poisson equation:

$$-\nabla \cdot [\epsilon_r(r)\nabla V(r)] = \frac{\rho(r)}{\epsilon_0}, \tag{4.2}$$

in which $\rho(r)$ is the charge distribution, $V(r)$ is the potential, $\epsilon(r)$ is the dielectric constant of the material, and ϵ_0 is the permittivity in a vacuum. It is used with the constitutive material equation (Eq. (4.3)):

$$J = -\sigma\nabla V, \tag{4.3}$$

and the continuity equation (Eq. (4.4)):

$$\frac{\partial \rho}{\partial t} + \nabla \cdot J = 0, \tag{4.4}$$

in which J is the current density and $\sigma(r)$ is the conductivity. This equation (Eq. (4.4)) is solved by an implicit Euler scheme:

$$\frac{\rho_n - \rho_{n-1}}{\Delta t} = \nabla \cdot (\sigma\nabla V_n), \tag{4.5}$$

where V_n is determined by

$$\frac{\rho_n}{\epsilon_0} = -\nabla \cdot (\epsilon_r \nabla V_n) = \frac{\rho_{n-1}}{\epsilon_0} + \frac{\Delta t}{\epsilon_0} \nabla \cdot (\sigma \nabla V_n), \tag{4.6}$$

giving a Poisson equation with modified material parameters:

$$-\nabla[(\epsilon_r(r) + \frac{\Delta t}{\epsilon_0}\sigma(r,t))\nabla V_n] = \frac{\rho_{n-1}}{\epsilon_0}, \tag{4.7}$$

The charges deposited during the time step by the Monte Carlo simulation are added to ρ_{n-1} before this equation (Eq. (4.7)) is solved, which works if we only make a single-time step between Monte Carlo simulations.

The conductivity $\sigma(r,t)$ in this equation depends on space by an induced conductivity model. The conductivity also depends on the electric field strength because we include a dielectric breakdown model. However, this dependency is suppressed here because the main numerical effort for the solution of the equation is as if the conductivity would be a fixed known function of space and time. (A more physical model would include the dependency of the conductivity on the electron and hole concentrations, but this dependency cannot be suppressed and the numerical solution of the resulting equations would be challenging.

The modified equation is harder to solve than the original equation since $\sigma(r,t)$ normally changes quickly in both space and time. We previously had the option to use a direct solver as a slow but robust and accurate reference solver. This is no longer possible since the expensive initial factorization must be repeated for each time step. Therefore, we integrated a modern algebraic multigrid solver, namely Daniel A. Spielman's modified implementation of Kyng and Sachdeva [39]. It was initially more than a factor 3 slower than the existing multigrid solver, but a *C++* port and tighter integration reduced that factor to 1.5. It was later used to enable more flexible meshing, which turned out to save a factor 2 to 3 (and possibly more) for certain use cases. The *C++* port has been parallelized, but parallel scaling is limited. The best speedup is achieved with four threads, but it is only slightly above a factor 2. The existing multigrid solver has also been parallelized. The best speedup is still achieved with four threads, but the scaling is better. This solver is used when explicit simulation times are reported.

The modified equation also affects the geometric multigrid solver. It becomes less robust because the material parameters are changing quickly on a very small spatial scale. We improved robustness by using a preconditioned conjugate gradient method, where the multigrid solver acts as a preconditioner. We also tried (and failed) to use another Krylov method, namely replacing the W-cycle by the K- cycle introduced by Notay and Vassilevski [40] for algebraic multigrid methods (AMG). However, what really improved the robustness significantly was to use locally either the continuity equation or the Poisson equation as they occur in Eq. (4.5) to update the charge distribution, depending on which is locally less affected by inaccuracies in the potential.

4.3.2. Tracing electrons

The electrons both in the sample and in vacuum are traced subject to the influence of the current electric field. The numerically solved electric field is discontinuous at cell boundaries since the finite-element method is used for discretization of the field equations. At material interfaces, the normal component of the electric field is discontinuous even for the exact solution. This severely limits the choice of reasonable integration methods. The velocity Verlet scheme is used because it leads to (piecewise) parabolic trajectories, for which it is easy to exactly compute the intersections with the mesh of the field solver (or the geometry). The velocity Verlet scheme approximates the equation:

$$\ddot{x}(t) = a[x(t)], \tag{4.8}$$

as

$$x(t + \Delta t) = x(t) + v(t)\Delta t + \frac{1}{2}a\Delta t^2, \tag{4.9}$$

$$v(t + \Delta t) = v(t) + \frac{a(t) + a(t + \Delta t)}{2}\Delta t, \tag{4.10}$$

This scheme is applied with respect to time, but the simulation needs the trajectory for a given distance. If the distance along the trajectory to the next intersection with an interface is shorter than the given distance, then the corresponding time step Δt can be determined exactly. If not, then Δt is determined from a given distance Δs via $\Delta t = \frac{\Delta s}{|v|}$ In theory, this inaccurate value for the time step seems to reduce the accuracy of the method. However, in practice, either the electron is inside a material and Δs is very small, or the electron is in vacuum and Δs is big but irrelevant.

4.3.3. Modeling of sample charging

The basis for sample charging is that the creation of a SE deposits a positive charge and stopping an electron deposits a negative charge. At room temperature, both positive holes and negative electrons would continue to move and also drift in local electric fields, but modeling the movements of individual holes and electrons with thermal energy is not practical. We implemented macroscopic models for induced conductivity, dielectric breakdown, and charge diffusion. We will ignore the charge diffusion model since we did not use it for the simulations presented later and do not have sufficient intuition of how to set its model parameters. The motivation, modeling, and implementation of the other two models are described in the following sections.

4.3.4. Induced conductivity

Slow electrons returning from the vacuum back to the sample tend to accumulate very close to the sample surface. The surface then tends to charge negatively and

develop a dipole layer, at least in the simulation. It is not clear whether there are physical effects, which could neutralize that dipole layer completely within a short time. One main charge redistribution effect is that the beam generates free holes and electrons, which locally turn insulators into conductors. This also counters dipole layer formation, so it would be nice if this charge redistribution effect could be included in the simulation.

To avoid the complicated physics of electron and hole transport, recombination and trapping, as a first step, an established empirical quasi-static electron beam-induced conductivity model is attractive. Induced conductivity, in general, occurs due to the local ionization of the material as long as free electrons or holes are locally present, i.e., the material is locally conductive. This will allow some surface conductivity as long as there is a charge imbalance due to recollected slow electrons by a positive surface potential. More specifically, the implemented model expresses the conductivity using the deposited energy (in Gray) per kilogram per time $\Delta(r,t)$ as follows:

$$\sigma(r,t) = k \cdot D(r,t)^{\Delta}, \tag{4.11}$$

where we used $k = 10^{-14} S/m(Gy/s)^{-14}$ (EBIC constant) and $\Delta = 1.0$ (EBIC exponent) for SiO_2 in the simulation. This model assumes a slowly changing (quasi-static) deposited energy per time. However, we use it (incorrectly) for the quick scanning and a finely resolved grid with very few electrons. Still, it allows studying the impact of this sort of charge redistribution effect and how it reduces the undesired dipole layer near the sample surface. Here, the deposited energy includes the energy lost in a scattering event and energy of trapped electrons.

In Ref. [21], this model is used correctly for a defocused (quasi-static) beam with $k = 7.7 \times 10^{-18} s^{\Delta}/(\Omega \cdot cm \cdot rad^{\Delta})$ and $\Delta = 0.89$ for a red polymethyl methacrylate (PMMA), as given by Tanaka et al. [41]. To convert this to SI units, one has to multiply by $100 \times 100^{\Delta}$, giving $k = 4.6 \times 10^{-14} S/m(Gy/s)^{\Delta}$.

4.3.5. Dielectric breakdown

Even with an empirical EBIC model, as described in the previous section, one can still sometimes observe unphysically huge electric field strengths. So, it makes sense to include a dielectric breakdown model as a fallback for those cases, where the electric field strength grows huge. That can be caused by simulation artifacts like a missing physical effect, or it can be a real physical effect, for example, if two conductors are separated by a very thin insulating layer.

Instead of modeling the detailed generation of electron-hole pairs in an avalanche breakdown event, it is assumed that an isolated material will become perfectly conducting locally at the places, where the field strength exceeds the dielectric strength of the material. During a breakdown event, the region where an insulator becomes conducting can travel (or grow) through space, as long as the underlying charge distribution is not sufficiently neutralized.

The model is implemented by setting the cells where the field strength currently exceeds a given threshold to perfectly conducting. Next, the field is computed again, the charges are redistributed accordingly, and then further perfectly conducting cells are added, where the new field exceeds the threshold. This procedure is repeated until either the field no longer exceeds the threshold anywhere, or after the procedure was repeated a predefined number of times. The perfectly conducting region grows during the simulation of the breakdown event, but after it is finished, the previous material properties are used again, as if the breakdown would not have harmed the isolator at all. Hence, it makes sense to remember any cell that temporarily got affected by breakdown (and the maximal field strength by which it got affected) for later inspection.

Although not based on first-principle physics, having a robust breakdown model, as described above, is important to prevent simulations from failing due to huge electric field strengths. It is unclear to what extent other simulators also rely on that. Grella et al. [42] wrote: "Breakdown effects are taken into account by limiting the field in the sample" and Shadman and De [43] say about the same simulator: "Still, the amount of charge that these currents deposit can potentially raise the electric field in a dielectric to induce a current. Makeshift conductivity models have been implemented to address the resulting redistribution of the embedded charge." Even the Java source code of JMONSEL includes a breakdown model, which was the initial motivation to investigate this sort of model.

4.4. Results

4.4.1. Effect of new scattering models - no charge up scenarios

In Fig. 4.2, the scattering clouds of the electrons were shown. The different forms of clouds will not only make a difference in the charge distribution profile in the material but also on the emission, especially for topographic structures. Therefore, we first test the effect of the improvements independent of the charging models on a topographic surface.

We simulated 200-nm pitch patterns from RM 8820 samples, which were introduced by NIST as a test and calibration standard for scanning probe microscopy [44, 45]. They consist of amorphous silicon lines deposited on top of a silicon substrate. In Fig. 4.8, the cross-section view of the simulated lines is given.

The experimental results are obtained from a publication [46]. Fig. 4.9 shows a comparison of an experimental line scan with line scans simulated using the phenomenological models from the previous study and using the first principle models introduced in this study. It is assumed that the detection efficiency is best at the top of the silicon line. Hence, the signals were aligned such that the intensities there coincide. The agreement between the experiment and the first principle model simulation used in this study is better than the simulation of the previous study.

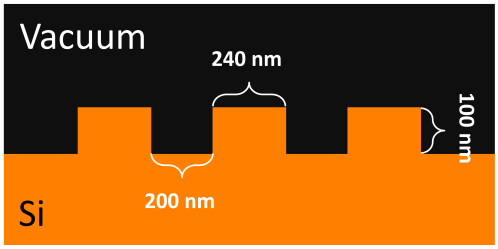


Figure 4.8: The cross-section view of an RM 8820 sample used to simulate. The line width is 240 nm and the height is 100 nm. The spacing is 200 nm.

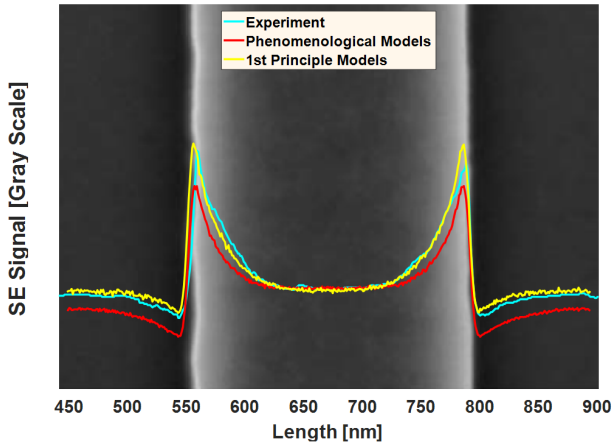


Figure 4.9: SE signal from a silicon line on top of a silicon surface, and an experimental line scan, a line scan simulated using our previous phenomenological models, and a line scan simulated with the present first principle models.

4.4.2. Effect of model improvements on SE emission

In theory, when the primary energy is in between the cross- over energies E_1 and E_2, as shown in Fig. 4.10, the total electron emission from the sample surface is more than the incident primary current ($I/I_p > 1$). Therefore, it is expected that a dielectric material gets positively charged. However, it is reported that the positive charging process is self-regulatory [3, 7, 47] due to the recollection of the electrons by the sample. Therefore, the total yield (SE + BSE) becomes ≈1.

The "nominal" SE yield, i.e., the yield ignoring all charging, from SiO_2 is ≈7 at 1 keV. In a more realistic scenario, when scanning the primary beam across the sample, the expectation is that the SE yield drops along the scan line due to the positive surface potential, i.e., a drop in the signal is observed. Therefore, we tested whether the simulator produces the described phenomenon.

The first two steps of a line scan on bulk material are shown in Fig. 4.11. The scan area is 100 nm and the pixel size is 2.5 nm. The beam energy and spot size are 1 keV and 3 nm (full width half maximum), respectively. The dose is 250 μC/cm^2 (100 electrons/pixel) and the electric field is updated for every pixel with the AMG solver. The beam current is 100 pA. The breakdown module is enabled with a threshold value of 50 MV/m [48].

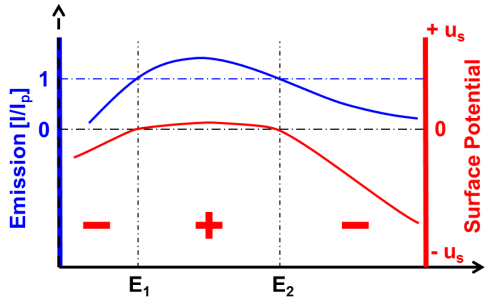


Figure 4.10: The surface potential of insulators during the charging process.

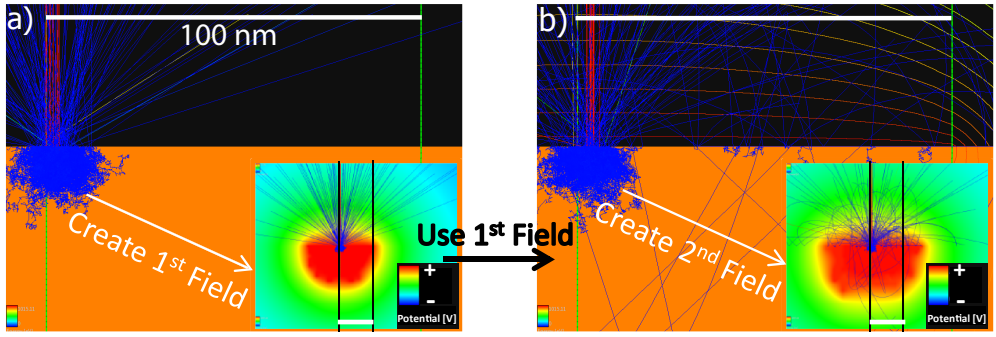


Figure 4.11: Charging simulation of a line scan: the initial two steps are depicted. At the beginning (a) big view, there is no field. Hence, the trajectories (red for high energy; blue for low energy electrons) are straight. After the scattering is completed, the electric field is calculated with the distributed charges in the material [the inset in (a), note that the scale is different from the big view image]. The simulator uses the computed e-field to trace the electrons at the next beam position. (b) Isolines indicate the presence of fields in big view. Similarly, the electric field is computed for the next beam in the line scan. As the SEs are recollected by the positive surface potential [the inset in (b)], the SE signal decreases. Scale bars are 100 nm, which indicate the scan area.

Until the first computation of the electric field, the SiO_2 sample stays neutral and all of the emitted electrons reach the detector above the sample (Fig. 4.11a). After the field is computed from the charge distribution obtained from the previous scattering events (inset Fig. 4.11a), electrons start to experience the positive potential at the surface and the electrons with energy less than the surface potential return to the sample (Fig. 4.11b), the inset shows the field and the returning electron trajectories]. It is observed that the (maximum) potential increases, 0 V, 3.47 V, 5.6 V, etc., for the first couple of pixels and then saturates around ≈11 V. The effect of the charging on the emission is shown in Fig. 4.12a.As expected, the total emission is high for the first couple of pixels, then decreases and saturates after ≈25 nm (10 pixels). Note that the frequency of the field update has an impact on the emission especially for the first couple of pixels. The sensitivity of the results will be discussed in Sec. 5. The stable BSE emission indicates that the surface potential stays rather small, affecting only the

low energetic SEs.

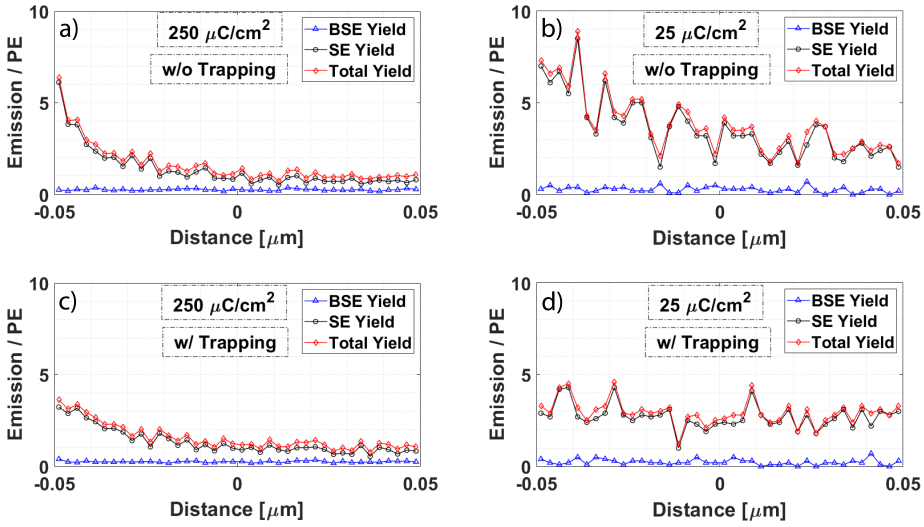


Figure 4.12: The effect of dose on electron emission: (a, c) the dose is 250 μC/cm^2; (b, d) the dose is 25 μC/cm^2. For (a) and (b), trapping cross-sections are not used; and for (c) and (d), trapping cross-sections are used. Beam energy is 1 keV.

When the dose is decreased to 25 μC/cm^2 (10 electrons/pixel), the number of created charge carriers per voxel is less. Therefore, the magnitude of the local field becomes smaller than at a higher dose and more electrons will reach the detector. In Fig. 4.12b, the corresponding signal drop saturates after about 100 nm, which causes a larger bright-to-dark transition area on the SEM image. The increased noise in the signal is due to shot noise, being larger for a lower amount of electrons in the probe. Similar behavior, but with smaller slopes, is observed when the trapping cross-sections are enabled. Fig. 4.12c and 4.12d show that in case the emission is not very high, the charging effect can be subtle.

The results show that the simulations are sensitive to parameters affecting the charge carrier density, such as the dose. This can lead to different results in measurements with dielectrics, where contrast is playing a role.

4.4.3. Effect of model improvements on the grating coupler simulations

In the previous study [20], the grating coupler is described in detail. In Fig. 4.13a, a top-down view of the device is shown. Fig. 4.13b shows a zoomed-in image of the second trench, and Fig. 4.13c shows the intensity profile across the middle of that trench. Note that the scan direction is from left-to- right (fast-scan axis) and top-to-bottom (slow-scan axis). The topographic contrast is visible on the surrounding

silicon structures and also on the oxide inside the trenches. In addition, there is an extra contrast in the trenches along the fast-scan direction, which is asymmetric in the intensity profile.

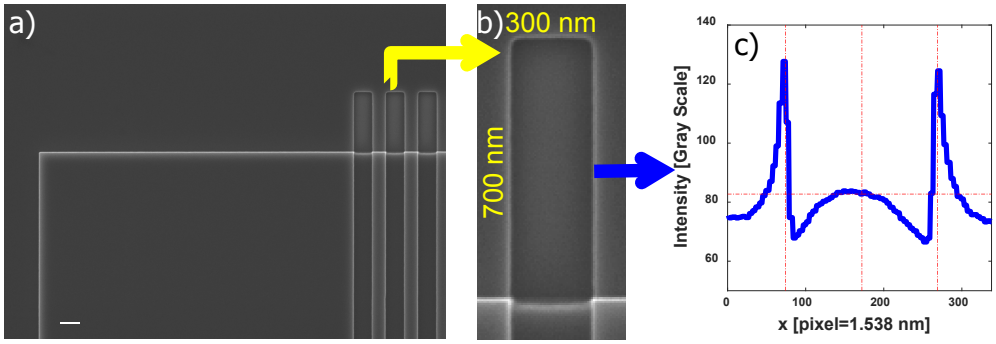


Figure 4.13: Experimental SEM image of a grating coupler is taken at 4 keV. (a) Top-down view of the vertical lines (scale bar: 300 nm), (b) zoomed-in view of the second trench (scale bar: 100 nm), and (c) SE signal profile of the middle image, integrated over 10 pixels along the y axis.

That is, the peak intensity along the x axis is positioned left from the center of the trench. This can be explained as follows. The electron probe visits the left side of the oxide in the trench first and creates a positive surface potential. As it visits the next pixels of the scanline, the surface potential slightly accumulates and causes a decreasing SE signal at those pixels. The phenomenon qualitatively agrees with the theory described in Sec. 4.2.

When simulating these trenches, including charging, a similar bright-to-dark contrast, as discussed above, is observed (see Fig. 4.14). It does show the asymmetry in the contrast across the trench, which could not be achieved in our previous work, but the asymmetry is much larger than observed in Fig. 4.13. We also clearly see the effect of EBIC in Fig. 4.14, the signal increasing toward the edges of the trenches. We then included trapping cross-sections, which leads to a lower nominal yield and thus a smaller positive surface potential. The results are shown in Fig. 4.15. When charging and trapping models are included, the asymmetry in contrast across the trench is clearly seen (the red dotted curve), compared to the case with trapping but without charging (the black solid curve). The positive surface potential due to the charging suppresses the emission from the middle of the trench toward the edge, where the EBIC effect comes into play. To quantify the asymmetric contrast in the simulated trench, the displacement of the maximum contrast in the trench from the middle of the trench is determined as 15 nm. This compares to the experimentally determined dis- placement, from Fig. 4.13c of 17 nm. And comparing the ratio of the areas under the SE signal profile left and right of the middle of the trench, in the experiment, a ratio of 1.17 is found, in the simulation with charging a value of 1.187, and in the simulation without charging a value of 1.05. The deviation from 1.00 is due to the noise. The areas were deter- mined with respect to the baseline connecting the lowest intensity

points at the edges of the trench. The agreement between experiment and simulation supports our reasoning above that the positive surface potential slowly builds up when scanning over a trench and it indicates that the experimental emission yield is slightly higher than unity at 4 keV, as was assumed in the simulations with scattering models and trapping. We have noticed that, close to the edges of the trench, there is no strong charging effect because of the EBIC effect, and this also agrees well with the experimental observations. The trapping cross-sections allowed us to tune the nominal yield such that it is more comparable to the one reported in Fig. 4.13 (page 36) by Schreiber and Fitting [31].

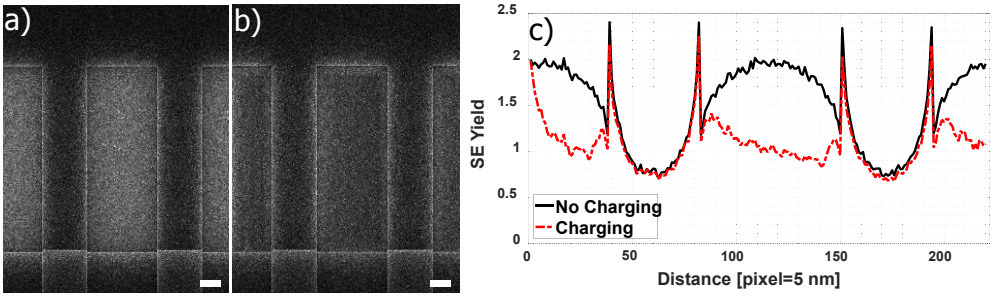


Figure 4.14: Trenches of the grating coupler simulated with first principle scattering models. (a) Image simulated without charging models; (b) image simulated with charging models; (c) SE signal profile of the panels (a) and (b) was integrated and averaged over 50 pixels along the y axis (between the dashed lines in a and b). The right y axis is for the surface potential value at the incident pixel after the interaction. Scale bars are 100 nm.

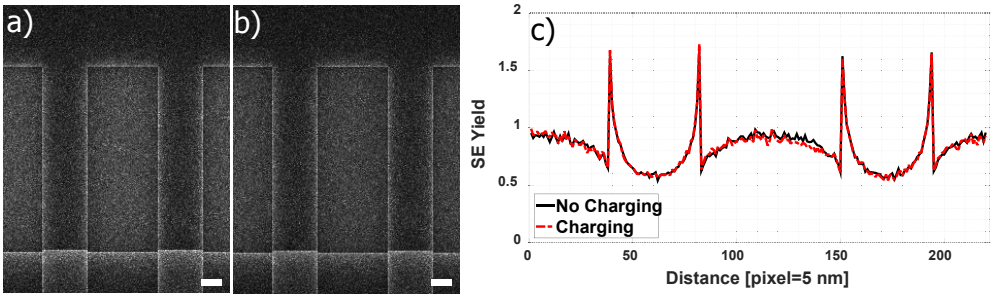


Figure 4.15: Simulated trenches of the grating couplers with first principle scattering models and a trapping model included. (a) Image simulated without charging models but with trapping; (b) image simulated with charging and trapping models; (c) SE signal profile of the figures (a) and (b), integrated and averaged over 50 pixels along the y axis [between the dashed lines in (a) and (b)]. The right y axis is for the surface potential value at the incident pixel after the interaction. Note the asymmetric signal (the red dashed curve) in the central trench and the signal suppression in the right half of the trench. Scale bars are 100 nm.

In this simulation, the region of interest is about ≈1.5 μC/cm^2 (1.1 μC/cm^2 × 1.5 μC/cm^2). The pixel size is 5 nm, and the charging dose is 25 μC/cm^2 (40 electrons/pixel). The simulation without charging took 30 min and 44 s on a 64-core work-

station. When the trapping cross-section is enabled, the simulation takes 13 min and 50 s. The simulations with charging took 5 h and 19 min and 4 h 20 min on a 32-core workstation without and with trapping, respectively, with Monte Carlo parallelization (32 threads) and parallelization of the field solver (4 threads).

4.4.4. Effect of the EBIC model

We now show the impact of the charge redistribution model on Cu pads embedded in a thin SiO_2 layer on top of a Si wafer. The pads 1, 2, and 4 are electrically floating (no contact to the underlying Si wafer), and pad number 3 is connected to the underlying Si wafer (see Fig. 4.16).

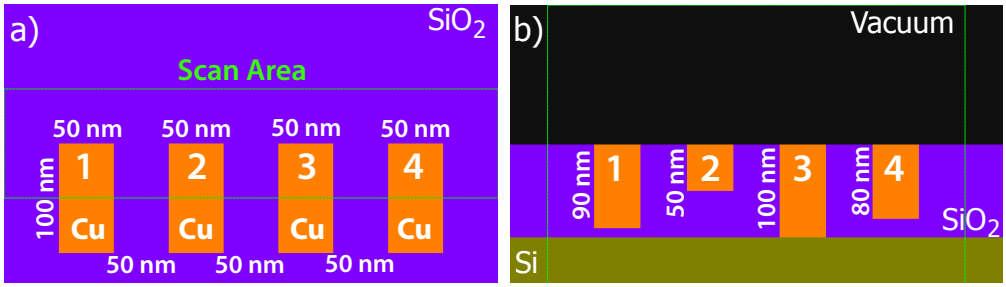


Figure 4.16: Sketch of the geometry of the four copper pads: (a) a topdown and (b) a cross-section view. The green lines correspond to the imaging area.

In Fig. 4.17, the effect on the simulated SEM images is shown when the charging model and/or EBIC model is switched on. When the charging model and the EBIC model are switched-off, the copper contacts appear darker in Fig. 4.1b due to their lower SE yield compared to SiO_2 at 0.75 keV (with 128 $\mu C/cm^2$ charging dose - 800 electrons per 10 nm × 10 nm pixel). Furthermore, the conductive pad (3) is indistinguishable from the others. When the charging model is switched on, but the EBIC and breakdown models are off, the emission of the oxide gets lower due to the positive, surface potential and the SE yield becomes comparable to that of the copper contacts (Fig. 4.17c). Note that the conductive pad appears different compared to the other pads because conductivity allows it to conduct charge carriers to ground. Switching on the EBIC model, however, leads to more realistic images of the contact pads and the surrounding insulating areas. When the EBIC and the breakdown models are switched-on, the oxide region surrounding the conductive pad experiences induced conductivity and charge carriers are conducted to ground and no charging occurs (Fig. 4.17d). As a result, the oxide shows the nominal SE yield and becomes brighter than other features.

Fig. 4.17e shows the line scan signals across the copper pads. The results in the main graph are simulated with trapping cross-sections and those in the inset without. In contrast to Sec. 4.3, the trapping has a minor influence on the results obtained with the charging models included. The reason is that the high dose that was applied

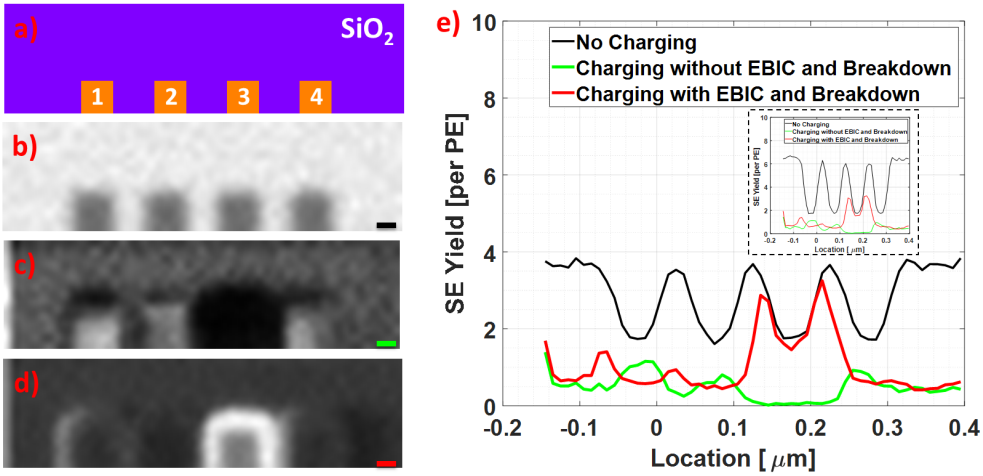


Figure 4.17: SEM image simulation of the buried copper pads in Fig. 16. (a) The schematic overview of the pads, (b) charging, EBIC, and breakdown models are switched-off; (c) charging is switched-on but EBIC and breakdown models are off, (d) charging, EBIC, and breakdown models are switched on. The intensity profiles in (e) are obtained at the position of the scale bars (25 nm) in the images (b), (c), and (d). The inset shows the same profiles but without trapping cross-sections. At 0.75 keV, positive charges on the surface retract secondary electrons and the signal intensity decreases. However, the electrically connected copper pad stays neutral, the surrounding area of the pad shows conduction due to EBIC, and the SE yield does not decrease that much (the red and black curves even partly overlap).

causes the positive surface potential to increase rapidly, right after the starting point of the exposure. This quickly lowers the SE yield to values below one, as is seen by the steep drop of the red and green curves on the left-hand side of Fig. 4.17e. For the remainder of the scan, the charge remains more or less in equilibrium.

Fig. 4.18 shows the surface potential of the sample for pixels, where the SE yields are given in Fig. 4.17e. The results are given with the same color code (see color online version). For the simulations where EBIC and breakdown models are off, the surface potential is mostly negative except at the copper pad number 3, because it is grounded.

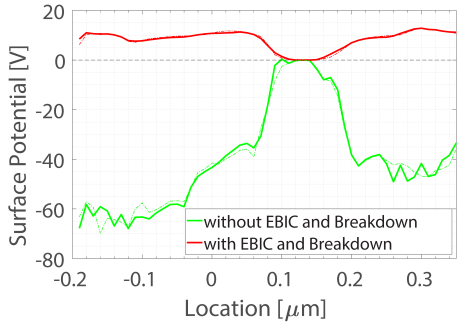


Figure 4.18: Surface potential at the pixels after the exposure, where the displayed yields in Fig. 17 are taken. The solid lines are without trapping cross-sections and the dotted lines are with trapping cross-sections.

4.5. Discussion

The frequency of the electric field update is a model parameter. Typically, these fields are updated after a particular number of primaries have completed their interaction with the sample, assuming that the charge accumulation is not significant. In some cases where the emission is very high, like in Fig. 4.12, the sample can stay uncharged for an unrealistically long time, which can cause an artifact on the emission yield in the first few pixels. However, once the e-field is updated as the simulation proceeds, the emission will be affected by the surrounding field, and the contribution of the current pixel decreases. Therefore, the approximation error will be only in the first few pixels, and the emission con- verges to its "true" value eventually.

The deposited energy per time was implemented as the energy deposited by the electrons during a single-time step of the implicit Euler scheme used to update the electric field and the charge distribution, divided by the duration of that time step. This works fine if there are sufficiently many electrons per time step (say > 100). However, Fig. 4.19 investigates the impact of the electric field update frequency and uses only 10 electrons per time step. For that investigation, we defined a timescale $\tau = \Delta t/3$ based on the time step Δt of the simulation with 100 electrons per time step.

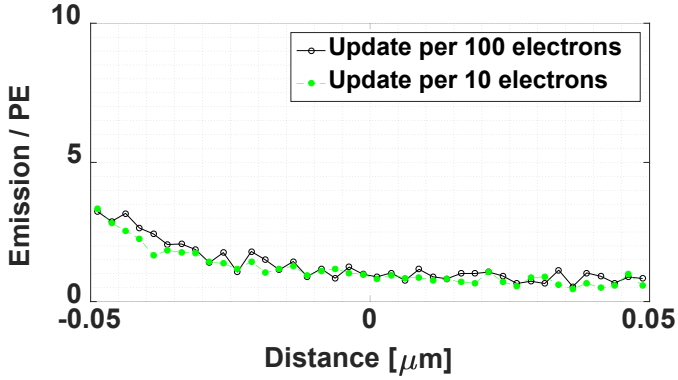


Figure 4.19: The effect of electric field update frequency on the results in Fig. 4.12c. The solid black line with circles shows when the electric field is updated per 100 electrons (= 1 time/pixel); the dashed green line with dots shows when the electric field is updated per 10 electrons (= 10 times/pixel).

The deposited energy $\Delta(r, t_{n-1})$ for a given time step is then computed as follows:

$$D(r, t_n) = (1 - C) * A(r, t_n) + C * D(r, t_{n-1}), \tag{4.12}$$

where the deposited energy from the previous time step is describes the energy deposited by the electrons during that added damped by the factor $C = exp(-\Delta t/\tau)$ and $A(r, t_n)$ describes the energy deposited by the electrons during that time step. We have $C = exp(-3) = 0.05$ for the simulations with 100 electrons, and $C = exp(-0.3) = 0.74$ for the simulation with 10 electrons.

Fig. 4.19 compares the SE emission of Fig. 4.12c to the case when the electric field is updated with 10 times the frequency. In the first few pixels, the SE yield is generally slightly lower, but the signal drop is still present.

The electron-matter scattering models, i.e., elastic and inelastic scattering, used in

this study are first principle models. Although they are based on established models, there are still model assumptions, especially at very low energies, which can lead to errors in SE emission. In addition, trapping and detrapping in insulators are well-known phenomena. Electrons and holes are trapped in defects, impurities, and dislocations. Electric fields and material heating can release the trapped electrons (detrapping) in case the added energy is greater than the trapping energy. Such kind of conduction mechanism is also known as Poole-Frenkel conduction [49]. To take that into account, many very low energy electrons should be traced to lower energies, even below the vacuum barrier height. The discrete modeling of these very low energy events would add a significant computational load since there is an excessive amount of electrons in this energy range. Furthermore, it is experimentally very hard to verify the cross-sections at very low energies. Although the first principle physics-based trapping/detrapping models will lead to a more accurate model, it is a very challenging task from many perspectives: physics, characterization of material at hand, and computationally.

As mentioned in Sec. 1, in our previous simulation work [20], we were not able to reproduce the smooth intensity drop seen in the experiments. There are two reasons for this: the lack of some essential model components and misinterpreting the experimental data. The latter was due to the tilt of the sample. The sharp signal drop on the oxide in Fig. 4.1a was first interpreted as a strong charging effect. However, we realized that the contrast change is mostly due to the sample tilt, the image being a combination of a complex topography and an asymmetric scattering cloud in the sample [50]. This sharp drop is not present in a common top-down image, as demonstrated in Figs. 4.13a and Fig. 4.13b. In this case, the charging effect appears subtly, which could be most dangerous, according to Postek et al. [3] because it could be easily overlooked by a microscopist. After adding the missing model components, this phenomenon was reproduced, as demonstrated in Sec. 4.3. The line scans over an insulator in Sec. 4.2 are preliminary tests of the signal drop, which qualitatively agree with the (spot mode simulation) results in Fig. 4.4 of Ohya et al. [36]., and Fig. 4.4 of Ref. [10]. However, experimental evidence is still missing for this case. An experimental dataset, as explained in Sec. 4.2, can be very useful to judge the effects of the models. This experiment can even be simplified to spot mode acquisition. Another related issue is the SE yield (curve) of SiO_2, which is dependent on current and time. Previously, Belhaj et al. [51]. have conducted yield measurements on alumina (Al_2O_3). A similar study for SiO_2 is required to verify SE yields and the models.

In Sec. 4.4, the effect of the models was demonstrated in a setup, typical for voltage contrast imaging in electron beam testing technology. In the simulations, the effect of the EBIC model is observed as brightening of electrically conductive parts and its surrounding oxide (Fig. 4.17d). Thong reported in Fig. 2.74 the brightening of passivation and oxide layers when the beam reaches a base-collector junction at higher energies [52]. Similarly, Leamy reported in Fig. 23 that the imaged surface brightens due to the EBIC effect, revealing the location of a buried junction [53].

Besides, conducting a similar experiment can reveal the extent of EBIC effect more quantitatively.

Moreover, the beam deflection due to induced-charging has been studied [54] at 50 keV with the models explained in this work. Simulation results agree with experimental results qualitatively for most of the experiments, quantitatively in some cases.

In the simulations, Monte-Carlo calculations are fully scalable, meaning that using more cores would make the calculations faster. At present, the electric field calculations are parallelized on four CPU cores. In principle, the field solution can be parallelized with a higher number of cores, but, in practice, we did not achieve a higher gain because of the increasing communication cost. In a benchmarking test, we found that the open-source multigrid solvers in PETSc (i.e., BoomerAMG and GAMG) are scalable up to 16 threads and giving a factor of 2 to 3 speed-up for our test matrices [55].

Using a more efficient grid (e.g., a triangular mesh) can speed up the calculations extra because the problem size will be much smaller (factor of 10). However, the speed-up is expected to be only a factor of 2 to 3 due to the increasing complexity of the solution in the multigrid regime.

4.6. Conclusions

Model improvements for Monte Carlo simulations were presented. These improvements include both low energy electron scattering models and the charging of dielectrics. First of all, we have included first principle scattering models to simulate electron-matter interactions in order to predict charge distributions in the material more precisely. The latter involves models that couple dynamically with the charge distribution, such as calculation of local fields, tracing of the electrons in the field, and redistribution of the charges in the materials. For instance, the redistribution models, EBIC and dielectric breakdown, help to include induced conductivity in dielectric materials.

We have shown that including first principle scattering models, especially electron-phonon scattering leads to a more realistic charge distribution inside the material. Although the generation and tracing of every electron in the field increase the computation time significantly, we tried to avoid simplifications/optimization of the scattering models. However, for the fine adjustment of the yield, we have used empirically modeled trapping cross-sections.

In an earlier study, the charge mobility was not allowed in the dielectrics. This was causing accumulation of unrealistically big potentials, causing beam deflections. Introducing redistribution of the charges helped to solve these artifacts. The models incorporate tracing of all the electrons with a higher accuracy in the electric field, enabling us to reproduce contrast changes due to the surface potential. This results in better yields and more realistic energy analysis of the emitted electrons.

In addition, the EBIC model allowed simulation of induced conductivity effects, where the presence of the beam increases the conductivity of the dielectric material, creating a conductive channel to neighboring conductive materials at ground potential.

Future steps will include a more effective meshing technique to reduce the problem size to speed up the simulations. Improvements in the modeling can be considered by including surface plasmons and a physics-motived trapping and detrapping model. To quantify the effects and error bars, a proper parameter and model sensitivity analysis as well as good experimental results is needed.

Acknowledgements

We would like to thank Dr. Jens Bolten for his assistance and for providing experimental results. K.T.A. would like to express his sincere thanks to Dr. Thomas Verduin, Annemarie Theulings, and Luc van Kessel for fruitful discussions on the physics of the electron-matter interactions. T.K. is grateful to Dr. John Villarrubia for providing the source code of JMONSEL, which provoked the idea of the dielectric break- down model. We also would like to thank Dr. Robert Polster for pointing out the role of charge imbalance to explain conductivity near the surface. We gratefully acknowledge GenISys-GmbH and RAITH B.V. for funding this research project. An earlier version of the work has been partially published in a SPIE Proceedings paper titled "Model improvements to simulate charging in SEM," https://doi.org/10.1117/12.2297478.

References

[1] M. Kotera and H. Suga, *A simulation of keV electron scatterings in a charged□up specimen,* Journal of Applied Physics **63**, 261 (1988).

[2] A. Seeger, A. Duci, and H. Haussecker, *Scanning electron microscope charging effect model for chromium/quartz photolithography masks,* Scanning **28**, 179 (2006).

[3] M. T. Postek and A. E. Vladár, *Does your SEM really tell the truth? How would you know? Part 4: Charging and its mitigation,* in *Proc. SPIE 9636*, Vol. 963605 (2015) pp. 1–12.

[4] T. Ichinokawa, M. Iiyama, A. Onoguchi, and T. Kobayashi, *Charging effect of specimen in scanning electron microscopy,* Japanese Journal of Applied Physics **13**, 1272 (1974).

[5] N. Okai and Y. Sohda, *Study on Image Drift Induced by Charging during Observation by Scanning Electron Microscope,* Japanese Journal of Applied Physics **51**, 1 (2012).

[6] J. Cazaux, *On some contrast reversals in SEM: Application to metal/insulator systems,* Ultramicroscopy **108**, 1645 (2008).

[7] L. Reimer, *Scaning Electron Microscopy*, 2nd ed., Vol. 45 (Springer, Heidelberg, 1998).

[8] J. Orloff, ed., *Handbook of Charged Particle Optics*, 2nd ed. (CRC Press, 2009) pp. 1–688.

[9] M. P. Davidson and N. T. Sullivan, *Investigation of the effects of charging in SEM-based CD metrology,* in *Proc. SPIE*, Vol. 3050 (1997) pp. 226–242.

[10] H. Abe, S. Babin, S. Borisov, A. Hamaguchi, M. Kadowaki, Y. Miyano, and Y. Yamazaki, *Contrast reversal effect in scanning electron microscopy due to charging,* Journal of Vacuum Science & Technology B: Microelectronics and Nanometer Structures **27**, 1039 (2009).

[11] Y. G. Li, P. Zhang, and Z. J. Ding, *Monte Carlo Simulation of CD-SEM Images for Linewidth and Critical Dimension Metrology,* Scanning **35**, 127 (2013).

[12] J. Ganachaud and A. Mokrani, *Theoretical study of the secondary electron emission of insulating targets,* Surface Science **334**, 329 (1995).

[13] H.-J. Fitting and M. Touzin, *Secondary electron emission and self-consistent charge transport in semi-insulating samples,* Journal of Applied Physics **110**, 1 (2011).

[14] M. Cao, F. Wang, J. Liu, and H.-B. Zhang, *Charging dynamics of a polymer due to electron irradiation: A simultaneous scattering-transport model and preliminary results,* Chinese Physics B **21**, 127901 (2012).

[15] L. Grella, G. Lorusso, T. Niemi, and D. L. Adler, *Simulations of SEM imaging and charging,* Nuclear Instruments and Methods in Physics Research Section A: Accelerators, Spectrometers, Detectors and Associated Equipment **519**, 242 (2004).

[16] S. Babin, S. Borisov, A. Ivanchikov, and I. Ruzavin, *CHARIOT: Software tool for modeling SEM signal and e-beam lithography,* Physics Procedia **1**, 305 (2008).

[17] K. Ohya and H. Kuwada, *Modeling of Electron Beam Charging of an Insulating Layer on a Silicon Substrate,* e-Journal of Surface Science and Nanotechnology **9**, 112 (2011).

[18] E. Ilgüsatiroglu, A. Y. Illarionov, M. Ciappa, P. Pfäffli, and L. Bomholt, *New integrated Monte Carlo code for the simulation of high-resolution scanning electron microscopy images for metrology in microlithography,* in *Proc SPIEs*, Vol. 9050, edited by J. P. Cain and M. I. Sanchez (2014) pp. 1–12.

[19] J. Villarrubia, A. Vladár, B. Ming, R. Kline, D. Sunday, J. Chawla, and S. List, *Scanning electron microscope measurement of width and shape of 10 nm patterned lines using a JMONSEL-modeled library,* Ultramicroscopy **154**, 15 (2015).

[20] K. T. Arat, J. Bolten, T. Klimpel, and N. Unal, *Electric fields in Scanning Electron Microscopy simulations,* in *Proc SPIE*, Vol. 9778, edited by M. I. Sanchez and V. A. Ukraintsev (2016) p. 97780C.

[21] M. Kotera, K. Yamaguchi, and H. Suga, *Dynamic Simulation of Electron-Beam-Induced Charging up of Insulators,* Japanese Journal of Applied Physics, Part 1: Regular Papers and Short Notes and Review Papers **38**, 7176 (1999).

[22] F. Salvat, A. Jablonski, and C. J. Powell, *ELSEPA—Dirac partial-wave calculation of elastic scattering of electrons and positrons by atoms, positive ions and molecules,* Computer Physics Communications **165**, 157 (2005).

[23] E. Kieft and E. Bosch, *Refinement of Monte Carlo simulations of electron–specimen interaction in low-voltage SEM,* Journal of Physics D: Applied Physics **41**, 215310 (2008).

[24] T. Verduin, *Quantum Noise Effects in e-Beam Lithography and Metrology*, Ph.D. thesis, Delft University of Technology (2017).

[25] M. Winter, *WebElements,* .

[26] M. N. Gray Theodore, Whitby Max, *Periodictable.com,* .

[27] W. M. Haynes, *CRC handbook of chemistry and physics : a ready-reference book of chemical and physical data* (CRC Press, Boca Raton, FL., 2011).

[28] S. O. Kasap, *Principles of electronic materials and devices. TT* -, 2nd ed. (McGraw-Hill„ Boston :, 2002).

[29] J.-C. Kuhr and H.-J. Fitting, *Monte-Carlo Simulation of Low Energy Electron Scattering in Solids,* Physica Status Solidi (a) **172**, 433 (1999).

[30] Bart J. Van Zeghbroeck, *Effective mass in semiconductors,* (1997).

[31] E. Schreiber and H.-J. Fitting, *Monte Carlo simulation of secondary electron emission from the insulator SiO2,* Journal of Electron Spectroscopy and Related Phenomena **124**, 25 (2002).

[32] O. Madelung, U. Rössler, and M. Schulz, *Silicon (Si), sound velocities: Datasheet from Landolt-Börnstein - Group III Condensed Matter · Volume 41A1β : "Group IV Elements, IV-IV and III-V Compounds. Part b - Electronic, Transport, Optical and Other Properties" in SpringerMaterials (http://dx.doi.* ().

[33] O. Madelung, U. Rössler, and M. Schulz, *Silicon (Si), deformation potentials: Datasheet from Landolt-Börnstein - Group III Condensed Matter · Volume 41A1β : "Group IV Elements, IV-IV and III-V Compounds. Part b - Electronic, Transport, Optical and Other Properties" in SpringerMaterials (http://d,* ().

[34] D. C. Joy and S. Luo, *An Empirical Stopping Power Relationship for Low-Energy Electrons,* Scanning **11**, 176 (1989).

[35] J. Ashley, *Interaction of low-energy electrons with condensed matter: stopping powers and inelastic mean free paths from optical data,* Journal of Electron Spectroscopy and Related Phenomena **46**, 199 (1988).

[36] K. Ohya, K. Inai, H. Kuwada, T. Hayashi, and M. Saito, *Dynamic simulation of secondary electron emission and charging up of an insulating material,* Surface and Coatings Technology **202**, 5310 (2008).

[37] M. Dapor, *Monte Carlo Simulation of Secondary Electron Emission from Dielectric Targets,* Journal of Physics: Conference Series **402**, 012003 (2012).

[38] T. Kaneko, *Energy distribution of secondary electrons emitted from solid surfaces under electron bombardment I. Theory,* Surface Science **237**, 327 (1990).

[39] R. Kyng and S. Sachdeva, *Approximate Gaussian Elimination for Laplacians - Fast, Sparse, and Simple,* in *IEEE 57th Annual Symposium on Foundations of Computer Science (FOCS)*, Vol. 2016-Decem (IEEE, 2016) pp. 573–582, arXiv:1605.02353 .

[40] Y. Notay and P. S. Vassilevski, *Recursive Krylov-based multigrid cycles,* Numerical Linear Algebra with Applications **15**, 473 (2008), arXiv:arXiv:1112.5346v3 .

[41] N. Tanaka, Ryuichi; Sunaga Hiromi; Tamura, *The Effect of Accumulated Charge on Depth Dose Profile in Poly(Methylmethacrylate) Irradiated with Fast Electron Beam,* IEEE Transactions on Nuclear Science **NS-26**, 4670 (1979).

[42] L. Grella, G. Lorusso, and D. L. Adler, *Simulations of Scanning Electron Microscopy Imaging and Charging of Insulating Structures,* Scanning **25**, 300 (2003).

[43] K. Shadman and I. De, *Analytic models for the kinetics of generating a voltage contrast signal from contact plugs used in integrated circuits,* Journal of Applied Physics **101**, 064913 (2007).

[44] R. L. Postek, Michael T.; Watters, *Report of Investigation: Reference Material 8820 Scanning Electron Microscope Scale Calibration Artifact*, Tech. Rep. July (Gaithersburg, 2009).

[45] M. T. Postek, A. E. Vladar, W. Keery, M. Bishop, B. Bunday, and J. Allgair, *Reference material (RM) 8820: a versatile new NIST standard for nanometrology,* in *Proc SPIE*, Vol. 7638, edited by C. J. Raymond (2010) p. 76381B.

[46] M. T. Postek, A. E. Vladár, J. S. Villarrubia, and A. Muto, *Comparison of Electron Imaging Modes for Dimensional Measurements in the Scanning Electron Microscope,* Microscopy and Microanalysis **22**, 768 (2016).

[47] D. C. Joy and C. S. Joy, *Dynamic Charging in the Low Voltage SEM,* Microscopy and Microanalysis **1**, 109 (1995).

[48] D. R. Lide, ed., *CRC Handbook of Chemistry and Physics*, internet v ed. (CRC Press, Boca Raton, FL., 2005) pp. 1–2661.

[49] N. Cornet, D. Goeuriot, C. Guerret-Piécourt, D. Juvé, D. Tréheux, M. Touzin, and H.-J. Fitting, *Electron beam charging of insulators with surface layer and leakage currents,* Journal of Applied Physics **103**, 064110 (2008).

[50] K. T. Arat, A. C. Zonnevylle, W. S. M. M. Ketelaars, N. Belic, U. Hofmann, and C. W. Hagen, *Electron beam lithography on curved or tilted surfaces: Simulations and experiments,* Journal of Vacuum Science & Technology B **37**, 051604 (2019).

[51] M. Belhaj, T. Tondu, and V. Inguimbert, *Effect of the incident electron fluence on the electron emission yield of polycrystalline Al2O3,* Applied Surface Science **257**, 4593 (2011).

[52] J. T. L. Thong, ed., *Microdevices Physics and Fabrication Techniques* (Plenum Press, New York, 1993) pp. 1–462.

[53] H. J. Leamy, *Charge collection scanning electron microscopy,* Journal of Applied Physics **53** (1982), 10.1063/1.331667, arXiv:arXiv:1011.1669v3 .

[54] K. T. Arat, T. Klimpel, A. C. Zonnevylle, W. S. M. M. Ketelaars, C. T. H. Heerkens, and C. W. Hagen, *Charge-induced pattern displacement in E-beam lithography,* Journal of Vacuum Science & Technology B **37**, 051603 (2019).

[55] S. Balay, S. Abhyankar, M. Adams, J. Brown, P. Brune, K. Buschelman, L. Dalcin, A. Dener, V. Eijkhout, W. Gropp, D. Karpeyev, D. Kaushik, K. Matthew, D. May, L. McInnes, R. Mills, T. Munson, K. Rupp, S. Patrick, B. Smith, Z. Stefano, H. Zhang, and Z. Hong, *PETSc Web page,* (2019).

5

Charge-Induced Pattern Displacement in E-Beam Lithography

Electron beam lithography (EBL) requires conducting substrates to ensure pattern fidelity. However, there is an increasing interest in performing EBL on less well-conducting surfaces or even insulators, usually resulting in seriously distorted pattern formation. To understand the underlying charging phenomena, the authors use Monte Carlo simulations that include models for substrate charging, electron beam-induced current, and electric breakdown. Simulations of electron beam exposure of glass wafers are presented, exposing regular patterns which become distorted due to charge-induced beam deflection. The resulting displacements within the patterns are mapped and compared to experimental displacement maps obtained from patterns in PMMA resist on glass substrates. Displacements up to several hundreds of nanometers were observed at a primary beam energy of 50 keV. Also, various scan strategies were used to write the patterns, in the simulations as well as the experiments, revealing their strong effect on pattern distortion, in shape and in magnitude. A qualitative, in some cases even quantitative, good agreement was found between the simulations and the experiments, providing enough confidence in Monte Carlo simulations to predict charge-induced pattern displacement and shape distortion and to find smart scan strategies to minimize the effects of charging.

This chapter is published as a journal paper:
Kerim T. Arat, Thomas Klimpel, Aernout C. Zonnevylle, Wilhelmus S. M. M. Ketelaars, Carel Th. H. Heerkens, Cornelis W. Hagen: Charge-induced pattern displacement in E-beam lithography. *Journal of Vacuum Science & Technology B* 09/2019; 37(5):051603, DOI:10.1116/1.5120631

5.1. Introduction

Electron beam lithography (EBL) is used for the production of a wide range of applications such as the production of superconducting nanowires [1] and quantum dots [2] because it combines very high resolution and flexible patterning capabilities [3–5]. However, when the sample is not sufficiently conducting, charging-related differences occur on the designed pattern [6]. One of these differences is due to the unintended deflection of the primary beam, which causes pattern distortion [7]. The literature discusses a few techniques to solve this problem: adding a charge dissipation layer [8, 9], using a conductive polymer [10, 11], using variable pressure conditions [12], or utilizing the critical energy [13]. So far, these techniques were not well adopted by the semiconductor industry, except the first one because of its practicality and low cost. However, using a coating layer introduces extra process complexity [14], a loss of resolution due to the increased electron scattering volume, and it does not solve the issue entirely, especially for thick resists [15].

In addition to the methods mentioned above, some authors investigated the effect of the scan (writing) strategy [16] on the charging effect. However, this is quite demanding experimental work because finding the right strategy is based on a trial and error method and restricted to the specific application. In the literature, modeling studies using Monte Carlo simulations are reported, which are aimed at providing a general solution for a given layout prior to the experimental fabrication [17–20]. However, these studies are either based on empirical electron-matter scattering models or do not take charge redistribution into account. The goal of this work is to use a Monte Carlo simulator that simulates charging by including first principle scattering models, electric fields, and charge redistribution models [21]. Specific test patterns were defined in PMMA resist on glass wafers. The same patterns were also obtained simulating electron beam exposure of a glass wafer and then compared to the experimentally obtained patterns. Furthermore, the influence of different writing strategies on the patterns was investigated.

5.2. Modeling

5.2.1. Monte Carlo simulator

In this study, we have used a Monte Carlo simulator, *virtualSEM*, to simulate the charge-induced effects on the primary electron beam. The first version of the simulator [22] included semiempirical scattering models and electric fields. Later, first principle scattering models and charge redistribution models were included in the simulator [21].

For modeling of the inelastic scattering, there are two choices in the simulation: (i) the dielectric function theory (DFT) which is a first principle model [23, 24] and (ii) the continuous slowing down approximation (CSDA) which is a semiempirical model [22, 25]. Although the first principle modeling is a rigorous approach, it comes at a price when considering the simulation speed. In this work, initially, we used the DFT

model for some of the simulated patterns studied to understand the effects of the charging. Later, we preferred to use the CSDA model for all simulations to reduce the simulation time. We will address the validity of this approach in subsection 5.2.3.

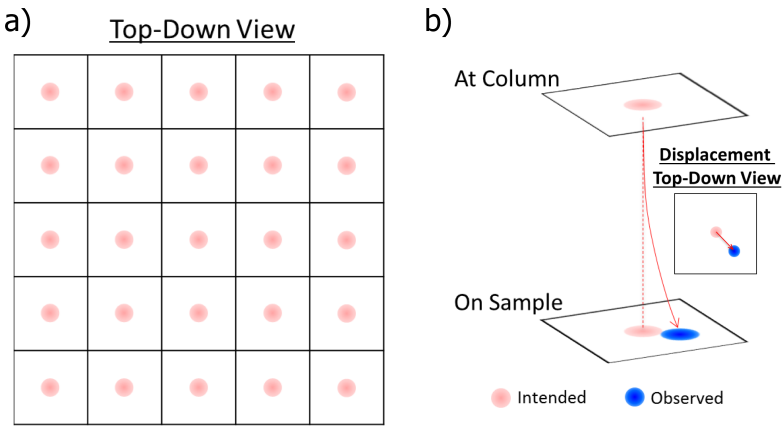


Figure 5.1: Test pattern. (a) A schematic drawing of the exposed dot array (5 × 5) is shown in a top-down view. The light gray dots (red dots in the color version) are the intended points of exposure. (b) The intended and deflected trajectory of the primary electron beam is presented. On the right-hand side, a top-down view of the dot displacement is shown.

5.2.2. Test pattern: Dot matrix

Here, we focus on the deflection of the primary electrons in vacuum due to substrate charging [7, 26] in high energy EBL. The test pattern we chose consists of a square array of dots such that the effect of the deflection can be easily determined by measuring the displacement of the dots with respect to their position in the design (see Fig. 5.1). Here, each dot represents the result of a single point exposure of the glass wafer by a high energy electron beam.

The array of dots can be written using various writing orders. To investigate the effect of scan strategy on the charge patterns, we have applied four different strategies, as shown in Fig. 5.2.

The pattern dimensions are 4.5 × 4.5 μm^2 (in x and y directions), which corresponds to the subfield size of the e-beam tool used in the experiments. Furthermore, all patterns were written for two different pitches, or dot spacings: 500 nm (9 × 9 dots) and 250 nm (17 × 17 dots).

5.2.3. Simulations

To obtain experimentally measurable displacements, we have used a 50 keV electron beam instead of 100 keV, as the 50 keV beam is more sensitive to electrostatic fields (E-fields). A range of exposure doses was simulated up to 250 $\mu C/cm^2$. To exaggerate the effect of the charging, we used exposure doses higher than usual [16].

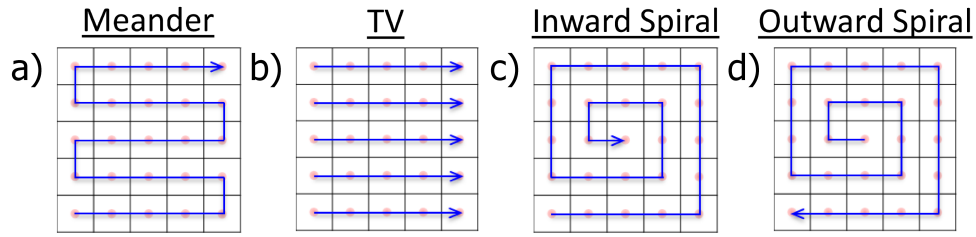


Figure 5.2: Four scan strategies (a) *Meander*, (b) *TV* (Raster), (c) *Inward Spiral*, and (d) *Outward Spiral* are shown from left to right. The dots are exposed in the order indicated by the blue arrows starting from the bottom left and ending top right except for the *Outward Spiral* mode, which starts in the middle and ends at the bottom left.

As a sample for the simulations, we chose to use glass, i.e., SiO_2, without a resist layer. At 50 keV, the penetration depth of the beam electrons is in the order of micrometers [27], which means that most of them end up in the substrate. Therefore, we assumed that most of the displacement is due to the substrate charging [7, 28], neglecting charging of a resist layer.

In Fig. 5.3, the displacement map is shown for the *Meander* mode, at 128 μC/cm^2 and at 250 nm pitch (17 × 17 dots). The design layout of exposure points is shown as a regular grid of circles (the blue circles in the color version) and the actual landing positions as a nonregular grid of circles (the red circles in the color version). The arrows indicate the displacement direction, and their size and color correspond to the magnitude of the displacement. The background color has a similar function for better visualization. The writing starts from the bottom left in the *Meander* mode (see Fig. 5.2). The displacement is very low in the beginning since the number of trapped charges is still low enough to not influence the beam trajectory. The size of the displacement increases as the beam continues to charge the sample toward the top of the array. The displacement is maximum at the top corners because the amount of deposited charge on the outside of the corners is much smaller than on the inside of the corners, creating stronger E-fields in the diagonal directions.

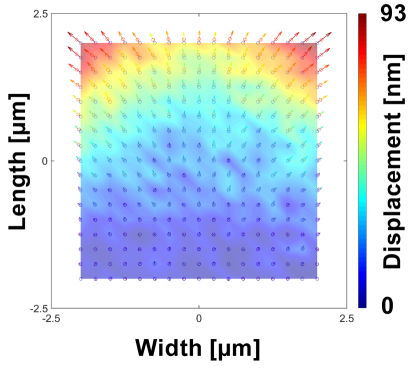


Figure 5.3: Displacement map of the *Meander* mode. The maximum displacement is 93 nm at 128 μC/cm^2 and at a pitch of 250 nm (17 × 17 dots).

The displacement maps of all four scanning modes are compared in Fig. 5.4. The maximum displacement is 93 nm for *Meander*, 93 nm for *TV*, 105 nm for *Outward Spiral*, and 40 nm for *Inward Spiral*. In Fig. 5.4, below the maps, cartoons are drawn indicating the deformation of the square arrays due to charging. Depending on the application, it can be crucial where the main displacements occur within the pattern. For instance, if a square structure is desired, then the *Inward Spiral* mode provides the best match because all displacements occur inside the pattern as depicted by Fig. 5.4, leaving the edges of the pattern unaltered.

Figure 5.4 shows that the scan mode has a significant impact on the landing positions. In the *Meander* and *TV* modes, the bottom of the pattern was exposed first, and the trapped charges repel the beam, away from the exposed area, such that the displacement vectors point in the direction away from the center of the already written area. In *Outward Spiral* mode, the charges are trapped mostly in the center of the pattern from the beginning of the exposure. This repels the beam away from the center in all directions, depending on the location of the point of exposure.

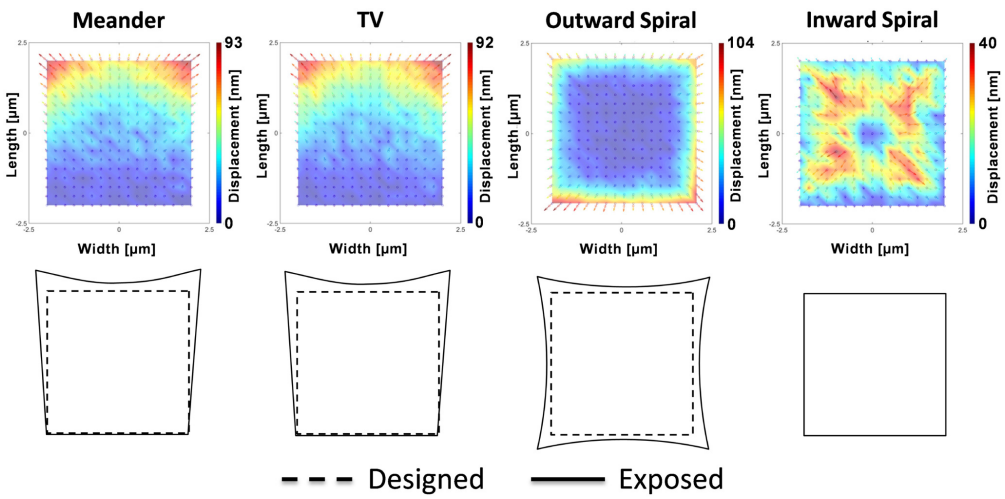


Figure 5.4: Displacement effect on the borders of the patterns.

In *Inward Spiral* mode, the beam exposes the borders first starting at the bottom left corner. During this first pass, the amount of trapped charge is not enough to significantly deflect the beam. The amount of trapped charge increases when the beam exposes a new spot, but it exposes another point soon after that, on the opposite side of the pattern, minimizing the lateral component of the electrostatic field. For example, there are undisplaced exposures in the middle of the pattern since the electrostatic fields around these points cancel each other in the x and y directions.

As the charge accumulates, the resulting field will not only deflect the electron beam in x and y directions but also influence the electrons in the z direction, in other words, affect the landing energy of the beam. In Fig. 5.5, the simulated surface

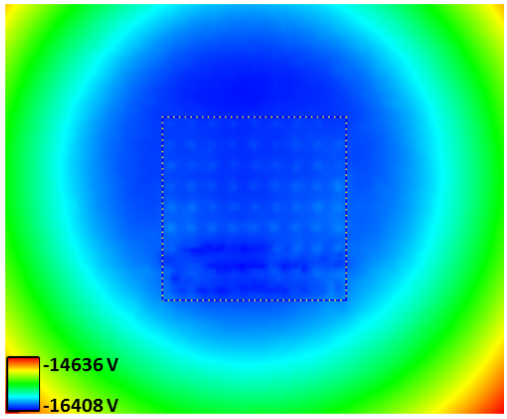


Figure 5.5: Surface potential at the end of the array exposure, in *Meander mode* for 128 μC/cm^2 and a pitch of 500 nm (9 × 9 dots). The color bar shows the maximum (-14636 V) and minimum (-16408 V) values of the potential at the surface. The field of view is 10 × 10 μm^2, and the dashed square (4.5 × 4.5 μm^2) indicates the exposure area.

potential at the end of the array exposure is shown. The potential takes values as high as -16 kV, and the surface potential acts as a deceleration field. That means the landing energy of the 50 keV beam drops to 34 keV toward the end of the array exposure, thereby enlarging the deflection of the beam in the x and y directions, as slower electrons are deflected more.

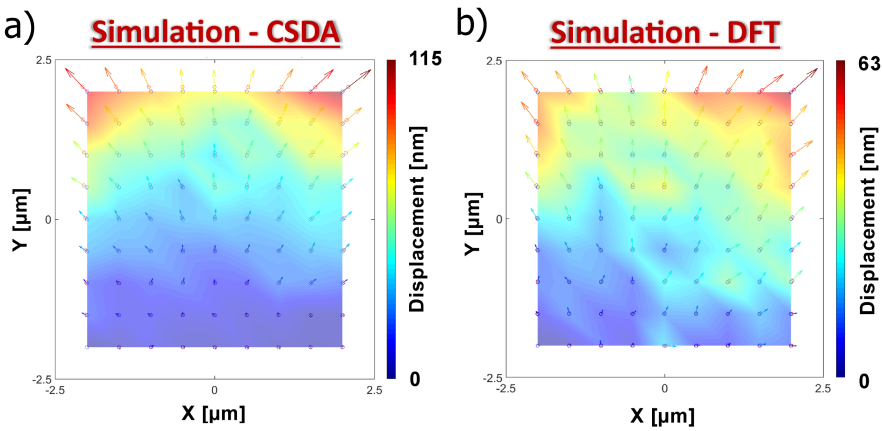


Figure 5.6: Sensitivity of the displacement maps to the choice of inelastic scattering model at 128 μC/cm^2 for the *Meander* mode: (a) CSDA vs (b) DFT.

This decrease in landing energy has another important effect on the exposure. At lower energy, the primary beam shows more beam broadening [29, 30]. Furthermore, the electrons penetrate less, so their scattering volume is closer to the surface, resulting in a larger intersection of the scattering volume and the substrate surface. As a result of this, we see that the center of the negative potential area in Fig. 5.5 is located above the center of the exposure area. Also, it is expected that the dots in the upper rows of the array have a larger size than those in the lower rows. We will verify this experimentally.

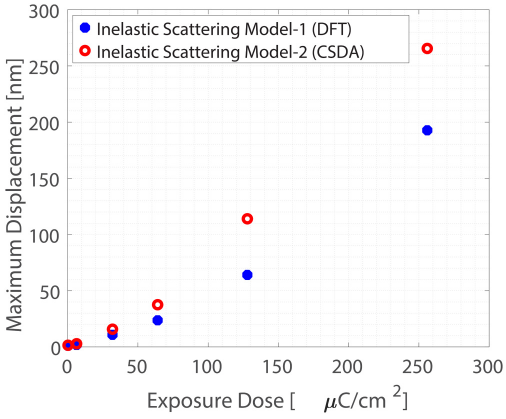


Figure 5.7: Sensitivity of the displacement to the choice of the inelastic scattering model. The maximum displacement vs exposure dose in *Meander* mode shows a factor of two difference for 9 × 9 arrays.

As promised above, we now address how the simulation results shown are influenced by the particular choice of an inelastic model used in the simulator: model (1) the CSDA and model (2) the DFT.

The two different models resulted in qualitatively very similar displacement maps independent of dose, except for the magnitude of the displacement, which does depend on the dose (see Fig. 5.6). The effect of statistical (shot) noise was also observed in Fig. 5.6b, which leads a slightly different symmetry between Figs. 5.6a and 5.6b. Figure 5.7 shows that the CSDA model results in a displacement twice as big as that of the DFT model for *Meander* mode.

It is worth noting that the displacement map is independent of the dose in the simulations unless dielectric breakdown occurs. The exposure dose changes the magnitude only.

5.3. Experiment

To experimentally verify the simulation results, glass wafers were (i) coated with resist, (ii) exposed, (iii) developed, and (iv) inspected.

5.3.1. Fabrication of the patterns

A 200 µm (±20µm) thick insulating SiO_2 wafer (2 × 2 cm^2) was spin-coated with 950k-PMMA resist. The expected resist thickness is 200 nm. After spin-coating, the sample was baked at 175 °C for 30 min. Also, a conducting reference sample was produced using a standard (525 ± 20 µm thick) silicon wafer (2 × 2 cm^2). The samples were exposed with a RAITH EPBG-5200 tool. The beam energy was 50 keV, and the beam current was 0.5 nA. The location of each dot array was reached by stage movement, to be able to write the array in the center of the so-called main field, thereby minimizing the aberrations of the main field deflectors.

After the exposure, the samples were developed in a 1:3 methyl-isobutyl ketone:isopropanol (MIBK:IPA) for 60 s, rinsed in IPA for 60 s and dried with dry nitrogen gas.

After development, the samples were sputter coated with molybdenum (Mo) for 8 s, corresponding to a layer thickness of ~4 nm. The conductive coating serves to eliminate possible charging effects during the subsequent inspection by scanning electron microscopy (SEM).

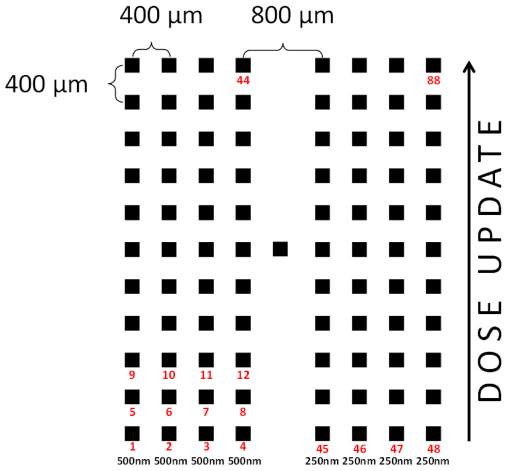


Figure 5.8: Layout of a main block consisting of dot arrays (indicated by the black squares) and a central marker. The arrays in the left four columns contain dots at a 500 nm pitch and in the right four columns at a 250 nm pitch. Moving upward along the rows, the dose increases by a factor of 1.2. The writing order of the arrays is indicated by the red numbers below the arrays.

5.3.2. Exposure layout

The sample layout consists of four main blocks, one for each scan strategy. Each main block, shown in Fig. 5.8, consists of 44 arrays of 9 × 9 dots, 44 arrays of 17 × 17 dots, markers, and labels.

In a main block, the arrays of 9 × 9 dots, with the dots at a 500 nm pitch, were written first. The exposure starts from the bottom left array. The writing order is indicated by the red numbers below the arrays in Fig. 5.8. In each horizontal row, four arrays are written, at a 400 µm pitch, with exactly the same dose. These patterns should be nominally the same. After that, above the first row, four arrays are written at the same pitch but with a 1.2 times larger exposure dose. In this way, 11 rows are written at increasing dose. After that, 44 arrays (11 rows and 4 columns) of 17 × 17 dots, with dots at a 250 nm pitch, were written at an 800 µm distance to the right of the first 44 arrays. The dose increase along the rows will provide information on the dose dependence of the charging effects. The four columns will give information on eventual long-range proximity effects on the charging. The latter effects will not be discussed in this work. After all arrays were written, large markers (200 × 200 µm^2) were written in *Meander* mode at 350 µC/cm^2 to facilitate optical inspection of the patterns after development. Also, 200 × 200 µm^2 markers were written 400 µm away at the leftmost and the rightmost side of each main block for navigation during SEM inspection. These are not shown in the layout of Fig. 5.8.

The arrays at the bottom row were written at a dose of 50 µC/cm^2. The dose was updated by a factor of 1.2 for each pattern above, up to a dose of 310 µC/cm^2 for

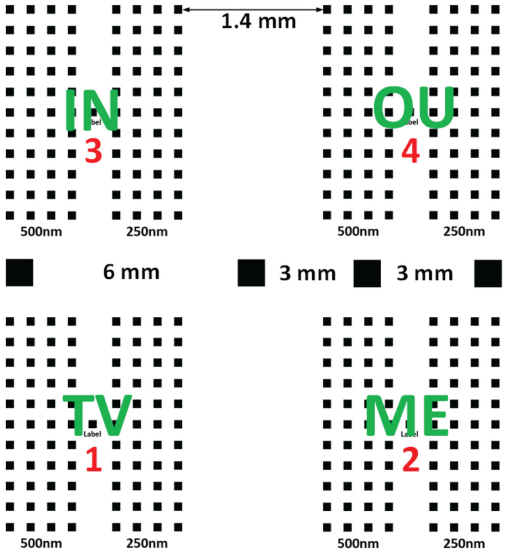


Figure 5.9: Entire layout of exposed patterns on the 2 × 2 cm^2 wafer. The horizontal pitch of the main blocks is 1.4 mm, and the vertical pitch is 1.4 mm. The different scan modes in each main block are indicated by two letter labels: TV, ME, IN, OU (in green in the color version). The main block writing order was TV > ME > IN > OU indicated by numbers below the scan mode (in red in the color version).

the uppermost row. The dose was increased by increasing the dwell time for each dot exposure. The dwell time is given by

$$DwellTime = \frac{10 \times BeamStepSize^2 \times Dose}{Current} \tag{5.1}$$

where *Beam Step Size* is the pitch of the dots in µm, *Dose* is the exposure dose in µC/cm², *Current* is the beam current in nA, and Dwell Time is the time spent per dot in microsecond. The entire layout of all exposed patterns written in all four scan modes is shown in Fig. 5.9. The main blocks are labeled according to the scan strategy within the arrays (the text with big fonts in the middle of main blocks, the green text in the color version) and the writing order of the main blocks (the numbers just below the scan strategy label, the red numbers in the color version).

5.3.3. Inspection

The patterns were inspected in a Raith "eLINE Plus" system equipped with an interferometric stage which allows automated inspection. At first, the operator needs to locate the positions of three markers on the sample to be able to determine the absolute position of patterns on the sample. During the setting up procedure, the operator calibrates the beam focus on the markers. Once the setup is done, the tool automatically moves to predetermined coordinates of patterns, automatically focuses the beam, and takes images of the patterns. Each structure was inspected only once (unless stated otherwise) to prevent beam-induced damage [31–33] during SEM inspection (Fig. 5.10).

All inspections were done with an 8 keV beam and a 15 µm aperture and at a working distance of 6.4 mm. The field of view was 12 µm. The brightness and contrast

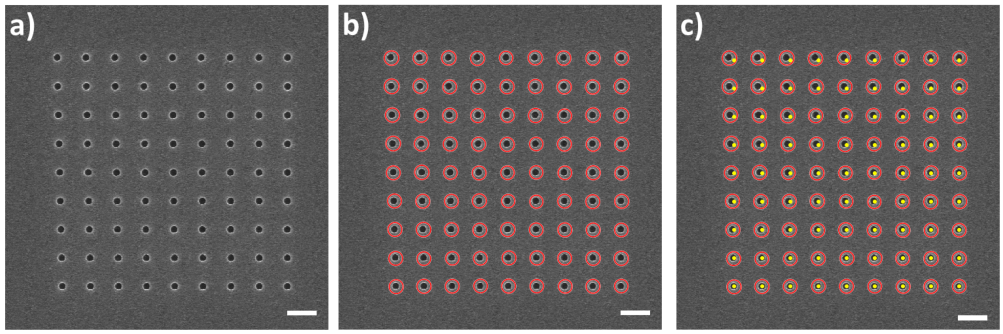


Figure 5.10: Example of dot detection. The scale bars are 500 nm. (a) An SEM micrograph of a 9 × 9 dot pattern written in *Meander* mode at 124 μC/cm^2; (b) the detected dots, marked by (red - in the color version) circles; (c) the image of (b) overlaid with the intended dot pattern marked by (yellow - in the color version) dots. The charge-induced displacements are clearly seen.

values were 50.1% and 31.4%, respectively, and the InLens detector of the GEMINI column was used.

5.3.4. Image processing

We have processed the images with a MATLAB script which can be found in the supplementary material*. The script covers the following image processing steps: (i) noise filtering based on a median filter (with a 9 × 9 square window) to preserve the feature edges and a sophisticated contrast adjustment based on adaptive histogram equalization [34], (ii) dot pattern recognition by using a disk shape structural element, (iii) determination of the center of mass for each dot, and (iv) comparison of the detected dot pattern with the designed dot pattern.

Once the dot positions are detected, the pattern is compared with the predetermined pattern, using the first exposed dot as a reference point. We assume that this dot is not affected by any beam-induced effect because there has not been any electron exposure nearby.

5.4. Results

The simulation shows that the charging can deflect the beam by more than a few hundred nanometers at 50 keV, and the displacement of the exposed dots increases when the exposure dose increases (see Fig. 5.7). The simulations also demonstrate that the impact of the scan strategy is significant (see Fig. 5.4). For the *Meander* and *TV* modes, the simulations and experiments show very similar trends, and even the magnitudes of the maximum displacement agree very well, as demonstrated in Fig. 5.11.

Simulations and experiments were also compared at different doses to demonstrate

*See supplementary material at doi.org/10.1116/1.5120631 for a file that contains a MATLAB script for analysis of SEM micro-graphs of the study

the effect of the exposure dose. For example, at lower doses, such as ~60 μC/cm^2, the quantitative match is less good, but qualitatively they still match, as seen in Fig. 5.12.

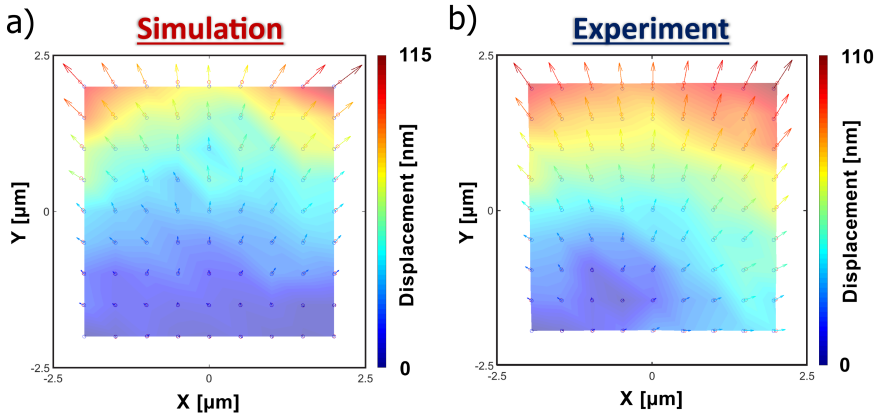


Figure 5.11: Comparison between (a) simulation at 128 μC/cm^2 and (b) experiment at 124 μC/cm^2 for the *Meander* mode for a 500 nm dot pitch at 128 μC/cm^2.

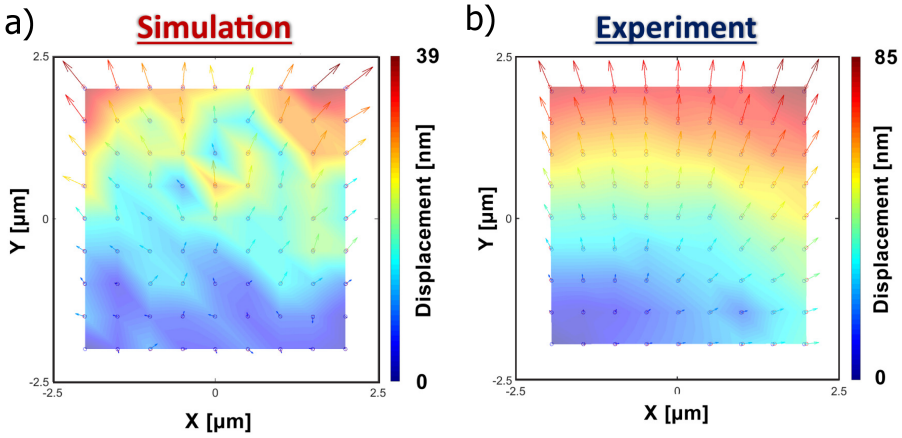


Figure 5.12: Comparison between (a) simulation at 64 μC/cm^2 and (b) experiment at 60 μC/cm^2 for the *Meander* mode for a 500 nm dot pitch.

For the *Outward Spiral* and *Inward Spiral* modes, we observe more significant differences between the simulations and the experiments. In Fig. 5.13, the simulation result for the *Outward Spiral* mode, at a dose of 128 μC/cm^2, is compared with experiments at two different doses. In the simulation, the magnitude of the displacement increases when more and more charge is deposited, taking its largest value at the bottom leftmost dot. The experimental result at 124 μC/cm^2 shows both a qualitative and quantitative mismatch to the simulation. Specifically, the displacement at the

top border is negligible and directed downwards. However, the experimental result at 150 µC/cm^2 matches qualitatively and quantitatively better with the simulation even though it is exposed at a higher dose: the displacement at all borders is larger than in the central area, and the maximum displacement in the experiment (98 nm) is very similar to the simulated one (125 nm).

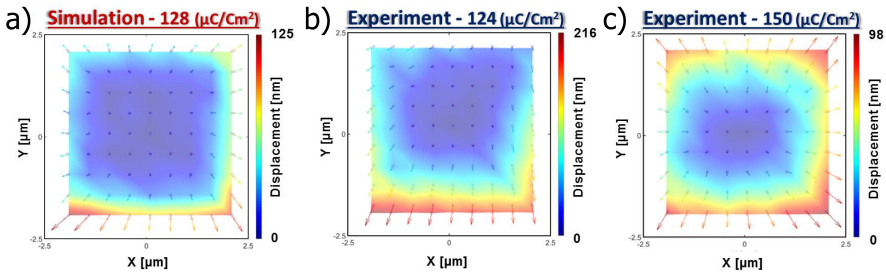


Figure 5.13: Comparison between (a) simulation at 128 µC/cm^2, (b) experiment at 124 µC/cm^2, and (c) experiment at 150 µC/cm^2 for the *Outward Spiral* mode for a 500 nm dot pitch.

Figure 5.14 compares the simulation and experiment written in *Inward Spiral* mode. As discussed in Sec. 1.2.3. Simulations, the displacement at the borders is limited in this writing mode as the charging is not strong enough to deflect the beam noticeably. However, the displacement maps do not match well at all. A similar mismatch also shows at other doses, although the experimental maximum displacement is somewhat closer, by a factor of ≈2, to the simulation result.

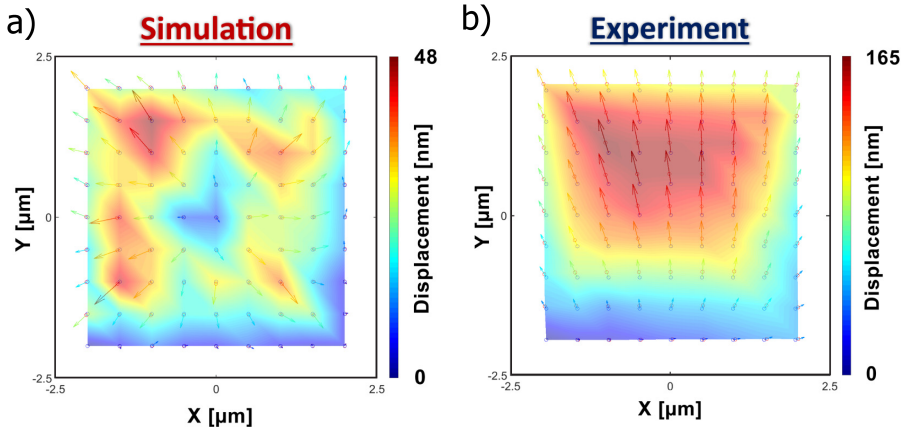


Figure 5.14: Comparison between (a) simulation at 128 µC/cm^2 and (b) experiment at 124 µC/cm^2 for the *Inward Spiral* mode for a 500 nm dot pitch.

Figure 5.15 compares the simulation and the experiment, also for the *Inward Spiral* scan mode, but at a smaller dot pitch (250 nm). At this pitch, a much better match is observed between experiment and simulation. Furthermore, the amount of

displacement also matches quite well.

Finally, we verified the expected influence of the charging on the dot size, originating from the increasing beam deceleration toward the last written dots. This effect should be more prominent at a higher dose than at a lower dose. In Fig. 5.16, the diameters of the dots in the top and bottom rows of a 9 × 9 array of dots, written in *Meander* mode, are compared for a dose of 50 and 258 μC/cm^2. At a dose of 50 μC/cm^2, the mean diameters of dots in the top and bottom rows are almost equal (80.7 vs 80.6 nm). At a dose of 258 μC/cm^2, the phenomenon is distinguishable. The mean diameter of the top row dots is 103.1 nm where the bottom row dots have a mean diameter of 98.7 nm. This demonstrates the effect of charging on feature sizes.

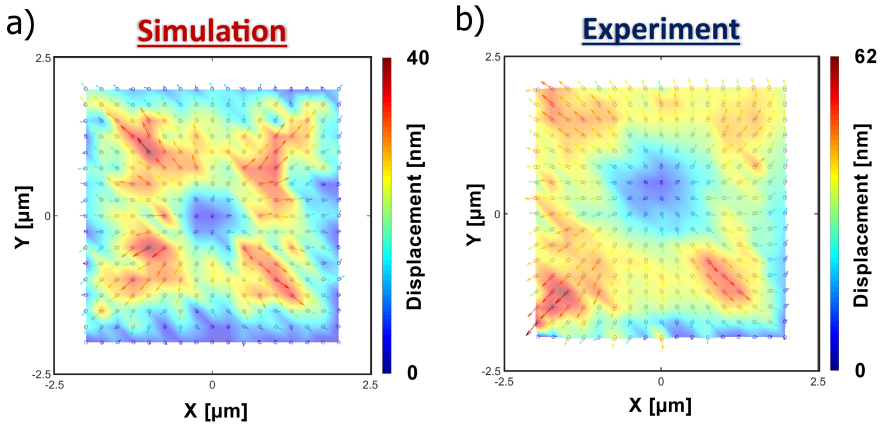


Figure 5.15: Comparison between (a) simulation at 128 μC/cm^2 and (b) experiment at 124 μC/cm^2 for the *Inward Spiral* mode for a 250 nm dot pitch.

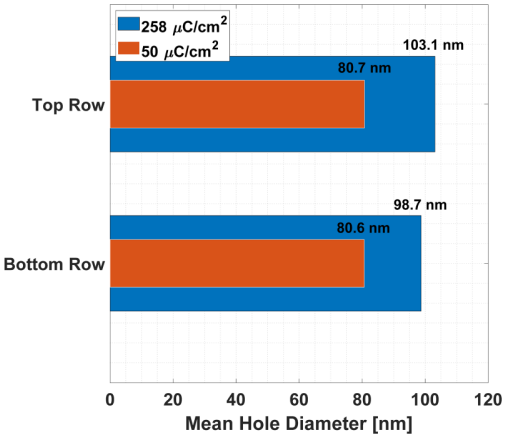


Figure 5.16: Effect of charging on dot diameters. The mean diameters of the top and bottom row dots are compared for a low (50 μC/cm^2) and a high (258 μC/cm^2) exposure dose for a 9 × 9 dot array written in *Meander* mode.

5.5. Conclusions

From the simulations, we predicted significant charging effects during EBL on glass wafers at 50 keV. These were also experimentally verified. Beam displacements as large as a few hundred nanometers, depending on the exposure dose, were observed, as well as charge-induced feature size changes. These, especially the beam displacement, pose a serious problem for accurate patterning of high-end structures and call for ways to minimize these effects.

From simulations, we concluded that the scan strategy influences pattern shapes. We tested four different scan strategies and found that a smart strategy, such as the *Inward Spiral* mode, can minimize the deformation of square patterns showing the power of simulations to identify the right strategy for a certain pattern shape. Although some experimental cases (like Fig. 5.14) deviate, the possibility of minimizing the deformations by a smart scan strategy was supported by most of the experiments.

We have also observed unexpected deviations between experiments and simulations such as shown in Fig. 5.13. These deviations decreased when increasing the exposure dose, resulting in a better qualitative match and less displacement. This is not understood yet but perhaps arises from possible errors in the entire process (exposure, inspection, and postprocessing). There is no reasonable physical explanation of why all the displacement arrows at the top of the middle image of Fig. 5.12 point downwards. The simulations did not show such dose-dependent, unexpected, changes in the displacement maps. The fact that such effects were observed in the experiments prevents us from drawing definite conclusions on the influence of the scan strategy and these should be investigated in further study. However, the qualitative agreement, and even sometimes the quantitative agreement, between the experiments and the simulations is remarkable. CSDA model was used for all simulations in the experimental comparisons to reduce the simulation time. It is noted here that there is an influence of the inelastic scattering model used on the magnitude of the displacements, which can amount up to a factor of 2. However, the relatively good agreement between the simulations and experiments is encouraging to make use of Monte Carlo simulations to predict the influence of charging in EBL, but also in SEM imaging.

The beam displacement phenomenon in EBL, leading to observable displacements of exposed dot patterns, is a valuable test case for the simulation of charging. It allows collecting data on charging phenomena in a much more controlled way than analysis of SEM images of charging samples, and it also avoids complexities caused by surface topography.

Acknowledgements

The first author is grateful to Pieter Kruit, for discussions on the charging phenomenon and nanofabrication; Wilco Zuidema and Marco Wisse, for discussions on imaging processing; and Martin Kamerbeek, for discussions on the sample prepara-

tion for SEM inspection and nanofabrication. The authors acknowledge GenISys-GmbH and RAITH B.V. for funding this research project.

References

[1] I. Charaev, A. Dane, A. Agarwal, and K. K. Berggren, *Enhancement of optical response in nanowires by negative-tone PMMA lithography,* IEEE Transactions on Applied Superconductivity **29**, 1 (2019).

[2] Y. Chen, *Nanofabrication by electron beam lithography and its applications: A review,* Microelectronic Engineering **135**, 57 (2015).

[3] A. E. Grigorescu and C. W. Hagen, *Resists for sub-20-nm electron beam lithography with a focus on HSQ: state of the art,* Nanotechnology **20**, 292001 (2009).

[4] V. R. Manfrinato, L. Zhang, D. Su, H. Duan, R. G. Hobbs, E. A. Stach, and K. K. Berggren, *Resolution limits of electron-beam lithography toward the atomic scale,* Nano Letters **13**, 1555 (2013).

[5] V. R. Manfrinato, J. Wen, L. Zhang, Y. Yang, R. G. Hobbs, B. Baker, D. Su, D. Zakharov, N. J. Zaluzec, D. J. Miller, E. A. Stach, and K. K. Berggren, *Determining the resolution limits of electron-beam lithography: Direct measurement of the point-spread function,* Nano Letters **14**, 4406 (2014).

[6] M. Rommel and B. A. Nilsson, *Estimating the optimum dose for arbitrary substrate materials based on Monte Carlo simulated point spread functions,* Microelectronic Engineering **155**, 29 (2016).

[7] K. D. Cummings, *Charging effects from electron beam lithography,* Journal of Vacuum Science & Technology B: Microelectronics and Nanometer Structures **7**, 1536 (1989).

[8] A. Aassime, F. Hamouda, I. Richardt, F. Bayle, V. Pillard, P. Lecoeur, P. Aubert, and D. Bouchier, *Anti-charging process for electron beam observation and lithography,* Microelectronic Engineering **110**, 320 (2013).

[9] S. Tirpanci, D. E. Bürgler, C. M. Schneider, B. Rameev, and B. Aktaş, *Charging effect reduction in electron beam lithography and observation of single nanopillars on highly insulating substrates,* Microelectronic Engineering **140**, 33 (2015).

[10] B. Leibold, J. Butschke, L. Bettin, D. Beyer, M. Irmscher, C. Koepernik, R. Plontke, A. Vix, and P. Voehringer, *Second-level imaging of advanced alternating phase-shift masks using e-beam lithography,* 23rd Annual BACUS Symposium on Photomask Technology **5256**, 1034 (2003).

[11] R. Abargues, U. Nickel, and P. J. Rodríguez-Cantó, *Charge dissipation in e-beam lithography with Novolak-based conducting polymer films,* Nanotechnology **19**, 125302 (2008).

[12] B. D. Myers and V. P. Dravid, *Variable pressure electron beam lithography (VP-eBL): A new tool for direct patterning of nanometer-scale features on substrates with low electrical conductivity,* Nano Letters **6**, 963 (2006).

[13] J. Joo, B. Y. Chow, and J. M. Jacobson, *Nanoscale patterning on insulating substrates by critical energy electron beam lithography,* Nano Letters **6**, 2021 (2006).

[14] R. Pintus, S. Podda, and M. Vanzi, *An automatic alignment procedure for a four-source photometric stereo technique applied to scanning electron microscopy,* IEEE Transactions on Instrumentation and Measurement **57**, 989 (2008).

[15] H. Itoh, *Charging effects on trilevel resist and metal layer in electron-beam lithography,* Journal of Vacuum Science & Technology B: Microelectronics and Nanometer Structures **9**, 3039 (1991).

[16] J. Zhang, M. Fouad, M. Yavuz, and B. Cui, *Charging effect reduction in electron beam lithography with nA beam current,* Microelectronic Engineering **88**, 2196 (2011).

[17] R. J. Hawryluk, H. I. Smith, A. Soares, and A. M. Hawryluk, *Energy dissipation in a thin polymer film by electron beam scattering: Experiment,* Journal of Applied Physics **46**, 2528 (1975).

[18] J. J. Hwu and D. C. Joy, *A study of electron beam-induced conductivity in resists.* Scanning **21**, 264 (1999).

[19] J. J. Hwua, Y.-u. Ko, and D. C. Joyatb, *Computer modeling of charging induced electron beam deflection in electron beam lithography,* Control **3998**, 239 (2000).

[20] Y.-u. Ko, J. J. Ha, and C. David, *Monte Carlo model of charging in resists in e-beam lithography,* Proceedings of SPIE **3998**, 694 (2000).

[21] K. T. Arat, T. Klimpel, and C. W. Hagen, *Model improvements to simulate charging in SEM,* in *Metrology, Inspection, and Process Control for Microlithography XXXII*, Vol. 10585, edited by O. Adan and V. A. Ukraintsev (SPIE, 2018) p. 43.

[22] K. T. Arat, J. Bolten, T. Klimpel, and N. Unal, *Electric fields in Scanning Electron Microscopy simulations,* in *Proc SPIE*, Vol. 9778, edited by M. I. Sanchez and V. A. Ukraintsev (2016) p. 97780C.

[23] E. Kieft and E. Bosch, *Refinement of Monte Carlo simulations of electron–specimen interaction in low-voltage SEM,* Journal of Physics D: Applied Physics **41**, 215310 (2008).

[24] T. Verduin, *Quantum Noise Effects in e-Beam Lithography and Metrology*, Ph.D. thesis, Delft University of Technology (2017).

[25] Y. Lin and D. C. Joy, *A new examination of secondary electron yield data,* Surface and Interface Analysis **37**, 895 (2005).

[26] K. D. Cummings, *A study of deposited charge from electron beam lithography,* Journal of Vacuum Science & Technology B: Microelectronics and Nanometer Structures **8**, 1786 (1990).

[27] H. J. Fitting, H. Glaefeke, and W. Wild, *Electron penetration and energy transfer in solid targets,* Physica Status Solidi (a) **43**, 185 (1977).

[28] N. Cornet, D. Goeuriot, C. Guerret-Piécourt, D. Juvé, D. Tréheux, M. Touzin, and H.-J. Fitting, *Electron beam charging of insulators with surface layer and leakage currents,* Journal of Applied Physics **103**, 064110 (2008).

[29] M. Aktary, M. Stepanova, and S. K. Dew, *Simulation of the spatial distribution and molecular weight of polymethylmethacrylate fragments in electron beam lithography exposures,* Journal of Vacuum Science & Technology B: Microelectronics and Nanometer Structures **24**, 768 (2006).

[30] Q. Dai, S. Y. Lee, S. H. Lee, B. G. Kim, and H. K. Cho, *Experiment-based estimation of point spread function in electron-beam lithography: Forward-scattering part,* Microelectronic Engineering **88**, 3054 (2011).

[31] J. J. Ritsko, L. J. Brillson, R. W. Bigelow, and T. J. Fabish, *Electron energy loss spectroscopy and the optical properties of polymethylmethacrylate from 1 to 300 eV,* The Journal of Chemical Physics **69**, 3931 (1978).

[32] R. F. Egerton, S. Lazar, and M. Libera, *Delocalized radiation damage in polymers,* Micron **43**, 2 (2012).

[33] R. Egerton, P. Li, and M. Malac, *Radiation damage in the TEM and SEM,* Micron **35**, 399 (2004), arXiv:arXiv:1011.1669v3 .

[34] K. Zuiderveld, *Graphics Gems IV,* , 474 (1994).

6

E-Beam Lithography on Curved or Tilted Surfaces: Simulations and Experiments

There is a growing interest for patterning on curved or tilted surfaces using electron beam lithography. Computational proximity correction techniques are well established for flat surfaces and perpendicular exposure, but for curved and tilted surfaces adjustments are needed as the dose distribution is no longer cylindrically symmetric with respect to the surface normal. A graphical processing unit accelerated 3D Monte Carlo simulation, based on first-principle scattering models, is used to simulate the asymmetric dose distribution. Based on that, an approximate adjustment is made to an existing high-performance proximity effect correction (PEC) algorithm aimed at the correct exposure of a pattern of nanowires on a 17° tilted surface. It was experimentally verified that using the adjusted PEC indeed leads to a more uniform exposure on tilted surfaces.

This chapter is published as a journal paper:
Kerim T. Arat, Aernout C. Zonnevylle, Wilhelmus S. M. M. Ketelaars, Nikola Belic, Ulrich Hofmann, Cornelis W. Hagen: Electron Beam Lithography on Curved or Tilted Surfaces: Simulations and Experiments. *Journal of Vacuum Science & Technology B* 09/2019; 37(5): 051604. DOI:10.1116/1.5120632

6.1. Introduction

In electron beam lithography (EBL), patterns are written in an electron sensitive material (resist) using a focused electron beam. During the exposure, the interaction of the electrons and the resist-substrate stack changes the resist's solubility. Depending on the tone of the resist, usually consisting of polymers, the change in the solubility occurs by breaking bonds in the polymer network or creating a stronger network by cross-linking the monomers to neighboring monomers. For instance, in a positive resist, when enough bonds are broken in a certain area, this area becomes soluble to a developer and the patterned feature shows up as a recessed shape in the resist. To control the size of the pattern, it requires control over the distribution of broken bonds, which is related to the electron dose distribution. As the electrons scatter in the resist-substrate stack they spread laterally, influencing the exposure of neighboring areas. This so-called proximity effect can be corrected if this lateral spread, often indicated as the point spread function (PSF), is known. The correction of this effect by adjusting the number of incident beam electrons (dose) is known as proximity effect correction (PEC), which has become standard in EBL [1–3]. When the electron beam is incident perpendicularly to a flat surface Fig. 6.1a, the PSF is cylindrically symmetric around the surface normal, a property that is often used for PSF calculations [4–10]. Once the PSF is known, the electron dose can be calculated for patterns in a given layout.

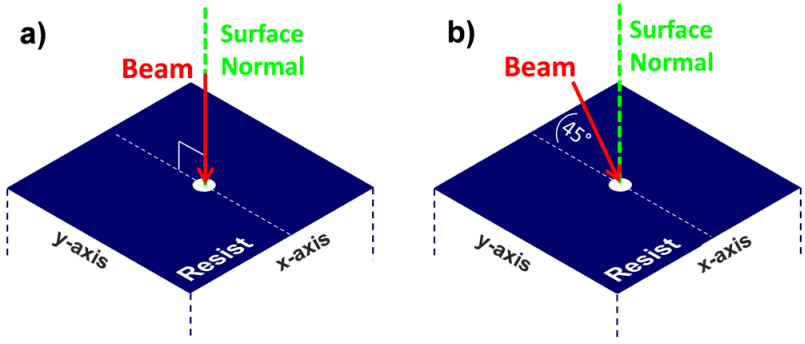


Figure 6.1: Exposure at different angles: the incident beam (arrow) (a) is perpendicular to the resist surface and (b) has a 45° angle with the surface normal (dashed line).

Recently, there is a growing interest to pattern tilted surfaces by EBL [11–15]. In this case, the beam has a non-zero angle with the surface normal Fig. 6.1b. For such applications, where the cylindrical symmetry no longer exists, the standardly used PSF calculation techniques are no longer suitable, and the PEC techniques [1, 2, 16] need to be adjusted accordingly. In this study, first the PSFs are simulated for a perpendicular surface and tilted surface using a 3D Monte Carlo simulator [17] and the asymmetry in the tilted case is verified experimentally. Then, an approximate method is used to adapt an existing high-performance PEC algorithm to the asymmetric PSF, and the resulting exposure of a tilted resist-substrate stack is compared to an exposure using the regular PEC, based on the symmetric PSF. In the discussion, the pitfalls of using the

regular PEC based on the cylindrically symmetric PSF, when exposing tilted surfaces, will be addressed.

6.2. Monte Carlo simulator

A common way to determine the PSF is using Monte Carlo simulations. It is crucial to use reliable electron-matter interaction models in the simulator, especially for low energy electron scattering since the bond-breaking rate is highest at low energies [18]. We have used the e-scatter Monte Carlo simulator [17], which contains first-principle elastic and inelastic scattering models and runs on a graphical processing unit to benefit from parallel processing.

In e-scatter, the elastic scattering cross sections are based on the relativistic Mott cross sections including solid-state effects using a "muffin-tin" approximation for the potential. These cross sections are calculated by ELSEPA [19] and used for energies above 200 eV. At very low energies, the electrons dominantly interact with the lattice rather than the atomic potential. Therefore, the interaction of electrons with acoustic phonons is taken into account [17, 20] at energies below 100 eV, where the Mott description is no longer applicable [21]. For energies between 100 and 200 eV, an interpolation between the cross sections for the two processes is used [17]. The inelastic scattering is modeled by using the dielectric function [21]. In addition, an electron trapping model [22] is used for the resist. The details of the models are explained in chapter 3 of the thesis of Verduin [17]. Fig. 6.2 shows the elastic and inelastic mean free paths of the materials used in this study, i.e., a silicon (Si) substrate and polymethyl methacrylate (PMMA) as resist.

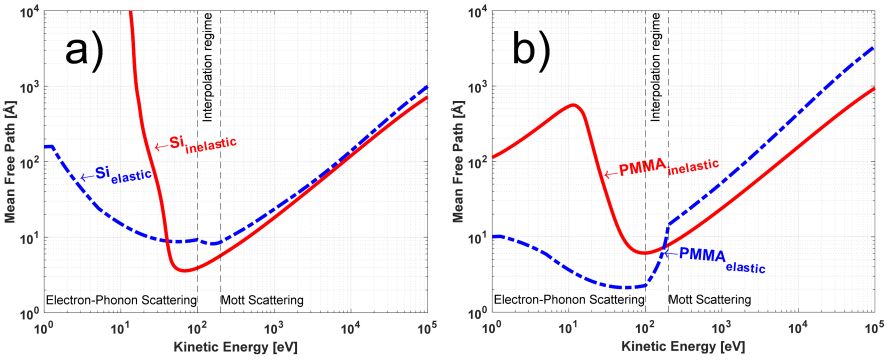


Figure 6.2: Elastic (dashed lines) and inelastic (solid lines) mean free paths of the materials used in this study; (a) silicon and (b) PMMA. The vertical dashed lines serve to distinguish the electron-phonon scattering regime (low energies) and the Mott scattering regime (high energies).

As the simulator models individual inelastic events, it would, in principle, allow for the determination of the number of bond-breaking events if the probability for bond-breaking was known. However, the cross sections for bond breaking are not well known. From the literature [18], it is known that the status of the carbon-carbon

backbone of the resist molecule plays an important role in the determination of its solubility. Wu and Neureuther [23] reported that the bondbreaking cross section vanishes at energies below 4.9 eV. In other words, electrons with energy lower than 4.9 eV cannot break a bond. Although the zero of energy is not defined by the authors [23], it is assumed here that it is the bottom of the valence band. Due to the lack of known bond-breaking cross sections, a common approach is to store the energy lost in an inelastic event or a trapping event, in the volume element (voxel) of resist where the event occurred [7, 8, 24], provided that more energy than a threshold value, assumed here as 4.9 eV, is lost. The number of broken bonds is then assumed to be proportional to the deposited energy per voxel, and the distribution of energy deposited in the resist is associated with the PSF.

6.3. Point exposure of resist on a curved surface

The Monte Carlo simulator is used to calculate the PSF for the electron exposure of an Si-substrate/100 nm PMMA stack in two cases: (i) exposure perpendicular to the stack and (ii) exposure under 45° with the surface normal of the stack. The beam energy is 50 keV, and a zero-diameter beam is assumed. The voxels in which the deposited energy is stored have a lateral size of 25 × 25 nm^2 and 100 nm perpendicular to the substrate (equal to the resist thickness). Fig. 6.3 shows the top-down views, i.e., viewing along the surface normal, of the PSFs in the resist, obtained in the two cases. In Fig. 6.3a, the PSF for perpendicular exposure is observed to be nicely cylindrically symmetric, both near the very center (inset) and further from the point of incidence. In contrast, the PSF for tilted exposure, as shown in Fig. 6.3b, is asymmetric and shifted compared to the perpendicular exposure case.

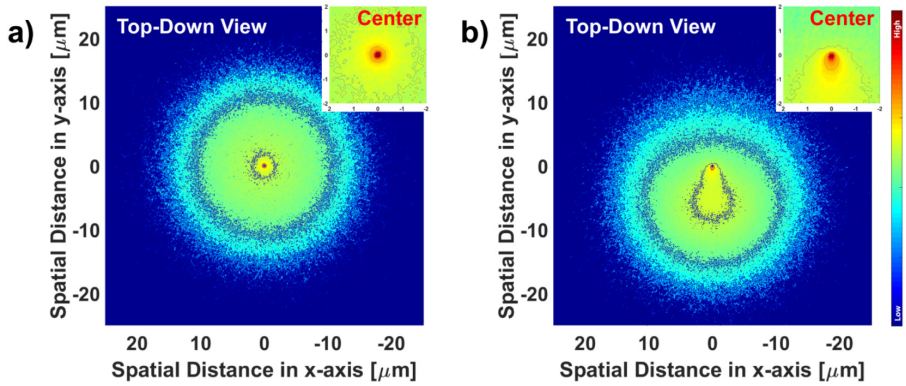


Figure 6.3: Top-down representation of simulated energy deposition profiles (PSF). The incident beam is (a) perpendicular to the resist surface and (b) under an angle of 45° with the surface normal. The insets (in micrometer) magnify the center of the exposure. The color map (logarithmic scale in energy/volume) qualitatively represents the energy deposition.

To experimentally verify the simulation results, a spherical glass lens was coated with a 4 µm thick layer of PECVD (plasma enhanced chemical vapor deposition) a-Si,

and spin coated with an ≈100 nm thick layer of 495 k PMMA in 3% Anisole. It was soft-baked for 10 min at 180 °C. The exposure was done at an electron beam energy of 50 keV, a beam current of 10 nA, and the exposure time was 2 s. The sample was exposed at two different locations. The sample geometry is depicted in Fig. 6.4. The first location was exposed along the surface normal, and the second at a 45° tilt with respect to the surface normal.

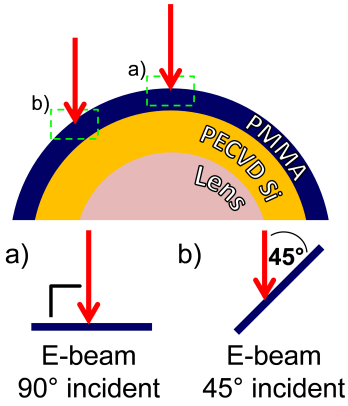


Figure 6.4: Exposure of a curved surface: the sample stack consists of 4 µm of PECVD a-Si on top of a spherical glass lens (radius = 25.7 mm) and an ≈100 nm layer of PMMA spin-coated on top. (a) Location of perpendicular exposure and (b) location of exposure under 45° tilt with the surface normal.

After development in methyl isobutyl ketone (MIBK) in 60 s, rinsed for 60 s with isopropanol (IPA) and dried with dry nitrogen gas. The exposed locations were imaged along the surface normal using an optical microscope. A similar approach to visualize the interaction volume is described by [10].

The results, shown in Fig. 6.5, qualitatively agree with the profiles obtained from the simulation. The asymmetric profile obtained for exposure of tilted substrates is so distinctly different from the symmetric one for perpendicular exposure that standard PEC techniques, based on cylindrically symmetric PSFs, are not suitable for exposures of tilted or curved samples.

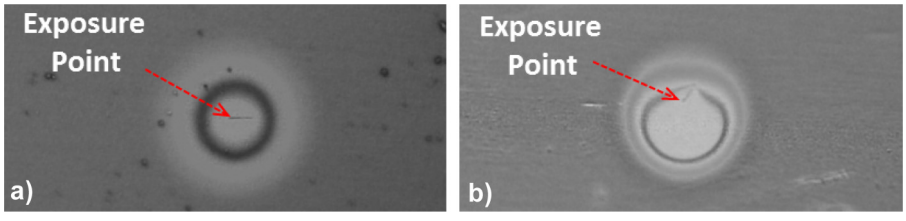


Figure 6.5: Optical microscopy images of point exposures of a 100 nm thick PMMA layer on a glass sphere, coated with a-Si, after development. (a) The exposure is perpendicular to the substrate. (b) The exposure is at a 45° (±2°) tilt from the surface normal. The electron beam energy was 50 keV, the beam current was 10 nA, and the exposure time was 2 s. Horizontal field view is ≈120 µm.

6.4. Proximity effect corrected patterning of tilted surfaces

In contrast to other applications [24] where 3D PEC is required, we here address how to optimize the exposure of a pattern on a tilted substrate. First, a test pattern was designed, suitable to clearly show the difference when an asymmetric PSF in the proximity effect correction is used instead of the usual symmetrical one. The pattern is written at 50 keV beam energy on a 17° tilted Si substrate with a 150 nm thick layer of PMMA resist, as shown schematically in Fig. 6.6. On this substrate, the same pattern was written twice with two different PSFs used for the PEC. The PEC of the first exposure was done with the symmetrical PSF for perpendicular exposure, and the PEC of the second exposure was done by taking into account the asymmetrical PSF for tilted exposure.

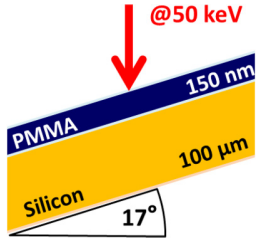


Figure 6.6: Cross-sectional view of exposure on a 17° tilted substrate. Note that structures on the right-hand side are positioned higher along the vertical coordinate than structures on the left-hand side.

The test pattern consists of a large square (50 × 50 µm^2) embraced at the upper right side and the lower left side by lines and spaces, as shown in Fig. 6.7. The lines are equal in width at both sides. The nominal linewidth is 0.1 µm, and the pitch is 0.3 µm. The size of the square was chosen such that a significant amount of background dose contributes to the exposure of the pattern of lines and spaces. It is noted that PMMA is a positive resist, and the exposed lines in the pattern will appear as trenches on the sample after development.

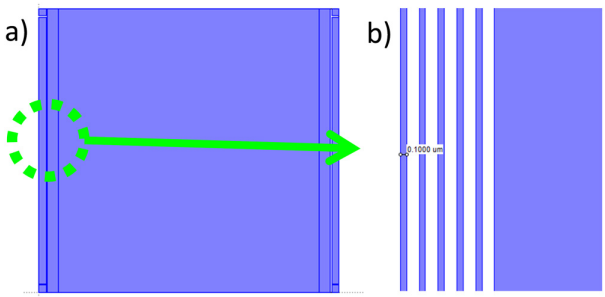


Figure 6.7: Test pattern consisting of a 50 × 50 µm^2 square, embraced by two patterns of lines (0.1 µm wide) and spaces (0.2 µm wide) on the left- and righthand sides of the square. (a) Overview and (b) zoomed-in drawing of the left-hand side of the pattern. The right-hand side (not shown as a zoomed-in drawing) is the mirror image of the left-hand side.

On a flat substrate, the proximity effect of exposing the middle square would be the same for both left- and right-hand patterns of lines and spaces, using the symmetrical PSF in the PEC. However, in the tilted substrate case, the effect of the middle square exposure will contribute more to the exposure of the lines on the left than to the

exposure of the lines on the right of the square due to the asymmetrical PSF. This will cause the lines on the left to develop differently from the lines on the right unless the exposure dose is corrected using the proper PSF, i.e., the asymmetrical PSF for exposure of tilted surfaces.

The PSFs needed for the PEC are obtained using Monte Carlo simulation. Fig. 6.8 shows the two simulation geometries: perpendicular beam exposure (Fig. 6.8a) and 17° tilted beam exposure (Fig. 6.8b).

The simulation volume is discretized in cylindrical coordinates for computational efficiency. The radial axis is divided into 76 points, logarithmically increasing from 1 nm to 50 µm. The azimuthal plane is divided into 60 segments of 6° each. The resist is discretized in 10 layers along the surface normal, each 15 nm thick, to enable an analysis of the asymmetry in 3D. In the simulation, a zero-diameter beam is used with 10^7 electrons.

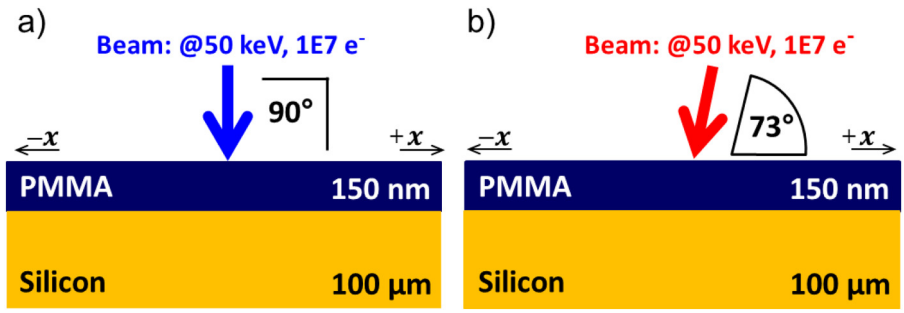


Figure 6.8: Simulation geometries to obtain the PSFs: 50 keV exposure of 150 nm PMMA resist on top of a 100 µm thick silicon substrate with the beam (a) perpendicular to the substrate and (b) at 17° tilted from the surface normal. A zero-diameter beam is used containing 107 electrons. The color code of the beams, blue solid line represents the perpendicular beam and red dashed line the tilted beam, is maintained in the following figures in the color online version.

The simulated PSFs in the topmost 15 nm thick layer, for both the perpendicular and tilted beam geometry, are shown in Fig. 6.9. The deposited energy density is plotted vs the x-coordinate, that is, the direction perpendicular to both the perpendicular and the tilted beam. As expected, the PSF is symmetric for the perpendicular beam (0°) and asymmetric for the tilted (17°) beam. In the latter case, more energy is deposited at the left-hand side (lhs), and the entire profile is shifted to the left (note the log-scale). The discontinuity at the center of the PSFs is due to the discretization and the logarithmic scale. When the tilted zero-diameter beam enters the resist, it travels mostly through the left-hand voxels with a height of 15 nm.

In Fig. 6.10, both PSFs are shown, along the x-axis, in the bottom layer of the resist, in contact with the substrate. As in the upper layers, the deposited energy profile is shifted to the left for the tilted beam. Also, a peak in the PSF is visible, which migrates to the left when the beam intersects deeper layers, amounting to a shift of 40 nm at a depth of 150 nm. This peak already appears in the first layer, seen as a plateau in Fig. 6.9 due to the logarithmic scale.

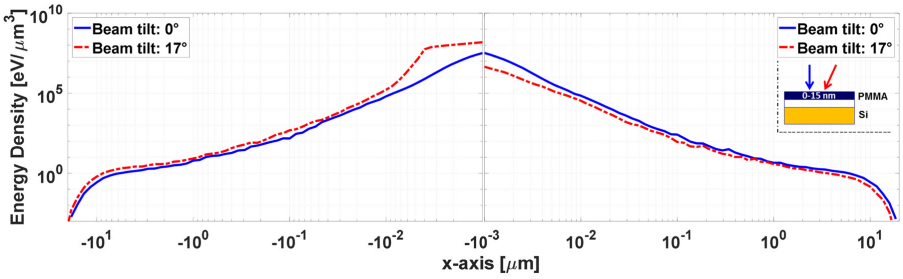


Figure 6.9: PSF comparison for the perpendicular and the tilted beam in the top-most surface layer (15 nm thick), plotted along the x-axis (the in-plane horizontal direction in the inset). The symmetrical solid blue curve is obtained for the perpendicular beam; the dashed red curve is obtained for the 17° tilted beam.

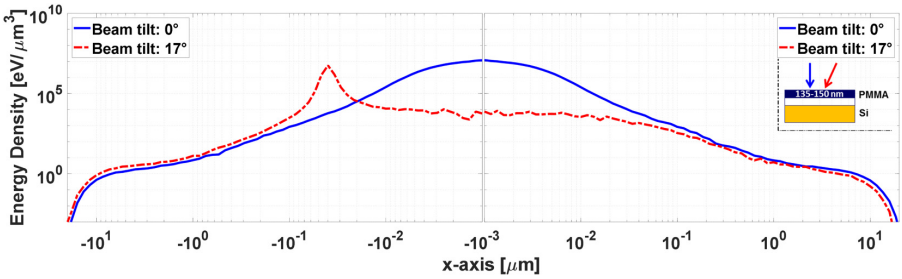


Figure 6.10: PSF comparison for the perpendicular and tilted beam in the bottom layer (15 nm thick).

The logarithmic plots of Figs. 6.9 and 6.10 are convenient to visualize the short-range effects, i.e., close to the point of incidence, but the long-range effect is less well visible. The latter is better visualized when plotted on a linear scale, such as in Fig. 6.11. Here, it is seen clearly that the tilted exposure profile is shifted to the left by ≈2.1 µm.

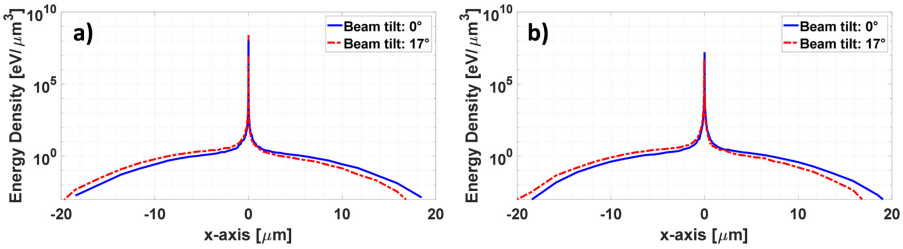


Figure 6.11: Comparison of the PSFs on a linear scale to show the asymmetry along the x-axis, i.e., the long-range shift: (a) in the top-most layer (vacuum interface) and (b) in the bottom layer (substrate interface).

In Fig. 6.12, the PSFs are plotted along the y-axis (x = 0) for both perpendicular and tilted substrates. There is no asymmetry observed in this case because there is no beam tilt with respect to this axis. However, the peak in the deposited energy drops dramatically in the bottom layer of the resist for the tilted beam, see Fig. 6.12b. This

is because the beam intersection with that layer has shifted from the point of incidence (x,y) = (0,0).

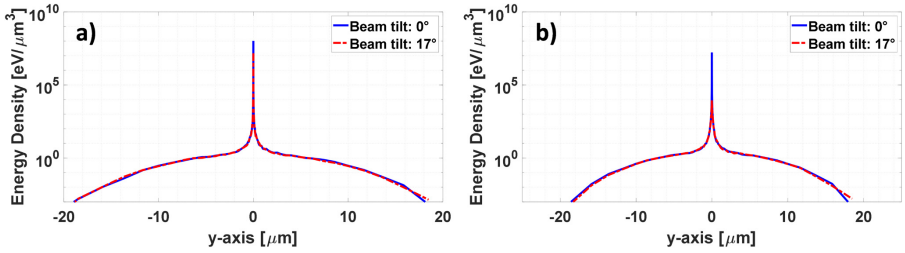


Figure 6.12: Comparison of the PSFs on a linear scale along the y-axis, to show the symmetry: (a) in the top-most layer (vacuum interface) and (b) in the bottom layer (substrate interface).

To summarize the results of the PSF simulations, the long-range shift of the PSF due to tilted exposure is in the order of micrometers which should be corrected for with PEC to minimize its influence on the exposure of neighboring features. The short-range effects, which are the beam shift (at maximum ≈40 nm here), beam diameter, and beam straggling, are smaller than the feature size (100 nm). Therefore, we do not expect that the short-range effects will significantly influence the linewidth, but the line shape may be affected. We will address this later.

Now we turn to the question of how to adapt the PEC for the tilted exposure PSF. The best result would be obtained by using the full 3D PSF in the PEC algorithm, but that would be computationally very time consuming, and we consider the design of an entirely new algorithm beyond the context of this work. Instead, we chose to use the PEC function of a commercially available e-beam software package (BEAMER) [25] for the proximity correction in 2D and modify the symmetric PSF. We start with separating the untilted exposure PSF, in the resist layer between 75 and 90 nm depth, into two functions: a short-range function f_{sr} that best matches the PSF up to ≈20 nm and a long range function f_{lr} that best matches the PSF above ≈1 μm. Both functions are rotationally symmetric around the beam axis and they are shown in Fig. 6.13.

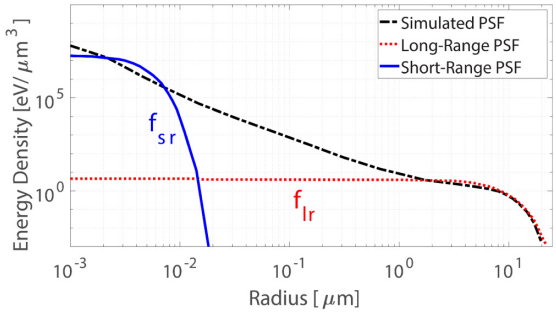


Figure 6.13: Comparison of simulated PSF, which was calculated by Monte Carlo simulator and approximated PSF is used in PEC.

For the exposure of tilted surfaces we found that the long-range shift of the energy distribution, originating from the backscattered electrons, is much larger than the shift

of the short-range distribution. For simplicity, we will ignore the latter shift, i.e., the same f_{sr} is used for tilted and untilted exposures. The effect of the tilted exposure is solely approximated by shifting the function f_{lr} over 2.1 µm. Note that we are shifting the entire rotationally symmetric distribution f_{lr} in one direction over 2.1 µm, ignoring the fact that the real distribution is not rotationally symmetric at all. Exposing the test pattern of Fig. 6.7 and adding up the dose received by the resist, using the approximated long-range PSF, f_{lr} in Fig. 6.13, one arrives at the long-range dose distributions of the tilted and nontilted exposures shown in Fig. 6.14.

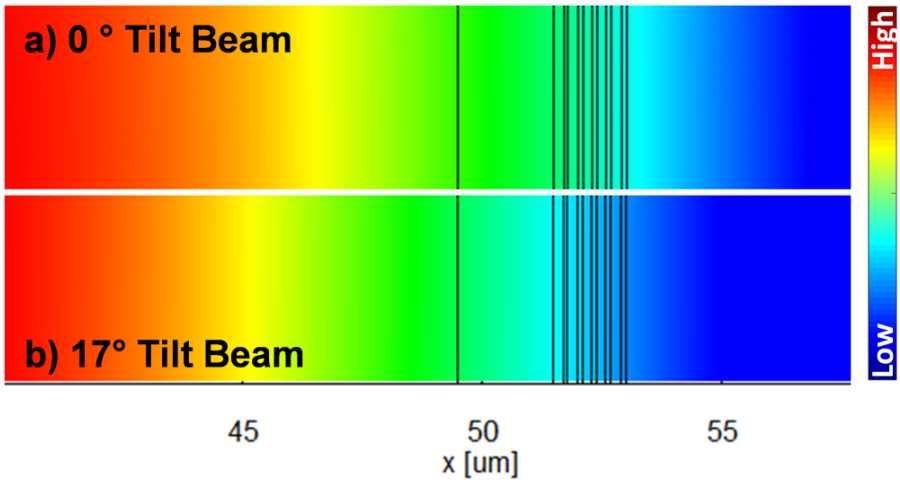


Figure 6.14: Long-range dose distribution: (a) nontilted beam and (b) 17° tilted beam. The color map represents the amount of dose received by the resist. To obtain the distribution for the 17° tilted beam exposure, the distribution for the nontilted beam exposure is shifted left by 2.1 µm. The dense narrow lines on the right are part of the geometry shown in Fig. 7, and the leftmost isolated line indicates the boundary between areas of constant dose.

To find the total dose distribution, the long-range and short-range effects are summed (see Fig. 6.15) where the long-range distribution is the shifted distribution for the 17° tilted beam exposure and the short-range distribution is assumed to be the one for the nontilted beam exposure.

Once the dose calculation is done, the PEC algorithm optimizes the exposure doses iteratively by calculating the normalized local exposure by convolving the PSF with the corresponding 2D coverage matrix of the layout. For the final dose assignment, the original pattern is divided into fragments required to assure optimal transcription into the exposure format. In Fig. 6.16, the dose-corrected exposure layouts, with and without accounting for the tilt, are shown. The color map shows the variation of dose (red-high, blue-low regions in the color online version) over the pattern. The image of the tilt-corrected Fig. 6.16b shows the exposure asymmetry required to compensate for the asymmetric PSF. The lines on the right require more dose than the lines on the left due to the left shift of the long-range distribution. In Fig. 6.16c, the PEC distributes equal amounts of dose to both the left- and right-hand side (rhs) lines

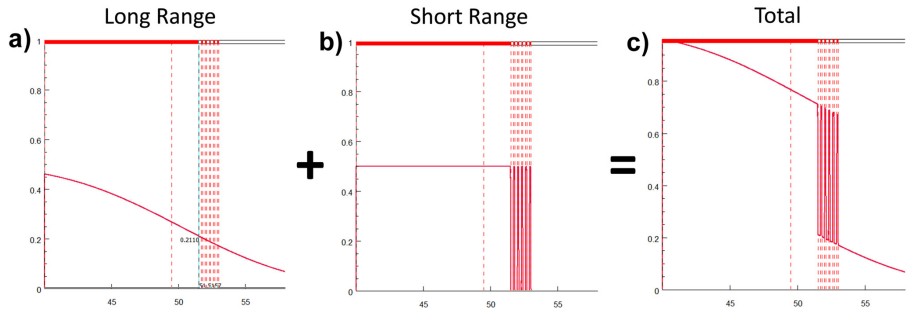


Figure 6.15: Total dose distribution. The dashed narrow vertical lines denote the lines of the test pattern. (a) The normalized long-range dose distribution; (b) the normalized short-range dose distribution; and (c) the total dose distribution for the 17° tilted beam exposure.

without considering the tilt of the sample, as the PSF is symmetric.

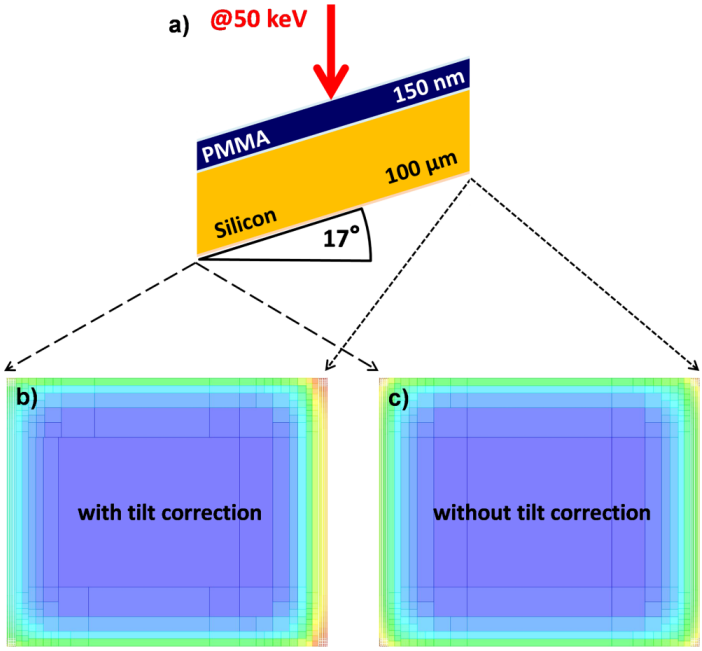


Figure 6.16: PEC (a) shows the experimental setup, (b) the dose map calculated when tilt is considered in PEC, and (c) the dose map calculated using the standard PEC. The color maps show the variation of dose over the pattern. Red (corners) and blue (in color online version) correspond to 1.58 and 0.70 relative base dose.

6.5. Experiments

The exposure was performed with a Raith EPBG 5200 tool, equipped with a z-stage for vertical stage control for a proper field correction. A series of different base doses

were done to find the correct dose. The beam energy was 50 keV, and the probe current was 6 nA using a 300 µm aperture. The Si sample was spin-coated with a 150 nm thick resist layer of 495 PMMA in 3% Anisole. It was soft-baked for 10min at 180 °C. After the exposure, at 0° and 17° tilt, it was developed for 60 s in MIBK, rinsed for 60 s with IPA and dried with dry nitrogen gas. After development inspection was done in a Thermo Fisher Scientific Helios G4 CX DualBeam™ SEM. The detector used was the through the lens detector in secondary electron mode with beam deceleration (-50V stage bias).

Figure 6.17 shows an SEM image of the exposed areas after development. The dark (black) tones represent PMMA resist and the bright (white) ones the silicon substrate. The upper block was exposed by taking the tilt correction into account; the lower block was not corrected for tilt but had the standard PEC applied.

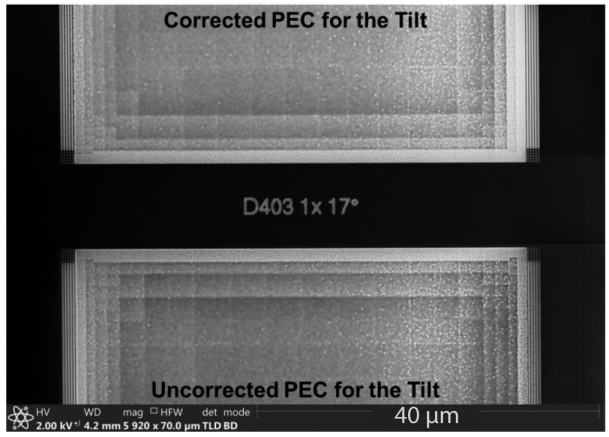


Figure 6.17: Two identical patterns were written on PMMA resist. A PEC algorithm which uses a PSF corrected for the tilt was applied for the top block, and a PEC algorithm with a standard PSF is applied for the bottom block.

It is observed that the lines (five on each side) were exposed and developed properly at both the left- and the right-hand sides of the squares. In Figs. 6.18 and 6.19, the lhs structures and the rhs structures are magnified to allow measurement of the linewidths, or critical dimension (CD). Note that the bright structures are in fact trenches, but we call them lines for convenience.

To measure the linewidths from these images, the intensity profiles across the top and bottom lines, integrated over 100 pixels, are plotted in Fig. 6.20. The signals do not look like the typical top-down inspection image signals of Manhattan structures [26]. They reveal multiple features such as peaks, dips, and glitches. These features arise from the fact that the tilted exposure also results in lines with tilted sidewalls after development, as schematically shown in Fig. 6.21. Here, the cross-sectional and top-down views are shown for line shapes resulting from tilted and nontilted exposures. The tilted exposure leads to the rhombuslike cross section of the lines, originating from the left-shift of the short-range peak visible in Figs. 6.9 and 6.10. Therefore, measur-

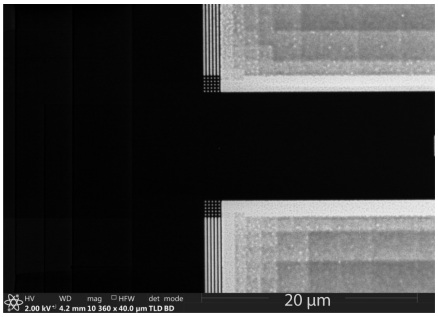


Figure 6.18: Lines at the left-hand side imaged at a higher magnification. The lines of the upper block were exposed with tilt correction. The lines of the lower block were exposed without tilt correction.

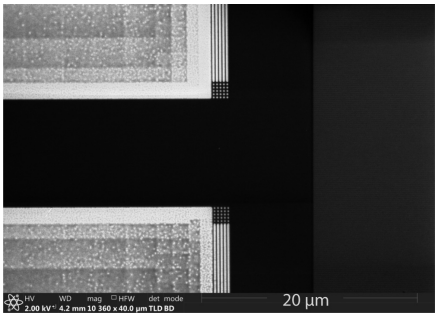


Figure 6.19: Lines at the right-hand side imaged at a higher magnification. The lines of the upper block were exposed with tilt correction. The lines of the lower block were exposed without tilt correction

ing the linewidths of these rhombuslike lines is less straight-forward than measuring the widths of the lines exposed without tilt, for which the standard CD measurement protocols [27] can be used.

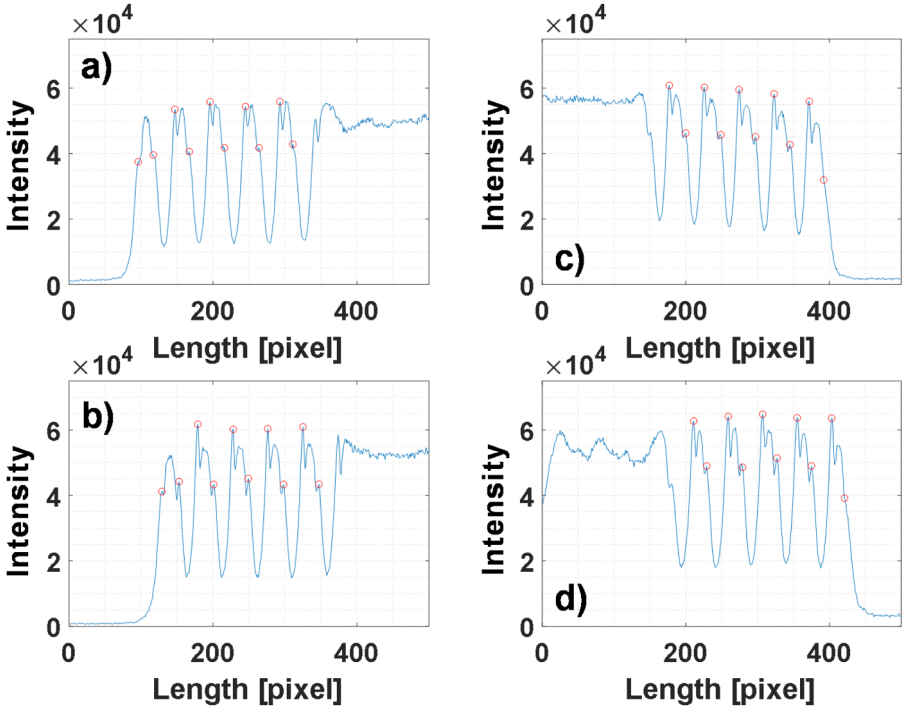


Figure 6.20: Integrated linescan profiles: (a) upper lines of Fig. 6.18, (b) lower lines of Fig. 6.18, (c) upper lines of Fig. 6.19, and (d) lower lines of Fig. 6.19. The pixel size is equal to 6.5 nm. The red circles indicate the edges depicted by solid dots (green in the online color version) in Fig. 6.22.

We adopted a simple CD measurement protocol, based on the cartoon of Fig. 6.22,

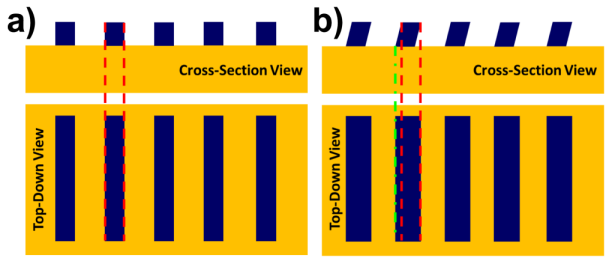


Figure 6.21: Shape of the resist lines. The yellow region represents the substrate; dark blue regions are the resist lines. (a) The images show the cross-sectional and top-down views of lines exposed without tilt. (b) The images show the cross-sectional and top-down views of the lines exposed with tilt. The dashed red lines are guides to the eye to judge the linewidth from the cross sectional view. The dotted green line on the right shows the linewidth as judged from the top-down view.

where the exposed regions are shown as trenches. The left and right peaks in the SEM linescan signal (the red circles in Fig. 6.22 in the color online version) are identified as the edge positions on the top surface of the resist (the green dots on resist corners in Fig. 6.22 in the color online version). The CD is then taken as the distance between these peaks. The red circles are also indicated in Fig. 6.20, from which the CDs are determined. The values are collected in Fig. 6.23 together with the CDs of the lines resulting from the nontilted exposures.

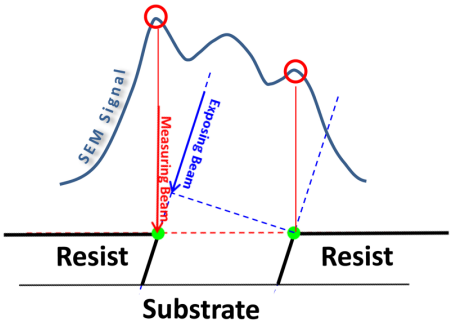


Figure 6.22: CD measurement protocol for the tilted lines. Exposure was done on a tilted sample along the tilted (blue) dashed line producing a trench with a nominal width of 100 nm (between the green solid dots). The inspection was done without a tilt such that the electron probe scans along the (red) horizontal dashed line. The nominal value of the measured width is 105 nm due to the uncorrected projection. The resulting SEM line scan signal is depicted above the geometry. The peaks (red empty circles) in the SEM signal correspond to the edges indicated by the (green) filled dots. Colors are visible on the online version.

Figure 6.23a shows the linewidths (of the trenches) for exposure without tilt correction and Fig. 6.23b shows the linewidths for exposure with tilt correction. The lines 1 to 5 are ordered from left to right. Notice that, the first line on the lhs and the fifth line on the rhs are the outermost structures.

In Fig. 6.23a, it is seen that the lines left of the big square are wider than those to the right of the square. Since the deposited doses are the same (see the dose map in Fig. 6.16c), the observed difference indicates the asymmetry in the dose distribution. The following explanations can be made on this structure to describe the phenomenon in details:

- The lhs lines received a larger long-range dose contribution than the rhs lines,

considering that the long-range PSF is left-shifted by 2.1 μm.

- On the rhs, the linewidth of the third line is larger than that of the fourth and fifth lines, even though the short-range dose contribution is lower (see Fig. 6.16c). This could be explained by the larger long-range dose contribution to the third line exposure when exposing the fourth and fifth lines, the total (short + long range) contribution reaching a maximum at the third line.

- The linewidth of the first and the second lines is smaller than the others on the rhs. This is because both short range and long-range contributions decrease when the e-beam moves to the left.

- On the lhs, the first line is the widest. This is mainly due to the strong short-range dose contribution. Secondly, the long-range contribution to the first line when exposing the lines to the right of the first line (still at the lhs) increases, the dose increasing gradually going left toward to first line.

- On the lhs, the fourth and the fifth lines are slightly wider than the third line. Although the short-range dose contribution decreases going right (Fig. 6.16c) the long-range dose contribution when exposing the high-density square pattern to the right of the fifth line contributes strongly to the exposure of the fourth and fifth lines. For the third line, the short-range dose contribution is larger than for the fourth and the fifth lines, but the long-range dose contribution, when exposing the patterns to the right of the third line, decreases more than the short-range dose contribution can compensate for.

When comparing Figs. 6.23a and 6.23b:

- The rhs lines are wider when correcting for the tilt, as expected, because the base dose is increased to compensate for the asymmetric PSF.

- For the same reason, the lhs lines received less dose in the tilt corrected case, and therefore they are narrower than in the noncorrected case.

Looking at Fig. 6.23b, the widths of the rhs lines are slightly larger (≈11 nm) than the lhs lines, although they are expected to be the same when taking the tilt correctly into account in the PEC. We think that this might be due to an overcorrection caused by the approximate PSF. In Fig. 6.13, it is seen that in the mid-range between 10 nm and 1 μm the approximate PSF used in the PEC is lower than the simulated PSF. This may enhance the short-range, and indirectly, the long-range dose effects during the PEC. It causes a directional effect in the tilt (-x) direction, in each block (rhs or lhs), a line located at the left always receives a larger total dose than any other lines in that block.

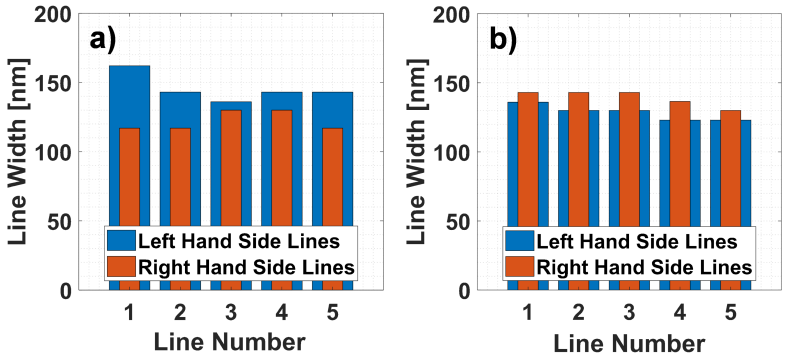


Figure 6.23: Comparison of CDs: (a) PEC without tilt correction, (b) PEC with tilt correction.

6.6. Discussion

We have shown that the PSF for exposure of a tilted surface is different than for perpendicular exposure. From the proof of principle experiments presented here, it is clear that standard PEC algorithms have to be adapted for the different PSF when exposing curved or tilted surfaces. It will improve the accuracy in the fabrication of nanostructures on such surfaces. Its effect will even be more prominent when using resist layers thicker than 150 nm, a beam energy lower than 50 keV, or an angle of incidence larger than 17°.

In this study, an energy deposition model was used to determine the number of broken bonds in the resist. However, it would be more realistic to consider individual bond breaking events [28]. Knowledge of the bond-breaking cross sections, or how to separate them from inelastic scattering cross sections, would help in achieving a more reliable PSF. However, such knowledge is still limited [23, 28, 29] even for well-known polymers such as PMMA.

In addition, in the PEC applied in this work, we have neglected the short-range effect, arguing that we expect this to be a minor effect for structure sizes of 100 nm or more. However, it should be considered for the fabrication of much smaller structures.

In the experiments, the big square structure in the middle is not fully bright in the SEM images and the inner borders (smaller squares) are visible. These regions were underexposed for the dose applied (403 $\mu C/cm^2$), but the smaller structures (lines) on the sides are overexposed at this dose. We assume that there is an imbalance between the short- and long-range dose distributions used in the tilt-corrected version, where the magnitude of the short-range dose is underestimated and the magnitude of the long-range effect is overestimated. However, the CD values of the lines on each side of the square are most relevant for this study and they are resolved well enough at this dose to perform a quantitative analysis. The CD comparison for the uncorrected exposure (Fig. 6.23a) demonstrates the asymmetry in the PSF. The rhs lines receive less dose than the lhs lines.

The adjustment made to the PEC kernel overestimates the tilt effect and leads to wider lines on the right side than on the left side (Fig. 6.23b). However, the difference in CD between the right and left sides is less in the corrected version compared to the uncorrected version.

Lastly, the asymmetric 3D PSF has been simplified into 2D, for the direction of the incident beam (-x), for ease of implementation, but a convolution kernel which uses the full 3D PSF will improve the accuracy and will solve the issues indicated above, especially for 3D structures such as circles or squares.

6.7. Conclusion

There is a growing interest in patterning nanostructures on curved or tilted surfaces using EBL. However, standardly used PSFs and PEC algorithms, developed for perpendicular patterning on flat surfaces, are not suitable for such applications.

In this study, we have demonstrated that the PSF is not radially symmetric for the exposure of tilted surfaces, using Monte Carlo simulations. The asymmetry is confirmed by a proof of principle experiment for a single point exposure.

To verify the effect more quantitatively, the nonsymmetric PSF was calculated, using simulations, and a PEC algorithm was adjusted for the exposure of a tilted substrate. A test pattern was written with and without PEC correction for tilted surfaces. The results show that it is possible to improve the fabrication accuracy in terms of critical dimension by taking the asymmetric PSF into account.

Acknowledgements

The authors want to thank Thomas Klimpel from GenISys-GmbH for helping to prepare the data, Hozanna Miro from the Kavli Nanolab Delft for allowing us to use the Helios NanoLab™ DualBeam™ microscopes, Janine Wilbers (RAITH) for helping with the exposure tool, and Carel Heerkens (Delft University of Technology) for discussions on the EBL experiments. Lastly, the authors acknowledge GenISys-GmbH and Raith B.V. for funding this project.

References

[1] J. M. Pavkovich, *Proximity effect correction calculations by the integral equation approximate solution method,* Journal of Vacuum Science & Technology B: Microelectronics and Nanometer Structures **4**, 159 (1986).

[2] M. Parikh, *Corrections to proximity effects in electron beam lithography. II. Implementation,* Journal of Applied Physics **50**, 4378 (1979).

[3] G. Owen, *Methods for proximity effect correction in electron lithography,* Journal of Vacuum Science & Technology B **8**, 1889 (1990).

[4] J. Zhou and X. Yang, *Monte Carlo simulation of process parameters in electron beam lithography for thick resist patterning,* Journal of Vacuum Science & Technology B: Microelectronics and Nanometer Structures **24**, 1202 (2006).

[5] M. Stepanova, T. Fito, Z. Szabó, K. Alti, A. P. Adeyenuwo, K. Koshelev, M. Aktary, and S. K. Dew, *Simulation of electron beam lithography of nanostructures,* Journal of Vacuum Science & Technology B, Nanotechnology and Microelectronics: Materials, Processing, Measurement, and Phenomena **28**, C6C48 (2010).

[6] Q. Dai, S. Y. Lee, S. H. Lee, B. G. Kim, and H. K. Cho, *Experiment-based estimation of point spread function in electron-beam lithography: Forward-scattering part,* Microelectronic Engineering **88**, 3054 (2011).

[7] Q. Dai, S.-Y. Lee, S.-H. Lee, B.-G. Kim, and H.-K. Cho, *Three-dimensional proximity effect correction for large-scale uniform patterns,* Journal of Vacuum Science & Technology B: Microelectronics and Nanometer Structures **29**, 06F314 (2011).

[8] V. R. Manfrinato, J. Wen, L. Zhang, Y. Yang, R. G. Hobbs, B. Baker, D. Su, D. Zakharov, N. J. Zaluzec, D. J. Miller, E. A. Stach, and K. K. Berggren, *Determining the resolution limits of electron-beam lithography: Direct measurement of the point-spread function,* Nano Letters **14**, 4406 (2014).

[9] T. H. P. Chang, *Proximity effect in electron□beam lithography,* Journal of Vacuum Science and Technology **12**, 1271 (1975).

[10] S. A. Rishton and D. P. Kern, *Point exposure distribution measurements for proximity correction in electron beam lithography on a sub-100 nm scale,* Journal of Vacuum Science & Technology B: Microelectronics and Nanometer Structures **5**, 135 (1987).

[11] D. Wilson, P. Maker, R. Muller, P. Mourolis, M. Descour, C. Volin, and E. Dereniak, *Diffractive optical elements for spectral imaging,* in *Diffractive Optics and Micro-Optics*, edited by T. Li (OSA Trends in Optics and Photonics, Québec City, 2000).

[12] D. W. Wilson, P. D. Maker, R. E. Muller, P. Mouroulis, and J. Backlund, *Recent advances in blazed grating fabrication by electron-beam lithography,* in *Proceedings of SPIE*, Vol. 5173 (2003) pp. 115–126.

[13] W. R. Johnson, S. J. Hook, S. S. Shoen, and B. T. Eng, *Hyperspectral Thermal Emission Spectrometer : Engineering Flight Campaign,* in *IEEE Aerospace Conference*, Vol. 91109 (2013) pp. 1–7.

[14] B. Van Gorp, P. Mouroulis, D. W. Wilson, and R. O. Green, *Design of the Compact Wide Swath Imaging Spectrometer (CWIS),* in *Proc. of SPIE*, Vol. 9222 (2014) p. 92220C.

[15] P. Mouroulis, B. Van Gorp, R. O. Green, H. Dierssen, D. W. Wilson, M. Eastwood, J. Boardman, B.-c. Gao, D. Cohen, B. Franklin, F. Loya, S. Lundeen, A. Mazer, I. McCubbin, D. Randall, B. Richardson, J. I. Rodriguez, C. Sarture, E. Urquiza, R. Vargas, V. White, and K. Yee, *Portable Remote Imaging Spectrometer coastal ocean sensor: design, characteristics, and first flight results,* Applied Optics **53**, 1363 (2014).

[16] S. J. Wind, P. D. Gerber, and H. Rothuizen, *Accuracy and efficiency in electron beam proximity effect correction,* Journal of Vacuum Science & Technology B **16**, 3262 (1998).

[17] T. Verduin, *Quantum Noise Effects in e-Beam Lithography and Metrology*, Ph.D. thesis, Delft University of Technology (2017).

[18] M. Stepanova and S. Dew, eds., *Nanofabrication: Techniques and Principles* (Springer Vienna, Vienna, 2012).

[19] F. Salvat, A. Jablonski, and C. J. Powell, *ELSEPA—Dirac partial-wave calculation of elastic scattering of electrons and positrons by atoms, positive ions and molecules,* Computer Physics Communications **165**, 157 (2005).

[20] E. Schreiber and H.-J. Fitting, *Monte Carlo simulation of secondary electron emission from the insulator SiO2,* Journal of Electron Spectroscopy and Related Phenomena **124**, 25 (2002).

[21] E. Kieft and E. Bosch, *Refinement of Monte Carlo simulations of electron–specimen interaction in low-voltage SEM,* Journal of Physics D: Applied Physics **41**, 215310 (2008).

[22] J. Ganachaud and A. Mokrani, *Theoretical study of the secondary electron emission of insulating targets,* Surface Science **334**, 329 (1995).

[23] B. Wu and A. R. Neureuther, *Energy deposition and transfer in electron-beam lithography,* Journal of Vacuum Science & Technology B: Microelectronics and Nanometer Structures **19**, 2508 (2001).

[24] N. Unal, D. Mahalu, O. Raslin, D. Ritter, C. Sambale, and U. Hofmann, *Third dimension of proximity effect correction (PEC),* Microelectronic Engineering **87**, 940 (2010).

[25] GenISys GmbH., *BEAMER,* (2015).

[26] J. Bolten, K. Arat, N. Ünal, C. Porschatis, T. Wahlbrink, and M. Lemme, *Challenges for scanning electron microscopy and inspection on the nanometer scale for non-IC application: And how to tackle them using computational techniques,* Proceedings of SPIE - The International Society for Optical Engineering **10446** (2017), 10.1117/12.2279564.

[27] Y. G. Li, P. Zhang, and Z. J. Ding, *Monte Carlo Simulation of CD-SEM Images for Linewidth and Critical Dimension Metrology,* Scanning **35**, 127 (2013).

[28] M. Aktary, M. Stepanova, and S. K. Dew, *Simulation of the spatial distribution and molecular weight of polymethylmethacrylate fragments in electron beam lithography exposures,* Journal of Vacuum Science & Technology B: Microelectronics and Nanometer Structures **24**, 768 (2006).

[29] P. Kruit and S. Steenbrink, *Local critical dimension variation from shot-noise related line edge roughness,* Journal of Vacuum Science & Technology B: Microelectronics and Nanometer Structures **23**, 3033 (2005).

7

Estimating Step Heights from Top-Down SEM Images

Scanning electron microscopy (SEM) is one of the most common inspection methods in the semiconductor industry and in research labs. To extract the height of structures using SEM images, various techniques have been used, such as tilting a sample, or modifying the SEM tool with extra sources and/or detectors. However, none of these techniques focused on extraction of height information directly from top-down images. In this work, using Monte Carlo simulations, we studied the relation between step height and the emission of secondary electrons (SEs) resulting from exposure with primary electrons at different energies. It is found that part of the SE signal, when scanning over a step edge, is determined by the step height rather than the geometry of the step edge. We present a way to quantify this, arriving at a method to determine the height of structures from top-down SEM images. The method is demonstrated on three different samples using two different SEM tools, and atomic force microscopy is used to measure the step height of the samples. The results obtained are in qualitative agreement with the results from the Monte Carlo simulations.

This chapter is published as a journal paper:
Kerim Tugrul Arat, Jens Bolten, Aernout Christiaan Zonnevylle, Pieter Kruit, Cornelis Wouter Hagen: Estimating Step Heights from Top-Down SEM Images. *Microscopy and Microanalysis*, 05/2019, DOI:10.1017/S143192761900062X https://doi.org/10.1116/1.5120631

7.1. Introduction

Scanning electron microscopy (SEM) based systems are major inspection and metrology tools to measure critical dimensions (CDs) in nanofabrication because they provide optimal functionality by combining high-resolution with high-speed, and non-destructive imaging [1, 2]. However, information from 3D samples reduces to a gray-scale value in SEM micrographs, where one cannot easily measure the structure height.

To obtain structure height, or a 3D map of the surface in general, combinations of tools and techniques are being employed such as stereo vision, structure from motion, or stereophotogrammetry [3–6]. In these methods, a sample is illuminated and/or viewed at different angles by introducing extra sources, detectors, and/or tilting the sample such that feature height is measured as a lateral distance, or at least can be calculated from the projection. However, this is not practical or even possible in many scenarios, especially in wafer-scale production [7]. Furthermore, the accuracy of state of the art commercial software packages is disputed in the literature [8, 9]. Although the aforementioned reconstruction methods have been in use for a few decades, height information embedded in top-down SEM images itself is not studied well enough. Extraction of the embedded information can improve the efficiency of available techniques and also lead to measuring the height directly from top-down (0° tilt angle) SEM images, which are already available for CD measurements.

In this work, we studied the relation between step height and the emission of secondary electrons (SEs) resulting from exposure with primary electrons (PEs) at different energies. The material of choice is silicon (Si). As visualized in Fig. 7.1, the SE emission on the sidewall of the step depends on the PE energy and the step height. By using this phenomenon, we present a method to determine the height of structures from top-down SEM images.

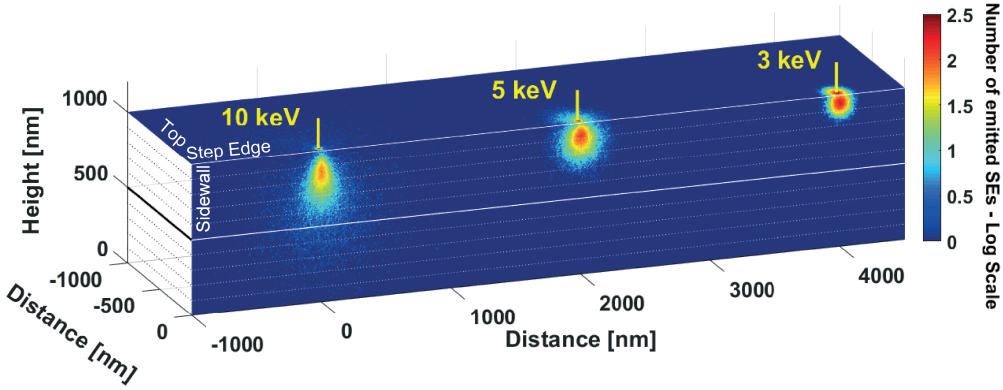


Figure 7.1: SE emission sites on the top and the sidewall of a (1 µm high) step are shown for three acceleration voltages (10, 5, and 3 keV). The zero-diameter electron beam (with 10^4 electrons) lands on top of the step, 50 nm away from the edge. The white dashed lines on the sidewall aid in judging how many electrons can actually be emitted from a particular depth of the step.

7.2. Theory and simulation

When a sample is exposed by using an electron probe, the size of the electron interaction volume inside the material is a function of material properties and beam energy. The number of electrons emitted from the sample is proportional to the intersection of the interaction volume and the sample surface.

Consider two step heights, formed by the sidewall of the Si step shown in Fig. 7.1, one bounded by a horizontal plane (Si) at 200 nm depth from the top surface, and the other bounded by a plane (Si) at 500 nm depth. The cross-sections of these steps are illustrated in Figs. 7.2a-7.2d.

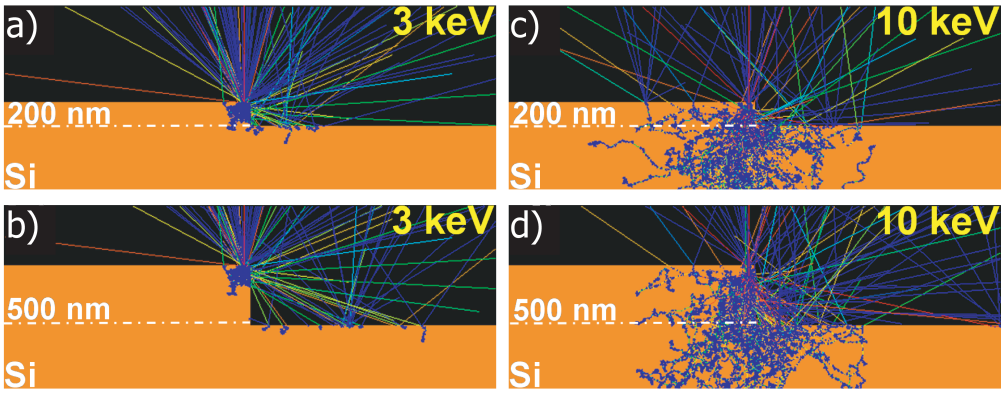


Figure 7.2: Cross-sectional view of the interaction volume with respect to step height and beam energy. The horizontal field of view is 4 µm and a zero diameter beam is focused 50 nm left from the step edge.

At low energy (e.g., 3 keV as in Figs. 7.2a, 7.2b), electrons do not penetrate deeper than the height of the steps. Therefore, the same number of electrons will be emitted, even though the steps are different in height. In other words, at this beam energy the emission is insensitive to step height.

If the beam energy is increased, the interaction volume becomes larger and effectively shifts down. At a certain energy, some of the electrons penetrate deeper than the height of the smaller step and are buried in the sample. However, those electrons can still escape from the lower part of the sidewall of the higher step and contribute to the detected signal, as illustrated in Figs. 7.2c and 7.2d.

The increase in the SE signal intensity when scanning over an edge is a well-known phenomenon (topographic contrast) [10], and frequently used to measure lateral sizes from SEM images, but its connection with the height, as described above, has not yet been exploited in a quantitative way. To establish this connection, we use Monte Carlo simulations.

A simulator, e-scatter [11] models the elastic scattering using Mott cross-sections for energies higher than 200 eV, including solid-state effects using a muffin-tin potential, as calculated using ELSEPA [12]. For energies lower than 100 eV, electron-phonon scattering is taken into account [13, 14]. For energies in between, the scattering cross-

sections of the two mechanisms are interpolated [11]. The inelastic scattering and the generation of SEs are based on dielectric function [15]. Boundary crossing is modeled based on momentum conservation and extended with the quantum mechanical transmission probability [16]. The simulator traces all electrons until they either reach the flat detector at the top of the sample or end up with energy too low to escape from the material. Moreover, the simulator runs on a graphics processing unit such that it benefits from massive parallelism [17].

Now, we extend the analysis from single spot exposure mode, as shown in Fig. 7.2, to line scan mode. Fig. 7.3 compares the simulated line scans, using 20,000 electrons per 1 nm x 1 nm pixel (these are default values, unless stated otherwise) over the 200 and 500 nm steps shown in Fig. 7.2. In Fig. 7.3a the topographic contrast is clearly seen, but the SE signal resulting from exposure with a 3 keV beam is the same for both step heights.

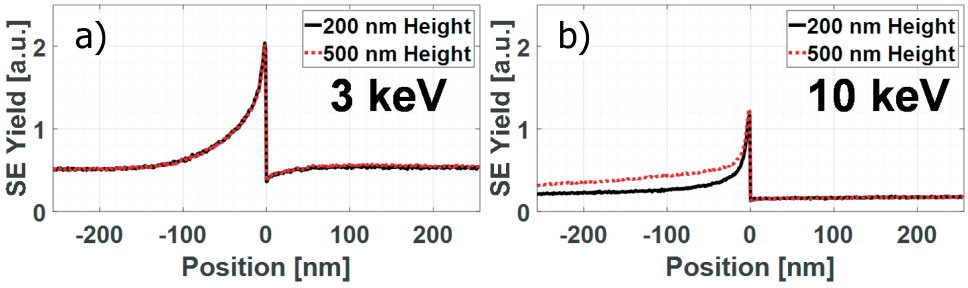


Figure 7.3: SE signal when scanning a PE beam of 3 and 10 keV over two step edges of 200 and 500 nm. a: The depth of the interaction is within the range of the step height at 3 keV and (b) more electrons intersect with the sidewall of the 500 nm step edge, leading to a larger signal intensity at 10 keV.

At 10 keV, electrons penetrate more than 200 nm in the material, where they intersect with a larger surface area on the sidewall of the 500 nm step (Figs. 7.1, 7.2c, 7.2d) than the 200 nm step. Therefore, the SE signal for the two step heights will be different (Fig. 7.3b) and that difference allows for the determination of the height difference. It is seen that the signal difference extends quite a distance away from the edge. Close to the edge, the signal may be influenced by the actual topography of the step edge, i.e., sidewall angle or edge rounding. To judge which portion of the signal is rather insensitive to such influences, and can therefore be used for the height determination, a few realistic step topographies are simulated first.

First, the effect of sidewall angle on line scans is investigated, with -5° and +5° deviations of a 90° sidewall. Fig. 7.4a shows the 90° sidewall. Fig. 7.4b has a negative sidewall angle and the dip at the foot of the steep signal drop disappears. Fig. 7.4c has a positive sidewall angle, and an additional feature appears in the peak of the signal. The comparison shows that the signal intensities in the peak and at the foot are very sensitive to variation in the sidewall angle. Therefore, the signal around the peak is to be avoided in the height analysis.

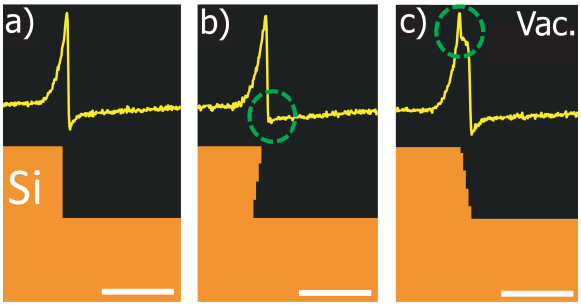


Figure 7.4: Effect of sidewall angle of a Si step edge on the SE line scan signal: (a) 90° sidewall, the signal has a peak and a dip at the foot; (b) -5° sidewall angle, creating an undercut, the dip at the foot disappears; and (c) +5° sidewall angle, an additional feature shows up in the peak. The scale bar is 100 nm and the beam energy is 1 keV.

It is also expected that the beam spot size will influence the scan signal near the step edge. Fig. 7.5 shows the simulated line scan over the 500 nm step height for four different spot sizes. The peak and the dip at the foot of the signal are both very sensitive to the beam spot size. However, the lateral region between -64 and -4 nm shows the same intensity for spot sizes smaller than 3 nm (full width at half maximum; FWHM), i.e., step height analysis in this region is insensitive to spot size variations. The 10 nm spot, however, provides so much blur that height information and spot-size effects will be difficult to separate.

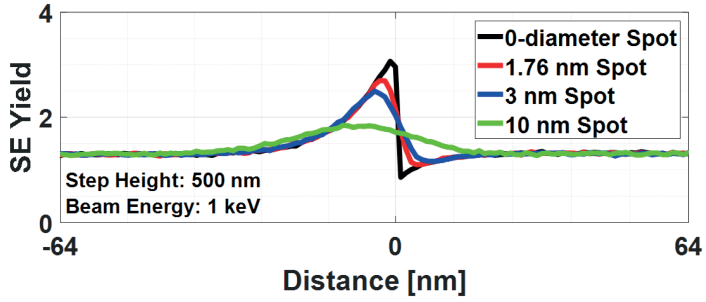


Figure 7.5: Spot size effect: the intensity and the position of the peak and the dip of the signal change with the incident beam diameter (FWHM).

Finally, the effect of slightly more realistic edge shapes on the line scan signals was simulated. Two infinitely long lines of different heights are placed at a pitch of 2 µm. Fig. 7.6 shows the cross-sectional view of these lines. The left edges of the lines have perfectly sharp edges with a 90° sidewall. The right-hand side edges have different curvatures.



Figure 7.6: Cross-section of lines of 500 and 200 nm in height. The top and the bottom widths of the lines are 500 nm, resp. 550 nm. The pitch is ≈2 µm. The left sidewalls of the structures are sharp vertical edges. The right edges are rounded and the side- walls follow the curvature of the edge.

Line scans were simulated at two different energies, 3 and 10 keV, and shown in Fig. 7.7. The signals were aligned in order to clearly see the differences. In Fig. 7.7a, the signals are identical for the left edge, but not for the right edge. At 3 keV, the effect of the edge shape and the sidewall angle is seen, but not the effect of the height difference. In Fig. 7.7b, when the energy is increased to 10 keV, the signal for the 500 nm step at the left side edge becomes different. This difference is even more visible all the way into the valley between both edges. Although the peak (intensity and shape) of the signal is very sensitive to the height, as well as all other imperfections close to the edge, fortunately the region in between the edges is less sensitive to the position of the edge and the shape of the sidewall, and still sensitive to the step height difference.

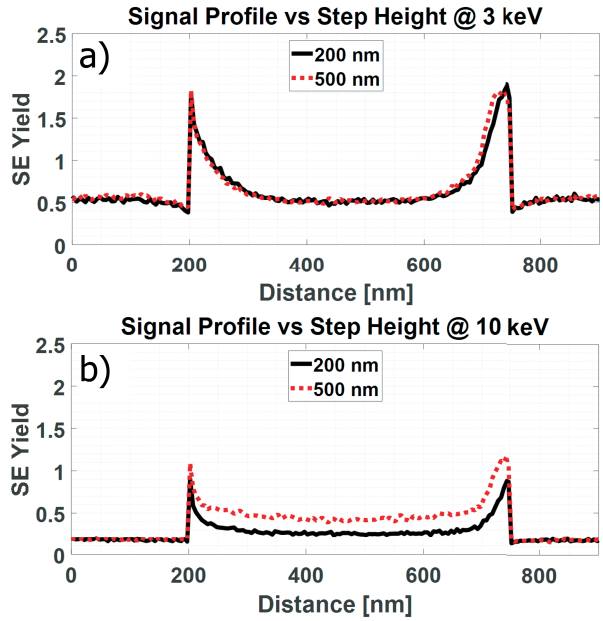


Figure 7.7: Line scan signal sensitivity to height differences and sidewall shape differences. The line scans are simulated for the structures in Fig. 7.6 at (a) 3 keV and (b) 10 keV, and a zero-diameter beam. In total, 10^4 electrons were used per pixel.

The analysis from simulations above demonstrates that there is a region in the line scan signal that is sensitive to height but not sensitive to the electron beam size and the actual edge shape. To make the height determination analysis more quantitative and less sensitive to the noise level, the area below the scan signal in the height sensitive region will be determined. Even if the noise level is high in SEM, integration over the signal (area) is a powerful noise suppression technique and will allow us to differentiate the step heights. This requires, first of all, the determination of the edge position as a reference point. This problem has also been addressed in the literature concerning CD measurements [18–22]. Although the model-based-library approach

[22] is a more accurate method, for practical reasons here the maximum intensity method is preferred, i.e., the edge position is assumed to be at the location where the signal attains a maximum. An example line scan signal, f_s, is shown in Fig. 7.8, where the peak indicates the edge position. The vertical dashed lines a_1 and a_2 indicate the left and right boundaries, respectively, between which the area below the signal is to be determined by integration. The right boundary a_2 needs to be chosen sufficiently far from the edge to avoid edge topography influences, as discussed above. The baseline level, f_b, determined by the SE yield at the beam energy used and by the brightness settings of the microscope, is subtracted from the signal.

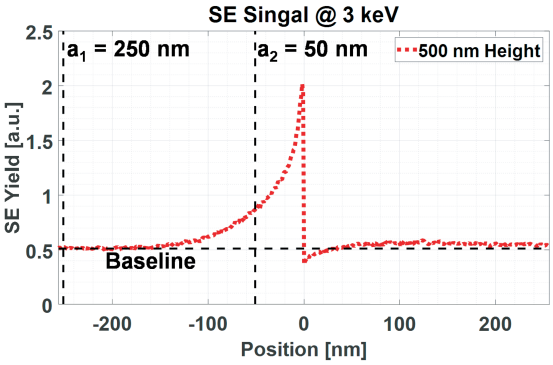


Figure 7.8: Illustration of the signal integration method. A simulated line scan signal of a 500 nm high step is shown as the red dotted line; the edge position is taken where the intensity is maximum; the integration boundaries are drawn by the two vertical dashed lines at a_1 (250 nm) and a_2 (50 nm) from the edge.

In brief, the height sensitive information, I_h is given by

$$I_h = \int_{a_1}^{a_2} [f_s(x) - f_b]dx \tag{7.1}$$

Fig. 7.9 shows the integrated area, I_h for simulated scan signals over different step heights integrated between 250 and 50 nm away from the edge and for beam energies ranging from 100 eV to 20 keV.

Initially the integrated signal increases with energy, as the interaction volume increases as well as its intersection with the sidewall of the step edge. When the interaction volume reaches depths larger than the step height, the integrated signal reaches a maximum, and decreases for even higher energies (20 keV) where less and less electrons can escape from the sample. The overlapping curves at low energies prevent resolving step heights at low energies. But at higher energies the curves are well separated.

For instance, at 1 keV one cannot distinguish the height difference between a 200 and a 500 nm step, but at 8 keV one easily can. To determine the best energy to distinguish step heights Fig. 7.10a and Fig. 7.10b show the integrated signals of Fig. 7.9 plotted versus step height for various primary energies. It is clearly seen that energies lower than 2 keV are not useful to distinguish step heights between 10 and 500 nm.

Only at higher energies do the curves start to increase with step height. At 5 keV

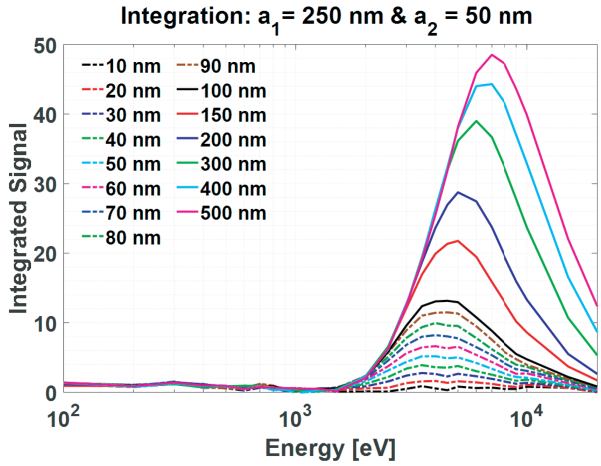


Figure 7.9: Integrated area below the line scan signals over step edges of various step heights and as a function of incident electron energy.

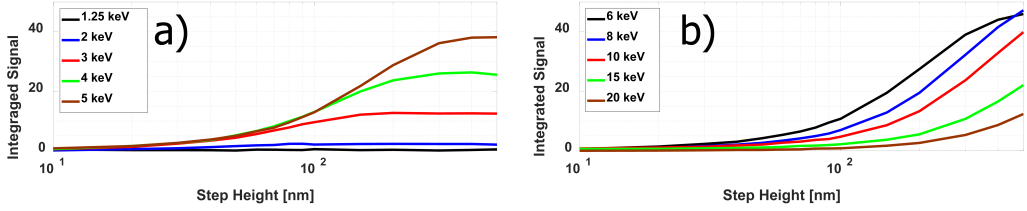


Figure 7.10: Integrated signal versus step height for primary energies between 1,000 eV and 20 keV.

heights up to 300 nm can be distinguished, although the height difference between 10 and 20 nm steps is better detected at lower energy, e.g., 3 keV. Fig. 7.10b shows that at 6 keV larger step height differences up to 500 nm can be detected, but at even higher energies the sensitivity decreases.

From Fig. 7.9 it is clear that to distinguish steps from each other in a set of step heights, the best energy to use is the energy where the integrated signal of the largest step height in the set attains its maximum. Fig. 7.11 shows the step height versus the energy, where the integrated signal is at maximum for that particular step height. It needs to be pointed out that the simulation results shown so far are affected by the particular choice of the integration boundaries. Fig. 7.11 also shows results for other choices of the integration boundaries. If the integration window is narrowed from the left (a_1) the maxima of the step height curves in Fig. 7.9 are pushed to lower energies for higher steps. If the integration window is narrowed from the right (a_2) the smaller step height curves are pushed to higher energies. But in both cases, it remains possible to find a best energy to distinguish between step heights.

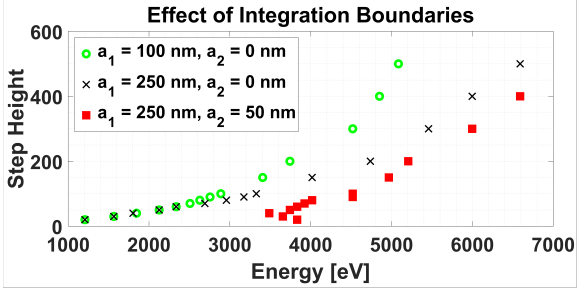


Figure 7.11: The effect of the integration boundaries on the step height versus energy where the integrated signal is at maximum. Crosses are for boundaries 250 nm to edge (50 nm); squares indicate that the area is narrowed from the right (boundary a_2) and circles indicate that the area is narrowed from the left (boundary a_1).

7.3. Experiments

To validate the technique, we have performed experiments on two available samples: (i) a grating coupler of a photonic integrated circuit (smaller step heights) and (ii) an inverted pyramid (larger step heights).

In Fig. 7.12, a cross-sectional view along the center of the device is sketched. The device consists, from bottom to top, of a 2 µm thick silicon dioxide SiO_2 slab and a 55 nm thick Si slab. These are supported by a Si substrate (not shown). There are three different structures: (i) the waveguide (on top of the Si slab), thickness ≈165 nm; (ii) the grating couplers (trenches in the top surface), trench depth ≈70 nm; and (iii) the trenches in the 55 nm thick Si slab, all the way down to the SiO_2 (the bright rectangles in Fig. 7.13), trench depth ≈55 nm. The latter one is not included in this study due to possible charging effects around the oxide.

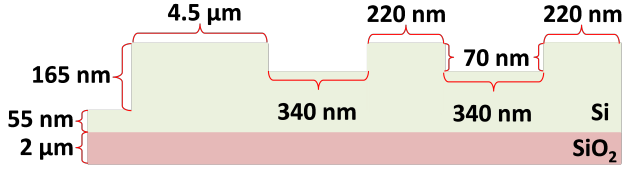


Figure 7.12: Description of the grating coupler geometry: the step height determination was performed for the 165 and 70 nm steps only.

Several SEM images of the grating coupler were acquired, at the AMO cleanroom facility, at energies ranging from 0.5 to 20 keV, using a Zeiss Supra 60 VP SEM (Oberkochen, BW, Germany) with an in-lens detector. The beam was manually refocused for each acceleration voltage. All other parameters were kept constant (pixel size = 2.9 nm, working distance = 3.0 mm, contrast = 35.6%, brightness = 49.9%).

In Fig. 7.14, the line scan signals are aligned by their peak positions and plotted on top of each other for demonstration purposes. As the beam energy is increased, the signals start to differ from each other. This very first comparison qualitatively illustrates that the step heights are different and it shows which step is the larger one of the two.

Next, the signal integration method is applied with the same integration boundaries

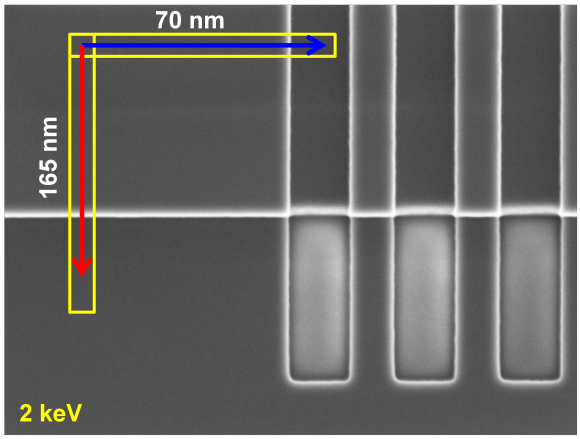


Figure 7.13: Top-down SEM image of the grating coupler at 2 keV. HFW: 2.969 µm. Regions are indicated where the line scans are made. Line scans are averaged over the yellow frames along the corresponding arrows. The arrows point from a higher to a lower position.

as used in the simulations, and the result is shown in Fig. 7.15. The integrated signal for the lower step (70 nm) reaches its maximum at 5.6 keV. Using the simulation results in Fig. 7.11 this maximum energy corresponds to a step height of ≈251 nm. Similarly, the integrated signal for the higher step (165 nm) reaches its maximum at 6.48 keV, which corresponds to a simulated step height of ≈393 nm. Both values are overestimated. However, 50 nm as the upper integration boundary a_2 is a large value for a small step height (70 nm). If a_2 is lowered to 10 nm, the method estimates the 70 nm step height as 189 nm. As expected, this change does not influence the larger step (398 nm). The ratio of the estimated heights becomes 2.10 (398 nm /189 nm), compared with the actual ratio of 2.35 (165 nm /70 nm).

The second sample is a staircase-like sample with a cross-section that looks like an inverted pyramid (see Fig. 7.16). The structures were fabricated using optical lithography and dry etching. A regular pattern of lines and spaces was first defined on the sample and then etched ≈500 nm deep into the silicon. Next, the sample was cleaned and, using the same mask, shifted by 700 nm, and with an identical etching process a second etch depth was realized. The same cycle was repeated three more times to create an inverted step pyramid with five steps, each step ≈500 nm deep and 700 nm wide.

Atomic force microscopy (AFM) measurements were performed to measure the step heights at two different locations on the same set of lines. The line scans shown in Fig. 7.17 show the same step height but the step heights deviate from the nominal value (500 nm) and are also different from each other. The maximum difference is 135 nm and the minimum difference is 26 nm.

A top-down SEM image is shown in Fig. 7.18. The SEM images were acquired at the AMO cleanroom facility with the same instrument in which the grating coupler was imaged. Images were taken at 42 different energies between 0.5 and 20 keV. For each acceleration voltage the beam was manually refocused. Moreover, inspection was performed at a new region along the same line in order to minimize potential

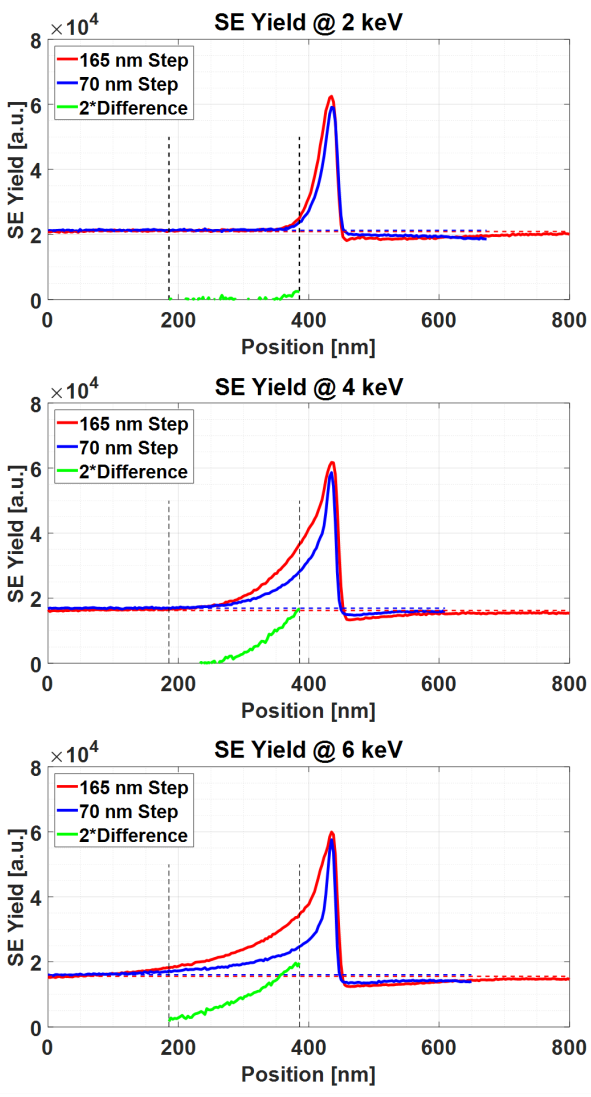


Figure 7.14: Experimental step height comparison for the grating coupler sample. Two different step heights are compared at different beam energies. The vertical dashed lines indicate the region where the signal is less sensitive to geometric imperfections. The green curve "2x Difference" indicates the difference signal, i.e., "70 nm Step" subtracted from "165 nm Step" and then multiplied by 2.

contamination from the previous acquisition. The entire acquisition process took approximately 30 min. All other parameters were kept constant 8horizontal field width, HFW = 10.035 µm, pixel size = 9.8 nm, working distance = 2.8 mm, contrast = 32.4%, brightness = 50.6%).

In the analysis the right-hand side stairs in Fig. 7.18 are not included because of the irregularities seen in the fourth and fifth edges from the right. Also, it should

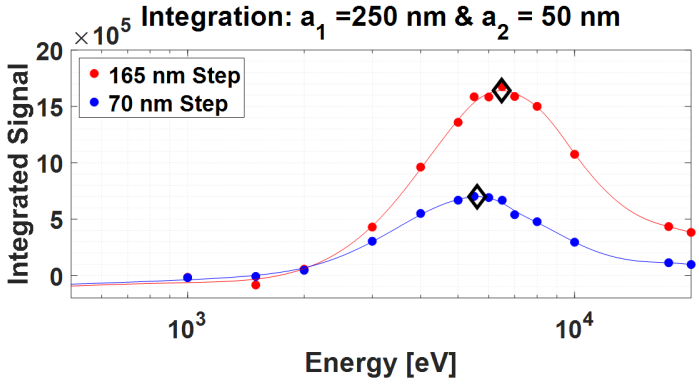


Figure 7.15: Integrated signal analysis for the grating couplers. The signals reach a maximum at 5,600 eV (70 nm) and 6,480 eV (165 nm), which are marked by diamonds (DIAMOND)

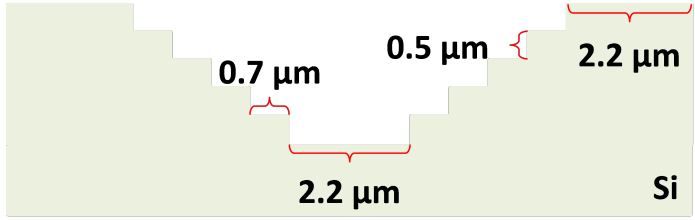


Figure 7.16: Cross-section of the inverted pyramid Si sample: from top to bottom five steps are present at each side. Nominally, each step height is 500 nm and the step width is 700 nm. Top and bottom widths are 2.2 µm.

be noted that the left most (the first) step is geometrically not quite identical to the others. All other steps have an obstacle (another step) to their left-hand side, which may prevent emitted electrons from reaching the detector. Therefore, the first step cannot be compared well with the other steps and is excluded from the analysis. The line scan plots can be found in the supplementary document. The integrated signals are plotted versus energy for all steps in Fig. 7.19.

There is some general agreement between the experiments and the simulations: the integrated signals coincide at low energies and at higher energies the higher step gives a larger signal. Only at very high energies (≈20 keV) deviation is observed: the 526 nm step gives a larger signal than the 552 nm step.

To learn how the result of this analysis depends on the specific imaging tool used and the experimental conditions, a sister sample from the same wafer was imaged using a Raith eLINE Plus system (Dortmund, NRW, Germany). At Raith's cleanroom

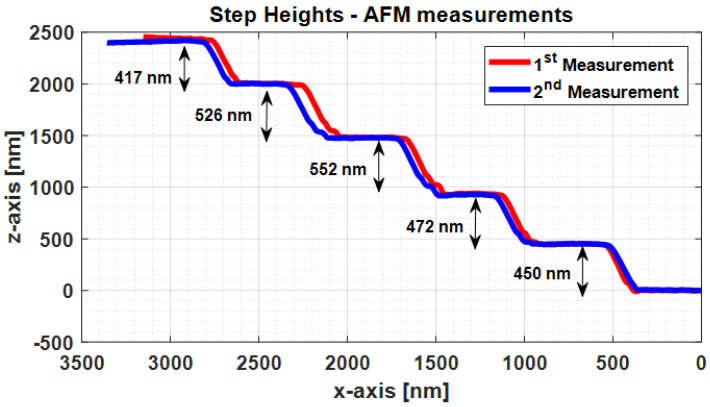


Figure 7.17: AFM measurements of the step heights in the inverted pyramid sample.

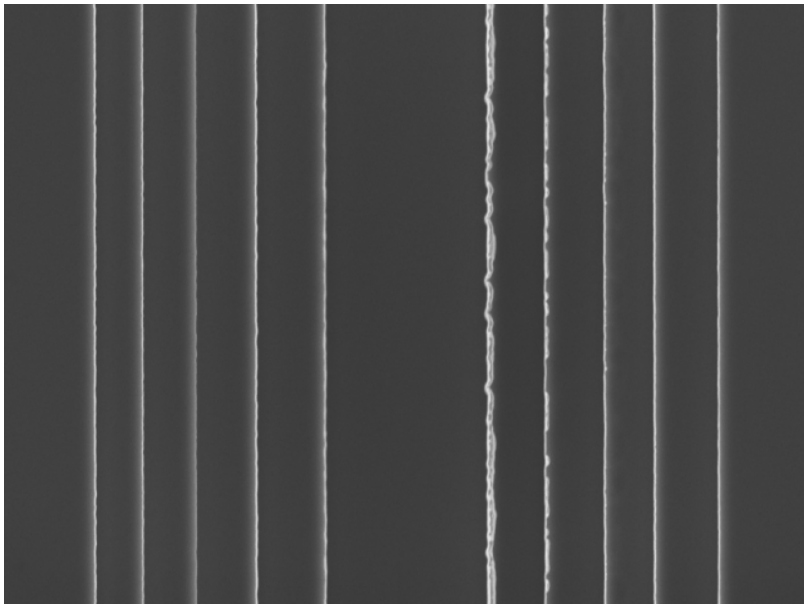


Figure 7.18: Top-down SEM micrograph of the inverted pyramid at 4 keV.

facility the same procedure was followed as used at AMO and subsequently plasma cleaning was applied for 15 min before inspection to minimize carbon deposition. For all energies the following parameters were kept constant: Field of view (FoV) = 6.0

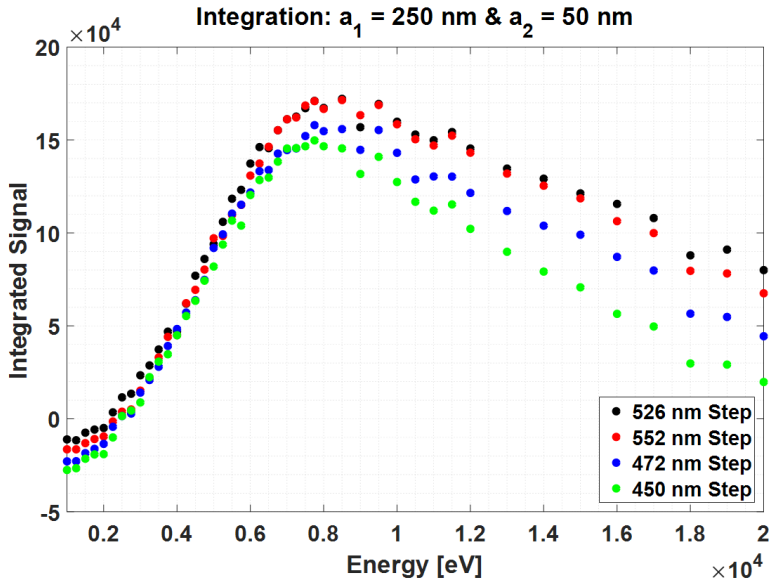


Figure 7.19: Integrated signal analysis of the inverted pyramid for the images acquired with a Zeiss Supra SEM (a_1 = 250 nm and a_2 = 50 nm).

µm, pixel size = 2.0 nm, working distance = 6.6 mm, contrast = 25.1%, and brightness = 49.3%. Fig. 7.20 shows an SEM image of the left stairs of the sample at 4 keV.

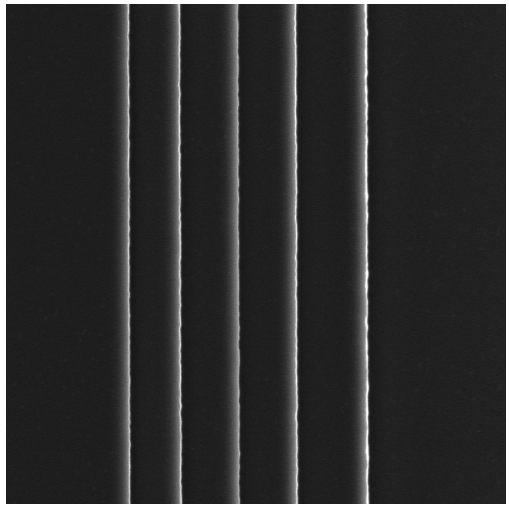


Figure 7.20: Top-down SEM image of the steps (only left-side) at 4 keV. FoV = 8.0 µm, taken with the RAITH eLINE Plus SEM.

The integrated signals of the line scans over these steps are shown in Fig. 7.21. At

higher energies (20 keV), the results are in conflict with the AMO results of Fig. 7.19, but agree with the simulation results. However, at lower energy (<10 keV), deviations from the simulations are observed: the signal of the 450 nm step is larger than the signal of the 526 nm step.

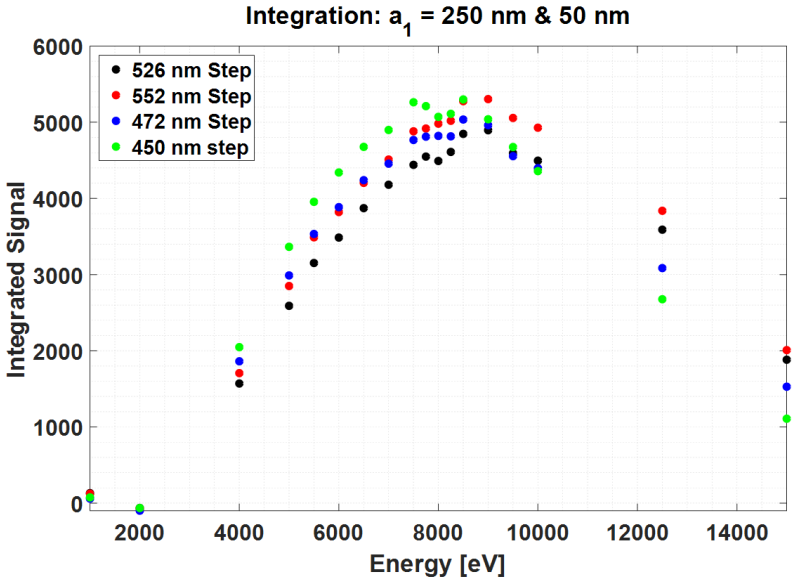


Figure 7.21: Integrated signal analysis of the inverted pyramid using images acquired with the Raith eLine plus SEM (a_1 = 250 nm and a_2 = 50 nm).

Similarly, as was done with the simulation results, in Fig. 7.21 the height of each step, analyzed in the AMO and Raith experiments, is plotted versus the energy where the integrated signal of the line scan over that step is maximum. The simulation data are also replotted.

The experimental results show a similar trend to the simulation results, i.e., for larger step heights the peak of the integrated signal versus energy curve shifts to higher energy. The simulated integrated signals peak at energies about 1.5 keV lower than the experimental signals, which all seem to lie close to a universal curve.

7.4. Discussion

The results show that by using the proposed method, height differences in step-like structures can be easily distinguished from top-down SEM images. This gives metrologists a quick impression of height differences in structures in a very early stage of the inspection. But the quantification of the actual step heights still leaves something to be desired. The simulation results being shifted to lower energies than the experimental data in Fig. 7.22 is something that needs an explanation. Possible causes could be:

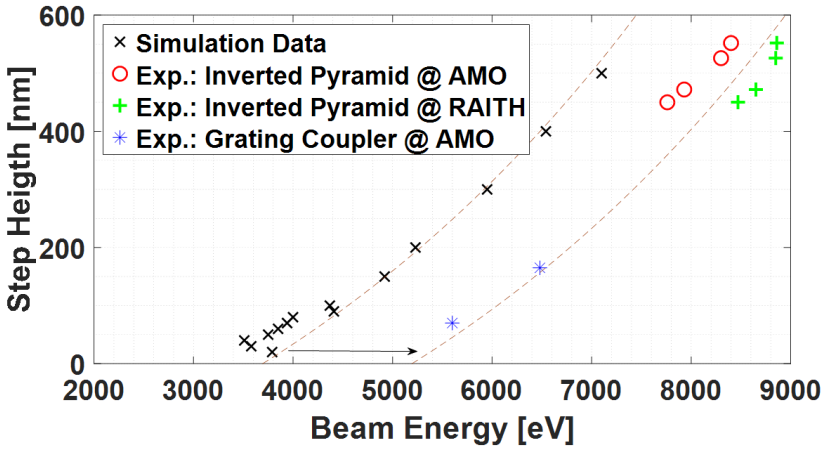


Figure 7.22: Simulations and experiments compared: step height versus energy where the integrated signal attains its maximum (a_1 = 250 nm and a_2 = 50 nm). The shift shown between the dashed lines is 1.5 keV.

1. The scattering models in the simulator do not sufficiently well describe the reality yet.

2. The sample that is being simulated is likely to be an idealized version of the real sample, which is probably covered with surface oxides, contamination layers, layers of water, etc. Specifically in the case of the grating coupler, at higher energies (3 keV) electrons will penetrate into the underlying silica layer, thereby influencing the size of the interaction volume, where in the simulation the sample consisted of Si only. And the results of the staircase-shaped-inverted pyramid sample may very well be influenced by extra emission or absorption, that is not present in the simulated isolated step edge.

3. Operation and tool effects [23] such as the detection efficiency, which is not taken into account yet in the simulation. It is interesting to see that, although the trends in the experimental results qualitatively agree with each other, the two different AMO experiments are located at lower energies (Fig. 7.22), but the Raith experiments are shifted toward higher energies. Furthermore, having automated acquisition systems such as an automated focusing function would decrease possible operator influence on the results. However, brightness and contrast values should be fixed.

The method was demonstrated using step edges, but is not limited to step edges only. It can also be applied to narrow lines. This could even give a better contrast

because the emission difference will originate from two sidewalls instead of one. However, one needs to consider the region omitted from the signal in the analysis. In this study 50 nm near the peak in the scan signal was omitted, which can clearly not be done for lines narrower than 50 nm. In that case a smaller region needs to be omitted, meaning that a better knowledge of the edge geometry is required.

Unfortunately, the method presented cannot be used in CD-SEMs as it is, which are mostly operated at low voltages 300-800 eV [2]. Fig. 7.9 and Fig. 7.10 show that 300 eV cannot resolve height information above 10 nm.

The method explained here, to find the energy that gives the maximum integrated signal, can be laborious in case there is no auto-focus function of the tool. In that case, it would suffice to take images at three different energies and apply a Gaussian-type fit to find the maximum.

7.5. Experiments

In this study step heights were determined from top-down SEM images, using Monte Carlo simulations and experiments. It was shown that the SE signal, when scanning over an edge, is very sensitive to various factors such as the actual edge shape, sidewall angle, beam spot size, but also the height of the structure. Using Monte Carlo simulations it was discovered that part of the scan line signal is sensitive to height but not sensitive to the other parameters stated above. This enables the use of standard top-down SEM images for the height measurement of step-like features. A practical method has been introduced to quantify the heights from top-down images. The method has been applied on three different samples that were imaged in two different SEMs. The step heights of samples were measured using AFM. The method consists of acquiring a series of top-down SEM images at a range of PE energies. The integrated scan line signals, when scanning over a step edge, show a maximum for a specific energy (E_{max}). The step heights, as determined from the AFM measurements, are found to lie close to a universal curve when plotted versus the experimentally determined E_{max}. Furthermore, this curve is in qualitative agreement with the simulation results. More data, on various samples, and in various tools, may provide more confidence in the method proposed, and will aid in making the method more quantitative.

Finally, this work is a nice example of how Monte-Carlo simulations can be used to analyze a complex scenario. Without the insight obtained by the simulations it would be very difficult to deduce such knowledge from experiments.

Supplementary material

The supplementary material for this article can be found at https://doi.org/10.1017/S143192761900062X.

Acknowledgements

We are grateful to Gaudhaman Jeevanandam and Luc van Kessel for reading and correcting the manuscript. We are thankful to Martin Kamerbeek for AFM measurements. We also acknowledge GenISys-GmbH and Raith B.V. for funding the research project on modeling of electron-matter interactions.

References

[1] E. Solecky, A. Rasafar, J. Cantone, B. Bunday, A. Vaid, O. Patterson, A. Stamper, K. Wu, R. Buengener, W. Weng, and X. Dai, *In-line E-beam metrology and defect inspection: industry reflections, hybrid E-beam opportunities, recommendations and predictions,* Proceedings of SPIE , 101450R (2017).

[2] N. G. Orji, M. Badaroglu, B. M. Barnes, C. Beitia, B. D. Bunday, U. Celano, R. J. Kline, M. Neisser, Y. Obeng, and A. E. Vladar, *Metrology for the next generation of semiconductor devices,* Nature Electronics **1**, 532 (2018).

[3] E. T. Faber, D. Martinez-Martinez, C. Mansilla, V. Ocelík, and J. T. M. De Hosson, *Calibration-free quantitative surface topography reconstruction in scanning electron microscopy,* Ultramicroscopy **148**, 31 (2014).

[4] M. Eulitz and G. Reiss, *3D reconstruction of SEM images by use of optical photogrammetry software,* Journal of Structural Biology **191**, 190 (2015).

[5] A. P. Tafti, A. B. Kirkpatrick, Z. Alavi, H. A. Owen, and Z. Yu, *Recent advances in 3D SEM surface reconstruction,* Micron **78**, 54 (2015).

[6] W. Shanklin, *2D SEM images turn into 3D object models,* CoRR **abs/1602.0** (2016), arXiv:1602.05256 .

[7] C. G. Frase, D. Gnieser, and H. Bosse, *Model-based SEM for dimensional metrology tasks in semiconductor and mask industry,* Journal of Physics D: Applied Physics **42** (2009), 10.1088/0022-3727/42/18/183001.

[8] F. Marinello, P. Bariani, E. Savio, A. Horsewell, and L. De Chiffre, *Critical factors in SEM 3D stereo microscopy,* Measurement Science and Technology **19**, 065705 (2008).

[9] V. N. Tondare, J. S. Villarrubia, and A. E. Vladár, *Three-Dimensional (3D) Nanometrology Based on Scanning Electron Microscope (SEM) Stereophotogrammetry,* Microscopy and Microanalysis **23**, 967 (2017).

[10] L. Reimer, *Scaning Electron Microscopy*, 2nd ed., Vol. 45 (Springer, Heidelberg, 1998).

[11] T. Verduin, *Quantum Noise Effects in e-Beam Lithography and Metrology*, Ph.D. thesis, Delft University of Technology (2017).

[12] F. Salvat, A. Jablonski, and C. J. Powell, *ELSEPA-Dirac partial-wave calculation of elastic scattering of electrons and positrons by atoms, positive ions and molecules,* Computer Physics Communications **165**, 157 (2005).

[13] H. J. Fitting, E. Schreiber, J. C. Kuhr, and a. Von Czarnowski, *Attenuation and escape depths of low-energy electron emission,* Journal of Electron Spectroscopy and Related Phenomena **119**, 35 (2001).

[14] E. Schreiber and H.-J. Fitting, *Monte Carlo simulation of secondary electron emission from the insulator SiO2,* Journal of Electron Spectroscopy and Related Phenomena **124**, 25 (2002).

[15] E. Kieft and E. Bosch, *Refinement of Monte Carlo simulations of electron–specimen interaction in low-voltage SEM,* Journal of Physics D: Applied Physics **41**, 215310 (2008).

[16] R. Shimizu and Z.-J. Ding, *Monte Carlo modelling of electron-solid interactions,* Reports on Progress in Physics **55**, 487 (1992).

[17] T. Verduin, S. R. Lokhorst, and C. W. Hagen, *GPU accelerated Monte-Carlo simulation of SEM images for metrology,* Proceedings of SPIE **9778**, 97780D (2016).

[18] A. Karabekov, O. Zoran, Z. Rosenberg, and G. Eytan, *Using monte carlo simulation for accurate critical dimension metrology of super small isolated poly-lines,* Scanning **25**, 291 (2003).

[19] M. Tanaka, J. S. Villarrubia, and A. E. Vladár, *Influence of focus variation on linewidth measurements,* in *Proceedings of SPIE*, Vol. 5752, edited by R. M. Silver (2005) p. 144.

[20] J. S. Villarrubia, A. E. Vladár, and M. T. Postek, *Scanning electron microscope dimensional metrology using a model-based library,* Surface and Interface Analysis **37**, 951 (2005).

[21] J. S. Villarrubia, A. E. Vladár, and M. T. Postek, *Simulation study of repeatability and bias in the critical dimension scanning electron microscope,* Journal of Micro/Nanolithography, MEMS, and MOEMS **4**, 033002 (2005).

[22] C. Shishido, M. Tanaka, and M. Osaki, *CD-bias reduction in CD-SEM line-width measurement for the 32-nm node and beyond using the model-based library method,* Proceedings of SPIE **7272**, 72722C (2009).

[23] M. T. Postek and A. E. Vladár, *Does your SEM really tell the truth? How would you know? Part 1,* Scanning **35**, 355 (2013).

8

Valorization

The scaling down of features in each process node poses various technical challenges to the semiconductor industry. Significant research activity is required to improve fundamental understanding, develop new methods, and standardize them. The research is a wide-scale and an expensive process. It has been suggested the industry to collaborate with universities [1]. The collaboration provides the industry cost-effective access to the ecosystem for early-stage research activities [2].

On the other side, universities seek funds for their research activities. In addition, the expectations to contribute to the economic growth [2] and development of the society [3] lead universities to team-up with industry to apply their knowledge to state of the art challenges.

This research is a very good example of a university-industry-collaboration. The parties actively shared their expertise for a real understanding of a range of problems. The university contributed with its fundamental knowledge within the ecosystem, but also the tools and facilities such as microscopes and a cleanroom. Besides funding, the industrial partners provided access to their software and programming support (GenISys-GmbH) and access to lithography and metrology tools in their cleanrooms (RAITH B.V.). Besides, the industrial partners provided interesting fundamental problems that the semiconductor industry faces. As a result, first of all, we have developed comprehensive knowledge of electron-matter scattering and charging. The applications introduced in chapters 4-7, providing solutions for 3D and charging related problems in imaging and lithography, were brought in by our industrial partners. The models and implementation of e-Scatter have been improved. And also the scattering and charging models in virtualSEM were advanced considerably. An example is the spiral scanning mode, which is implemented in RAITH's EBPG and in GenISys' lithography software BEAMER during this period [4].

As a contribution to scientific knowledge, beside this dissertation, 5 scientific journal papers were published. Furthermore, the results were disseminated at 12 different international conferences on 3 continents, and presented in numerous meetings within the university. Moreover, some of the results became part of the course mate-

rials in ”High Resolution Imaging”, 1st year M.Sc. course for Nanobiology and elective for biomedical engineering, applied physics, and life science & technology. 5 bachelor students in Applied Physics participated in the research and completed their final projects.

In a nutshell, we believe that the university, industry and society benefited directly and indirectly from this collaboration. Its impact will continue with the further exploitation of the tools and applications in the future.

References

[1] ITRS, *ITRS*, Tech. Rep. (2015).

[2] S. Ankrah and O. AL-Tabbaa, *Universities-industry collaboration: A systematic review,* Scandinavian Journal of Management **31**, 387 (2015).

[3] K. Mona and I. van Engelshoven, *Beleidsreactie op de evaluatie van het Valorisatieprogramma 2010-2018*, Tech. Rep. (Ministerie van Economische Zaken en Klimaat, DEN HAAG Datum, 2018).

[4] GenISys GmbH, *BEAMER v5.6.1 Manual,* (2018).

9

Conclusion

The goal of the thesis was to develop a Monte Carlo simulator that can simulate 3D effects and charging effects such that it can be used for industry-driven applications. We achieved these goals by improving the electron scattering and charging models in the available simulators, performing a sensitivity analysis on the models, and developing metrology and lithography use cases from the semiconductor industry.

The following conclusions, grouped into three subcategories, can be drawn from the thesis.

9.1. Monte Carlo simulator, SEM signal, and the CD measurement

The simulation models were verified by comparison to experimental and calculated data for silicon and copper. This data contains SE/BSE yields, energy spectra, angular emission distributions, and the yield versus angle of incidence. Our simulated SE yield curves are a factor of two higher than the literature data, but the relative trends match well. This allows studying SEM images where the signal intensity is a relative value of emitted electrons.

Different choices of atomic potentials (free atom, muffin-tin, etc.) for the calculation of the Mott cross-sections do not affect the yields or line scan signal of a Manhattan feature significantly, if the cross-sections are used for energies > 200 eV. On the other hand, SE yields are shown to be sensitive to model and parameter changes for energies < 200 eV.

Novel multi-energy SEM images are introduced for a sensitivity analysis of simulated CD to model ingredients over a broad energy range.

We found that the quantum mechanical interface transmission model (QT) is an essential model for reproducing the shadowing feature in the line scan signal of Manhattan structures.

Sensitivity analysis showed that the AC-phonon scattering model and QT model significantly impact the signal intensities for energies up to 1 keV.

Both AC phonon and QT models change the emission in a topography dependent way; this will affect height measurements based on signal intensities.

Two different CD measurement methods based on 50 % of the threshold were used to measure CDs at different energies. The two methods differ in the choice of the signal minimum. One uses the absolute minimum signal, and the other uses an average value for the minimum. However, the effect of this difference on the CD measurement is insignificant for energies up to 1 keV. Above 1 keV, the shadowing effect on the line scan signal disappears. This increases the uncertainty in the determination of the signal minimum, and as a result, leads to a difference in the CD measurements resulting from the two methods.

Using AC phonon-scattering cross-sections instead of Mott cross-sections affects the linewidth measurement error of 32 nm lines by less than 2 nm.

9.2. 3D effects

We have shown that Monte Carlo simulations can be very useful for developing applications for 3D SEM metrology and e-beam lithography. This is very important since the 3D effects become prominent as structures get smaller, the sample is tilted, or non-flat surfaces are used.

We have introduced a technique to estimate the height of step-like structures from top-down SEM images. With this technique, the signal and beam energy versus structure height relationship for top-down images is demonstrated and quantified for the first time. The phenomenon was verified by experiments. The simulation and experimental results were within approximately a factor of two.

We have shown that the method cannot be used to resolve height information above 10 nm at typical CD-SEM energies (≈300 eV).

In 2D lithography applications, a radially symmetric point spread function (PSF) is often employed in the proximity effect correction (PEC) process. However, for 3D applications, it is important to take the 3D electron-matter interaction volume into account. We have shown that using a non-radially symmetric PSF and an adapted PEC algorithm improves the e-beam patterning accuracy on tilted and curved surfaces.

9.3. Charging

A state of the art Monte Carlo simulator has been developed to simulate charging effects. This simulator contains sophisticated electron-matter interaction models and charge redistribution models. This version is superior to its earlier version, with more accurate low-energy electron scattering models and more elaborate models for charging dynamics. This is important because it allows studying the charging effect in SEM metrology and e-beam lithography using more reliable simulations.

A charge mobility model is required in the simulators to simulate charging. Otherwise, unrealistically big potentials occur. Introducing redistribution models helped to solve this problem.

We succeeded to simulate charging contrast versus dose in SEM images. In addition, the simulator can simulate induced-conductivity on insulators. This is an important electron-beam testing technology for inspecting active components of electronic circuits.

We found that, at 50 keV, the charging effect is significant during EBL on glass wafers. Both simulations and experiments prove this.

Smart writing strategies can help to reduce charge-induced beam displacement during e-beam writing. We showed the effect of four different scan strategies. We predicted displacement patterns by simulations and verified them by experiments. The agreement was qualitatively good and quantitatively within a factor of 2.

EBL experiments prove that not only the pattern fidelity but also the feature size can be affected dynamically as the charge accumulates in the sample.

With these results, we have fulfilled the research goals, which is the development of Monte Carlo simulations and providing computational solutions for the issues related to charging and 3D effects in metrology and lithography.

Acknowledgements

During the course of my Ph.D., I received the support of many people. One way or another, they all contributed to my doctoral experience, which became a precious memory to cherish forever. I owe each of them special thanks.

First and foremost, I want to express my sincere thanks to my promoters, Kees and Pieter. Their supervision and knowledge which help me to grow a lot.

Our weekly meetings with Kees, trips to Orlando and Minneapolis, going over again and again on my presentations, giving him hard times with my complicated manuscripts, and also having hard times with his questions. Once, after an acceptance from a journal in 3 weeks, he came to congratulate me. I needed to reply: "it is not three weeks; it is a year (referring Kees' initial review process) plus three weeks". I appreciate all these efforts. Thank you very much!

I still remember my interview with Pieter in Delft. I asked him what do you expect from me as a graduate student. He stood up, walked to his wardrobe, opened and showed me the theses that he supervised, telling "I want one from you too!". I am happy to fulfill this request now. Besides, our trip to San Jose, project meetings, I always remember his questions when I use the word "good" in a technical context: "What is good?; Define it; Can you quantify it?". A big lesson for a young metrologist. Thank you!

I am grateful to GenISys and Raith, who financially and technically supported this project: Uli, Nezih (thanks for always pushing me hard), Thomas, Nicola, Kai, and Robert from GenISys; and Christiaan, Bas, and Janine from Raith. Most of these names are the co-authors of my papers. Thanks again.

I especially want to thank Thomas Klimpel, who has a great contribution to my knowledge, both during my master's years and doctoral journey. So many nights, you supported me from Munich in hunting the bugs on the codes, implementing new algorithms, and discussing the models.

I want to thank another Thomas too. Thomas Verduin was close to finishing his PhD but still helping me learn the details of electron-matter scattering with his outstanding teaching skills.

Jens Bolten who is my first SEM supervisor and co-author. Thanks for always being there whenever I have questions about SEM.

Wilco, Dusan, me, Gaudhaman, Aditi and Maurice the last big wave of CPO (now it is MinT). We all started our PhDs so close to each other, i.e. Gaudhaman (my first officemate) just started the next day. They all made this journey such a memorable experience all the group discussions, (strong) coffee breaks, day outs, and many more. Of course, there is much more: Jacob, Gerward, Marijke, Sangeetha, Shammi, Leon, Yan Ren, Aya, Luc (I am glad for opportunities to discuss physics with you, and thanks

for your feedback on chapter 2 of this thesis), Anne-Marie, Vidya, NGC (also known as Nicolo), Neda, Xiaoli, Lixin (the master-chef), Laura, Sergey, Xin, Ryan, Mathijs, Yoram, Marco, Elizabeth, Dan, Huma, Leoni, Sebastian, Yuri, and Wouter. Thank you all.

The best support team of CPO: Dustin, Martin, Han, Johan, especially Carel, my dear cleanroom supervisor. Thanks for your all support.

Anjella, I want to thank you specially. You were there whenever I need help even before I came to Delft.

The Turkish crew in TU Delft: Nalan, Ulaş (thanks for Turkish coffees), Sabri, Selman, Umut, İsmail Abi, Ahmet, Adem, Faruk, Yunus Emre, Çağlar, and Prashanth :).

Shan and Ulaş thank you for hosting me and being great housemates.

İbrahim Abi and his team, Çağrı and Zülfi Abi who supported me with their great food and greater friendship before long-shifts.

My rowing friends Jeannette, Martin, Sanne, Jurjen, Marjon, Marjolein, Maarten, and Suha who all helped me to have great time during rowing.

My friends Rıdvan, Orhun, Altuğ, Gökçe and Emirhan who all visited me in Delft. Erkin, Ertan, Gökhan, Berk, Alper, Başar, Methmet, Fatih, Uygar, Cem, Anıl and Begüm thanks for your nice calls.

Mehmet Hocam, Muhrammem Abi, Abdurrahim Abi, thanks for all the support.

My dear friends in Germany: Mido, Bengi, Elif, Setenay, Osman, Esra, Zehra, Kujtim, Ahmet, Veli, Karl, and especially Familie Ünal. Thank you!

And those who supported me in the US while I am finalizing this thesis, Shadi, Yalkın, Brigitte, Sammy, Irek, Andras, John, Glenn, especially Cali, my dear housemates Marlou and Yogi.

Doktora yolculuğumun başından sonuna kadar yanımda olan sevgili Tuğba. Mülakatlar sırasındaki heyacanımı paylaştın. Münih'ten Delft'e beraber taşındık. Acı tatlı bir çok anımız oldu. Aramızdaki arkadaşlık bağının hep çok sağlam kalacağına eminim. Her şey için çok teşekkür ederim.

Lieve Marijn, we had such a great connection. You colored my life not only in the Netherlands but also so many other places. I did not know microscopy could attract someone. Do you remember our first conversation on atomic force microscopy. That lead to such an amazing relationship. You always supported me for my long working nights, and you are one of the unique people who read all of my chapters. Our friendship will be forever. Thank you and all your family.

Calanthe, I am amazed by someone's teaching ability. You are the one learning Turkish to be able to teach me how to pronounce English words better. We had so many technical discussions. Not only that one you also helped me a lot not to miss home with supply of "şalgam suyu". The best guide ever in DC. Thank you also for proofreading my thesis reading truly. The jig is up!

Sevgili büyük ailem, babannem, ananem, dedelerim, amcalarım, teyzelerim, enişte m ve kuzenlerim, sizin varlığınız bana her zaman güç kattı.

Baba'cım Mustafa, Anne'cim Işık, kardeşlerim Ayşe Nur ve Dilnur. You have always

supported me, shared my bitter-sweet moments. Never left me alone and always encouraged me to follow my dreams. My biggest treasure!

Curriculum Vitæ

Kerim Tuğrul ARAT

Born in 10-September-1989,
Samsun, Turkey.

Education

2013 - 2015	M.Eng. in Electrical Engineering & Information Technology, Rosenheim University of Applied Sciences, Germany Thesis: ”Electric Fields in SEM Simulations” (Grade A)
2007 - 2012	B.Sc. in Electrical and Electronics Engineering, Bilkent University, Turkey Thesis I: ”Designed and implemented (in VHDL) an underwater acoustic telephone.” (Grade A-) Thesis II: ”Designed and implemented (in C) of a fire & motion detector” (Grade A)

List of Publications

Kerim T. Arat, Cornelis W. Hagen: Model sensitivity analysis of Monte-Carlo based SEM simulations,*Results in Physics*, Volume 19, 12/2020, 103545, DOI:10.1016/j.rinp.2020.103545

Kerim T. Arat, Thomas Klimpel, Cornelis W. Hagen: Model improvements to simulate charging in scanning electron microscope. *Journal of Micro/Nanolithography, MEMS, MOEMS*. 12/2019; 18(04):1. DOI:10.1117/1.JMM.18.4.044003

Kerim T. Arat, Aernout C. Zonnevylle, Wilhelmus S. M. M. Ketelaars, Nikola Belic, Ulrich Hofmann, Cornelis W. Hagen: Electron Beam Lithography on Curved or Tilted Surfaces: Simulations and Experiments. *Journal of Vacuum Science & Technology B* 09/2019; 37(5): 051604. DOI:10.1116/1.5120632

Kerim T. Arat, Thomas Klimpel, Aernout C. Zonnevylle, Wilhelmus S. M. M. Ketelaars, Carel Th. H. Heerkens, Cornelis W. Hagen: Charge-induced pattern displacement in E-beam lithography. *Journal of Vacuum Science & Technology B* 09/2019; 37(5):051603, DOI:10.1116/1.5120631

Kerim Tugrul Arat, Jens Bolten, Aernout Christiaan Zonnevylle, Pieter Kruit, Cornelis Wouter Hagen: Estimating Step Heights from Top-Down SEM Images. *Microscopy and Microanalysis*, 05/2019, DOI:10.1017/S143192761900062X

Kerim T. Arat, Thomas Klimpel, Cornelis W. Hagen: Model improvements to simulate charging in SEM. *Proc. SPIE 10585, Metrology, Inspection, and Process Control for Microlithography XXXII*; 03/2018, DOI 10.1117/12.2297478

Jens Bolten, Caroline Porschatis, Thorsten Wahlbrink, Max C. Lemme, Nezih Ünal, **Kerim T. Arat**: Challenges for scanning electron microscopy and inspection on the nanometer scale for non-IC application: and how to tackle them using computational techniques. *Proc. SPIE 10446, 33rd European Mask and Lithography Conference*; 09/2017, DOI:10.1117/12.2279564

K. T. Arat, J. Bolten, T. Klimpel, N. Unal: Electric fields in SEM simulations. *Proc. SPIE 9778, Metrology, Inspection, and Process Control for Microlithography*; 03/2016,DOI:10.1117/12.2219182